Advancements in converter-based frequency stability

Recommendations for industrial applications

PhD Thesis

Sam Lachlann Harrison

Wind and Marine Energy Systems CDT & PEDEC Group
Department of Electronic and Electrical Engineering
University of Strathclyde, Glasgow

July 11 2023

This thesis is the result of the author's original research. It has been composed by the author and has not been previously submitted for examination which has led to the award of a degree.

Signed: Sam L Harrison

Date: 11/07/23

Abstract

The burning of fossil fuels and related carbon emissions are driving the ongoing climate crisis. A critical path to fully decarbonise the power system is to enable low-carbon converter-interfaced devices to take on responsibility for the generation of electrical energy. However, a low-carbon electrical power system also requires the converters to provide the features that fossil-fuel-powered synchronous machines (SMs) conventionally provide to stabilise the electrical grid.

The electrical frequency is one key system parameter that needs to be stabilised. Converter-based frequency stabilising solutions have been proposed but the nuance of their operation is not fully understood. Therefore, this thesis aims to address some of the critical hurdles that the solutions must overcome.

The thesis initially outlines the technical characteristics that are required to provide inertial and droop responses. Academic and industrial data are assessed to identify the technologies that are techno-economically suited to provide the support.

The impact of different controller choice for droop provision is assessed. Previous works have suggested that certain droop controllers are equivalent but often only consider the steady state. Models of Synchronverter and Grid-forming (GFM) Droop controlled ideal energy storage systems are assessed to identify the equivalence of the controllers' frequency support. A tuning guide developed earlier in the thesis enables the controllers to provide equivalent inertial and droop responses but the dynamics of each controller are shown to be different. The impact of the GFM Droop's cascaded controllers and its parametric tuning on the frequency support are then assessed and suggestions are made for their tuning.

The industrial attempts to quantify useful inertial response are then assessed. Parametric sweeps of example GFM and grid-following (GFL) controllers are carried out to compare their full capability with the industrial specifications. A more detailed power system model is also used to validate the findings of the parametric sweeps and to assess the impact of the controllers’ properties on the system frequency. The study highlights that useful inertial provision is not unique to GFMs, that GFLs should not be subject to blanket disqualifications from inertial support, and that transient phase responses may require more consideration in converter dominated systems.

Finally, the ability of system operators (SOs) to measure wind turbine (WT) based inertial support is assessed. Experimental data of a grid-connected wind farm are used to identify the impact that the wind has on the inertial response. A review is carried out to assess the methods that are currently available to measure WT inertial response (including the existing industrial standard). The accuracy of the existing methods are assessed using a model of a WT and its converters, which resolves the dynamics from wind energy source to grid. Two new approaches are proposed that improve the accuracy of WT inertial response measurement.

Contents

List of figures

List of tables

Nomenclature and abbreviations

Table 1 Abbreviations and nomenclature

AC	Alternating current	PC	Power control(ler)
ACC	Acceptable	PCC	Point of common connection
AEMO	Australian Electricity Market Operator	P-F	Power-frequency
APP	Apparent	PFR	Primary frequency response
AVLB	Available	PHS	Pumped-hydro storage
BESS	Battery energy storage system	PI	Proportional-integral
CAES	Compressed air energy storage	PLL	Phase-locked loop
CAPEX	Capital-expenditure	PMSG	Permanent-magnet synchronous generator
CC	Current control	PSS	Power system stabiliser
DC	Dynamic Containment	PU	Per-unit
DR	Droop response	PV	Photovoltaic
EMT	Electromagnetic transient	PWM	Pulse-width modulation
ESS	Energy storage system	Q-V	Reactive power-voltage
EST	Estimated	RES	Renewable energy source
EXP	Expected	ROCOF	Rate of change of frequency
FDF	Frequency-divider formula	RT	Rise time
FESS	Flywheel energy storage system	SC	Supercapacitor
FFR	Fast frequency response	SCC	Short circuit current
FS	Frequency support	SCR	Short circuit ratio
GB	Great Britain	SFR	Secondary frequency response
GBR	Gearbox ratio	SG	Synchronous generator
GFL	Grid-follower(ing)	SM	Synchronous machine
GFM	Grid-former(ing)	SMES	Superconducting magnetic energy storage
GFMD	Grid-forming droop	SO	System operator
IC	Inner control(ler)	SPR	ScottishPower Renewables
IEC	International Electrotechnical Commission	SSM	Small signal model
IEEE	Institute of Electrical and Electronics Engineers	ST	Settling time
IGBT	Insulated-gate bipolar transistors	SYN	Synchronverter
IR	Inertial response	TFR	Tertiary frequency response

KE	Kinetic energy	TN	Transmission network
LCL	Inductor-capacitor-inductor	UK	United Kingdom
LI-ION	Lithium ion battery	VC	Voltage control(ler)
LPF	Low-pass filter	VDE FNN	Verband der Elektrotechnik, Elektronik und Informationstechnik (Network Operator)
MPPT	Maximum power point tracking	VRB	Vanadium redox battery
NAS	Sodium sulphate battery	VS	Voltage source
NFP	Network-frequency perturbation plot	VSC	Voltage source converter
NG ESO	National Grid Electricity System Operator	VSM	Virtual synchronous machine
NMC	Lithium Nickel Manganese Cobalt Oxide battery	WF	Wind farm
OC	Outer control(ler)	WT	Wind turbine
OPEX	Operating expenditure	ZNBR	Zinc Bromine battery
OS	Overshoot		

Acknowledgements

First of all, I would like to thank Agusti, my primary supervisor, for your support throughout these years from the basic to more complex topics, your academic direction, and your humour. Then Panos, for your additional guidance and support, which was needed at times. I would also like to thank those at ScottishPower Renewables who enabled, supported, and showed interest in the PhD and research topics. Then I would like to thank some of my collaborators: Hector, who offered a very enjoyable first academic collaboration, and Callum, whose mathematical and modelling guidance has been greatly appreciated.

I would like to recognise my PEDEC and power systems colleagues, whom I have enjoyed sharing meetings and knowledge with, and have particularly enjoyed sharing a workspace since returning. I also want to thank my Wind and Marine Energy System CDT colleagues. Thank you for giving me the opportunity to move into this field and providing me with the tools to progress. Specifically, I'd like to thank Drew for his support throughout the first year and beyond, and Alasdair for his mentorship. Then I would like to thank the other members of the CDT, particularly my cohort, whom I have enjoyed many days and evenings with.

I would like to thank all of my friends for providing me with a space to take my mind off the PhD. I would like to thank my family – Amy, Helen, and Mark – for their support, which has given me the fundamental confidence to pursue anything and to continue persevering throughout it, which this thesis may be the clearest example of so far. Finally, I would like to thank Laura, for her happiness, excitement, and belief in me, who has made the last three years much more enjoyable.

Chapter 1. Introduction

1.1. Background

Anthropogenic emissions resulting from the burning of fossil fuels are driving the ongoing climate emergency and rising global temperatures [1] These fossil fuels are used to power SMs. Accordingly, the decarbonisation of the energy system is seen as a critical issue and the GB System Operator (SO), National Grid Electricity System Operator (NG ESO), have pledged to achieve net zero carbon emissions operation by 2050 [2]. Efforts to decarbonise have already seen the rapid decommissioning of coal and oil SMs, the worst offenders in terms of carbon emissions, with a target to completely phase coal off of the GB electricity network by 2024 [3]. The decommissioning of other SMs is ongoing.

Meanwhile, alongside the decommissioning of SMs to reduce emissions, the penetration of converter interfaced devices is increasing. Converter interfaced devices are increasingly observed on systems for several reasons. Firstly, key low carbon renewable energy source (RES) generators such as wind turbines (WTs) and Solar photovoltaic (PV) are interfaced by converters. Secondly, these RES technologies possess the lowest costs of energy of any generation type [4]. The desire for low carbon and cheap generation has unsurprisingly resulted in an explosion of RES capacity: in 2021 16% of European electricity demand was met by WTs [5] and 25.9 GW of new Solar PV capacity was installed on the European Grid [6] while the UK government alone pledged to install 40 GW of WTs to power its nation [7]. Converters are also used to interface interconnectors and energy storage systems, which are increasingly desirable to achieve flexible system operation. GB already has 4 GW of interconnectors and plans 7.7 GW of new capacity [8].

Although decommissioning SMs provides benefits for carbon emissions, it can also result in issues for the grid stability, which has been identified as a key issue for future power systems [9]. Among the stability features of SMs, loss of inertial energy storage and sources of frequency support have been highlighted as some of the most important [10]. The electromagnetic coupling between SMs and the grid enables inherent and instant responses to grid changes but this coupling is not present in converters. The displacement of SM stability sources resulting from increased converter-based capacity has been explicitly linked to increased frequency variations and reduced frequency stability [11], [12].

To avoid these issues and maintain stability, systems have to limit the penetration of converters [13], [14], thereby slowing the rate that net zero and cost-effective transitions can occur. The GB system is an example that has been found to be at risk of low inertia and hence been forced to curtail considerable existing RES capacity [15]. Considerable cost is forecast to be required to reinforce the grid [16] and/or to find new sources of stability to support further grid transition to high converter penetrations.

In recent years, SOs in the critical systems with rapidly increasing converter penetration have been required to begin to apply other solutions to maintain stable operation on their transforming systems. A simple but expensive approach has been the re-dispatch of SMs to ensure sufficient inertia is online at any given time [17] but this is not sustainable to achieve low carbon operation. The Australian Electricity Market Operator (AEMO) and NG ESO have both deployed synchronous condensers as an alternative to increase the inertia and provision of short circuit current (SCC) [18], [19]. The synchronous condensers provide synchronous stability features to the grid, similar to standard SMs, but require energy input to spin up. Several examples of long-term tendering or the development of markets to stimulate inertia delivery have also been observed [17], [20], [21]. Another quick fix to minimise undesired side-effects of increased frequency deviations has been the extension of protection Rate of Change of Frequency (ROCOF) relays to wider settings to minimise the disconnection of distributed generation during disturbances [13], [22].

However, it is also desirable to stimulate stability provision from converters as these devices are likely to make up a large proportion of the generating capacity on future grids. The investment in the future grid can be minimised by utilising these existing energy sources [23]. For example, delivery periods of primary frequency services have been adapted to allow the most effective use of converter-interfaced energy source response times to constrain frequency deviations on many systems around the world [24]. Moreover, control solutions exist that allow converters to emulate the fast dynamics of SMs that have conventionally stabilised the grid [25]–[28]. Grid-following solutions exist that can support the grid while maintaining desirable converter focussed operating objectives to ensure safe operation of the converter hardware [25]. Alternatively, Grid-forming solutions offer a grid focussed response type that may offer improved grid stability [29], [30]. Any (voltage-source) converter-interfaced technology is capable of providing these stability features to the grid so long as there is sufficient energy stored on the DC-side of the converter [31]. However, the critical nature of the climate emergency means that SOs are trying to stimulate the rapid roll-out of these solutions without a full understanding of the nuances of different control and technological approaches.

1.2. **Thesis objectives**

This thesis aims to identify and solve some of the hurdles that limit the rate at which frequency support can be implemented using converters (and hence the rate at which the power system can decarbonise). The review of the state of the industry and literature shows that existing technologies and control strategies are capable of providing the desired support functionality. The remaining hurdles are related to the understanding of these solutions, their impacts on the grid's dynamics and stability, and the means to integrate these solutions into the complex power system.

Tuning guides are developed and validated that allow the exact specification of frequency support characteristics from different converters. However, this poses the question: do controllers possess different frequency support features? Analyses are made of different control configurations to compare their stability and dynamic properties during inertial and droop provision. The impact of implementing cascaded controls below the outer controller are assessed. The impact of the cascaded tuning is also considered. These conclusions can inform device owners on the appropriate control strategies, configurations, and tunings to implement the desired frequency support (defined by system operators in terms of specifications) in a straightforward and informed manner.

Grid codes and requirements are being developed to specify desirable frequency supporting converter solutions [18], [32], [33], however, their assumptions regarding different control approaches and confusion of different dynamic features appears to be leading to the disqualification of entire families of controllers. This thesis will provide explicit definitions of the different frequency stabilising features. The capability of controllers will be compared to the critical stabilising features and to the proposed specifications to ensure that: 1) the requirements directly correspond to the inertial response feature they are attempting to qualify and 2) all of the critical stabilising features are being accounted for. This analysis can inform the development of industrial specifications to ensure that the grid remains sufficiently secure. The analysis can also support the inclusion of a wider set of solutions to be considered for grid stabilisation and ease the transition to net zero.

Finally, the dynamics of the specific energy source are often neglected when considering the provision of frequency support to the grid. One device that is being considered for frequency support that has particularly complex dynamics is the wind turbine. Experimental data is assessed to identify the dynamics of WT inertial response. The methods to measure WT inertial response are assessed and proposals are made to improve their accuracy. The analysis can improve the understanding of the complex interaction between energy source and grid support to better inform the system operator about the WT's capabilities. Then, the proposed methods can be used to qualify, integrate, and potentially monitor WT grid support.

1.3. **Summary of work**

Chapter 1 provides an overview of the features of SM operation that have stabilised conventional power systems. The fundamental features of converter operation are then described, which highlights the need for new stabilising solutions. Finally, the grid-following and -forming converter families are introduced, and their abilities to support power system frequency are discussed.

Chapter 3 provides a techno-economic assessment of converter-interfaced technologies to provide frequency support. This assessment highlights that there are several converter-interfaced technologies that possess suitable power and energy density, durability, and costs to provide the inertial and droop responses that are needed to stabilise the power system. The remainder of the chapter introduces the hurdles to the implementation of these solutions that will be studied later in the thesis. The equivalence between GFM Droop and Synchronverter controllers is introduced, as well as the impact of the presence of cascaded controllers. Then, the efforts to develop grid code specifications to describe useful inertial response and the potentially inappropriate disqualification of grid-following controllers are discussed. Finally, the impact of WT dynamics on inertial monitoring and the disagreement between measurement methods on the impact of the wind is overviewed.

Chapter 4 describes the modelling approaches used throughout the thesis. The reference frames and model types are introduced. The mechanical and electrical systems used to model an ideal battery energy source, a wind turbine, power converters, and the power system are described. The control strategies to manage the wind turbine, the generator-side converter, and the network-side converter are detailed and tuning guides are provided to set the frequency response properties of the latter. The considerations for small-signal modelling are then described.

Chapter 5 carries out several functions. Firstly, the tuning guides developed in Chapter 4 are validated. Secondly, the steady-state and dynamic capabilities of the GFM Droop and Synchronverter controllers to provide inertial and droop response are compared.

Thirdly, the impact that the presence and tuning of the cascaded controller on the GFM Droop is assessed. Recommendations are made to tune the GFM Droop and to identify the damping of the different control configurations.

Chapter 6 describes the existing industrial specifications that are used to describe and qualify useful inertial response. Then, an ideal battery energy source controlled by either an example GFM or an example GFL inertial strategy are subject to parametric sweeps to identify the impact that all of the control settings have on the inertial delivery. The optimal tuning to meet the inertial specifications are identified for each controller. The optimal tunings are validated on a multi-bus power system model. The impact of the different control features on the system's frequency stability is assessed. The chapter aims to identify 1) if useful inertial response can only be sourced from GFMs and 2) how effective the inertial specifications describe the effective containment of the initial power system frequency excursion.

Chapter 7 uses experimental data to assess the impact that a wind turbine's dynamics have on inertial provision. The methods to measure inertial response are reviewed in detail and the accuracy is assessed using the experimental data. Two proposals are made to improve the inertial measurement, one simple adaptation using a new baseline reference and another system identification-based approach that accounts for the response dynamics. The accuracy of the methods from the literature and the proposed methods are assessed using a model of a wind turbine connected to the grid and then validated using the experimental data.

1.4. Scientific contributions

- Overview of the steady-state and dynamic features of the Synchronverter and multi-loop GFM Droop to provide inertial and droop responses on different grid strengths
    - Confirmation of the impact of cascaded controller configuration and tuning on the stability and dynamics (overshoot and settling time) of a GFM controller's active power response to a frequency disturbance

    - Suggestions are made to update the damping expression of GFM with a cascaded controller and to tune the voltage controller to improve its damping
- Highlight the confusion of inertial response with instantaneous GFM voltage-source properties
    - Make suggestions to ensure that specifications explicitly describe useful inertial responses
    - Prove that an example GFL controller is capable of providing as fast and effective inertial response on medium to high strength grids, suggesting that they should be allowed to participate in inertial services
- Identification that voltage-source properties can be critical for the initial containment of grid frequency, highlighting the need for their explicit definition in specifications for frequency stabilising solutions
- Confirmation of the impact of a wind turbine's dynamics on inertial response using experimental data from a grid-connected wind farm
- Proposal of two new methods to measure inertial response from wind turbines more accurately throughout wind variations: the Improved IEC Method and the Equivalent Swing Method
    - Assessment of the accuracy of the existing industrial and the proposed wind turbine inertial response measurement methods throughout different wind and frequency disturbance conditions and for different inertial contributions, which proves that the proposed methods are more accurate than the existing methods

1.5. **List of publications**

- S. Harrison, P. N. Papadopoulos, R. D. Silva, A. Kinsella, I. Gutierrez and A. Egea-Alvarez, "Impact of Wind Variation on the Measurement of Wind Turbine Inertia Provision," in IEEE Access, vol. 9, pp. 122166-122179, 2021, doi: 10.1109/ACCESS.2021.3109504.

- S. Harrison, C. Henderson, P. N. Papadopoulos and A. Egea-Alvarez, "Assessment of droop and VSM equivalence considering the cascaded control dynamics," The 17th International Conference on AC and DC Power Transmission (ACDC 2021), 2021, pp. 126-131, doi: 10.1049/icp.2021.2456.
- S. Harrison, C. Henderson, P. N. Papadopoulos, A. Egea-Alvarez, "Demystifying inertial specifications; supporting the inclusion of grid-followers." in IET Renew. Power Gener., 2023, doi: 10.1049/rpg2.12711

- H. Beltran, S. Harrison, A. Egea-Àlvarez, and L. Xu, "Techno-Economic Assessment of Energy Storage Technologies for Inertia Response and Frequency Support from Wind Farms," *Energies*, vol. 13, no. 13, p. 3421, Jul. 2020, doi: 10.3390/en13133421.

Chapter 2. Frequency stability phenomena on converter dominated power systems

2.1. Introduction

Power system stability roughly depends on the balance of generation with demand but can be resolved on different timescales and for different phenomena. Conventionally, stability can be considered as a hybrid problem composed of three distinct fields: rotor angle, voltage, and frequency stability [34].

- Rotor angle stability requires sufficient capability of SMs to maintain angular equilibrium with one another, manifesting as the instantaneous conditions that determine SM operating conditions following disturbances, loss of which can materialise as angular swings and loss of synchronism between generators.
- Voltage stability is the ability of the system to achieve sufficient reactive power balance to support the desired transport of active power and manifests as the maintenance of constant voltages at all the nodes in the power system.
- Frequency stability describes the longer-term ability of the power system to maintain a balance between the generated and demanded active power. The network frequency can be used as a proxy to describe this balance (frequency decreasing as demand exceeds generation and vice versa) and has been incorporated into much of the power system's operational systems to signal the re-dispatch of generation or disconnection of load [35]

Additional fields have also been introduced to describe the interactions between converter interfaced devices [36]. The additional fields are defined as fast and slow interaction converter driven stabilities, which are impacted by the dynamics of converter controllers that can interact with electromechanical devices across a much larger frequency range than SMs do [37], [38]. Although significant for the operation of a converter-dominated power system, these stability types are not considered in this thesis.

Although all of the fundamental phenomena are interrelated, the stability types are often considered independently to enable the tackling of a more manageable problem. This thesis will focus on the frequency stability problem for power system operation. To generalise, frequency stability can be considered to exist as long as the frequency varies relatively little and remains within the acceptable boundaries to ensure the safe operation of devices on the power system following a disturbance.

Conventionally, on short timescales, frequency stability is founded on the physical properties of the SM. The inherent voltage source behaviour of the SM combined with its ability to endure short periods of overcurrent allow instant injections of current to respond to variations in the grid and determine the evolution of electrical operating conditions [39]. This behaviour is a feature of angular stability and related to the synchronising torque contribution of SMs on the network (in response to large disturbances) but is a prerequisite for stable power transfer and therefore frequency stability. Another physical property of the SM that contributes to frequency stability is the large inertial mass associated with the SM’s spinning turbine and generator. This kinetic energy is linked to the grid dynamics due to the direct coupling across the stator and is transformed to electrical energy (known as an inertial power injection) once there is an imbalance in the power being fed and being demanded from the SM before the control strategy can respond [39]. The inertial power injections have been critical for limiting the severity of power imbalances and maintaining frequency stability on power systems.

A wide range of services have been developed to recover and rebalance the system state on longer timescales following the (often inherent) stabilising features of SMs. Again, due to their historical abundance, many of these slower services have also been developed to utilise the electro-mechanical properties of SMs. For example, a chain of response services have been developed that a system operator (SO) can use to ramp SM energy output up or down within given timescales using their fossil-fuel reserves to restore the system to a balanced state of generation and demand following power disturbances [35].

Renewable energy sources (RESs) offer low-carbon solutions that are capable of taking over large amounts of the generation capacity conventionally sourced from SMs. As well as the increased sustainability of RESs, they also now offer the cheapest methods to generate electricity [4] thanks to their freely available energy sources. As a result, massive increases in the deployment of RESs (and the effective displacement of SM generating capacity) has been observed [5], [6]. While certain operational issues are associated with the increasingly variable fraction of generating capacity associated with RESs, other issues are also associated with the dynamics of the power converter devices that interface the RESs to the grid and the complication of the conventional stability phenomena described above. In fact, power converters are also used to interface other devices that are increasingly common on modern power systems, such as energy storage systems (ESSs) and interconnectors, multiplying the scale of the converter-related stability issues.

Power converters are electrical devices that use controlled semiconductor switches to manage the properties of electrical quantities. Therefore, they are widely used to fit the properties of variable AC or DC output RESs, as well as DC output ESSs and interconnectors, to within the specific acceptable ranges that are required to maintain stability on the grid [40]. This action may take the form of increasing or decreasing the voltage magnitudes, transforming from DC to AC, and/or synchronising the AC output with the grid voltage frequency. There are three critical features of converter operation that differs from SM operation and impacts power system frequency stability: their limited thermal capability, their conventional operation as a current source, and their dependence on internal controls to balance the grid power. These features are introduced corresponding to the timescale of each phenomena.

Both SMs and converters establish voltages at their terminals to deliver power. This means that a transient (virtually instantaneous) response will automatically be provided when the grid impedance changes. The stator coils of a SM are capable of supporting significant current above the generator's rated (thermal) level for a continued period. Therefore, large transient currents can be pulled from the SM when the grid is subject to unexpected disturbances. In contrast, a converter's semiconductor switches have a low capability to endure current above their rated thermal capability [41]. This means that a converter will be unable to provide the same transient overcurrent that an equivalently sized SM can.

The next significant difference is related to the dependence of a converter's output on its control logic. The controllers use pre-programmed algorithms to respond to voltage and current measurements on the grid. Therefore, the converter's output is not electromagnetically linked to the grid dynamics. While a SM's operation is also determined by high level controllers, there is an additional electromagnetic coupling between the generator and the grid that impacts the output. This means that changes in the grid are physically linked to the dynamics of the SM. For example, the inertial energy storage associated with the spinning mass of a SM is described by the balance between the mechanical power input from the turbine and the electrical power demanded by the grid. When more electrical power is demanded than the available mechanical power the inertial energy storage will be used to meet the demand until the slower high-level controllers can respond by increasing the input power. The significance of the lack of dynamic coupling is that converters can only balance the grid power when their control algorithm is designed to fulfil the given function and can only do so once the analogue or digital measurement of the signals have been processed, after the transient instantaneous phenomena described above.

The final significant difference between SMs and converters results from the conventional control strategy that has been used to control the first generations of converter interfaced devices: Current Control. Current Control has been developed to achieve desirable operational objectives such as the independent control of active and reactive power flows while ensuring the physical capabilities of the converter are not exceeded [40]. To achieve these objectives, Current Control aims to ensure that the current that flows through the semiconductors does not exceed the rated level, irrespective of the grid conditions. Therefore, Current Control converters are controlled to behave as current sources on the grid [42], whereas, SMs are controlled to behave as voltage sources.

2.2. Conventional frequency stability from SMs

Power system stability has historically been classified into three categories: rotor-angle, voltage, and frequency stability [34]. The physical properties of synchronous machines (SMs) and a long-developed approach to system operation enabled the maintenance of these stability types. Recently, the stability classifications were extended to include converter interaction related stability [36].

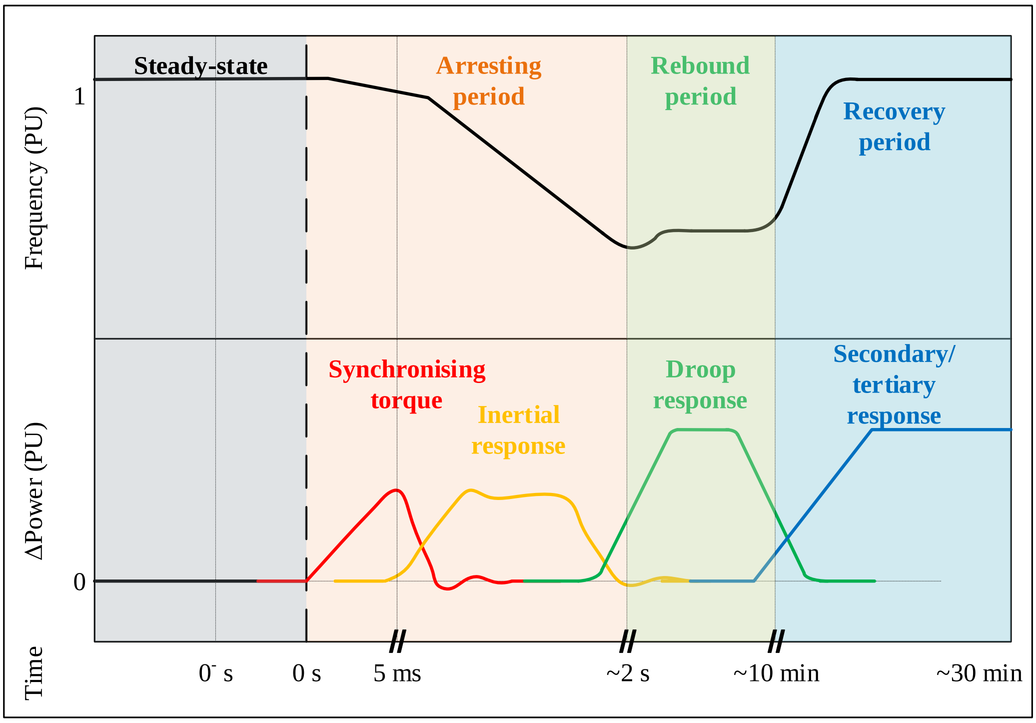

Figure 2-1 Progression of frequency stabilising features and services conventionally source from SMs represented in terms of their power injections and the corresponding frequency conditions. The magnitude of the power injections are not to scale and the x-axis time scale is broken into different resolutions of time periods of interest.

Frequency stability describes the ability of a system to maintain its equilibrium operating point on timescales of less than seconds to minutes, where the power output by generation balances that demanded by loads. Importantly, frequency stability is a slower manifestation of active power balance and hence stability. In contrast, rotor-angle stability, which describes the ability of the SMs to remain in synchronism with one another throughout angular disturbances, is the transient and therefore virtually instantaneous phenomenon that enables the stable transfer of power and is a pre-requisite for frequency stability.

With some simplification of the system dynamics, including the neglection of voltage stability phenomena, the critical features that ensure robust frequency stability on power systems dominated by SMs can be arranged with increasing dynamic time periods as pictured in Figure 2-1. The figure adapts conventional depictions of frequency stability services with additional resolution in the short period following a disturbance at $t = 0\ s$. The discrete contributions of each stabilising feature/service and the corresponding frequency conditions that coincide or drive these provisions are pictured, where a real SM response to a disturbance would likely resemble the aggregated sum of each power injection. The stabilising features and services are described in more detail below. The SM’s ideal responses to angular and frequency changes are simulated using the simple swing equation model detailed in Section 4.5.2.1 and the response to load changes on a multi-bus power system are simulated using the model described in Section 4.5.2.

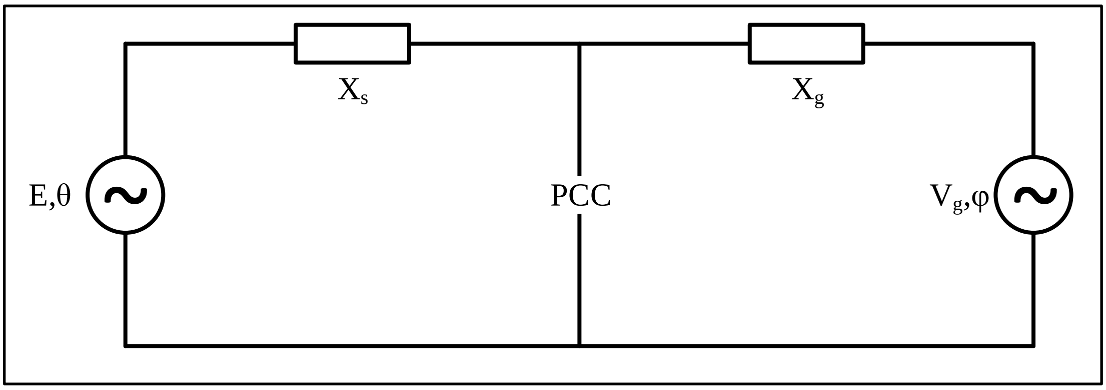

Figure 2-2 Circuit diagram of a simple network composed of two connected voltage sources, each with a series connected reactance.

2.2.1. Synchronising torque

Synchronising torque describes the instantaneous retarding forces that act to keep SMs in synchronism with one another. The forces describe the initial evolution of electrical properties on the grid in response to angular disturbances. To define the action of the synchronising torque, consider the equivalent circuit in Figure 2-2, which shows two voltage sources, each representing the ideal electrical behaviour of two connected SMs, connected to one another via a coupling impedance X_L (itself composed of a synchronous and grid reactance, X_s and X_g respectively) (1).

$$X_L = X_s + X_g \tag{1}$$

The sending voltage source has magnitude E and angle θ while the receiving voltage source has magnitude V and angle ϕ. The angle between the two voltage sources is represented by δ (2).

$$\delta = \theta - \phi \tag{2}$$

The active power transferred between the two representative SMs P can be found according to (3), when the dynamics are simplified by assuming stator resistance to be negligible.

$$P = \frac{EV}{X_L}\sin(\delta) \tag{3}$$

(3) describes the instantaneous power transfer conditions on the grid; if any parameter in the equation changes there will be an immediate change in the power transferred between the two SMs. Synchronising torque (which can be represented by the synchronising torque coefficient K_s) is the partial derivative of this instantaneous power transfer equation (3) with respect to a change in the angular difference (4).

$$K_s = \frac{\partial P}{\partial \delta} = \frac{EV}{X_L}\cos(\delta) \tag{4}$$

Therefore, the synchronising torque can be understood as the instantaneous power injection from a SM that responds to angular disturbances and maintain synchronism with the other generators on the grid. It is essential in maintaining the stable operating conditions of the generators, without which angular swings or complete runaway might occur and the stable transfer of power would break down. An example of a SM's response to a $\Delta\delta = -5^{o}$ angular disturbance on an infinite bus representation of a power system is shown in Figure 2-3 (during a sweep of the SM's inertia constant setting H, the significance of which will be discussed in more detail later). The Figure shows that the power injection occurs nearly immediately after the grid angle changes at $t = 0\ s$, depending only on the time constants of the electrical system to propagate the change.

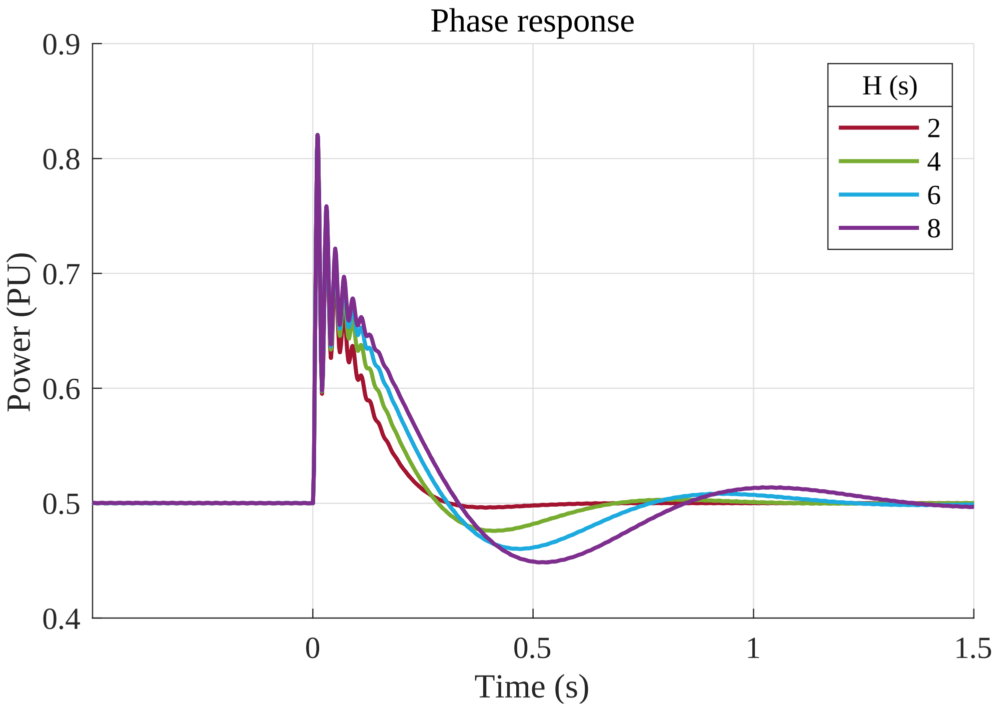

Figure 2-3 Phase response power of a SM to an angular disturbance of $\Delta\delta = -5^{o}$ *at t=0 s as the SM's inertial constant varies from H=2 to 8 s.*

The magnitude of the nearly instantaneous transient phase response does not vary with the inertial constant of the SM, however, the dynamics following the initial delivery do. As the inertial constant increases, the speed of the recovery to the nominal operating point slows. This points to a key transient feature of SMs for frequency stability: synchronising torque describes the instant response of a SM's voltage source that sets the initial electrical power change following a disturbance. Following this purely electrical phenomenon the resulting system conditions can interact with the electromagnetic and mechanical dynamics of the SM, such as the inertial energy storage.

2.2.2. Inertial response

Before discussing the SM's inertial energy storage and response, it is important to recognise its synchronous properties. A SM's stator electromagnetically couples its mechanical dynamics with the electrical properties of the grid. Due to the electromagnetic coupling, the SM's rotor speed ω_r is synchronised with the frequency of its electrical power output ω (proportional to the number of pole pairs P_n according to (5)) [39]. In this case, the electrical output frequency is that of the power system.

$$P_n \omega_r = \omega \tag{5}$$

The Swing Equation describes the balance between power input to a SM's rotor and extracted from its stator and the change in its rotational kinetic energy that results from any mismatch due to the electromagnetic coupling between the two (6).

$$\frac{d^2\theta_r}{dt^2} = \frac{d\omega_r}{dt} = \frac{\omega_0}{2H}(P_m - P + K_d \Delta\omega_r) \tag{6}$$

Where ω_r is the rotor speed (shown to be equal to the derivative of the SM's electrical frequency in (5)), ω_0 is the synchronous speed, P_m is the mechanical power input, and K_d is the damping coefficient of the SM, which acts on the displacement of the rotor speed away from its nominal synchronous speed $\Delta\omega_r$.

In steady state we can assume that a SM exists in equilibrium, where the mechanical power input to and the electrical power output by the machine are equal. According to (6), the derivative of the rotor speed must equal zero, and we can assume that this rotor speed equals the synchronous speed. Therefore, the damping component will also equal zero. Then, if a disturbance occurs on the grid, the electric power pulled from the SM will vary instantly as defined by (3) and it will differ from the mechanical power input to the SM. According to (6), this power imbalance must result in a change in the rotor speed of the SM.

For example, when more electrical power is demanded than injected to a SM the KE stored in the large rotating masses of the turbine and generator are transformed to electrical power to meet the demand. The transformation of the KE results in the slowing of the SM's rotor speed. This phenomenon can also be observed in power system dynamics (due to the electromagnetic coupling between SMs and power system electricity), where the power system's frequency will decrease when there is more demand than generation across the entire system. The larger the inertia of the SM or the power system, the more KE that is available to balance the initial mismatches in mechanical and electrical power, and the smaller (or slower) the resulting change in rotor or electrical angle and frequency. Alternatively, the relationship between inertial mass, KE, and rotor speed or frequency can be considered from an inverse perspective for both SMs and power systems. Where previously the impact of inertial response has been described as a transformation of KE to meet a power balance and resulting change in rotor speed or frequency, the dynamics can also be considered as a change in the active power injection from a SM due to a change in the frequency at its stator, which drives a change in the rotor frequency and therefore associated KE. The former perspective is useful to consider the expected frequency changes of a power system, whereas, the latter is useful to consider the expected active power injection of a device in response to a frequency disturbance.

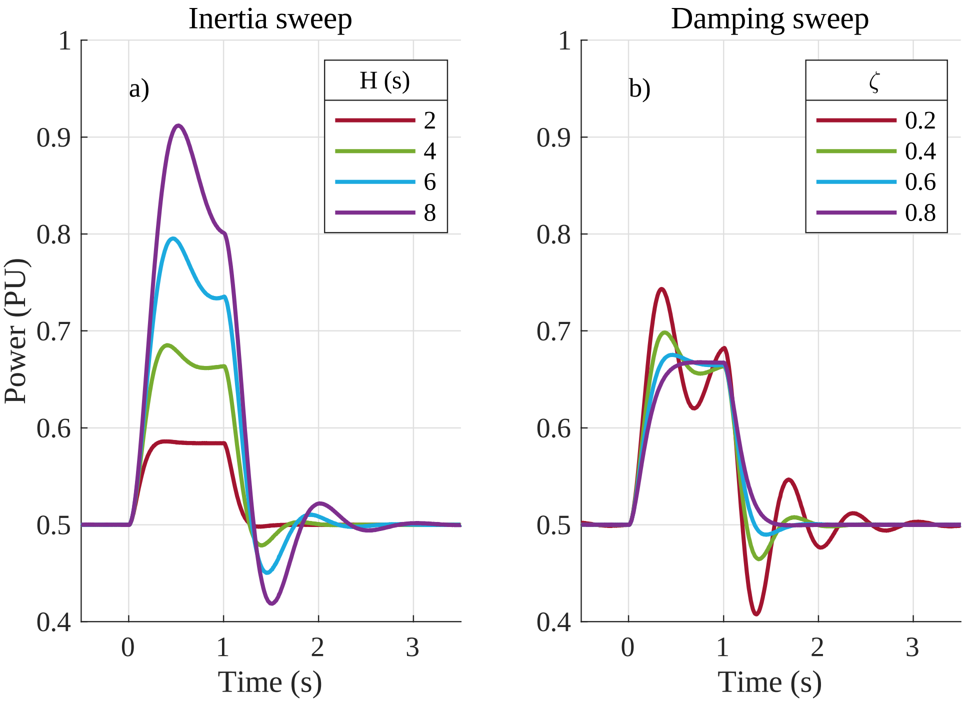

Figure 2-4 Inertial power injection by a SM in response to a frequency change Δf=-1 Hz with ROCOF=-1 Hz/s at t=0 s on an infinite bus representation of a power system as a) the inertia constant is varied from H=2 to 8 s for a constant damping coefficient K_d *and b) the damping coefficient is varied to achieve a range of damping ratios ζ=0.2 to 0.8 for a constant inertia H=4 s.*

Inversely, the SM's transformation of KE to meet increased load is often visualised as a power injection in response to a reduction in grid frequency, as pictured for a standard SM in Figure 2-4. Figure 2-4 a) shows the increase in the magnitude of electrical power injected to the grid as the inertia constant of the SM increases. The SM response takes longer to settle as the inertia increases. It is important to note that unlike the synchronising torque's response to an angular disturbance, the inertial injection does not reach its desired output for the constant ROCOF immediately. Figure 2-4 b) shows the inertial response of the SM to the same disturbance but now as its damping ratio ζ varies. For a constant inertia $H = 4\ s$, the SM is shown to achieve faster ramp rates but increased oscillations as the damping ratio decreases.

A power system disturbance (such as a step in the load) could be resolved as a hybrid combination of a coincident angular and frequency change. A SM's response to such a hybrid event is pictured in Figure 2-5. The same trends observed for the individual phase and frequency disturbances are observed in the hybrid event. The response shows the roughly constant magnitude of the synchronising torque injection immediately after the disturbance, irrespective of the inertial constant setting. The inertial injection is then slowly output, with the magnitude and time to settle both increasing as the inertial constant increases.

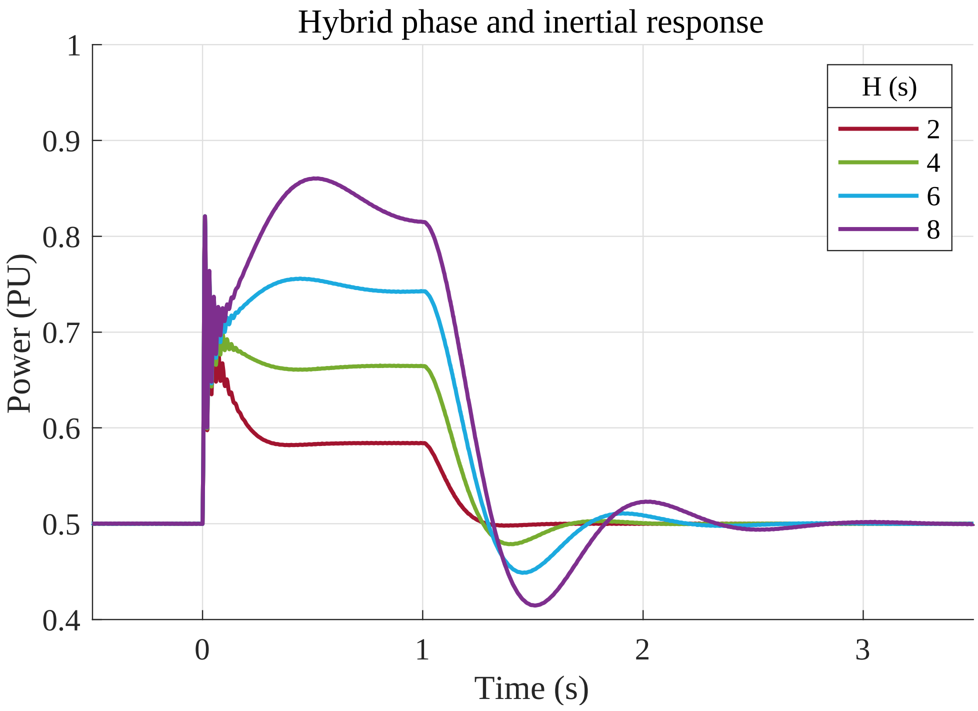

Figure 2-5 Power response of a SM to a hybrid angular Δδ=-5^0 and frequency disturbance Δf=-1 Hz, ROCOF=-1 Hz/s at t=0 s as the inertia constant varies from H=2 to 8 s.

Finally, Figure 2-6 shows the power and frequency signals of two SMs on a small power system model in response to a load step at $t = 1\ s$. The disturbance is a close representation of one that might occur on a real system and appears to include the hybrid combination of the initial angular disturbance and sustained frequency change. Both machines provide a rapid synchronising injection immediately after the load step that does not vary significantly during the sweep of the SM inertial constant (Figure 2-6 a) and b)). This initial transient injection corresponds to the synchronising torque's phase response. The inertial contribution is then delivered within the following second. The inertial power injection clearly varies with the different inertia configurations. An additional slower variation of power is also present, which will be discussed in 2.2.3.

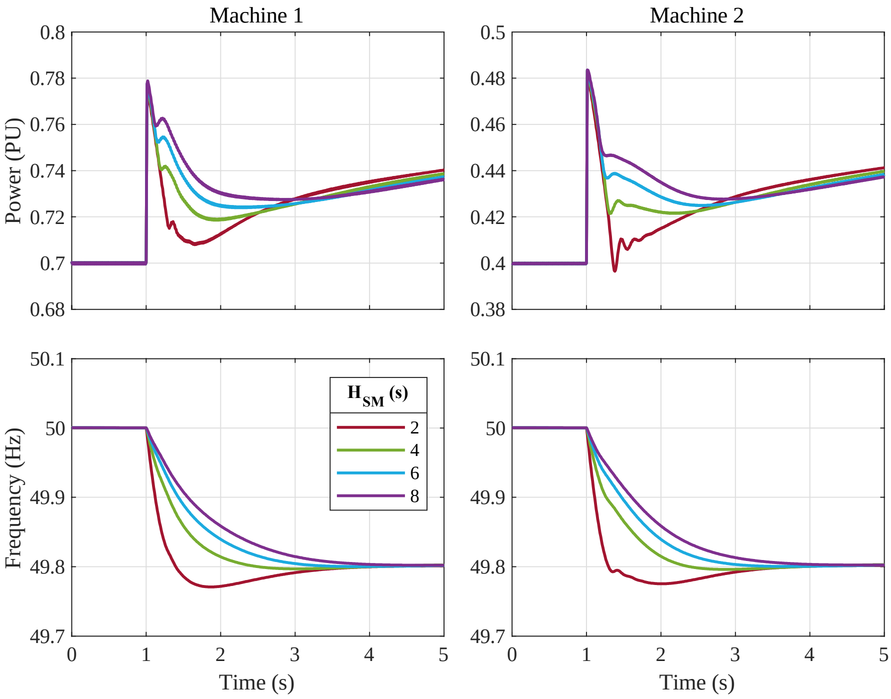

Figure 2-6 Power response of two machines, each with rated power S_n*=100 MVA, on a simple power system model that is initialised to deliver a load of* P_L*=110 MW, before an increment in the load* ΔP_S*=11 MW is added at t=1 s. The machines inertial constants are varied from* H_{SM}*=2 to 8 s.*

As described above, the initial ROCOFs of each machine following the initial disturbance (inferred as the rate of change of the frequency signals in Figure 2-6 and detailed in Table 2-1) should be determined as a result of the combined action of the synchronising torque and the inertia on the system. The synchronising torque injection remains roughly constant throughout the set of simulations, meaning that the ROCOF should only vary because of the different inertia levels. The simulations agree with (6), which show that the ROCOF magnitude becomes larger as the power system's inertia decreases and the otherwise equivalent systems experience lower frequency nadirs as a result of these more extreme ROCOFs (both shown in Table 2-1). This phenomenon has been widely recorded/ forecast on low inertia power systems and often as a result of the displacement of SMs by power converter interfaced devices [11], [13], [41], [43].

Table 2-1 Frequency stability indicators as SM inertia varies

System inertial constant (s)	Minimum ROCOF (Hz/ s)		Nadir (Hz)	
	Machine 1	Machine 2	Machine 1	Machine 2
2	-0.95	-1.03	49.77	49.78
4	-0.49	-0.52	49.80	49.80
6	-0.33	-0.35	49.80	49.80
8	-0.25	-0.26	49.80	49.80

2.2.3. Primary frequency response

Primary frequency response uses the machine/system frequency as a signal to inform the slower dispatch of energy to contain the system following the initial responses to a disturbance such as those pictured in Figure 2-6. The dispatch is possible due to the coupling between the grid's electrical frequency and the balance of generation and demand that is described by (6). For example, if the frequency decreases the load must exceed the generation and the SMs can be dispatched to increase their output.

The SMs can be dispatched to increase or decrease their output to any level within their rated power thanks to the fossil-fuel reserves that they are powered with. However, the response speed of the machines is limited by the capability of the mechanical systems [44]**.** The limited response speed of SMs highlights the need for stabilising features such as synchronising torque and inertial injections that can respond inherently to mitigate the system imbalance before the SMs can be re-dispatched.

Primary frequency response is generally driven using a droop mechanism, which allows the magnitude of the SM power response to be determined and implemented for a given frequency change without the need for communication between generators. The droop mechanism is represented by (7), where ΔP_{DR} is the change in power resulting from the droop mechanism, $K_{\omega D}$ is the P-f droop coefficient, and $\Delta\omega$ is the frequency difference from the nominal level:

$$\Delta P_{DR} = K_{\omega D}(\omega_0 - \omega) = K_{\omega D}\Delta\omega \qquad (7)$$

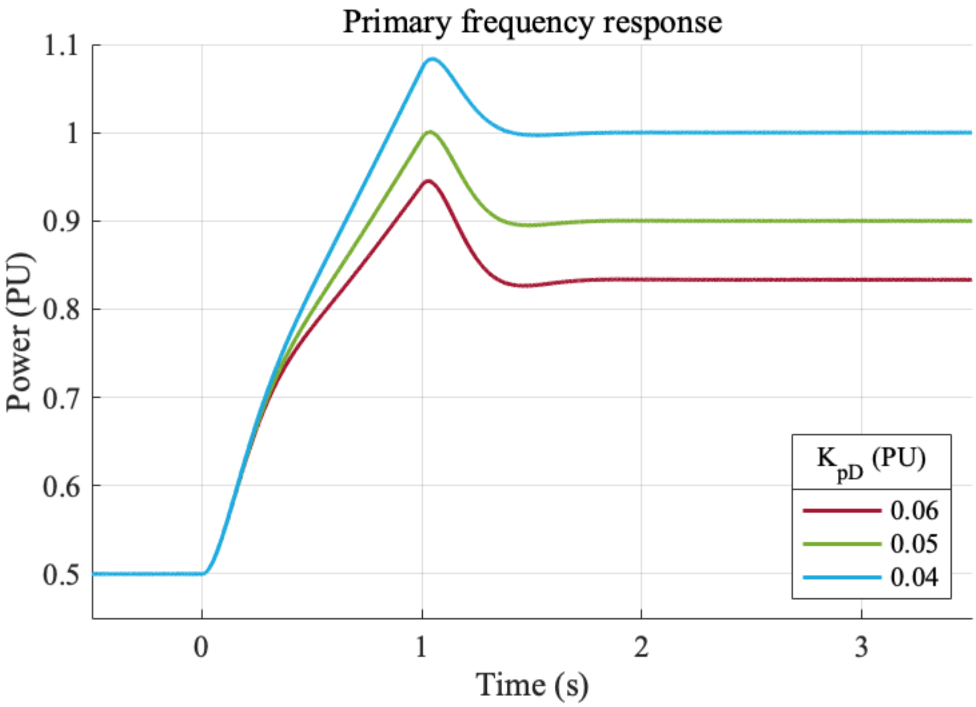

Figure 2-7 Power response of a SM responding to a frequency disturbance with Δf=-1 Hz and ROCOF=-1 Hz/s at t=0 s as the droop coefficient K_{pD} decreases.

The purpose of this droop is twofold. Firstly, in the sense of frequency stability, the droop response acts to limit the magnitude of the frequency excursion (and therefore reduce the severity of the nadir) [35] following the action of the inertial response to limit the magnitude of the ROCOF. Secondly, the droop also enables SMs to achieve effective power sharing as a larger droop magnitude will dispatch one SM to input more power for a given frequency excursion compared to another. The variation in a SM's power output in response to a frequency change as its droop coefficient increases is pictured in Figure 2-7, where K_{pD} is the inverse of the droop coefficient described in (7).

$$K_{pD} = \frac{1}{K_{\omega D}} \qquad (8)$$

Figure 2-7 shows the SM providing more primary frequency response as K_{pD} decreases. The change in power is now a steady-state change as long as the frequency remains disturbed the same amount from the nominal synchronous speed ω_0. The synchronising and inertial injections are not steady-state as they depend on the angular and ROCOF disturbances, respectively, both of which return to zero within the pictured 3 seconds of simulation.

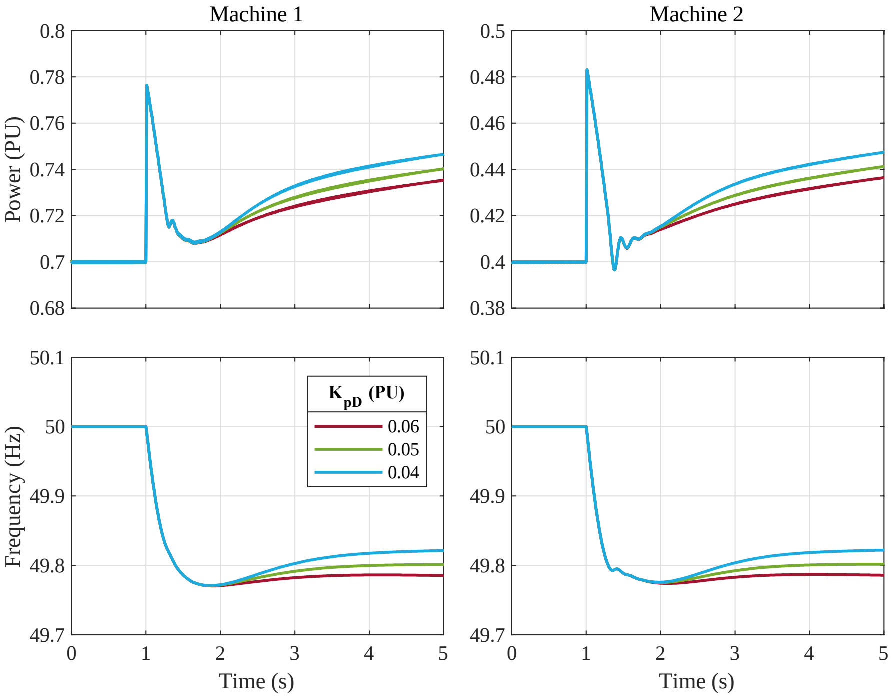

Figure 2-8 Power response of two machines, each with rated power S_n=100 MVA, on a simple power system model that is initialised to deliver a load of P_L=110 MW, before an increment in the load ΔP_L=11 MW is added at t=1 s. The machines' droop coefficients are varied from K_{pD}=0.06 to 0.04 PU.

Figure 2-8 exhibits the power and frequency responses of two SMs on the simple power system model following a load step and as their droop coefficients are varied. Both machines show identical synchronising and inertial power injections within the first seconds of the disturbance before the droop action can be dispatched (Figure 2-8 a) and b)). As a result, there is no difference between the frequency excursion of the different droop coefficient machines during this period (Table 2-2). However, a difference can be seen between the different droop settings once the turbine governor has time to respond. As a result, the systems with the larger power responses (corresponding to smaller droop coefficient K_{pD}) achieve more effective constraint of the steady-state frequency excursion, despite the reasonably consistent minimum ROCOFs (shown in Figure 2-8 c) and d) and Table 2-2).

Table 2-2 Frequency stability indicators as SM droop coefficient varies.

SM droop coefficient (PU)	Minimum ROCOF (Hz/ s)		Nadir (Hz)	
	Machine 1	Machine 2	Machine 1	Machine 2
0.06	-0.95	-1.03	49.77	49.77
0.05	-0.95	-1.03	49.77	49.78
0.04	-0.95	-1.03	49.77	49.78

2.2.4. Secondary and tertiary frequency response

Secondary and tertiary frequency responses (sometimes described as Automatic Generator Control) are then allocated by the System Operator on timescales of minutes and longer to rebalance system power and return the system frequency to the nominal value [35].

2.3. **Conventional grid-following converter control**

Some of the stability issues associated with the increasing penetration of converters are associated with the conventional control approach, Current Control (CC). CC is based on instantaneous power theory, which is discussed in detail in [40]. The control strategy, which is pictured and discussed in more detail in Chapter 4.6.3.1, aims to deliver a current to the grid that corresponds to the desired active and reactive power. Therefore, a CC appears as a current source to the grid. In a similar manner to the SM, a CC connected to the grid can be represented using the equivalent circuit in Figure 2-9, where the SM’s voltage source (VS) and series connected internal impedance are now replaced with the CC’s current source and parallel impedance.

The desired current output is achieved using feedback control to set a corresponding voltage magnitude and by synchronising the converter’s voltage angle with the grid voltage angle, plus some constant phase offset [45]. The controller is described as grid-following (GFL) as it synchronises with the PCC voltage. The feedback control enables the strategy to achieve fast reference tracking and good stability (on strong grids) as well as the decoupled control of active and reactive power [40]. Furthermore, effective current limitation is achieved due to the current source nature of the control strategy [46], which is critical to remain within the thermal limits of the converter structure. However, the focus on the converter's operation and physical limits means that the CC actively attempts to keep its output constant irrespective of the events on the grid. Therefore, as SMs are displaced by CC RESs, the sources of frequency stability are diminished and the frequency is likely to vary more following a disturbance.

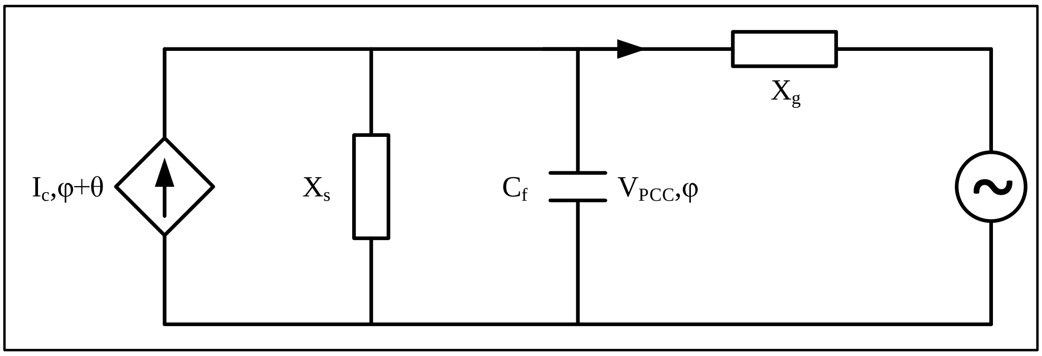

Figure 2-9 Equivalent circuit of a GFL CC (represented by current source with current magnitude I_c and angle $\phi+\theta$, with parallel internal impedance X_s, connected to a single VS representation of the grid).

GFL solutions have, however, been adapted to support the grid. [25] proposed a CC that emulates inertial and droop power responses to support grid frequency stability. The controller uses the frequency measurement from the PLL and its derivative to set adjustments to the power reference to emulate a SM's frequency supporting features. By utilising the CC to support the grid frequency, the growing capacity of converter-based devices that are present on the grid can contribute to grid robustness while maintaining the desirable features that are suitable for converter operation. Examples of a CC with different frequency supporting capabilities are shown in Figure 2-10.

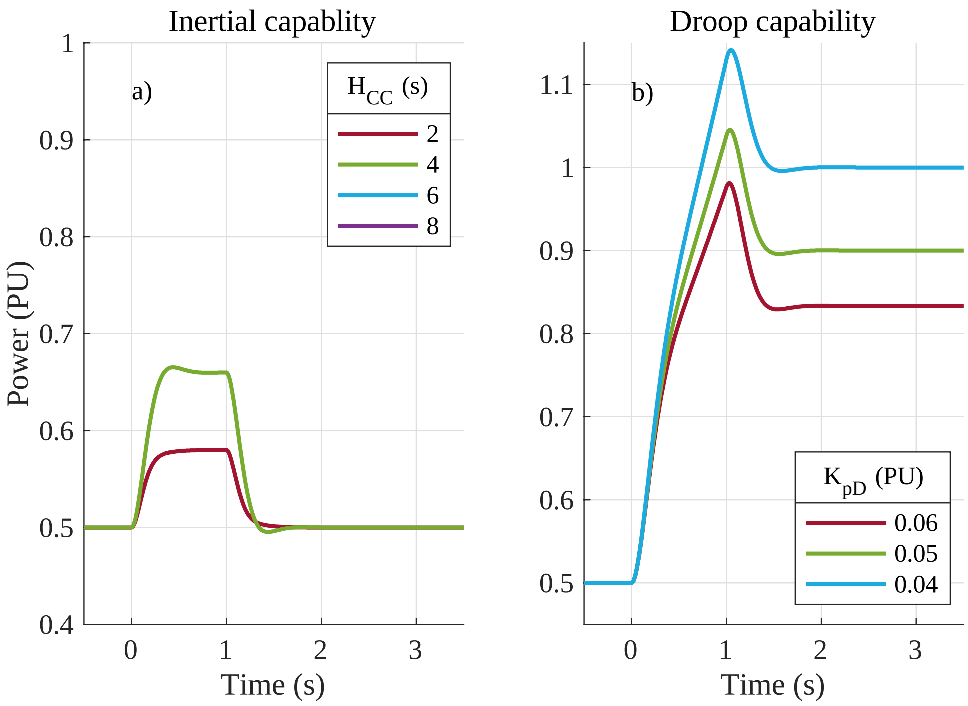

Figure 2-10 Power response of a CC with a) inertial and b) inertial + droop capability responding to a frequency disturbance with Δf=-1 Hz and ROCOF=-1 Hz/s at t=0 s on an infinite bus representation of a power system for a range of inertia constants.

Figure 2-10 a) shows the CC with inertial capability responding to a frequency disturbance by providing a power injection proportional to the derivative of the PLL frequency. The inertial magnitude is equivalent to the corresponding SM inertial injection when both generators have an inertia constant of $H \leq 4\,s$. However, the GFL controller is unstable when attempting to provide inertia constants of $H > 4\ s$ on this particular grid configuration with $SCR = 5$. Figure 2-10 b) shows the CC with inertial and droop capability responding to the same frequency disturbance, now tuned to provide an inertial constant $H = 4\ s$ and a range of droop coefficients. The GFL controller is capable of providing all of the droop settings for the given inertia setting.

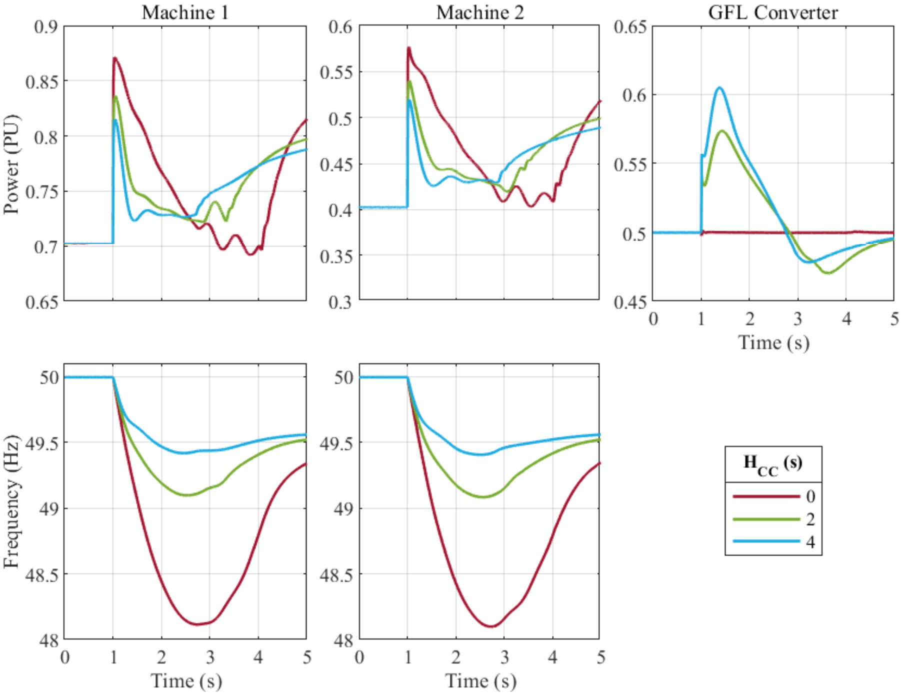

Figure 2-11 Power response of two machines, each with rated power S_n=100 MVA and inertia constants H=2 s, and a GFL converter with rated power S_n=200 MVA, on a simple power system model that is initialised to deliver a load of P_L=220 MW, before an increment in the load ΔP_S=22 MW is added at t=1 s. The converter's inertia constant is varied from H_{CC}=0 to 4 s.

Table 2-3 Frequency stability indicators as GFL inertia varies

GFL inertial	Minimum ROCOF (Hz/ s)		Nadir (Hz)	
constant (s)	Machine 1	Machine 2	Machine 1	Machine 2
0	-2.14	-2.18	48.11	48.10
2	-1.69	-1.73	49.10	49.08
4	-1.42	-1.47	49.42	49.40

Figure 2-10 proves the ability of the GFL to provide power injections in response to grid frequency disturbances. The impact that these injections have on grid frequency stability is then pictured in Figure 2-11. Figure 2-11 a)-c) shows the power responses by two SMs and an additional GFL converter on the otherwise identical small power system that was used to discuss SM stability features in Section 2.2. An equivalent 10 % of generating capacity load step is forced at $t = 1\ s$. Figure 2-11 d) and e) shows the corresponding frequency signals of the two SMs during the same period.

Simulations are carried out for the low SM inertia settings $H = 2\,s$ and show the impact of connecting CCs with increasing inertia contributions to the grid. The minimum ROCOFs and nadirs for each simulation are shown in Table 2-3.

The $H_{CC} = 0\,s$ scenario in Figure 2-11 experiences a larger frequency excursion with a severe ROCOF, despite the equivalent SM-only system being stable (as shown in Figure 2-8). The frequency excursion in Figure 2-11 is more extreme than that in Figure 2-8 as the constant inertial contribution from the SMs has a reduced impact on the larger capacity of the system with the added converter interfaced generation. The significant ROCOFs and frequency excursion would stretch the capability of connected devices and could result in the disconnection of generation and load, depending on the protection settings. The results highlight the issue of displacing SM with converter capacity that is incapable of taking responsibility for the grid's stability.

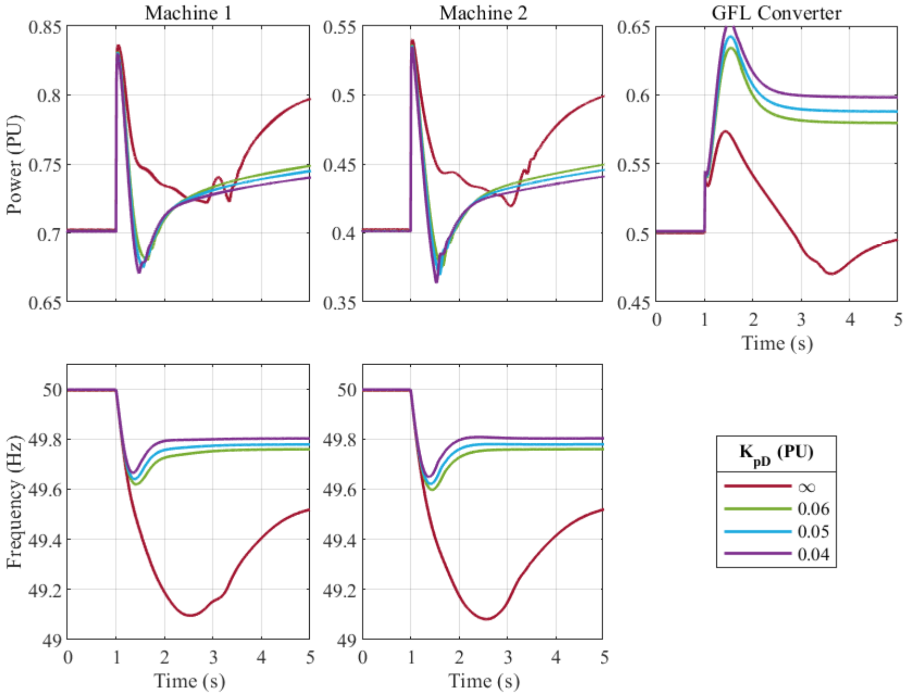

Figure 2-12 Power response of two machines, each with rated power S_n=100 MVA and inertia constants H=2 s, and a GFL converter with rated power S_n=200 MVA and inertia constant H_{CC}=2 s, on a simple power system model that is initialised to deliver a load of P_L=220 MW, before an increment in the load ΔP_L=22 MW is added at t=1 s. The converter's droop coefficient is varied from K_{pD}=∞ to 0.04 PU.

The following scenarios incrementally increase the inertial constant of the CC, while maintaining the same inertial contribution of the SMs. The initial increase allows the CC to contribute inertial power following the load step and helps to contain the system ROCOF. As a result, the system frequency varies less. The further increase to $H = 4\ s$ allows the CC to better contribute towards the containment of the ROCOF and the frequency excursion (Table 2-3). As the inertial constant of the CC increases less energy is required to be delivered by the SMs to stabilise the system and more can be sourced from the low carbon GFL converter (Figure 2-11 a)-c)).

Figure 2-12 shows the power and frequency signals of the same power system subject to the same load step but where the CC also has droop capability. Figure 2-12 shows the corresponding maximum ROCOF and frequency nadir for the different scenarios. Again, the SMs have a low inertia constant $H = 2\ s$ and the CC has inertia constant $H = 4\ s$ and is tuned with a range of droop coefficients, where $K_{pD} = \infty$ corresponds to zero power response for any frequency deviation. As the droop capability is introduced the converter begins to ramp up to dispatch power according to the frequency deviation (Figure 2-12 c)). However, the converter can dispatch power much faster than a SM so is capable of containing the frequency deviation more effectively (Figure 2-12 d) and e) and Table 2-4) than the equivalent system configuration using only SMs (pictured in Figure 2-6 and Table 2-2). As expected, the smaller the CC’s droop coefficient K_{pD} the more power it dispatches and the smaller the frequency excursion. Although the rapid delivery capability of converters with droop capability has the potential to effectively contain frequency excursions, it can be difficult to find suitable low carbon energy sources with sufficient energy capacity to support the provision. The energy requirement and corresponding suitable low-carbon solutions will be discussed in more detail in Section 3.2.

As well as requiring sufficient energy capacity to provide the frequency stabilising features, the ability of a CC to support the grid can be limited by its instability in weak grids. This instability can be considered in several ways, many of which are interrelated, and could form the foundation of many theses. However, some fundamental features are mentioned here. A key relationship for this instability is the fact that conventional system strength degrades as more GFL converters are connected (due to the increasing impedance associated with their current source operation [47] and the lack of transient injections in response to disturbances [45]). This means that as more GFLs connect to a system, the system weakens, which in turn degrades the ability of the GFL to operate.

Table 2-4 Frequency stability indicators as GFL droop coefficient varies

GFL droop coefficient (PU)	Minimum ROCOF (Hz/ s)		Nadir (Hz)	
	Machine 1	Machine 2	Machine 1	Machine 2
∞	-1.69	-1.73	49.10	49.08
0.06	-1.64	-1.69	49.62	49.60
0.05	-1.63	-1.68	49.64	49.62
0.04	-1.62	-1.67	49.67	49.65

CCs are widely thought to be unstable on weak grids due to the mis-operation of their synchronisation process [48], [49]. The synchronisation process generally uses a phase-locked loop (PLL), which was initially associated with the lack of a well-defined voltage [48]. These conditions are increasingly prevalent as fewer SMs are available to “set” the grid voltage. Some studies suggest that this issue can be bypassed by reducing the bandwidth of the PLL [48], [50], however, this degrades the dynamic performance of the CC by effectively reducing the controller’s damping. Alternatively, the complementary tuning of the PLL and the outer loop control gains has been shown to resolve this issue [51], [52]. The PLL mis-operation is further explained as a breakdown in the CC’s ability to provide large powers on weak grids in [49]. At low powers the CC can track the AC voltage angle accurately, however, as the power increases the angular error increases and begins to oscillate [49]. This introduces oscillations to the CC’s power output. The stability of inertial or droop configurations of the CC can be further degraded by the introduction of a transient feedback loop between the PLL angle and the output voltage [53]. This degradation in the stability can be visualised in Figure 2-10 a) where the GFL is incapable of supporting inertia constants $H > 4\ s$.

Other studies have linked the instability of GFLs to the large impedance that their current source attempts to establish [54], [55]. This weakening of grid strength has been observed in the form of a high bandwidth voltage instability in the CC [54]. An analytical assessment outlines the drivers for the change in CC stability as the grid impedance varies [55]. On strong grids the voltage at the terminals of the converter is determined by the stiff grid voltage and remains constant as a result. Although the instantaneous power equation (3) depends on this voltage, the constant voltage means that the two are decoupled and the CC's outer loops can effectively control both variables. However, as the penetration of GFLs increases the voltage at the terminals of the converter becomes increasingly dependent on the power flow from the converter (due to the increased impedance separating it from the grid). The voltage becomes increasingly variable. The active power and the voltage become coupled and, in some conditions, the outer loops can become incapable of effectively controlling either variable [55]. Of course, a CC's stability will be effected by a combination of the phenomena described here and above.

Other than the retuning of the CC [48], [50]–[52], solutions exist to rectify some of these issues. Angular compensation strategies have been proposed to reduce the CC's angular error when injecting large powers in weak grids [49]. Voltage feedforward adaptations have been proposed that can improve the fast control of the AC voltage so that it remains constant on weak grids and maintains its effective decoupling from the converter's active power [55]. Ultimately, however, there will be two critical issues for future converter dominated systems as long as GFL controllers are used and they follow their ideal current-source behaviour. Firstly, there will be no devices to establish the system voltage. Secondly, there will be a lack of transient stabilising features that can response to disturbances instantaneously and balance the grid. Both issues are related to the lack of voltage-source operated devices.

2.4. **Grid-forming converter control**

An alternative to GFL control is the grid-forming (GFM) family of controllers. GFMs behave as voltage sources by establishing an internal voltage magnitude and angle in the same manner as SMs [56]. This formation of an internal voltage is capable of providing voltage rigidity (and stability) to the grid and is necessary to maintain conventional stability on a system with a large penetration of converters [41]. As a GFM operates as a voltage source its power delivery can be represented by the same equivalent circuit as a SM (Figure 2-2) and its ideal behaviour is governed by the same dynamic equation (3); as a result GFM converters will provide an inherent and instant response to any changes in the grid, similar to SMs [9], [42], [56]. The behaviour resulting from the GFM's voltage-source operation is visible in Figure 2-13, which shows a GFM converter's response to an angular disturbance on an infinite bus representation of a power system. The GFM shows an instantaneous power injection following the change in grid angle similar to the action of the synchronising torque that is observed from the SM (in Figure 2-3). As expected, the magnitude of the transient injection does not vary with the converter's inertial constant but the following dynamics do vary.

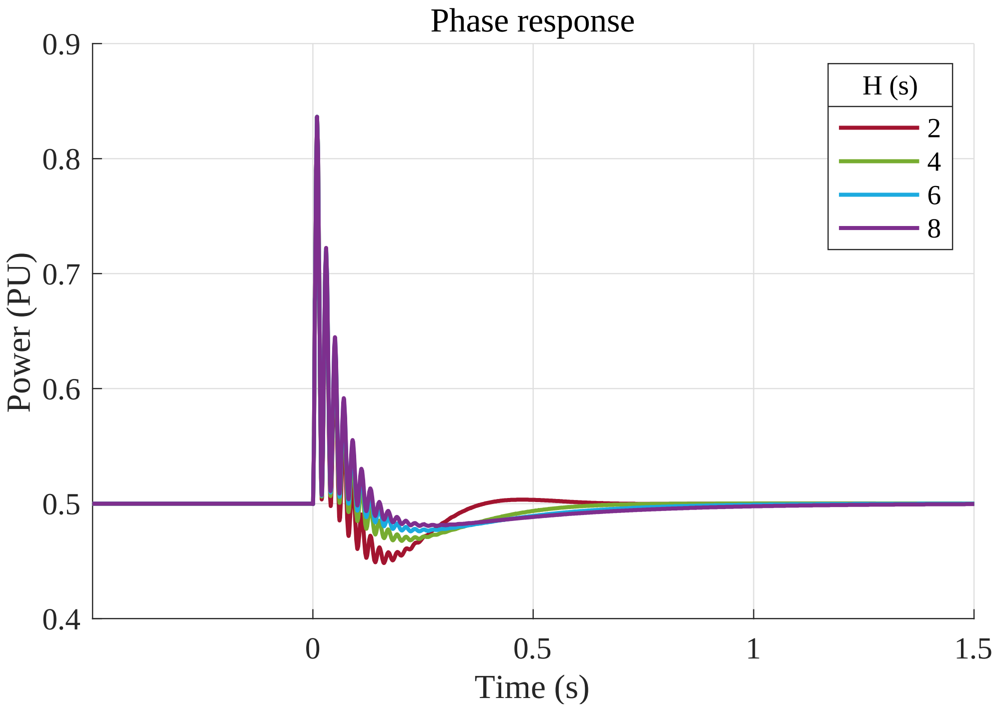

Figure 2-13 Power response of a GFM converter to an angular disturbance $\Delta\delta=-5^o$ *at t=0 s on an infinite bus representation of a power system as the converter's inertia constant varies from* $H_{GFM}=2$ *to 8 s.*

GFMs are different to SMs in the sense that their software-based configuration allows their properties to be tuned [57], unlike the SM properties that depend on the physical characteristics of the machine. Therefore, some studies have identified the potential for GFM controllers to support grid stability better than SMs [44], [58]. Another difference between GFM converters and SMs is the converter's reduced thermal capability compared to the SM, above which their desirable features will be limited [41].

Initial proposals of GFM controllers stemmed from the equations that represented SM dynamics. [26] proposed a first-order droop-relationship GFM that established the coupling between voltage angle and active power and between voltage magnitude and reactive power. [28] proposed a controller that emulated the SM voltage-flux and torque equations, which was one of the first strategies that fell into the Virtual Synchronous Machine (VSM) family of GFMs. The strategy was adapted from a current-reference to voltage-reference basis in [59]. The Synchronverter was developed in [60] using a combined electrical and mechanical model of a SM and can also be described as a VSM. An alternative PI-based VSM has been proposed that simplifies the internal voltage angle and magnitude dynamics using two separate PI controllers [61].

Recently, GFM control has been a focus of much research due to its applicability to stabilise grids with high penetrations of converters. The similarity between VSM and droop type controllers was identified in [62], where the introduction of a low-pass filter (LPF) acting on the power was found to introduce the desired second order dynamic to achieve inertial response. The presence of the Swing Equation in VSMs versus the introduction of the second order dynamic in droop controllers and the variation of damping was assessed in [63]. The Synchronous Power Controller (similar to the GFM Droop) was proposed with a virtual admittance to ensure current limitation and smooth start-up in [64]. An adaptive GFM was developed in [65] to optimise the controller's response with consideration of a WT's energy limitation and the grid needs. The PI VSM, Synchronverter, and second order GFM Droop control strategies are pictured and described in full detail in Sections 4.6.3.2, 4.6.3.3, and 4.6.3.4, respectively.

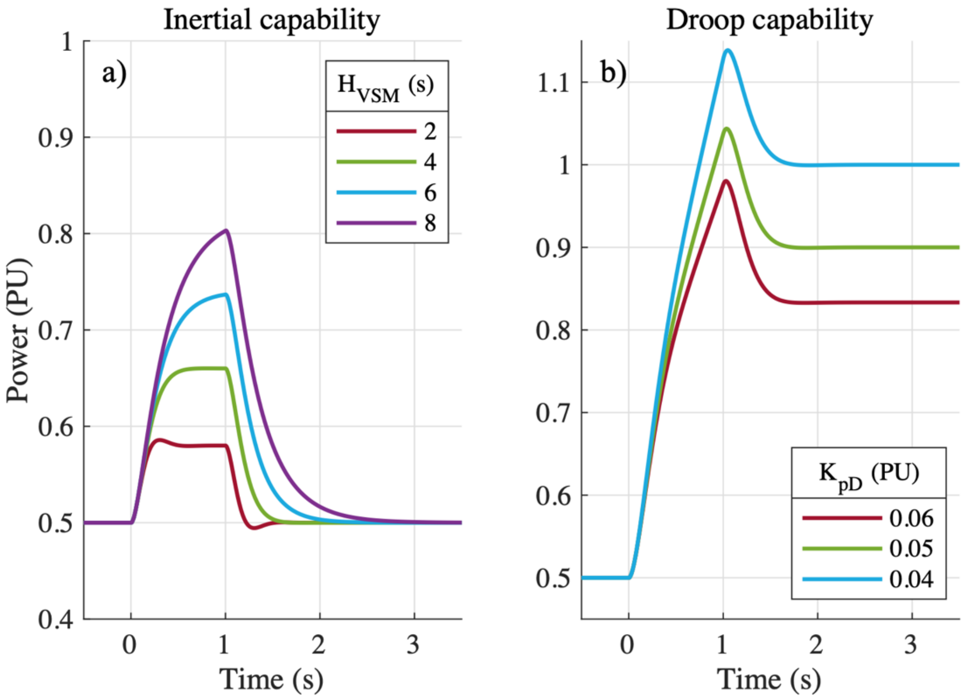

Figure 2-14 Power response of a GFM VSM controller with a) only its inherent inertial and b) inertial + droop capability in response to a frequency disturbance with Δf=-1 Hz and ROCOF=-1 Hz/s at t=0 s as the inertia constant is varied from H=2 to 8 s.

Figure 2-14 a) shows the inertial capability of a GFM VSM controller in response to a frequency disturbance on the grid. The controller is capable of supporting the full range of tested inertial constants up to $H = 8\ s$. The range of stable operation suggests that restructuring converter objectives to focus on grid support may offer some benefits compared to the simple inclusion of additional paths that was required to achieve inertial capability with the GFL CC. Figure 2-14 a) also highlights the ability of the GFM to be tuned to provide a more damped response compared to the SM, which depends on the physical properties of the machine.

Figure 2-14 b) shows the response of the GFM VSM to the same frequency disturbance, but now tuned with an inertial constant $H = 4\ s$ and additional (varying) droop capability. The VSM is capable of supporting all of the tested droop coefficients.

Figure 2-15 depicts the impact that these GFM capabilities have on grid frequency stability. As expected, the converter's power injection increases with the inertial constant, resulting in the better containment of the system's ROCOF and frequency excursion and requiring less inertial and droop power to be provided by the SMs (Figure 2-15 and Table 2-5). Table 2-5 also shows that the power system configurations that are stabilised by GFM inertial response experience similar frequency excursions as those that are stabilised by GFLs (Table 2-3), although the GFM appears to be able to contain the system ROCOF more effectively. These findings agree with some studies that suggest GFL inertial response is slower and less capable of containing system frequency than GFM inertial response. This assumption will be explored in more detail in Chapters Chapter 3 and Chapter 6. The impact of the GFM's varying droop coefficient on system frequency is not pictured as it matches the trends observed for the GFL shown in Figure 2-12.

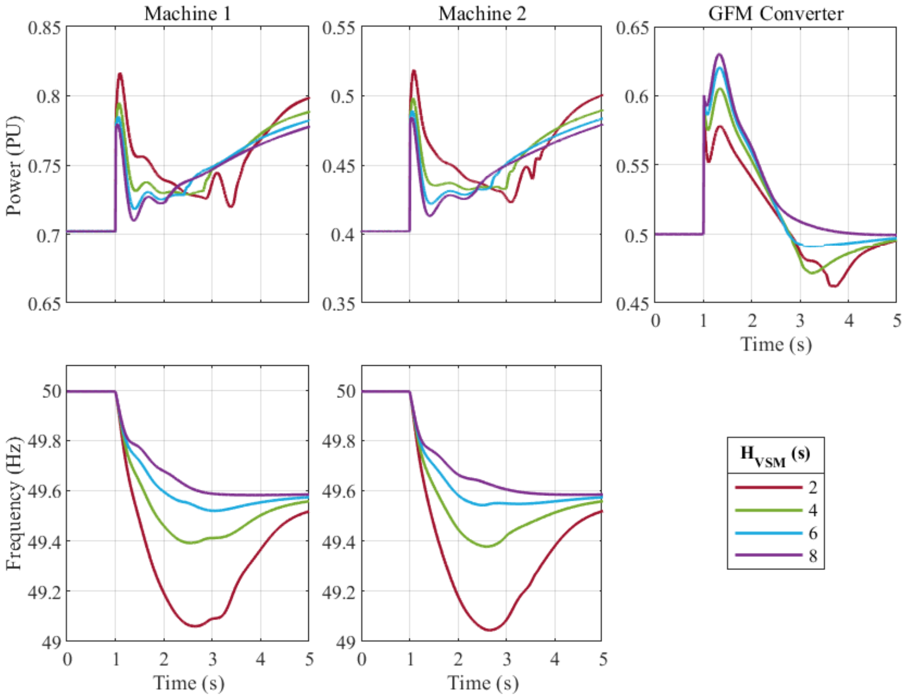

Figure 2-15 Power response of two machines, each with rated power S_n=100 MVA and inertia constants H=2 s, and a GFM converter with rated power S_n=200 MVA, on a simple power system model that is initialised to deliver a load of P_L=220 MW, before an increment in the load ΔP_S=22 MW is added at t=1 s. The converter's inertia constant is varied from H_{VSM}=2 to 8 s.

Although GFM controllers offer solutions that are suited to stabilise the grid, some issues will constrain their roll-out on power systems. Firstly, GFM dynamic behaviours are not fully understood. Some control strategies are suggested to be equivalent [62], [63], [66], however, others suggest that the specific configuration [67] and tuning [68] can drive different dynamics and stability. Furthermore, the exact specification of desirable stability features is not clear. Many of the features are inherent properties of the previously governing SMs and the capability of GFM converters to replicate them has not been exhaustively assessed [42]. For example, confusion exists between the definition of inertial delivery periods, which are considered to be instant in some cases [18], [56] and only considered to be initiated instantly in others [32], [33]. Another issue is the apparent destabilisation of some GFMs on strong grids [69], where GFLs can perform better. Finally, implementing these solutions with specific energy sources can introduce additional dynamics that can degrade the expected support [70]. and need to be resolved to ensure the secure operation of the system.

Table 2-5 Frequency stability indicators as the GFM inertial constant varies.

GFM inertial constant (s)	Minimum ROCOF (Hz/ s)		Nadir (Hz)	
	Machine 1	Machine 2	Machine 1	Machine 2
2	-1.46	-1.47	49.06	49.05
4	-1.17	-1.21	49.39	49.38
6	-1.04	-1.09	49.52	49.54
8	-0.97	-1.03	49.58	49.58

The emulation of slow SM dynamics, particularly inertial response, means the fast dynamic capability of converters may not be optimally utilised [63], [65], [71]. In fact, a system where the coupling between frequency and active power is no longer present could exist in the future [72], meaning the dependence on the Swing Equation and associated inertial response dynamics could be eliminated and converter response speeds could be utilised more effectively. However, the path to emulate SMs using converters appears to be necessary to support the stable operation of a hybrid system where both technology types exist, which is expected to continue throughout the foreseeable future [41].

2.5. **Summary**

This chapter has provided an overview of the stability phenomena in power systems, as well as the availability of converter-based solutions to support the grid. The thesis is particularly interested in frequency stability, which has been described in terms of the critical components that contribute to the stability-type on different timescales. The fundamental features of conventional grid-following controllers were then introduced. This converter control strategy does not inherently support grid frequency, and can struggle to operate in weak grid conditions, but solutions have been proposed to mitigate both of these operational features. The development of grid-forming controllers, which are capable of taking control of the grid's voltage, was then described. Grid-forming controllers are shown to emulate the voltage-source behaviour of synchronous machines but are also found to possess complicated dynamic characteristics, which are not yet fully understood.

This introduction to the state of power system frequency stability lays a foundation to explore the nuances of converter operation in more detail and therefore identify the critical areas that are limiting the deployment of converter-based frequency-stabilising solutions.

Chapter 3. Feasibility of converter-based frequency stabilising solutions

3.1. Introduction

This chapter provides an outline of the technical requirements to provide frequency stability to the grid and details the energy sources that could feasibly meet these requirements (Section 3.2). It shows that solutions exist to support the grid. Although some of these solutions are beginning to be implemented, the rate of decarbonisation needs to be improved. The following Section 3.3 introduces some of the hurdles that are limiting the effective deployment of frequency stabilising solutions from converters. These hurdles will be addressed throughout the studies in the remainder of the thesis.

3.2. Technical requirements and suitable solutions to provide frequency stability from converters

The frequency supporting capability of any of the control strategies mentioned in Chapter 1 can be achieved with any technology (behind a converter) that has sufficient instantly available power and energy density as pictured in Figure 3-1. For example, the kinetic energy stored in the rotating mass of WTs can be converted to electric power in a similar manner to the conversion of inertial energy storage in SMs [73]. Alternately, the chemical or magnetic energy stored in energy storage systems (ESSs) can be used to support the grid, assuming the technology has sufficiently fast discharge rates [74]. Solar PV generation is capable of providing frequency but requires to be operated below the maximum available power level as none of the energy production is stored [75]. Some studies have suggested the implementation of renewable generators with parallel ESSs to either minimise the undesirable impacts on the generator’s operating strategy, or, to simply enable frequency support by a hybrid system that would have previously been unable to, as would be the case for solar PV farms [31], [75].

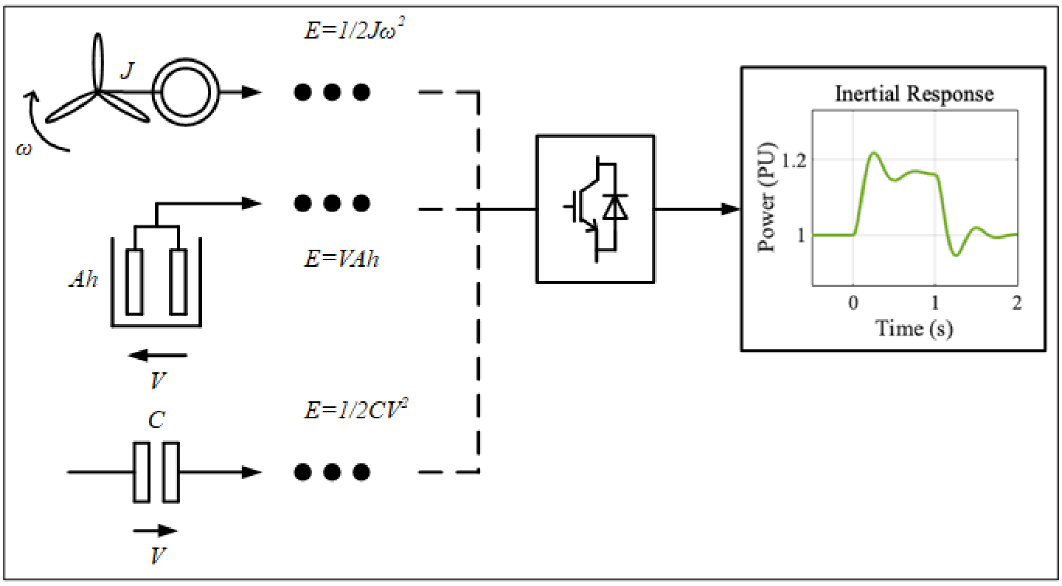

Figure 3-1 Illustrative diagram showing the potential to use any technology with sufficient energy storage (including but not limited to the kinetic, chemical, and electromagnetic energy types pictured) to enable an appropriate converter control strategy to provide inertia to the grid.

Detailed assessment of the capability of technologies to participate in frequency support is necessary to ensure that the technologies can support the desired energy provision. Many of the power system simulations mentioned above have pictured the benefit in providing larger and faster power and energy injections in the forms of inertial and droop responses to contain system ROCOFs and frequency excursions (e.g. Figure 2-11 and Figure 2-12). Therefore, it is important to identify the technologies that are most capable of supporting the grid, which can be carried out in three steps: firstly, by deriving the specific power and energy requirements to provide the support, secondly, by assessing the technical capabilities and identifying the suitable technologies, and thirdly, by considering the wider techno-economic features of the technologies that will affect its ability to provide the service cost-effectively. These steps are overviewed in the following subsections.

3.1.1. Power and energy requirements for frequency support

To identify appropriate technologies that can provide different frequency support services it is necessary to identify the power and energy requirements for the given functionality. The active power requirement to provide an inertial response (IR) is defined by a rearranged form (9) of the Swing Equation (6). The faster this power increment ΔP_{IR} can be delivered the better the converter will be able to constrain the ROCOF on the grid.

$$\Delta P_{IR} = \frac{2HS_n}{\omega_0}\dot{\omega}_{max} \tag{9}$$

The energy required to deliver the inertial response is defined as the inertial power increment ΔP_{IR} multiplied by the time period the inertial response is sustained Δt_{IR}, as depicted in (10). Theoretically, the inertial response is a power injection that is proportional to the ROCOF, so the inertial period would only extend as long as the grid ROCOF does not equal zero. However, a rapid reduction in inertial power could further degrade the stability of the grid, so the inertial injection will be defined to be delivered for $\Delta t_{IR} = 10\ s$ from the onset of the disturbance, which ensures that the inertial magnitude can be sustained into the initiation of other primary frequency response services [76].

$$\Delta E_{IR} = \Delta P_{IR}\Delta t_{IR} \tag{10}$$

Table 3-1 Power and energy requirements to provide inertial response for a standard rated power, the maximum ROCOF that converter devices are required to remain connected throughout, and a standard range of inertial constants.

Case	$\boldsymbol{S_n}$ $(\boldsymbol{MW})$	$\boldsymbol{\Delta\omega_{max}}$ $(\boldsymbol{Hz})$	$\boldsymbol{H}$ $(\boldsymbol{s})$	$\boldsymbol{\Delta P_{IR}}$ $(\boldsymbol{MW})$	$\boldsymbol{\Delta E_{IR}}$ $(\boldsymbol{kWh})$
1	3	0.5	1	0.06	0.2
2	3	0.5	8	0.48	1.3
3	501	0.5	1	10.02	27.9
4	501	0.5	8	80.16	222.7

The European Grid connection requirements state that a WT on the GB network must remain connected to the grid throughout frequency disturbances with a ROCOF as large as $\dot{\omega}_{max} = 0.5\ Hz/\ s$ [77]. Accordingly, the range of power and energy requirements for a 3 MW WT to provide an inertial response to the maximum ROCOF it would be expected to remain connected to and for a range of standard SM inertia levels (between $H = 1 - 8\ s$ [39]) are shown in Table 3-1. The requirements for the same inertial response to be provided for an entire wind farm composed of 167 of these turbines is also detailed, where the rated power is simply scaled up to $S_n = 501\ MW$. The results show that a high power and lower energy density capability is required for inertial response.

The requirements for (droop) frequency support are different as the initial injection is less critical, whereas the provision lasts longer and therefore a larger energy density will be required. However, similar to the inertial response, the energy density of the droop response (DR) depends on the magnitude of the power injection and the duration of the delivery. The power increment required from the droop response ΔP_{DR} is defined according to (7). Although this power does not need to be delivered instantly, the timescale is still important and is being shortened to stabilise the increasingly variable grid frequency and to take advantage of the fast delivery speed of converters. For example, a new frequency response service being used in GB, Dynamic Containment, requires the full delivery of the frequency support (FS) for frequency deviations between $\Delta f_{FS} = 0.2 - 0.5\ Hz$ within time period $\Delta t_{pDR} = 1\ s$ [76].

The frequency service duration Δt_{FS} then determines how long the frequency supporting power injection should be sustained. Although a duration period for Dynamic Containment is not explicitly defined, a duration test for the service is detailed to ensure technologies can provide full power injection for a sufficiently long period, which requires participating units to sustain provision for $\Delta t_{FS} = 15\ min$ [76]. This period will be used as the time duration for frequency service provision. The energy requirement to provide droop frequency support is defined:

$$\Delta E_{DR} = P_{DR} \Delta t_{FS} \tag{11}$$

The power and energy requirements for droop frequency support are exhibited in Table 3-2 for the largest frequency deviation and delivery durations defined for the

Dynamic Containment service [76] and for the upper and lower values of standard SM droop coefficients, which generally vary between $K_{pD} = \frac{1}{K_{\omega D}} = 3 - 5\ \%$ [73].

Table 3-2 Power and energy requirements to provide droop response for a standard rated power, the maximum frequency deviation that converter devices are required to remain connected throughout, and a standard range of droop coefficients.

Case	$\boldsymbol{S_n\ (MW)}$	$\boldsymbol{\Delta\omega_{max}\ (Hz)}$	$\boldsymbol{K_{pD}\ (PU)}$	$\boldsymbol{\Delta P_{DR}\ (MW)}$	$\boldsymbol{\Delta E_{DR}\ (MWh)}$
1	3	0.5	5	0.6	0.15
2	3	0.5	3	1	0.25
3	501	0.5	5	100.2	25.05
4	501	0.5	3	167	41.75

Again, the requirements are repeated for both individual turbine ratings (Cases 1 and 2) and for entire wind farm ratings (Cases 3 and 4). The results show that standard SM droop coefficients require a larger power density, and due to the much longer period of delivery, this corresponds to an energy density two orders of magnitude larger than the largest inertial response case for the corresponding rated power.

3.1.2. Power and energy capability of different technologies

A standard power and energy map highlighting the technical capabilities of a range of ESSs is pictured in Figure 3-2 [78]. The range of power and energy requirements to provide inertial response for either the single turbine with $S_n = 3\ MW$ (Cases 1 and 2 in Table 3-1) or an entire wind farm with $S_n = 501\ MW$ (Cases 3 and 4 in Table 3-1) are highlighted in the blue Turbine and green Farm boxes, respectively. The characteristics of a WT that provides inertial response itself (without the support of an ESS) can also be overlain onto the map, however, it is important to consider the WT's operational constraints as well as the physical capabilities. If only the physical characteristics were considered, the extraction of excessive energy would slow the WT rotor unacceptably, driving the WT away from the desired operating strategy, potentially towards structural frequencies that could result in increased fatigue, and decrease the energy capture.

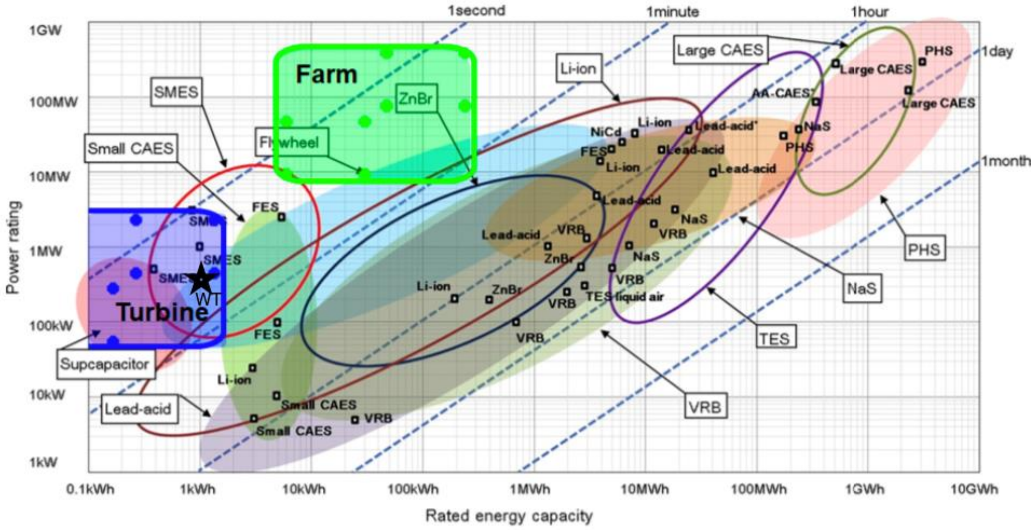

Figure 3-2 Map of power and energy characteristics of energy storage system technologies with the requirements to provide inertial response for either a single wind turbine (blue Turbine box) or for an entire wind farm (green Farm box) [78]. The characteristics of a wind turbine to provide inertial response are added and overlain with a star marked WT.

The ability of 1.5 and 5 MW WTs to provide inertial and droop response was assessed in [73] with respect to acceptable torque-speed operating conditions and machine fatigue. The WTs were found to be capable of providing inertial power injections of $\Delta P_{1.5IR} = 0.2\ MW$ and $\Delta P_{5IR} = 0.6\ MW$ in response to a frequency disturbance with $\dot{\omega}_{max} = 0.6\ Hz/\ s$ without moving outside of an acceptable range of torque-speed operating conditions (where the numbers in the subscripts refer to the size of the WT). Some of the WT components are found to experience minor increases in load but these changes are also thought to be within the acceptable limits. The inertial constants that correspond to these power injections and frequency disturbances are found using another rearranged form of the swing equation (12).

$$H = \frac{\Delta P_{IR} \omega_0}{2HS_n \dot{\omega}_{max}} \tag{12}$$

(12) shows that the two WTs are capable of providing $H_{1.5} = 5.6\ s$ and $H_5 = 5\ s$, respectively. For the purposes of this study, and assuming that the 3 MW WT achieves at least the same operation as the less capable 5 MW WT, the power capability with

inertial constant $H_3 = 5\ s$ for the same frequency disturbance would be $\Delta P_{3IR} = 360\ kW$. This power capability fits within the desired inertial ranges detailed in Table 3-1 and Figure 3-2 for the individual turbine size. [73] also considered the impact of sustained provision of this inertial response and found the WT torque-speed conditions and loading to remain within acceptable limits, suggesting the WT is capable of meeting the inertial energy requirements equivalent to an inertial constant $H = 5\ s$ ($\Delta E_{IR} = 1\ kWh$) without adversely affecting the operation of the machine.

From the power and energy map we identify three key ESS technologies – flywheel (FESS), supercapacitor (SC), and different Lithium ion batteries families (Li Ion BESS) – as well as the WT itself to be technically capable of meeting the requirements to provide inertial response. Several other energy storage technologies are also capable of meeting the inertial power and energy requirements but are disqualified from consideration due to different features: Superconducting magnetic energy storage (SMES), compressed air energy storage (CAES), and hybrid ion capacitors are all disqualified due to the low maturity of the technologies, while sodium sulphur batteries are disqualified due to the high internal temperature required to maintain their molten electrolytes, which is not suitable for high power applications.

The ESSs that are capable of providing the droop responses defined in Table 3-2 must at least meet the same power capacity as the largest inertial cases, while also achieving a greater energy density. Therefore, only the FESS and Li Ion BESS technologies with an energy density greater than ~150 kWh are deemed to be capable of meeting the requirements for the droop functionality (defined in terms of the Dynamic Containment service provision). Any ESS technologies that were disqualified from the inertial provision despite meeting the power and energy requirements are also automatically disqualified from the droop provision.

The power and energy map cannot be used to assess the ability of the WT to provide droop response. The larger energy density required to provide droop response means that the WT would be pulled unacceptably far from the desirable operating conditions if operated normally, however, [73] suggests that operating the WT with upward power headroom would allow the WT to take part in droop support. Increased energy can be pulled from the WT by either reducing the power output during normal operation below rated wind speeds (leaving headroom for support during a frequency disturbance) or by pitching the WT blades to output greater than rated power in the case of a frequency disturbance above rated wind speeds. [73] deems the increase above rated power to be acceptable for the standard range of SM droop coefficients and for frequency disturbances up to $\Delta\omega_{max} = 0.2\ Hz$ (resulting in $\Delta P_{DR} = 400\ kW$ for the more strenuous $K_{pD} = 0.03$) as the WT converter is conventionally capable of supporting ~120 % of nominal power for up to 20 minutes without exceeding its thermal capacity. The adaptation to the WT strategy was found to record less than 5 % reduction in energy capture (due to the reduction in power below rated wind speeds) and achieve an improvement in loading on the WT.

Although these findings suggest that WTs could participate in droop frequency support, the requirements for devices participating in NG ESO's Dynamic Containment provision are more strenuous. Dynamic Containment requires units to provide a droop response up to $\Delta\omega_{max} = 0.5\ Hz$, which corresponds to a droop power injection of $\Delta P_{DR} = 1\ MW$ for the same droop coefficient $K_{pD} = 0.03$ %. This power injection corresponds to 33 % of the WT converter's rating, so could not be sustained for the full duration of the frequency support without risk of exceeding its thermal capability. Moreover, the increased power injection would require a larger headroom to be maintained below rated wind speeds, which would further reduce the energy capture of the WT. Therefore, WTs do not appear to be suited to take part in droop frequency support services such as Dynamic Containment.

3.1.3. Discussion of optimal technologies for frequency support

The technologies that have qualified to provide frequency support in terms of power and energy capability are assessed in more detail in terms of techno-economic characteristics to identify the optimal approach. Datasheets for the specific technologies are used to overview critical features including weight, volume, and lifetime/ durability while a pricing framework is developed from a set of reports that discusses trends in ESS costs [79]–[82]. Figure 3-3 depicts the features of the different ESS technologies that are critical to identify the optimal technology for delivery and are discussed further in the following paragraphs.

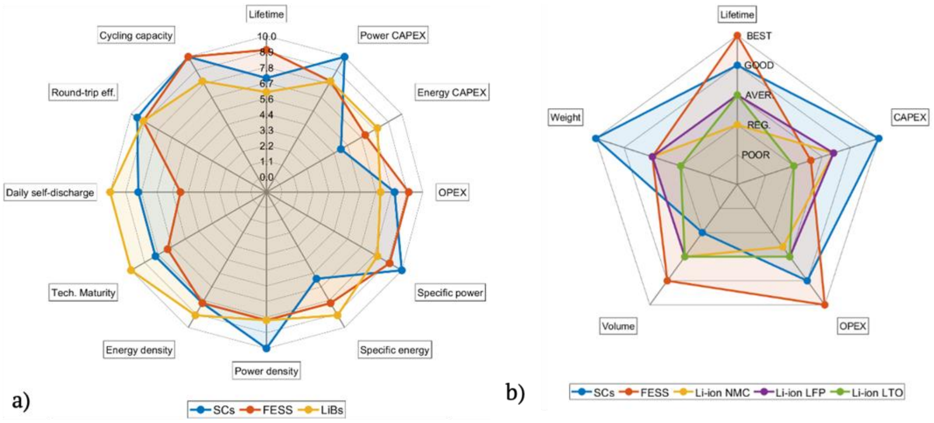

Figure 3-3 Spider plot comparison of a) the potential characteristics of the candidate ESS technologies and b) constraining indicators that determine the ESS selection for inertial response [31].

SCs are suited for very fast high power delivery, have a high round trip efficiency, reasonable calendar and cycling lifetimes, but become very expensive to achieve any significant energy density [83]–[85]. However, a SC with high power and low energy density has median CAPEX and OPEX, meaning it is the cheapest ESS to provide IR. Overall, SCs are deemed to be applicable for IR and potentially other short-term grid-supporting functions (such as phase-response) but not for longer term droop support. SCs are likely to be implemented in parallel with renewable generators to improve their grid-supporting capability and not in standalone capacity, as there may not currently be sufficient revenue tracks to support their deployment.

FESSs are very durable, have good power density, and certain technologies also have good energy density [86]. The machine requires a large CAPEX but the good durability achieves a low OPEX, meaning FESSs become more financially desirable as the required lifetime and frequency of delivery increase. FESSs are deemed to be appropriate for both inertial and droop response and could be implemented in a hybrid (parallel to renewable generator) or standalone capacity due to its ability to provide both short term grid-supporting functionality and to fit with the more established dynamic containment revenue stream.

Li Ion BESSs include many families of chemistries due to the active industrial action to develop cost-effective BESS solutions. Several of these families fit either one or both of the inertial and droop response functionalities in terms of power and energy capability, however, the Lithium Nickel Manganese Cobalt Oxide family (NMC) is deemed to be most desirable due to its especially good power and energy density as well as good cost. In comparison to the other ESSs, the NMC Li Ion BESS possesses good power density, very good energy density, low CAPEX, but higher OPEX associated with the low lifetime and hence requirement to be replaced more regularly [87]. The higher OPEX means Li Ion BESSs are currently less suited to provide regular inertial response but when considered with wider functionality such as droop response, the BESS becomes more desirable due to its good energy density. This high energy density makes the BESS most applicable for standalone application with potential short- and long-term grid-supporting revenue streams.

Although the WT essentially provides inertial response as a FESS, the consideration of the WT's primary objective of energy capture complicates its application for grid supporting functionality. The benefit of using WTs to provide inertial response is the reduced cost (potentially zero CAPEX) assuming that huge capacities of WTs will be deployed on future grids to meet general electrical demand. However, to avoid significantly affecting the energy capture, large power injections (corresponding to inertial responses beyond $H = 5\ s$) and any significant energy delivery cannot be achieved (hence the inability of WTs to provide droop support without overrating the converter, which would begin to introduce an increase in CAPEX). [73] also recorded an increase in loading when WTs provided inertial response, which would reduce the WT's lifetime and increase its OPEX. A link between inertial response delivery and increased drivetrain oscillation identified in [88] might explain the observed increase in loading. Overall, WTs are shown to be capable of providing short-term grid-supporting functionality such as inertial response, but an optimally configured power system may only utilise small inertial injections from the generators to minimise the effect on energy capture and lifetime costs.

3.3. Hurdles to the deployment of converter-based solutions

Section 3.2 has shown that several converter-interfaced technologies are suitable to provide frequency support to the grid. The following sections will describe some of the hurdles that are limiting the deployment of these solutions. These hurdles are the basis of the studies carried out throughout the remainder of the thesis.

3.3.1. Transparent frequency support characteristics and the impact of control configuration

Primary Frequency Response services are already being adapted in the form of Fast Frequency Response (FFR) to maximise the benefit to the grid of fast converter droop responses [24] and inertial solutions are being sought after [19]. Given the identification of appropriate technologies to provide the support in Section 3.2, developers need to choose a control strategy to implement the frequency support and then tune the controller to provide the exact specifications that are agreed with the System Operator. Section 4.6.3 will provide details of potential control strategies and their tuning guides, which are derived to set the inertial and droop contributions.

How can a developer know which control strategy should be used? Any given controller possesses two distinct operational features that can inform its application for a given function: robust stability and desirable dynamic performance. In the case of frequency support, a robust controller is required (among other things) to be able to implement the appropriate range of inertial and droop settings and to maintain its stability across the range of grid strengths that the converter is expected to be exposed to.

Desirable dynamic performance is required to optimise the effect of the frequency support on the power system’s dynamics and stability. The desirable dynamic features of inertial response are explored in more detail in Sections 3.3.2 and Chapter 6, however, some initial comments can be made regarding the impact of dynamics on Primary Frequency Response. [20], [89] highlighted the importance of the delivery speed of the FFR services to increase the effective constraint of frequency excursions on low inertia grids. As well as highlighting the dependence of the frequency excursion on the droop characteristics, [90] identified the link between droop response and oscillation attenuation, which was particularly critical for the stability of systems with high penetrations of converters. In this case, it is important to identify which control strategies offer acceptable stable operating ranges and desirable dynamic performance for Primary Frequency Response.

Several comparisons have been made between the GFM Droop and Synchronverter (sometimes referred to as Virtual Synchronous Generator) controllers. The equivalence of the frequency support provision by the GFM droop (with a low-pass filter (LPF) on the active power channel) and Synchronverter controllers was first shown in [62], however, the transient responses of the two were thought to be different due to the presence of cascaded control in the GFM Droop. [44] finds that systems governed by either controller experience improved frequency stability due to their fast response times compared to those governed by SMs, however, the exact frequency dynamics were not identical. Moreover, both controllers are shown to exhibit different reference tracking behaviour due to the different implementations of the inertia [66]. The same study identifies an advanced Synchronverter that emulates the separate channels of a SM to provide droop and damping separately, which is thought to exceed the damping capability of GFM Droop controllers [66]. Further work adapts the GFM Droop using a lead-unit on the power error to better emulate this high-damping-capability Synchronverter in [63].

The exact configuration of the GFM Droop and Synchronverter controllers can vary and the impact that this configuration has on the stability and dynamics of the frequency stability is not fully understood. [67] suggests that the implementation of cascaded controls in the GFM Droop (which are useful for the straightforward limitation of the converter current [62]) moves the location of the voltage control, thereby altering the effective reactance between the controller and the grid, and affecting its operation. This difference between single-loop (without cascaded controls) and multi-loop (with cascaded controls) configurations is confirmed for the GFM Droop controller but not between the single-loop Synchronverter and multi-loop GFM Droop (whose dynamics are often compared [62], [63], [66]). Moreover, [67] shows the difference between single- and multi-loop GFM Droop configurations on low X/R microgrid systems but not on the high X/R ratios that can be expected of transmission networks, where frequency stabilising converters are likely to be deployed. The higher grid reactance on the transmission network may mask the difference between the effective reactances of the different control approaches.

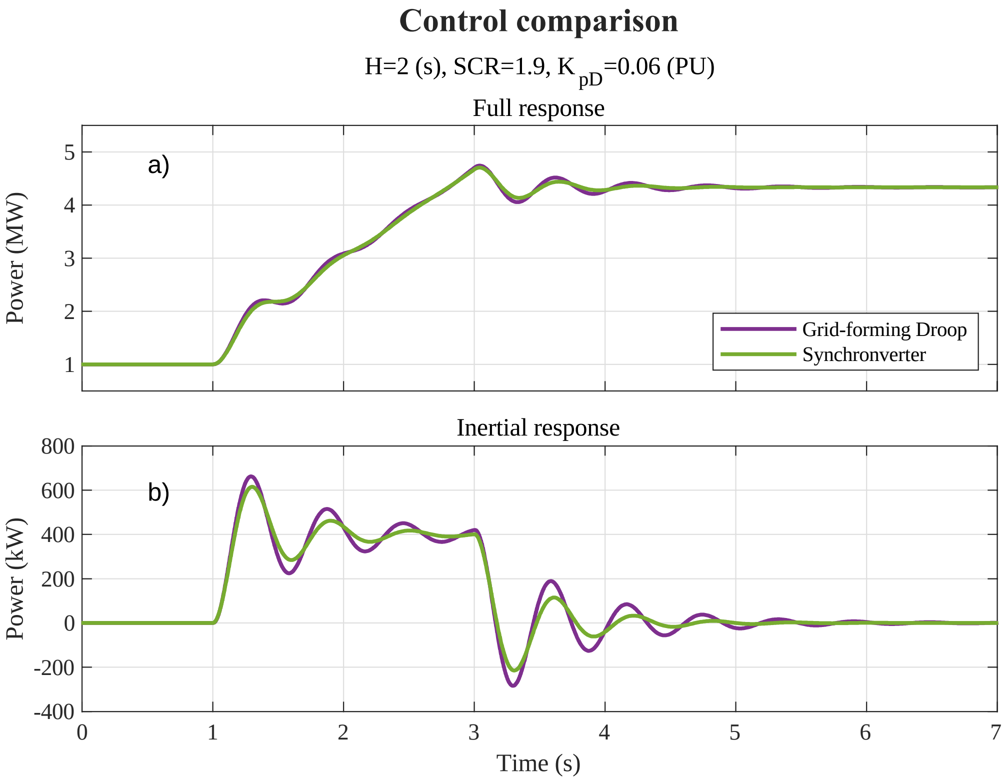

Figure 3-4 Example of inequality between multi-loop Grid-forming Droop and single-loop Synchronverter controllers in response to the same frequency disturbance, despite being tuned to provide the same inertial and droop magnitudes.

Finally, the conventional approach to tune cascaded controllers aims to achieve a large frequency separation between the inner current controller and the outer voltage controller [91]–[93] and is often used as a safe and standard approach that can be widely applied to all converter control configurations. However, [68] assessed the impact that the cascaded control tuning had on a multi-loop Synchronverter controller and found that both the stability and dynamics were affected. An explicit study of the impact of the cascaded control tuning on the multi-loop GFM Droop's stability and dynamics has not been carried out, despite [67] suggesting that their tuning may be important.

Figure 3-4 shows an example case where a single-loop Synchronverter and a multi-loop GFM Droop controller are tuned (using the guides detailed in Chapter 4) to provide the same inertial and droop contribution. Despite the equivalent tuning, the pictured active power responses to the frequency disturbance are different. Does the difference stem from the different outer control loops or the presence of the cascaded controllers? If the cascaded controllers impact the performance, can the dynamics be improved using a non-standard tuning approach? The source of these differences should be identified to ensure that the nuances of each control approach can be understood and the optimal strategy can be selected.

3.3.2. Confusion surrounding inertial specifications

GFM stability solutions are especially desirable due to their ability to take over governance of the power system from SMs. Their voltage-source behaviour allows them to stabilise the grid voltage waveform on all timescales [41] and minimises variations in grid voltage angle [29]. Moreover, this voltage rigidity supports synchronism across the grid [56], as defined by (3). GFMs have also been shown to improve grid stability by increasing the damping of electromechanical modes [94].

The inherent frequency supporting capability of inertial GFMs (which needs to be stressed, as some GFMs do not provide inertial response e.g. [26], [95]) has been observed to offer improved stability compared to GFLs, which require an additional channel to be added to achieve frequency response [30], [96]. These observations have coincided with the separation of inertial provision by converters (and SMs) into two fields: "true" and "synthetic" inertial response. True inertial response is deemed to be an inherent feature of a device (whether resulting from converter control or the physical laws governing SM operation) that is delivered rapidly and therefore effectively constrains the grid ROCOF [57]. On the other hand, synthetic inertial response emulates this inertial power injection but is thought to achieve less effective constraint of the grid ROCOF due to the delay introduced by its frequency measurement period [43], [97]. Confusingly, synthetic inertia is a term that has also been used to describe fast-frequency droop-type active-power responses to frequency deviations, but this terminology has been shown to be incorrect [98].

Although true GFM inertial response has been suggested to provide improved frequency stability compared to synthetic GFL inertial response, the studies making the suggestions often fail to make fair comparisons between GFM and GFL controls. [54] showed that an averaging window configuration used for a GFL’s ROCOF measurement constrained the IR speed and significantly reduced its ability to support the grid’s frequency compared to a GFM. However, this assessment only considered one specific ROCOF measurement approach. [30] compares systems using GFM and GFL inertial responses, and determines that the ability of the GFM to deliver a significant portion of the inertial response before the nadir enables the better constraint of the ROCOF. However, the study only assesses a single tuning of the GFL, despite identifying that its response could be sped up by adapting the inertial-filter time-constant. [99] develops a method to identify synchronous (true) from non-synchronous (synthetic) inertial responses and assumes that the two are distinct in terms of the measurement delay and the response shape, claiming that the features of the former enable it to determine the initial ROCOF following the event. Similarly, [96] determines that GFL inertial provision struggles to contribute to the containment of the initial ROCOF. The studies link the slower delivery of the given inertial tunings or configurations of the GFL controllers to a reduced ability to contain the ROCOF. All of these assumptions neglect other studies that show GFL’s to be able to support a range of inertial-filter time-constants [100] and that this tuning has a large impact on the response’s dynamic properties [101].

Meanwhile, due to their critical ability to replace SM functionality and some evidence of their greater effectiveness in providing frequency stability with respect to GFLs, SOs are developing specifications to encourage and standardise the development of GFM solutions. The technical regulator for the German power system, VDE FNN, defined the desirable features of GFMs and described upper and lower envelopes that a response should fit within, in terms of active or reactive power injection against time [33]. GB's National Grid Electricity System Operator (NG ESO), recently added an update to the grid code that outlined GFM characteristics and detailed the acceptable time-domain features that these characteristics would be expected to be delivered with [32]. Similarly, the Australian Electricity Market Operator (AEMO) outlined the critical issues facing their system and defined the properties that needed to be delivered by converters to resolve the issues [18]. The specifications generally describe the desirable functionality in terms of power injection magnitudes and critical time limits to describe the need for rapid stabilising support. Throughout them all, there is an undercurrent argument that disqualifies GFLs from providing inertial response due to the perceived slow response and critical link to frequency stability that has trickled in from the academic literature (e.g. [30], [54], [96], [99]). As a result, GFL inertial support is considered to be a fast frequency response that is useful for limiting frequency deviation but not for containing the initial ROCOF of a disturbance.

Another issue with the industrial specifications may exist in relation to their description of true inertial delivery periods. [32], [57] describe true inertial response as one that is inherent to the device so is initiated instantly without need for frequency/ROCOF measurement. Alternatively, [56] relates the inertial response to the instant initiation resulting from the internal voltage source nature of the device, and [18] expects GFM inertial response to be able to deliver an instant change in current. In fact, [18] describes this instant response as the result of a difference between the converter and grid voltage angles (the phenomena described by (3) that should actually be referred to as phase response or the action of the synchronising torque). Some confusion may exist surrounding the features of GFMs that are related to their voltage source nature versus their inertial capabilities. Using knowledge of the dynamic frequencies that inertial behaviour manifests across (roughly between 0.04:2

Hz with a resonant peak occurring between 1:3 Hz), we could argue that the fastest possible inertial response time is equal to the inverse of the largest of these frequencies, which is detailed in (13).

$$\tau_{IR} = \frac{1}{f_{IRmax}} = \frac{1}{3}\ s \tag{13}$$

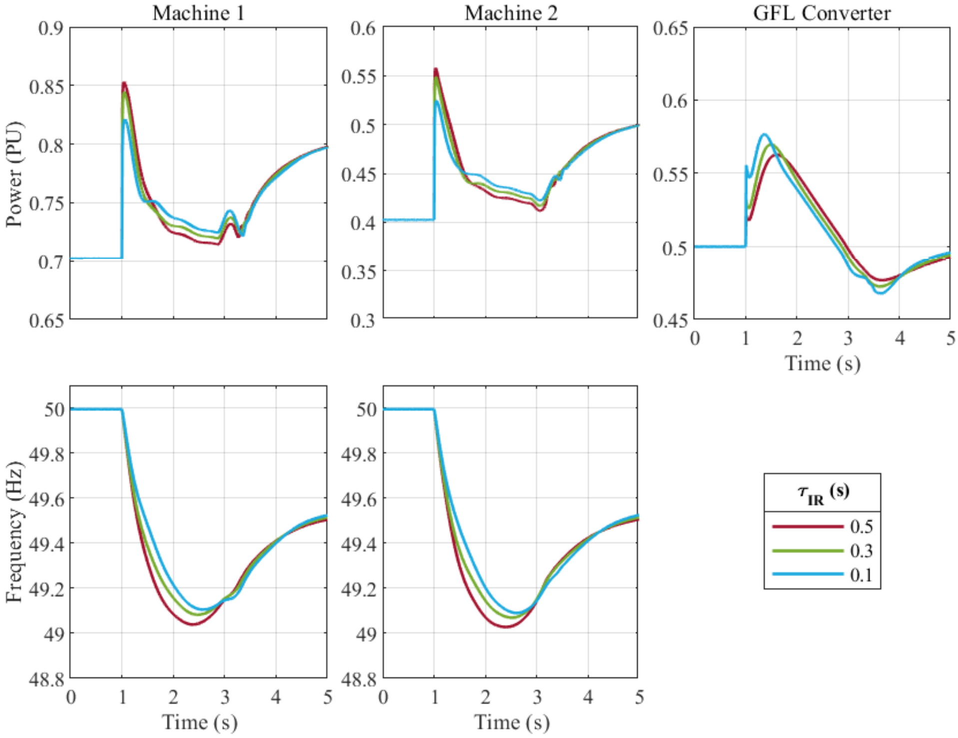

Figure 3-5 System a)-c) power and d)-e) frequency signals following a load step on a small power system as the inertial delivery speed τ_{IR} of a power converter varies. All of the SMs and converter are tuned to provide an inertial constant H=2 s.

Figure 3-5 shows simulations of a small low-inertia power system with an inertial converter that supports the two online SMs. The simulations agree with [30]'s findings that the ROCOF and the frequency excursion degrade as the converter's inertial delivery slows (Figure 3-5 and Table 3-3). However, the ROCOF resulting from the different inertial delivery speed scenarios does not differ significantly until after the initial transient, several hundreds of a millisecond after the disturbance. The difference in the converter's power signals are also greatest several hundred milliseconds after the disturbance, suggesting the industrial standards that expect inertial response to be delivered within the first 50 milliseconds are not providing an achievable delivery speed objective.

Table 3-3 Frequency stability indicators as converter inertial delivery speed varies.

Inertial delivery speed τ_{IR} (s)	Minimum ROCOF (Hz/ s)		Nadir (Hz)	
	Machine 1	Machine 2	Machine 1	Machine 2
0.5	-1.90	-1.95	49.04	49.03
0.3	-1.80	-1.84	49.08	49.07
0.1	-1.50	-1.53	49.11	49.09

Although adapted configurations of GFMs have been proposed to improve their performance in different conditions (e.g. improved damping by decoupling inertial and droop responses [102], decoupled active and reactive channels to minimise undesired transient variations [103], improved small-signal stability on a range of grid strengths by using a current-control framework [104], and adaptive inertial settings to account for system conditions [100]), none of these adaptations will change the inherent properties of the inertial dynamics.

The lack of transparency surrounding the contribution of different response features to grid stability means that the specifications may not be formulated effectively. Firstly, the specifications should clearly and transparently describe useful inertial response, and nothing else. It is critical that the SO knows which features contribute to system stability so that there is no scope for oversight. Secondly, if GFM inertial response is unique in its ability to stabilise the grid then the specifications should be able to distinguish GFM provision from GFL provision. If the specification cannot distinguish between the two then either: the specification needs to be adapted to better identify the critical feature of the GFM provision that stabilises the grid or else, if there is no difference, GFLs should be allowed to participate in the inertial service. GFLs could offer an additional solution that developers have expertise in that can contribute to grid support alongside GFMs.

3.3.3. Measurement of wind turbine inertial response

System inertia monitoring has garnered interest due to the links between inertia and stability (and therefore economic costs) [2], [20], [32]. Inertia monitoring identifies the inertial state of the system (either in real-time or offline using historical data) to enable SOs to take actions to increase the robustness of the system in the most economically effective routes. Inertia monitoring is distinct from the measurement of inertial response, where the former is carried out throughout system operation and can inform decision making on different timescales. For example, on short (hourly to daily) timescales, knowledge of the inertial state of the system could inform advanced unit commitment scheduling or balancing mechanism actions to increase the online inertia to maintain the system within a critical stable operating range [17], [105]. Alternately, on longer planning timescales, inertia monitoring could guide a SO to reduce the system's largest single loss event, change the grid code, or modify protection settings [105]. In contrast, the measurement of inertial response is carried out before grid-connection to ensure that a device provides the support that is specified. The benefits of inertial response measurement for inertia monitoring will be discussed later in this Section.

Simple inertia monitoring methods can estimate the state of the system by tracking the number of online SMs, where their inertial contribution is known as a physical feature of the machine. However, frequency stability is a complicated phenomenon that can vary depending on the given instantaneous system configuration and becomes increasingly difficult with the uncertainty of system parameters, which is increasing with the penetration of (variable) converter interfaced generation, and the provision of new less-known stability solutions [106].

As such, more advanced methods have been proposed that often relate power and frequency measurements at locations around the system to some form of the Swing Equation (6) to describe the instantaneous inertial state of the system. [107] inputs ambient power and frequency measurements to an ARMAX system identification model to estimate the impulse response function, which can then be used to calculate the inertia of the system. The accuracy of the approach is improved in [108] by processing the low-confidence frequency data to achieve a more accurate expression of the maximum ROCOF.

Inertia measurement methods have also been adapted to maintain accuracy on power systems with large penetrations of converter interfaced devices. [97] uses a polynomial fit equation to describe the frequency signal, which can then provide the maximum ROCOF for inertia estimation. Alternatively, [109] models the system inertia as the sum of periodic and stochastic parts to account for the stochastic nature of RESs. [110] compares several inertia measurement approaches and confirms that most are accurate when the majority of the inertia provision is sourced from SMs, but begin to struggle when converter interfaced devices provide frequency support.

Methods have been proposed to monitor the inertia provided by converter interfaced devices. [111] uses the frequency divider formula (FDF), as proposed in [112], alongside the regulating power, derived from the FDF in [113], to develop a heuristic function that monitors the inertia of individual devices (SMs or converters). In a review of inertia monitoring approaches with consideration of converters, [106] highlights that different methods may be required for different control approaches and that nonlinearities can complicate the measurement due to the capacity/ technological features of the converters.

Indeed, further complications are likely to be present when monitoring the inertia provided by WTs. The ScottishPower Renewables trial of a grid-connected GFM wind farm (WF) in 2019 highlighted the masking of the inertial response due to coinciding wind variations [70]. Figure 3-6 depicts the experimental data from this study, highlighting that the visibility of the WF’s inertial injection varies depending on the wind conditions that coincide with the frequency disturbance.

Despite these findings, the few methods that have been proposed to measure WT inertial response disagree if it is necessary or how to account for the wind’s impact. An early measurement approach (of the actual inertia associated with the WT’s drivetrain and blades) suggested that the wind could be assumed to be constant across the WF for the short period during the frequency disturbance, thereby simplifying the inertia measurement approach to allow the insertion of the power and frequency change to the Swing Equation [114]. The Swing Equation is expressed in a discrete form to monitor inertial provision in [27], which again neglects the impact of the wind, but now validates this approach by assuming that the slow mechanical dynamics of the WT system will not vary during the electric disturbance. This discrete approach is extended to use a fourth order equation and hence achieve more accurate inertial monitoring in [115] but neither iteration of the approach is tested in variable wind conditions. Another method that is developed to monitor both SM and converter-based inertia is subject to variable wind conditions and suggests that its inaccuracies result from the WT rotor deviations [99].

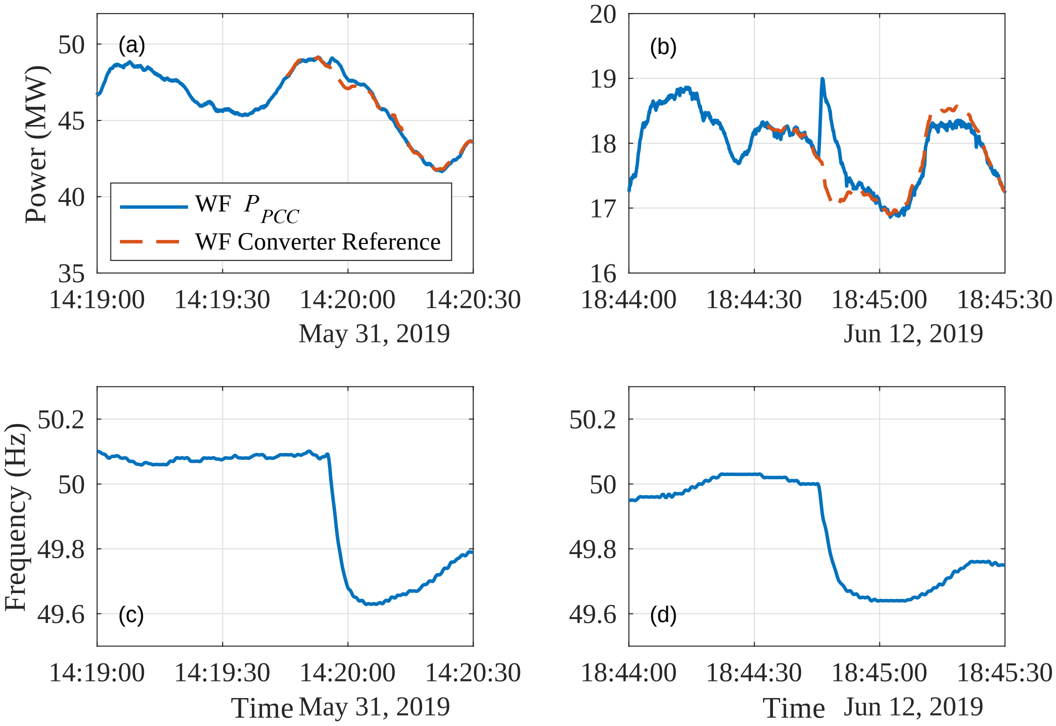

Figure 3-6 Dersalloch WF PCC power and reference power in response to two different frequency disturbances on a) the 31st of May and b) the 12th of June. The corresponding frequency excursions are shown in c) and d).

The accuracy of methods that suggest that the mechanical WT power does not vary during the inertial period can be tested using the Dersalloch experimental data pictured in Figure 3-6. The approaches in [27], [114], [115] measure the inertial power injection as the difference from the peak inertial power at the point of common connection (PCC) from the initial power at the PCC at the start of the frequency disturbance. The inertial power injection ΔP_{PCC} is then input, along with the maximum recorded system ROCOF, to the rearranged form of the swing equation (12) to estimate the device's inertial constant (14). This estimation is carried out with respect to the rated kinetic energy of the device (for rated power and rotational speed) to simplify the discussion of the WT's operation from the grid perspective. Otherwise, the variation of the kinetic energy with the WT's operating point could result in a WT being described as possessing the same inertial constant despite its power injection to a given frequency disturbance varying.

$$H = \frac{\Delta P_{PCC}\omega_0}{2\dot{\omega}_{\max}S_n} \tag{14}$$

Using the assumption that the WT's inertial response can be measured from its initial power in (14), the inertial power injections recorded for Dersalloch WF during the frequency disturbances on the 31st of May and the 12th of June are $\Delta P_{PCC,31/05} = 0.54\,MW$ and $\Delta P_{PCC,12/06} = 1.21\,MW$, respectively. During these two events the maximum ROCOFs were $\dot{\omega}_{max,31/05} = 0.69\,rad/s$ and $\dot{\omega}_{max,12/06} = 0.50\,rad/s$ and the rated powers were $S_{n,31/05} = 69\,MW$ and $S_{n,12/05} = 60\,MW$. Using the measured inertial power injections and the known WF and frequency disturbance information the inertial constant can be estimated (est) for each event as $H_{est,31/05} = 1.8\,s$ and $H_{est,12/06} = 6.3\,s$. However, the two WFs were known to be operated at $H_{31/05} = 4\,s$ and $H_{12/06} = 7.5\,s$ [70]. The inaccuracy suggests that the methods that use the initial power approximation do not measure WT inertial response effectively, potentially due to their underestimation of the wind's impacts on the inertial dynamics.

The IEC proposed an alternative approach as an industrial standard to validate inertial response from WTs before connecting to the grid, which suggests that the wind should be accounted for when measuring inertia [116]. The standard approach is pictured in Figure 3-7 and uses a Power Available baseline that accounts for the wind's impact to measure the inertial injection from. Although the standard is somewhat unclear, the Power Available signal is deemed to represent the power in the rotor of the WT. While the approach takes steps to better account for the wind's impact, the Power Available baseline may not be an appropriate solution as the signal is not expected to properly account for the stages that convert the kinetic energy in the wind into electrical energy at the PCC. Therefore, the IEC standard's inertia measurement may be skewed and could also be inaccurate. The nuances of inertial provision by WTs and the interaction with the wind should be explored in more detail to ensure firstly, that SOs are aware of the contribution from WTs and are therefore capable of dispatching a stable system, and secondly, that WTs are properly compensated/recognised for the support they provide, which is critical for the stimulation of new converter-based stabilising solutions.

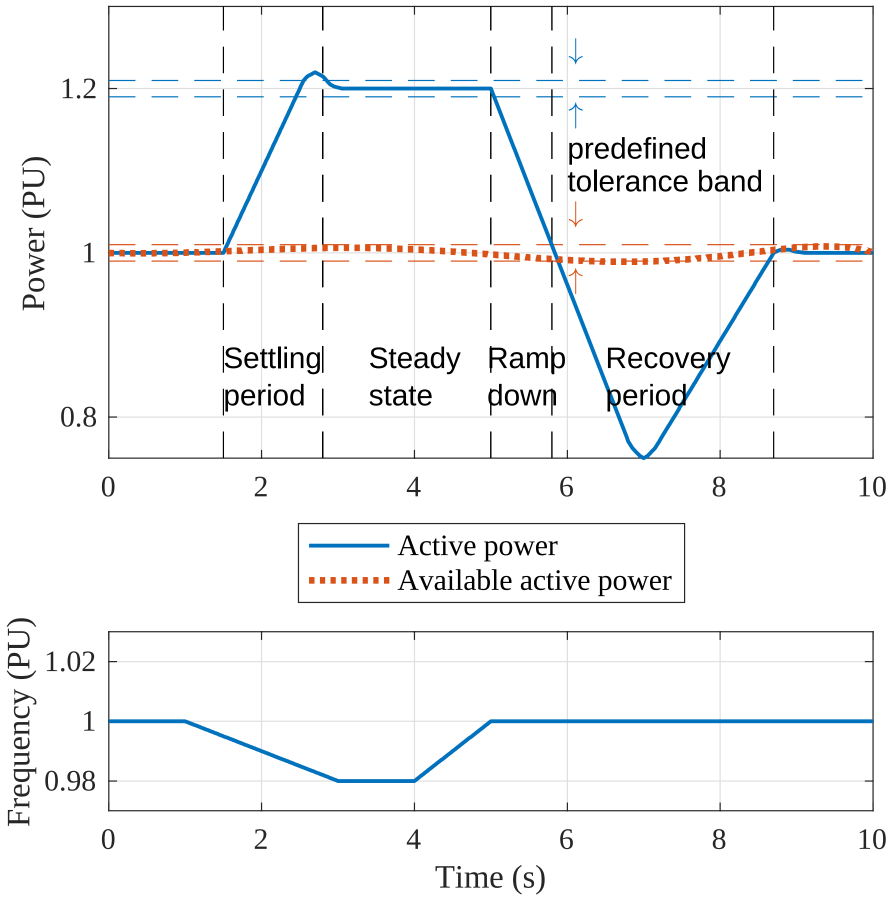

Figure 3-7 IEC WT inertia test methodology, reconstructed from [116]. The power and frequency signals, inertial power bands, and operating time periods are included.

3.4. Summary

This chapter has provided a techno-economic assessment of energy source technologies to provide inertial and droop responses. The assessment highlights the capability of multiple energy sources to provide one or other component of the primary frequency response by matching the power and energy requirements for the support to the technologies' capacities. The most suitable technologies were explored and identified by considering a wider range of their techno-economic features that are relevant to the response components. The results highlight that technological solutions to provide frequency support to the grid already exist, which suggests that some other hurdles are limiting the rate at which they can be deployed.

The hurdles that are thought to be limiting converter-based frequency-stabilising solutions (following extensive review of the literature) were then introduced. The equivalence between two frequency supporting controllers was discussed and shown to be untrue (in terms of stability and dynamics) in some cases. The differences may result from the exact configuration or tuning of the inner controller, whose impact is sometimes neglected from consideration. The features of different controllers need to be fully understood to ensure that the most effective strategies can be selected to support the grid, so that operators are aware of their operational limitations, and so that the impact of the inner controller does not unexpectedly impact their stability or dynamic properties.

The confusion surrounding inertial specifications was then discussed. Grid operators are attempting to stimulate the provision of grid-stabilising solutions using these specifications but some appear to be confusing inertial dynamics with voltage-source behaviour. All existing specifications disqualify grid-followers from participating in inertial support, potentially due to its confusion with grid-forming voltage-source functionalities. It is important that grid services are specified transparently to ensure that the grid is effectively dispatched to survive disturbances, but also, to allow all the solutions that are capable of providing useful support to do so.

Finally, the conflicting assumptions surrounding the wind’s impact on wind turbine inertial response was discussed. Despite experimental results showing the masking of of a grid-connected wind farm's inertial response due to coincident wind variations, methods to measure wind turbine inertial response disagree if and how to account for the wind’s impact. Although the industrial standard approach uses a baseline signal to account for the wind, it may not accurately represent the wind’s impact on inertial power. Accurate inertial response measurement is critical to ensure that devices are effectively tested before connecting to the grid to ensure they respond as required, but also has implications for tracking the system state using network monitoring.

Solving the above-mentioned issues can support a quicker transition to net-zero power system operation while maintaining its security and robustness.

Chapter 4. Modelling and control of converter-interfaced devices

4.1. Introduction

This chapter details the modelling approaches that are used throughout the thesis to describe and test the ability of converters to support power system frequency. Several systems need to be resolved to understand the capability and nuances of converter operation and to assess the means that these solutions might be integrated with. The relevant systems include: the source of energy, the mechanical and electrical components used to capture and transfer the energy, the algorithms used to control these components, and the dynamics of the power system.

In terms of the converter’s energy source and mechanical and electrical components, this thesis will model an ideal battery energy source, to allow a simple and effective comparison of converter controller algorithms, and a detailed WT system, to analyse the impact that the energy source dynamics have on the converter’s output. The ideal battery energy source configuration only resolves the grid-connected inverter (assuming that sufficient energy is always available to support the control demand), whereas, the detailed WT system includes a back-to-back power converter configuration that interfaces the wind energy source to the power system via a dynamic DC-link.

The power system is modelled using either an infinite bus representation, to allow the explicit assessment of specific dynamic phenomena that can be hard to replicate in more detailed models, or using a multi-bus representation, to allow the validation of results on a more realistic power system model and to assess the impact that the converter contributions have on power system frequency. The multi-bus configuration includes parallel connected SMs that also contribute power (depending on their dispatch and control algorithms) to the adjustable loads and losses in the system. The control systems that are used to manage the power flows from energy source to power system are described in Section 4.6.

All of these relevant systems can be represented using different tools, each of which are suited to describe different phenomena in empirical or analytical manners. All of the modelling approaches are founded on the physical laws that describe the relevant mechanical and electrical components, which can be represented in their most accurate form using electro-magnetic transient (EMT) analysis. The EMT models simulate a period of a system’s operation by solving the dynamic differential equations that describe its physical (and software) components for every sequential timestep. The equations that describe all of the components in each of the systems mentioned above are detailed throughout Sections 4.3 to 4.5. The reference frames that these equations are implemented in are described first in Section 4.2 alongside any of the procedures that are used to transform the signals from one frame to another.

Although EMT analysis provides the most accurate resolution of any given system’s operation, it is computationally burdensome and does not allow for the easy representation of a system’s characteristics or its relationship between inputs and outputs. Instead, system’s can be linearised and then represented at a given operating point using small signal models (SSMs) to allow the application of linear control theory. This modelling approach allows the faster resolution of systems and the application of control tools that can provide analytical insight to the key features of different phenomena that is not possible using EMT modelling. Additional details of any systems that are resolved using SSMs are provided in Section 4.7.

4.2. The abc and Synchronous reference frames

Electrical quantities are generally expressed in the abc Reference Frame, where each axis corresponds to one of the three phases separated by 120 degrees from one another that electricity is conventionally transmitted on. The electrical quantities of interest are generally the instantaneous voltage and current that can be measured at different locations around the network. Throughout this section that discusses reference frames for modelling, these quantities will be signified using an example parameter label x, whose abc vector representation will be labelled x_{abc}.

The abc Reference Frame closely relates to the electrical quantities in the real world, however, it can be cumbersome to integrate the three-phase time-varying signals with analytical and control tools. Therefore, the Park Transform [117] is useful to move the abc quantities into the Synchronous Reference Frame, which allows the three time-varying abc quantities to be transformed to three constant electrical quantities (reducing to two quantities for balanced systems) that can simplify the analytical and control approaches. The Park Transform achieves this simplification using a combination of the Clarke Transform to the Orthogonal Reference Frame [118] plus an angular transformation that aligns the Orthogonal Reference Frame with the synchronous frequency of the AC abc quantities. The Park Transformation from abc to Synchronous Reference Frames is visualised in Figure 4-1.

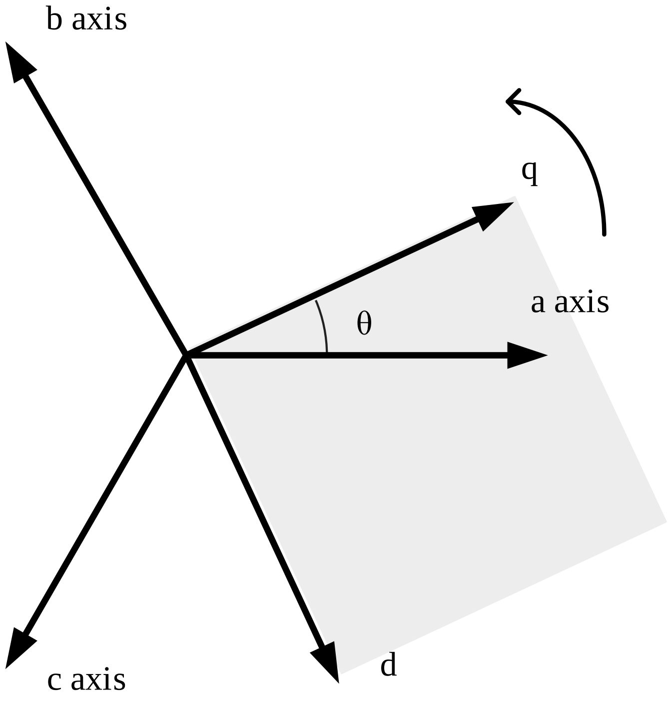

Figure 4-1 abc and Synchronous qd0 reference frames (where the 0 axis is perpendicular to the qd axes and comes out of the page).

The Park Transform T_{qd0} moves the abc quantities x_{abc} to the Synchronous Reference Frame, which is described in terms of its perpendicularly displaced q, d, and 0 axes x_{qd0} (15). The transform is detailed in (16). The inverse relationship and transform to return from the $qd0$ quantities to the abc quantities are detailed in (17) and (18), respectively.

$$[x_{qd0}] = [T_{qd0}][x_{abc}] \tag{15}$$

$$T_{qd0}(\theta) = \frac{2}{3}\begin{bmatrix} \cos(\theta) & \cos\left(\theta - \frac{2\pi}{3}\right) & \cos\left(\theta + \frac{2\pi}{3}\right) \\ \sin(\theta) & \sin\left(\theta - \frac{2\pi}{3}\right) & \sin\left(\theta + \frac{2\pi}{3}\right) \\ \frac{1}{2} & \frac{1}{2} & \frac{1}{2} \end{bmatrix} \tag{16}$$

$$[x_{abc}] = [T_{qd0}]^{-1}[x_{qd0}] \tag{17}$$

$$T_{qd0}^{-1}(\theta) = \begin{bmatrix} \cos(\theta) & \sin(\theta) & 1 \\ \cos\left(\theta - \frac{2\pi}{3}\right) & \sin\left(\theta - \frac{2\pi}{3}\right) & 1 \\ \cos\left(\theta + \frac{2\pi}{3}\right) & \sin\left(\theta + \frac{2\pi}{3}\right) & 1 \end{bmatrix} \tag{18}$$

The instantaneous balanced abc voltage or current phasors can be expressed using (19).

$$\begin{gathered} x_a(t) = \sqrt{2}Xcos(\omega t + \phi) \\ x_b(t) = \sqrt{2}Xcos\left(\omega t + \phi - \frac{2\pi}{3}\right) \\ x_c(t) = \sqrt{2}Xcos\left(\omega t + \phi + \frac{2\pi}{3}\right) \end{gathered} \tag{19}$$

Therefore, when the Park Transform is implement using an angle aligned with the electrical voltage $\theta = \omega t + \phi$ the $qd0$ phasors can be expressed by (20) after being transformed from the abc phasors in (19). x_0 is zero for balanced three-phase abc systems.

$$\begin{gathered} x_q = \sqrt{2}Xcos(\omega t + \phi - \theta) \\ x_d = -\sqrt{2}Xsin(\omega t + \phi - \theta) \\ x_0 = 0 \end{gathered} \tag{20}$$

(20) shows that the correct alignment of the $qd0$ frame with the abc frame (e.g. aligning the q axis with the a axis) obtains constant quantities from the previously time-varying quantities.

The voltage and current phasors can be expressed in (21) and (22).

$$\sqrt{2}V_{qd} = v_q - jv_d \tag{21}$$

$$\sqrt{2}I_{qd} = i_q - ji_d \tag{22}$$

Using (21) and (22), the power of a three-phase system can be expressed in the Synchronous Reference Frame as (23). The active and reactive powers P and Q can then be expressed as (24) and (25), respectively.

$$S = P + jQ = 3V_{qd}I_{qd}^{*} = 3\left(\frac{v_q - jv_d}{\sqrt{2}}\right)\left(\frac{i_q + ji_d}{\sqrt{2}}\right) \tag{23}$$

$$P = \frac{3}{2}\left(v_q i_q + v_d i_d\right) \tag{24}$$

$$Q = \frac{3}{2}\left(v_q i_d - v_d i_q\right) \tag{25}$$

(24) and (25) show that the correct alignment of the $qd0$ Synchronous Reference Frame also continues the effective decoupling of the active and reactive channels that is introduced by the Clarke Transform [40], hence its utilisation throughout the modelling and control applications described throughout the remainder of this Chapter.

4.3. **Wind turbine system**

This section will detail the aerodynamic, mechanical, and electrical equations that represent the dynamics of a wind-turbine that connects to the grid. These equations are used to build the wind-turbine time-domain EMT model. Section 4.3.1 describes the configuration of the WT model from rotor to generator. Section 4.3.2 details the average converter model that represents the back-to-back configuration that interfaces the wind turbine energy source to the grid.

4.3.1. Wind turbine energy source

To resolve the impact that a WT energy source's dynamics have on converter grid-support a full electromechanical model is required that accounts for the dynamics of the wind, the electrical generator, and the mechanical system that connects the two (as well as the converter and grid dynamics). This thesis will model a direct-drive WT (mid-level power rating considering existing WTs connected to the grid) with a permanent-magnet synchronous generator (PMSG). The model resolves the torque/power input to the WT rotor by the wind, a single-lumped-mass model of the WT drivetrain, and the electrical current that is output by the generator to the machine-side rectifier (pictured in Figure 4-2).

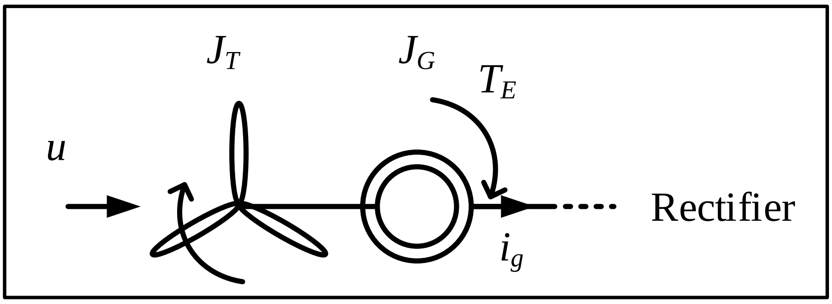

Figure 4-2 Electro-mechanical model of the wind turbine rotor connected to PMSG via a single-lumped-mass model of the WT drivetrain.

The power in the wind that is captured by the WT rotor P_t can be expressed by:

$$P_t = \frac{1}{2}\pi R^2 \rho C_p(\lambda, \beta)\mathrm{u}^3 \tag{26}$$

Where R is the radius of the WT rotor, ρ is the density of the air, u is the wind speed, and C_p is the power coefficient, which depends on the pitch angle β and the tip-speed ratio λ (itself depending on rotor speed ω_t).

$$\lambda = \frac{\omega_t R}{u} \tag{27}$$

The power coefficient can be expressed deterministically for a given WT using its characteristic parameters $[c_1 \ldots c_9]$ in (28) and (29) [119]:

$$C_p(\lambda, \beta) = c_1 \left(c_2 \frac{1}{\Lambda} - c_3 \beta - c_4 \mathrm{B}^{c_5} - c_6 \right) e^{-c_7 \frac{1}{\Lambda}} \tag{28}$$

$$\frac{1}{\Lambda} = \frac{1}{\lambda + c_8 \beta} - \frac{c_9}{1 + \beta^3} \tag{29}$$

The power in the wind can be transformed to a rotor torque (T_t):

$$T_t = \frac{P_t}{\omega_t} \tag{30}$$

Therefore, the WT rotor subsystem can be built from (26) to (30) to become a system that is input wind speed and outputs a turbine rotor torque. This rotor torque is fed to the single-mass drivetrain model, as detailed in [120], along with the electrical torque output of the PMSG T_e to find the generator rotor speed ω_r:

$$\omega_r = \frac{1}{J_{WT} s} (T_e + T_t) \tag{31}$$

$$\omega_t = \omega_r \tag{32}$$

As the WT is a direct-drive machine the turbine rotor and generator speeds are equal. J_{WT} is the inertial mass of the WT, which accounts for the inertia of the turbine and the generator:

$$J_{WT} = J_T + J_G \tag{33}$$

The generator stator angle (θ_s), and hence internal rectifier voltage angle, can be found by integrating the generator stator frequency, which is the product of the rotor speed and the number of generator pole pairs p:

$$\theta_s = \frac{\omega_r p}{s} \tag{34}$$

The electrical torque output is calculated using a model of the PMSG in the qd synchronous reference frame, as described in [88], [121]:

$$s i_{gd} = \frac{1}{L_{sd}} v_{gd} - \frac{R_s}{L_{sd}} i_{gd} + \frac{L_{sq}}{L_{sd}} p\omega_r i_{gq} \tag{35}$$

$$s i_{gq} = \frac{1}{L_{sq}} v_{gq} - \frac{R_s}{L_{sq}} i_{gq} - \frac{L_{sd}}{L_{sq}} p\omega_r i_{gd} - \frac{\psi p \omega_r}{L_{sq}} \tag{36}$$

$$T_e = \frac{3}{2} p \psi i_{gq} \tag{37}$$

i_{gqd} are the generator current components, L_{sqd} are the stator inductance components, v_{gqd} are the generator internal voltage components, R_s is the stator resistance, and ψ is the flux linkage of the generator.

4.3.2. Back-to-back power converter system

A 2-level voltage source converter (VSC) is made up of 3 IGBT branches, one for each phase, and each containing an upper and lower arm [40]. The back-to-back converter topology used for AC-output generators is composed of two of these VSCs: a rectifier that changes the AC generator output to DC and an inverter that changes the intermediate DC current to AC to be injected to the grid.

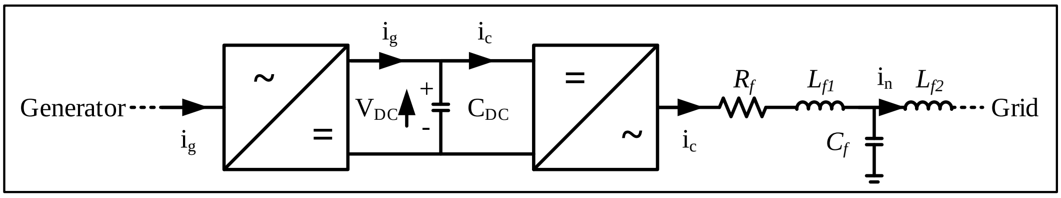

Figure 4-3 Electrical model of back-to-back 2-level VSC configuration including resistive, inductive, and capacitive components of the network-side filter.

The back-to-back configuration includes a parallel capacitance in the DC link to ensure that the DC voltage remains within acceptable values throughout fluctuations in the DC current as the two converters work together to vary the power transfer. A combination of inductor and capacitor components are then used on the AC side of the inverter to filter the switching harmonics that would otherwise be injected to the grid due to the waveform modulation, thereby improving the power quality of the injection. The rectifier and inverter VSCs are identical in terms of electrical components but use slightly different high-level control strategies to determine the power flows. The high-level controls determine the voltage references that allow the low-level waveform modulation strategy to control the order of the switching of the 3 arms to either transform AC current inflow to DC current output (rectification) or vice versa (inversion). Both converters are modelled in this thesis using average representations, which assume that the low-level modulation strategy achieves accurate tracking of the references fed by the high-level controls. This assumption neglects any switching dynamics, which are outside the scope of this thesis.

To simplify the modelling of a VSC, the AC and DC parts are modelled independently. The two can be separated by representing the DC part as a DC current source and the AC part as a 3 phase AC voltage source. The physical connection between the two can then be implemented by ensuring equivalent power transfer occurs from one to another. For the back-to-back VSC configuration (pictured in Figure 4-3), the total DC current in the intermediate link I_{DC} is described as the summation of currents (powers) fed by the rectifier i_g (P_g) and pulled by the inverter i_c (P_c):

$$i_{DC} = \left(i_g - i_c\right) = \frac{P_g - P_C}{V_{DC}} \tag{38}$$

Where V_{DC} is the DC voltage, the inverter power P_c is determined by the objective of the network side controller (whose reference is P_c^*) and P_g is defined as the power output by the PMSG:

$$P_g = \frac{3}{2}\left(V_{gq}i_{gq} + V_{gd}i_{gd}\right) \tag{39}$$

The DC voltage depends on the balance between the two converters and the capacitance C_{DC} that links them:

$$V_{DC}s = \frac{i_{DC}}{C_{DC}} \tag{40}$$

The filter characteristics are determined using standard configuration approaches [122] and can take either LC or LCL topologies. R_f is the filter resistance, C_f is the filter capacitance, and L_{f1} and L_{f2} are the inner and outer filter inductances. If an LC filter topology is used L_{f2} is set to zero.

4.4. Ideal battery energy source inverter system

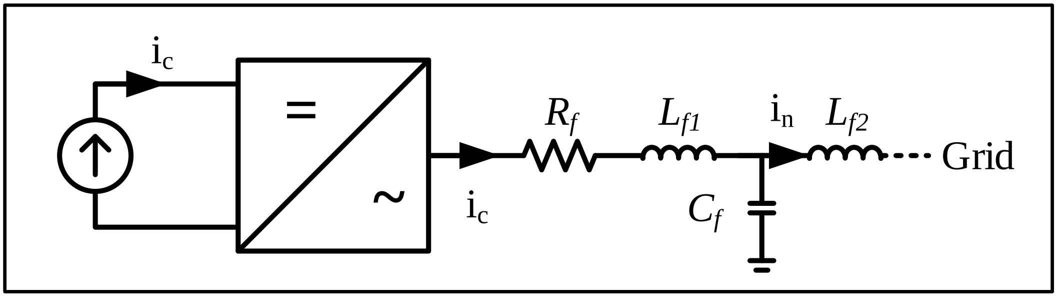

Figure 4-4 Electrical model of the ideal battery energy source 2-level VSC configuration including resistive, inductive, and capacitive components of the network-side filter.

An ideal battery energy source system (pictured in Figure 4-4) can be modelled instead of the fully resolved energy source to reduce the computational burden and isolate network-side converter dynamics if these are the features of interest. In this case, the DC side of the inverter is represented as an infinite current source. Any current that is pulled out of the inverter (i_c) is assumed to be able to be supported by the DC source

(i_g). Additional DC current source dynamics are neglected and the waveform modulation references can be fed directly to the average representation of the 3-phase voltage source output on the AC side of the inverter, which uses the same standard LCL or LC filter configurations as the network-side of the fully resolved back-to-back converter configuration.

4.5. **Power system**

This section details the mechanical and electrical equations that represent the dynamics of a power system. The energy source systems are integrated with either power system representation to assess how the two interact. Section 4.5.1 describes the infinite bus representation of a power system that aggregates all of the system components upstream of the inverter in terms of a voltage source and impedance. Section 4.5.2 details the multi-bus representation of a power system that explicitly models all of the components of a small power system.

4.5.1. Infinite bus network model

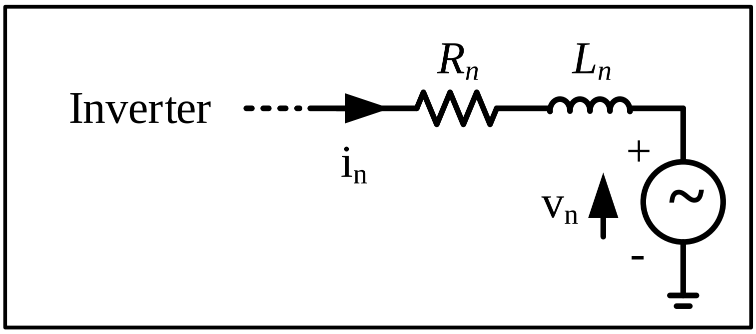

Figure 4-5 Electrical model of an infinite bus representation of the power system.

An infinite bus representation is used to model the network in some studies. The infinite bus represents the entire system that a device connects to as a single aggregated equivalent voltage source (pictured in Figure 4-5). The voltage source has Thevenin Equivalent voltage magnitude v_n and impedance:

$$Z_n = R_n + j\omega L_n \tag{41}$$

which represents the transmission that connects the device to the network. The fundamental frequency of the voltage source (and hence grid) is $\omega_0 = 2\pi 50\ rad\ s^{-1}$, however, the grid frequency ω_g can also be used as an input to the model. The grid frequency can be varied away from ω_0 to represent a frequency disturbance and to observe the frequency supporting capability of the connected devices. The voltage magnitude can also be varied away from its nominal value $V_n = 690\ V$ to assess the devices' capabilities in different operating conditions. The magnitude of the equivalent impedance can be varied to represent the strength of the grid. Short circuit ratio can be used as a description of the grid's strength, where the impedance depends on SCR according to:

$$R_n = \frac{1}{X/R}\frac{Z_n}{SCR} \tag{42}$$

$$L_n = \frac{Z_n}{\omega_0 SCR} \tag{43}$$

Where X/R is the ratio of the network's reactance X to resistance R. The equivalent voltage source represents such a large aggregation of devices compared to the individual device under test that although the network's properties are imposed on the individual devices any response from the device does not affect the properties of the network.

The model of the network can be expressed in terms of the voltage and current equations between the converter and grid voltage sources [123]. The final differential equations are expressed in the qd frame for the 6 independent variables:

$$i_{cd}s = \frac{v_{cd}}{L_{f1}} - \frac{v_{PCCd}}{L_f 1} - \frac{R_f}{L_{f1}} i_{cd} + \omega_g i_{cq} \tag{44}$$

$$i_{cq}s = \frac{v_{cq}}{L_{f1}} - \frac{v_{PCCq}}{L_{f1}} - \frac{R_f}{L_{f1}} i_{cq} - \omega_g i_{cd} \tag{45}$$

$$v_{PCCd}s = \frac{i_{cd}}{C_f} - \frac{i_{nd}}{C_f} + \omega_g v_{PCCq} \tag{46}$$

$$v_{PCCq}s = \frac{i_{cq}}{C_f} - \frac{i_{nq}}{C_f} - \omega_g v_{PCCd} \tag{47}$$

$$i_{nd}s = \frac{v_{PCCd}}{L_{f2} + L_n} - \frac{v_{nd}}{L_{f2} + L_n} - \frac{R_n}{L_{f2} + L_n} i_{nd} + \omega_g i_{nq} \tag{48}$$

$$i_{nq}s = \frac{v_{PCCq}}{L_{f2} + L_n} - \frac{v_{nq}}{L_{f2} + L_n} - \frac{R_n}{L_{f2} + L_n} i_{nq} - \omega_g i_{nd} \tag{49}$$

Where i_{cqd} and i_{nqd} are the converter and network current components, respectively, v_{cqd}, v_{PCCqd}, and v_{nqd} are the converter, PCC, and network voltage components, L_{f1} and L_{f2} are the filter inner and outer inductances, and R_f and C_f are the filter resistance and capacitance.

4.5.2. Multi-bus power system model

Alternatively, a multi-bus model that represents more of the components on the power network can be used. The increased system resolution allows the assessment of the converter capability in more realistic event conditions, the validation of the results observed on the infinite bus representation, and the assessment of the impact that the converter functionality has on the system dynamics (such as frequency stability).

The multi-bus system simulated in this thesis (pictured in Figure 4-6) is adapted from a two-area power system model that was originally designed in [124], and then adapted in [125], to study low frequency electromechanical oscillations in large interconnected power systems. The original model consisted of two structurally symmetrical areas connected by a weak tie.

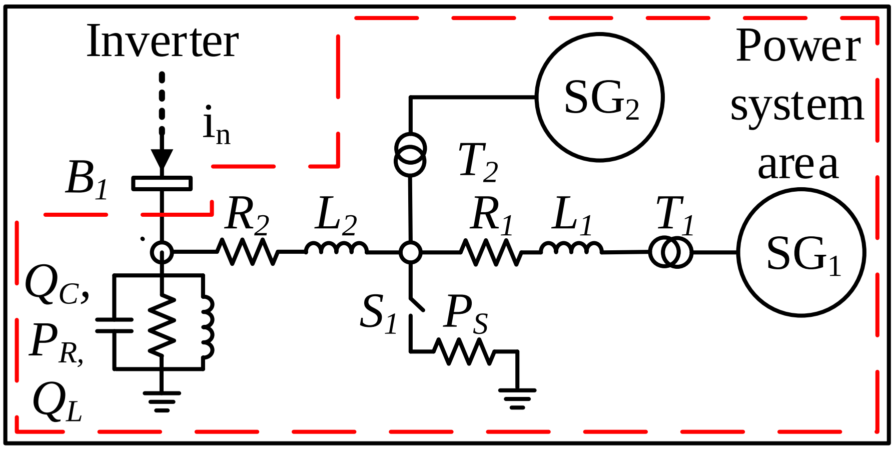

Figure 4-6 Electrical model of multi-bus power system model, including transmission, load, and SG components, developed from power system Area 1 in [125].

Each area is composed of two coupled 100 MVA synchronous generator (SG) units that inject power at different points along the same feeder. The SGs' 20 kV voltage outputs are stepped up to the 230 kV transmission network (TN) by identical 100 MVA transformers, T_1 and T_2, each with transformer ratios $r = 11.5$. The loads in each area are modelled as constant impedances, including an inductive reactance Q_L and a resistance P_R. A shunt capacitance Q_C is added to support each area's voltage profile. Resistive R_i and inductive L_i components are included to represent the different transmission components between the devices. All of the base impedance values used in this thesis' model (unless otherwise stated) are detailed in Table 4-1.

Table 4-1 Impedance parameters for Area 1 in multi-bus power system model.

Parameter	Value
Q_C	20 MVAr
P_R	100 MW
Q_L	50 MVAr
P_S	20 MW
R_1	$5*10^{-3}$ PU
L_1	$4.17*10^{-2}$ PU
R_2	$2*10^{-3}$ PU
L_2	$1.67*10^{-2}$ PU

The model used in this thesis is adapted further from the configuration detailed in [125]. As the thesis is mostly interested in the interaction between the converter and the grid frequency dynamics but is not specifically designed to analyse inter-area oscillatory modes, the tie line and second area can be disregarded. Only the first area (including the components up to bus B1) is used. Instead of a distant second area, an aggregated ideal battery energy source converter system is connected to the Power System Area at bus B1. The converter system has an identical topology and coupling impedance configuration as that detailed in Section 4.4 (and pictured to be upstream of the grid in Figure 4-4). However, the converter on the multi-bus power system uses different parameters to represent a large converter park instead of an individual device, as is often studied for the infinite bus system configurations. The specific parameterisation is detailed for any relevant studies in later chapters.

Finally, an additional active power load P_S is included in the model behind a controllable switch S_1 to enable the introduction of a disturbance that the converter station can respond to. The load is tuned to account for $5\,\%$ of the total generating capacity (SGs plus any converter devices) (Table 4-1). The system is initialised with the switch open until $t = 21\ s$, when the load is connected and the system is disturbed.

4.5.2.1. Synchronous generator model

The SGs in the power system area are modelled identically to the example in [125], other than the adaptation of some parameters. A sixth order model is used to resolve the round rotor SG dynamics. The SG is connected to a steam turbine via a single mass shaft model. The turbine is controlled using a speed regulator, with droop coefficient K_{pD} that can be tuned using (8). The SG excitation systems are modelled as direct current commutator exciters and use the IEEE type DC1 automatic voltage regulator control. The SGs also use a single input ($\Delta\omega$) power system stabiliser, which is modelled as described in Example 12.6 in [39] apart from the introduction of a transducer time constant τ_{tr} by [125] and the variation of the power system stabiliser (PSS) gain K_{PSS}. The two SGs are dispatched to active power levels of P_{SG1} and P_{SG2}, respectively, to meet the total system demand. The base parameters used to model the

SGs on the multi-bus power system model throughout Chapter 1 and the rest of the thesis (unless stated otherwise) that are different from those described in [125] are detailed in Table 4-2.

Table 4-2 Base SG parameters used in the multi-bus power system model.

Parameter	Value
H_{SM}	2 s
K_{pD}	0.05 PU
P_{SG1}	70 MW
P_{SG2}	40 MW
K_{PSS}	15
τ_{tr}	15 ms

Characteristics of synchronous generator frequency response

To analyse the characteristic features of a SM's response (and then relate to converter capabilities) it can be useful to express the system as an active power response to a grid frequency disturbance. The SG can be simplified in terms of only the relevant 2nd order swing equation (6) dynamics. The linearised state-space form of the system is represented by Figure 4-7, which can be expressed the transfer function:

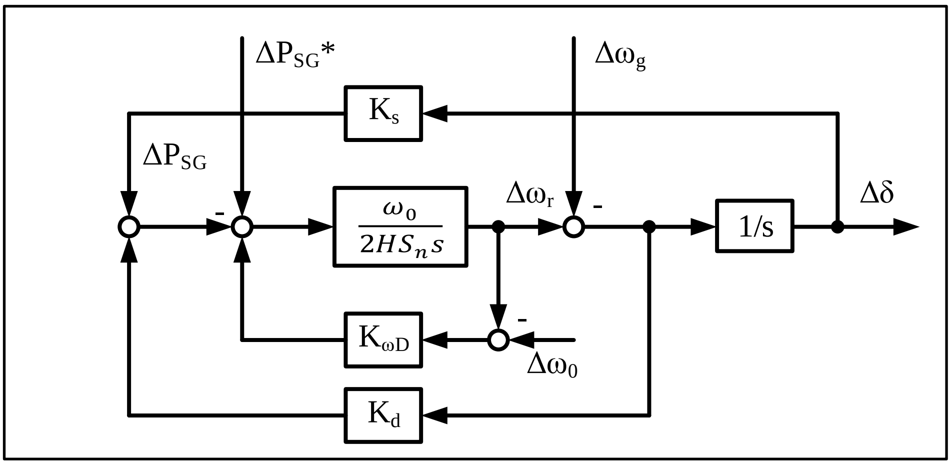

Figure 4-7 Boxplot of the linearised 2nd order SM system's active power response to grid frequency disturbances.

$$\frac{\Delta P_{SG}(s)}{\Delta\omega_g(s)} = \frac{-K_s s - \frac{K_{\omega D}\omega_0 K_s}{2HS_n}}{s^2 + \frac{(K_{\omega D} + K_d)\omega_0}{2HS_n}s + \frac{K_s\omega_0}{2HS_n}} \tag{50}$$

The standard unity s^2 form of a second order transfer function is:

$$\frac{Y(s)}{X(s)} = \frac{K\omega_n^2}{s^2 + 2\zeta\omega_n s + \omega_n^2} \tag{51}$$

Where K is the gain, ω_n is the natural frequency, and ζ is the damping ratio of the system. Therefore, if we assume that the SM takes the standard unity s^2 form we can express the natural frequency of the SM’s power response to a frequency disturbance as:

$$\omega_n = \sqrt{\frac{K_s\omega_0}{2HS_n}} \tag{52}$$

And the damping ratio as:

$$\zeta = \frac{K_{\omega D} + K_d}{2}\sqrt{\frac{\omega_0}{2HS_nK_s}} \tag{53}$$

If the droop response is neglected (not appropriate for real-world SMs but can be relevant for the assessment of system frequency dynamics and converter tuning), the natural frequency remains the same as (52) and the damping ratio becomes:

$$\zeta = \frac{K_d}{2}\sqrt{\frac{\omega_0}{2HS_nK_s}} \tag{54}$$

4.6. **Control**

The following section details the different control algorithms that are used to operate any of the converter configuration models. Section 4.6.1 details the maximum power point tracking control strategy that is used to control the wind turbine power output. Section 4.6.2 describes the current control strategy used to control the PMSG. Section 4.6.3 then overviews the control of the network-side converter, with Section 4.6.3.1 detailing the grid-following current control strategy, Section 4.6.3.2 detailing the PI virtual synchronous machine strategy, Section 4.6.3.3 detailing the Synchronverter strategy, and Section 4.6.3.4 detailing the GFM Droop strategy (where the last three are all grid-forming approaches).

4.6.1. WT control

A maximum power point tracking (MPPT) control algorithm is used to control the turbine rotor speed of the WT below rated wind speeds [119], [126]. The strategy maximises the power coefficient and hence power capture of the WT. The maximum efficiency tip speed ratio (27) is identified at a maximum-efficiency pitch angle (which is kept constant) and is maintained across the range of below-rated wind speeds by varying the generator rotor speed inversely. The generator rotor speed is managed by controlling the current that is pulled by the machine-side converter and hence the PMSG.

The torque reference T_{MPPT}^* can be calculated by multiplying the square of the turbine rotor speed with the inverse of the gearbox ratio (GBR) and the turbine coefficient K_{MPPT}, which defines the maximum power efficiency in terms of the WT's physical properties (and representative coefficients).

$$T_{MPPT}^* = \frac{1}{GBR} K_{MPPT} \omega_t^2 \tag{55}$$

$$K_{MPPT} = \frac{1}{2} \rho A R^3 \frac{c_1 (c_2 + c_6 c_7)^3 e^{-\frac{(c_2 + c_6 c_7)}{c_2}}}{c_2^2 c_7^4} \tag{56}$$

The turbine rotor speed is used as a proxy for the wind speed meaning that a wind speed sensor can be avoided. If needed, the torque reference can be transformed to a power reference P^*_{MPPT} for converter's that aim to control power flows:

$$P^*_{MPPT} = T^*_{MPPT}\omega_t \tag{57}$$

Above rated wind speeds the turbine and generator rotor speeds are kept constant and the power output is controlled instead by pitching the blades. Throughout this thesis, the pitching control is assumed to achieve ideal tracking of the constant rated power target P_n above-rated wind speeds, allowing the pitching algorithm to be neglected. The following variable domain function shows the variation in the power objective P^*_c as the wind speed varies and the MPPT power moves across the rated boundary:

$$P^*_c(P_{MPPT}) = \begin{cases} P_{MPPT} & if\ P_{MPPT} < P_n, \\ P_n & if\ P_{MPPT} \geq P_n. \end{cases} \tag{58}$$

The total WT control configuration, including the integration of the MPPT control strategy with the controllers for the back-to-back converter configuration, is pictured in Figure 4-8.

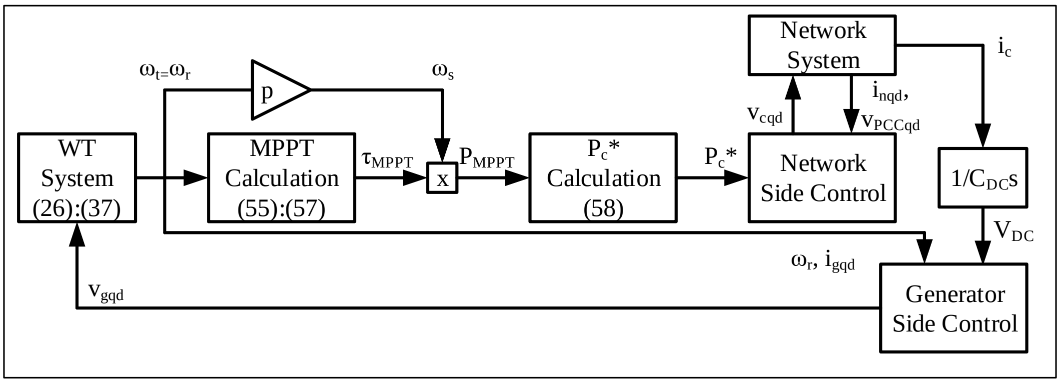

Figure 4-8 WT control configuration.

4.6.2. Generator-side converter control

A conventional generator current control strategy (pictured in Figure 4-9) is used to control the current that is pulled from the generator-side converter, and hence the current output and rotor speed of the generator itself. The current control equations are:

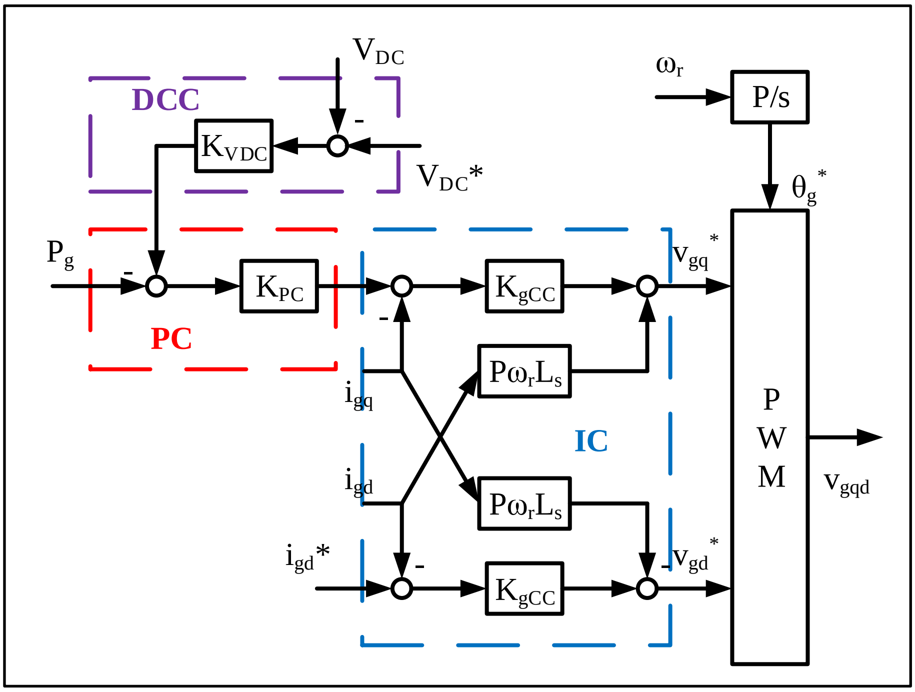

Figure 4-9 Generator Current Control strategy.

$$v_{gq}^* = L_s \omega_s i_{gd} + K_{gcc}\left(i_{gq}^* - i_{gq}\right) \tag{59}$$

$$v_{gd}^* = -L_s \omega_s i_{gq} + K_{gcc}\left(i_{gd}^* - i_{gd}\right) \tag{60}$$

Where $L_s = \sqrt{L_{sq}^2 + L_{sd}^2}$ is the magnitude of the stator inductance, ω_s is the stator electrical speed, and K_{gcc} is the inner loop PI controller, composed of proportional gain K_{pgcc} and integral gain K_{igcc}:

$$K_{gcc}(s) = \frac{K_{pgcc}s + K_{igcc}}{s} \tag{61}$$

K_{gcc} can be tuned using the same standard laws as a network-side current control strategy [127], where the equations use the appropriate generator properties and desired time constant τ_{gcc}:

$$K_{pgCC} = \frac{L_s}{\tau_{gCC}} \tag{62}$$

$$K_{igCC} = \frac{R_s}{\tau_{gCC}} \tag{63}$$

An outer controller is included that sets the active current reference i_{gq}^* by tracking the DC voltage reference V_{DC}^* using the DC voltage controller K_{VDC} and ensuring that sufficient power is being transferred to maintain this voltage using the power controller K_{gPC}. The reactive current reference i_{gd}^* is set to zero. Therefore, the outer loop equations are:

$$i_{gq}^* = K_{gPC}\left[K_{VDC}(V_{DC}^* - V_{DC}) - P_g\right] \tag{64}$$

$$i_{gd}^* = 0 \tag{65}$$

4.6.3. Network-side converter control

This thesis assesses the ability of network-side converter controllers to support the grid frequency and the dynamics that are associated with the support. To analyse the controllers, many of the studies use some configuration of the energy source-converter-grid system described above and interchange the control strategy that determines the behaviour of the network-side converter. The following Sections 4.6.3.1 to 4.6.3.4 outline the collection of control strategies that are assessed throughout the thesis, which include: a Current Controller with frequency supporting capability, a PI Virtual Synchronous Machine (VSM), A GFM droop controller, and a Synchronverter VSM. Each of the controllers uses a different approach to set the voltage magnitude and angle references that directly feed the converter’s 3 phase voltage source output (due to the neglection of the low-level waveform modulation control). However, the controllers generally all require network current and voltage measurement inputs to facilitate the desired control response in normal and disturbed conditions.

When the model system uses the simplified ideal energy source to focus simply on the network-side converter dynamics, the higher-level converter references are assumed to be fed by higher level control decisions. In this case, the references can simply be set and input to the model by the user. When the model system uses the full back-to-back VSC configuration with DC link, generator-side converter, and resolved WT energy source as well as the network-side converter model the active power reference is instead fed by the MPPT strategy described in Section 4.6.1. The reactive power or voltage reference is still assumed to be determined by higher level control decisions for this back-to-back VSC model configuration. Therefore, in this modelling case, the voltage or reactive power references are input by the user again, but the active power reference is fed by the output of the WT control block.

4.6.3.1. Current Control with inertial response

The full current control with frequency support (CC w. FS) strategy is pictured in Figure 4-10, where the derivation of the current control foundation is detailed in [40]. The CC w. FS is based on three distinct parts: the synchronisation process (PLL), the outer controllers (OC), and the inner current controllers (IC). The hierarchical control structure transforms the desired active power and voltage references to corresponding current injections before transforming these current references to corresponding voltage magnitudes for the waveform modulation. Meanwhile, the synchronisation process measures the PCC angle that is used to align the modulated voltage.

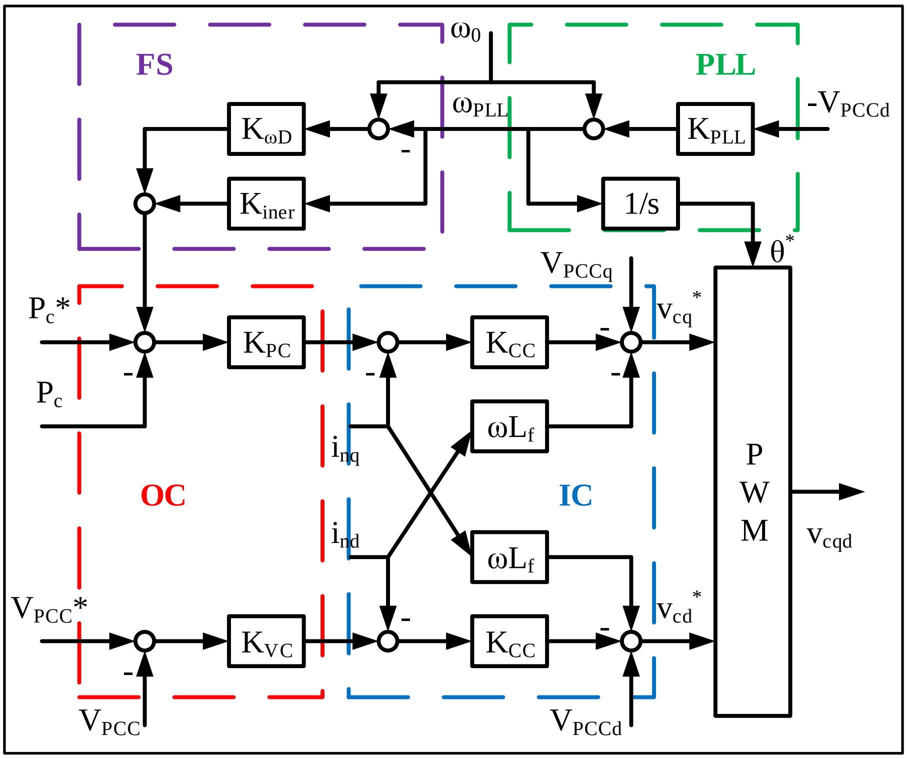

Figure 4-10 Current control with frequency support capability strategy.

The outer controls are composed of a Power and Voltage Controller. The Power Controller compares the Active Power Reference with a power measurement to set the Active Current Reference using a PI controller:

$$K_{PC} = \frac{K_{pPC}s + K_{iPC}}{s} \tag{66}$$

The power measurement can be determined using the $qd0$ expression of active power in terms of the voltage and current measured at the PCC:

$$P_c = \frac{3}{2}\left(v_{PCCq}i_{nq} + v_{PCCd}i_{nd}\right) \tag{67}$$

The voltage controller compares the Voltage Reference with a voltage measurement and sets the Reactive Current Reference using the PI controller:

$$K_{VC} = \frac{K_{pVC}s + K_{iVC}}{s} \tag{68}$$

The inner Current Controllers compare the current references output by the outer controls with the corresponding current measurements to determine the desired voltage magnitudes using:

$$K_{CC} = \frac{K_{pCC}s + K_{iCC}}{s} \tag{69}$$

The voltage magnitudes set by the Current Controllers are summed with cross-coupling and grid voltage components to determine the final voltage reference for the waveform modulation to achieve independent control of the active and reactive channels. The Current Controller gains can be tuned using the standard internal model control technique to achieve a given control response time τ_{CC} [127] according to:

$$K_{pCC} = \frac{L_f}{\tau_{CC}} \tag{70}$$

$$K_{iCC} = \frac{R_f}{\tau_{CC}} \tag{71}$$

Where L_f and R_f are the filter inductance and resistance, respectively. Conventionally, the CC uses a phase-locked loop (PLL) as a synchronisation tool. The PLL aligns the reactive component of the converter’s synchronously rotating voltage with the reactive component of the grid’s voltage using the PI controller:

$$K_{PLL} = \frac{K_{pPLL}s + K_{iPLL}}{s} \tag{72}$$

The desired damping ζ, natural frequency ω_n and response time-constant τ_{PLL} characteristics, along with the grid voltage magnitude E, can be used to define the PLL gains:

$$K_{pPLL} = \frac{2\omega_n\zeta}{E} \tag{73}$$

$$K_{iPLL} = \frac{K_{pPLL}}{\tau_{PLL}} \tag{74}$$

Frequency supporting capability can be added by feeding additional channels to the Active Power Reference [25]. Two channels can be included, which both utilise the grid frequency measurement by the PLL ω_{PLL}, to provide droop response and/or inertial response functionality. The droop channel adjusts the Active Power Reference by the increment ΔP_{DR}. The power increment varies in opposition to the measured frequency change (relative to the base frequency equilibrium operating point) with a magnitude that is determined by the droop coefficient $K_{\omega D}$:

$$\Delta P_{DR} = -K_{\omega D}\Delta\omega = -K_{\omega D}(\omega_{PLL} - \omega_0) \tag{75}$$

The droop coefficient can be tuned in the same manner as a SM, by choosing the desired active power response to a frequency disturbance in PU terms:

$$K_{\omega D} = \frac{\frac{\Delta P_c}{S_n}}{\frac{\Delta\omega_g}{\omega_0}} \tag{76}$$

The inertia channel adjusts the Active Power Reference by increment ΔP_{IR}, which depends on the derivative of the frequency change $\dot{\omega}_{PLL}$ (otherwise known as the ROCOF). The frequency derivative is determined (with minimal noise) by passing the PLL frequency measurement through a filtered derivative block. This derivative is then multiplied with the negative inertial gain K_{pIR} to achieve the desired inertial response, also in opposition to the direction of the frequency change:

$$\Delta P_{IR} = -K_{pIR}\dot{\omega}_{PLL} = -K_{pIR}\frac{Ds}{\tau_{IR}s + 1}\,\omega_{PLL} \tag{77}$$

Assuming that the derivative gain $D = 1$, the inertial gain is tuned (79) by relating it to the expected power response from a SM with the desired inertia constant (78):

$$\Delta P_{IR} = -\frac{2HS_n}{\omega_0}\dot{\omega}_{max} \tag{78}$$

$$K_{pIR} = \frac{2HS_n}{\omega_0} \tag{79}$$

The filter time constant, τ_{IR}, doesn't affect the magnitude of the inertial response but has been shown to impact the dynamics and the stability of the controller [101].

4.6.3.2. PI Virtual Synchronous Machine Control

The PI VSM control strategy (pictured in Figure 4-11) emulates the dynamics of a SM using two parallel PI channels. The active power channel emulates the Swing Equation by comparing the Active Power Reference with the power measurement from the terminals of the converter and sets the converter's internal frequency by passing this power difference through the active power controller:

$$K_{PVSM} = \frac{K_{pPVSM}s + K_{iPVSM}}{s} \tag{80}$$

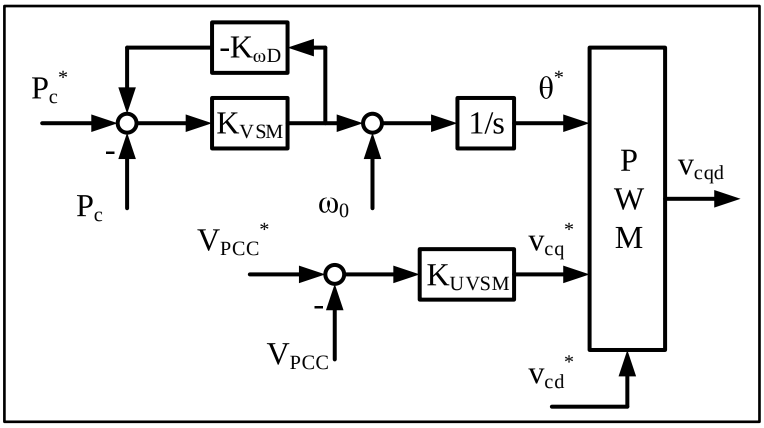

Figure 4-11 PI VSM control strategy.

The inertial magnitude is set by equating the parameters of the control system to the equivalent parameters of the SM system that are detailed in Section 4.5.2.1. The comparison requires the linearisation of the VSM system and expression as a boxplot from an input of grid frequency disturbance to an output of active power as shown in Figure 4-12. This boxplot is then expressed as the following transfer function:

$$\frac{\Delta P_c}{\Delta \omega_g} = \frac{-K_s s}{s^2 + K_s K_{pPVSM} s + K_s K_{iPVSM}} \tag{81}$$

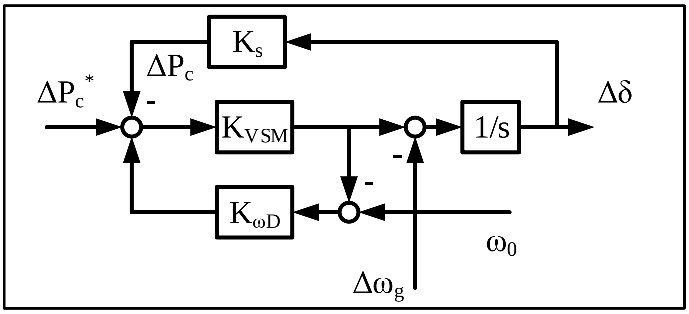

Figure 4-12 PI VSM system boxplot with grid frequency input and active power output.

Assuming the VSM system takes the standard second order system form, as detailed in (51), its natural frequency is found to be:

$$\omega_n = \sqrt{K_s K_{iPVSM}} \tag{82}$$

And its damping ratio is:

$$\zeta = \frac{K_{pPVSM}}{2} \sqrt{\frac{K_s}{K_{iPVSM}}} \tag{83}$$

The VSM integral gain can be tuned to achieve a given inertial constant by comparing its natural frequency with the natural frequency of an equivalent SM system (taken from (52) and input to (84)) before rearranging as (85):

$$\sqrt{K_s K_{iPVSM}} = \sqrt{\frac{\omega_0 K_s}{2 H S_n}} \tag{84}$$

$$K_{iPVSM} = \frac{\omega_0}{2HS_n} \tag{85}$$

Equally, (83) can be rearranged to tune the VSM proportional gain to achieve a given damping ratio:

$$K_{pPVSM} = 2\zeta \sqrt{\frac{K_{iPVSM}}{K_s}} \tag{86}$$

The voltage channel compares the Voltage Reference with the voltage measurement from the terminals of the converter and sets the converter reference for the active voltage component for the waveform modulation using the voltage PI controller:

$$K_{UVSM} = \frac{K_{pUVSM}s + K_{iUVSM}}{s} \tag{87}$$

The PI VSM controller achieves droop supporting using the feedback droop channel. The channel takes the frequency increment calculated by the active power controller and passes it through the droop coefficient $K_{\omega D}$. The droop coefficient is tuned in the same manner as for the current controller, as described in (8).

The reference for the reactive voltage component is set to zero. This form of the VSM feeds the voltage component and angle references directly to the waveform modulation, however, other forms of the control exist that utilise different control components to limit the current provision within the converter capabilities.

4.6.3.3. Synchronverter Control

The Synchronverter (sometimes referred to as a Virtual Synchronous Generator) uses mechanical and electrical equations to emulate the voltage behaviour of a SM and is proposed and detailed in [60]. Accordingly, it is another VSM-type GFM controller. Figure 4-13 depicts the Synchronverter control strategy. The electro-mechanical swing equation determines the angular behaviour of the converter while a set of electrical equation describe the voltage magnitude behaviour. The voltage angle and magnitude references set by these outer control channels can then be fed either directly to the waveform modulation or via cascaded controls (such as an inner current controller), which are implemented to achieve more robust limitation of the converter current output. Throughout this thesis, the references will be fed directly to the waveform modulation. This configuration represents only the fundamental dynamics of the GFM controller and can provide an accurate representation of the entire controller including cascaded components assuming that the fast-inner controls achieve ideal tracking of the voltage references.

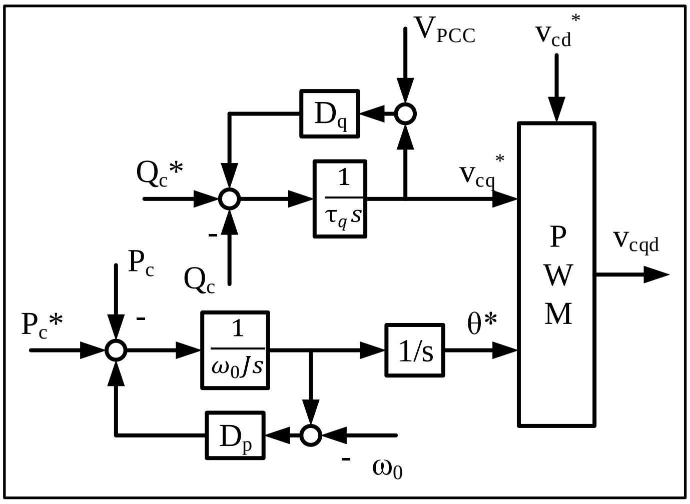

Figure 4-13 Synchronverter VSM control strategy.

As stated above, the angle and hence frequency behaviour of the Synchronverter is determined by the swing equation, which can be represented as:

$$\omega(s) = \omega_0 + \frac{1}{Js + D_p}\left(P_c^*(s) - P_c(s)\right) \tag{88}$$

Where J is the inertia of the virtual machine, D_p is the frequency droop coefficient that contributes to damping, P and P^* are the active power measurement and its reference, ω_0 is the base frequency, and ω is the Synchronverter's internal frequency. The internal angle $\theta(s)$ of the Synchronverter can then be defined as the integral of this frequency:

$$\theta(s) = \frac{\omega(s)}{s} \tag{89}$$

As the Synchronverter explicitly emulates the dynamic equations of the SM, the desired inertial and droop responses can be tuned explicitly in terms of the corresponding SM parameters. The inertial constant J can be defined in terms of an inertia constant H according to:

$$J = \frac{2HS_n}{\omega_0^2} \tag{90}$$

The droop coefficient D_p is then defined according to the desired active power response to a given frequency change in the same manner as for the CC (8):

$$D_p = \frac{\frac{\Delta P_c}{S_n}}{\frac{\Delta\omega}{\omega_0}} \tag{91}$$

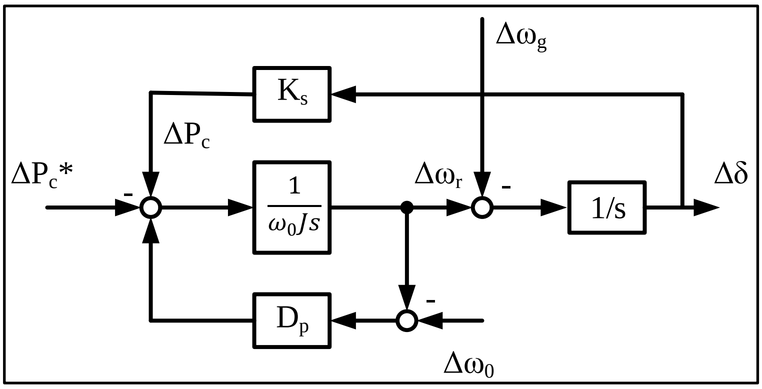

Figure 4-14 Synchronverter VSM system boxplot with grid frequency input and active power output.

The dynamic features of the Synchronverter's response to frequency disturbances can be found using the controller's boxplot shown in Figure 4-14. The system is rearranged to express a transfer function that responds to frequency disturbances with active power injections:

$$\frac{\Delta P_c(s)}{\Delta \omega_g(s)} = \frac{-K_s s - \frac{K_s D_p}{\omega_0 J}}{s^2 + \frac{D_p}{\omega_0 J} s + \frac{K_s}{\omega_0 J}} \tag{92}$$

Assuming that the transfer function in (92) takes the standard s^2 form of a second order transfer function, which is detailed in (51), the natural frequency of the Synchronverter can be expressed:

$$\omega_n = \sqrt{\frac{K_s}{\omega_0 J}} \tag{93}$$

And the damping ratio of the Synchronverter is:

$$\zeta = \frac{D_p}{2\sqrt{\omega_0 J K_s}} \tag{94}$$

The voltage magnitude behaviour of the Synchronverter is defined by the relationship between the desired reactive power output and the internal voltage required to produce it. however, the desired reactive power output is itself defined by the sum of the reactive power reference Q_c^*, a Q-V droop increment, and the measured reactive power Q_c at the PCC. The Q-V droop coefficient is defined to achieve a change in reactive power for a given change in the PCC voltage:

$$D_q = \frac{\frac{\Delta \mathrm{Q_c}}{\mathrm{S_n}}}{\frac{\Delta V_{PCC}}{V_n}} \tag{95}$$

The sum of the reactive power components is related to the SM electrical properties that define its reactive power output according to:

$$Q_c = -\dot{\theta} M_f i_f \langle i, \widetilde{\cos}\theta \rangle \tag{96}$$

Where θ is the converter's internal angle, $\dot{\theta} = \omega$ is the derivative of the internal angle (equal to its internal frequency), M_f is the mutual field inductance of the equivalent SM, i_f is the field current of the equivalent SM, and i is the stator phase current of the equivalent SM. According to [60], the internal voltage of the equivalent SM can be defined using (97), so long as the field current component is assumed to remain constant:

$$V_c = \dot{\theta} M_f i_f \widetilde{\sin}\theta \tag{97}$$

Which resembles the definition of the reactive power in (96). Therefore, the internal voltage of the Synchronverter is defined by integrating the sum of reactive power components and multiplying this value with the inverse of gain K. K relates to the time constant of the voltage controller τ_v according to (98), so can be tuned to achieve a given response time:

$$K = \frac{\tau_v}{\dot{\theta} D_q} \tag{98}$$

4.6.3.4. Grid-forming Droop Control

The GFM Droop controller strategy (pictured in Figure 4-15) explicitly emulates SM droop dynamics. The active power channel compares the Active Power Reference with the power measurement and passes this power difference through a P-f droop gain K_{pD} to find the controller's internal frequency increment. The frequency increment is summed with the base frequency of the system ω_0 and integrated to find the converter's internal angle θ that is fed to the waveform modulation. As for the CC, the droop coefficient can be defined explicitly in terms of the desired power change for a given grid frequency variation, although the two droop coefficients ((8) and (99)) are the inverse of one another:

$$K_{pD} = \frac{1}{K_{\omega D}} = \frac{\frac{\Delta\omega}{\omega_0}}{\frac{\Delta P_c}{S_n}} \tag{99}$$

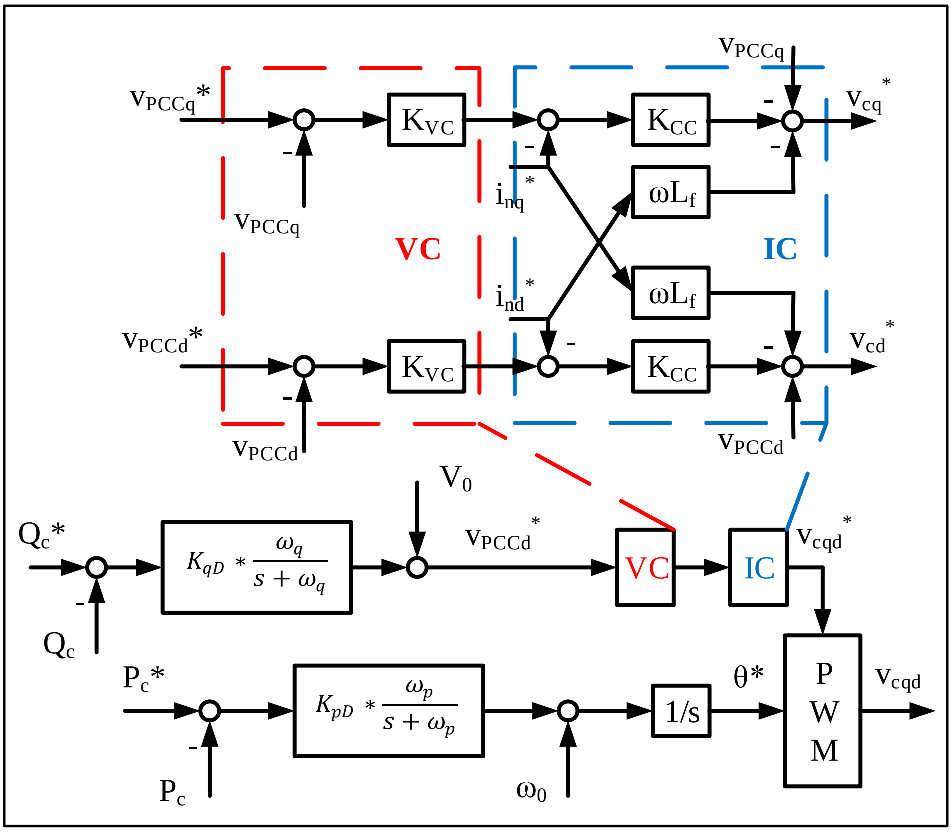

Figure 4-15 2nd order GFM Droop control strategy.

Inertial capability can be added to the GFM Droop controller by introducing a low-pass filter (LPF) with cut-off frequency ω_p on the active power channel, which increases the system order to second. The inertial magnitude can be set in a similar magnitude as the VSM by comparing the characteristic features of the GFM Droop system to the corresponding features of a SM with an equivalent droop response. The GFM Droop system, from grid frequency to power output, can be represented by the boxplot in Figure 4-16, which itself is represented by the transfer function:

$$\frac{\Delta P_c(s)}{\Delta\omega_g(s)} = \frac{-K_s s - \omega_p K_s}{s^2 + \omega_p s + K_s K_{pD}\omega_p} \tag{100}$$

Again, assuming the GFM Droop system takes the standard second order unity s^2 form detailed in (51), the natural frequency of the system is:

$$\omega_n = \sqrt{K_s K_{pD} \omega_p} \tag{101}$$

And the damping ratio is:

$$\zeta = \frac{1}{2}\sqrt{\frac{\omega_p}{K_s K_{pD}}} \tag{102}$$

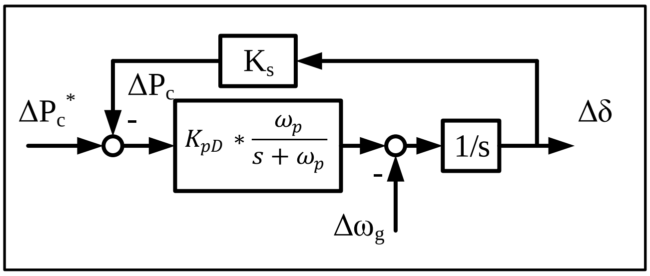

Figure 4-16 2nd order GFM Droop system boxplot with grid frequency input and active power output.

Assuming that the droop response is already determined, the desired inertial response magnitude (inertia constant) can be achieved by equating the GFM Droop natural frequency (101) with that of the SM (52) to give (103) and (104).

$$\sqrt{K_s K_{pD} \omega_p} = \sqrt{\frac{K_s \omega_0}{2HS_n}} \tag{103}$$

$$\omega_p = \frac{\omega_0}{2HS_n K_{pD}} \tag{104}$$

Alternately, a developer might be interested in setting the damping ratio of the converter response. To achieve a given GFM Droop damping ratio for some Droop coefficient, (102) can simply be rearranged as (105).

$$\omega_p = 4\zeta^2 K_s K_{pD} \tag{105}$$

Or, to tune for a damping ratio and inertia constant, the ratio of the two tuneable parameters can be expressed using (106).

$$\frac{\omega_p}{K_{pD}} = 4\zeta^2 K_s \tag{106}$$

And, by rearranging (104), the product of the two tuneable parameters can be expressed as (107).

$$\omega_p K_{pD} = \frac{\omega_0}{2HS_n} \tag{107}$$

(106) can then be multiplied with (107) to give (108) and then (109).

$$\omega_p^2 = \frac{2\zeta^2 K_s \omega_0}{HS_n} \tag{108}$$

$$\omega_p = \sqrt{\frac{2\zeta^2 K_s \omega_0}{HS_n}} \tag{109}$$

And (107) can be divided by (109) to give (110).

$$K_{pD} = \frac{\omega_0}{2HS_n}\frac{1}{\omega_p} \tag{110}$$

As there are only two controllable parameters, K_{pD} and ω_p, all three of the response characteristics of interest (droop magnitude, inertial magnitude, and damping ratio) cannot be achieved simultaneously. So the two critical characteristics must be chosen before a tuning approach can be followed.

The GFM Droop voltage channel emulates the inverse of the Automatic Voltage Regulator droop characteristic of a SM. The reactive power reference is compared with the reactive power measurement at the terminals of the converter and is passed through a Q-V droop coefficient K_{qD} and LPF to determine the Voltage increment. The Q-V Droop Coefficient can also be determined as an explicit expression of the desired PU voltage change (with respect to the base voltage V_0) for a given variation in the converters PU reactive power capacity (111).

$$K_{qD} = \frac{\frac{\Delta V_{PCC}}{V_0}}{\frac{\Delta Q_c}{S_n}} \tag{111}$$

The cut-off frequency of the LPF ω_q can be set to achieve the desired bandwidth of the reactive power control.

The GFM Droop control features a cascaded control configuration similar to that in the CC, but which uses two identical Voltage Controllers K_{VC} (112) to transform the PCC voltage references to current references.

$$K_{VCD} = \frac{K_{pVCD}s + K_{iVCD}}{s} \tag{112}$$

The Current Controllers take the exact same form as those in the CC and are tuned using the same approach detailed in Section 4.6.3.1.

4.7. Small-signal modelling

Small-signal modelling (SSM) allows the use of standard linear control methods by assessing linear models at given operating points and assuming that small disturbances around these points do not break the linearity of the systems. SSMs can be developed from the system models described above but require: 1) the linearisation of any non-linear components of the systems and 2) the identification of the equilibrium operating point of the system for the given conditions of interest. Although any of the model configurations described above can be transformed into SSM form, only the simplified network-side converter with ideal battery energy source will be modelled in small-signal form in this thesis. The two network-side converter controls used in the SSMs are the CC and the PI VSM. The remainder of this Section will detail the linearisation of the simplified network-side converter models, which is largely based on the work described in [88], [128].

The non-linear components of the network-side converter with ideal battery energy source model are: the PLL, the park and inverse park transforms, the electrical system variable calculations (to provide voltage magnitude, active and reactive power measurements at the PCC), and the measurement sensors. The remaining components of the model are linear and can be incorporated directly into the SSM by expressing the corresponding dynamic equations from Sections 4.3 to 4.6 in the standard state-space equation form of (113) and (114).

$$\dot{x} = Ax + Bu \tag{113}$$

$$y = Cx + Du \tag{114}$$

Where x is a vector of state variables, u is a vector of input variables, y is a vector of output variables, A is the state matrix, B is the input matrix, C is the output matrix, and D is the direct transition (or feedthrough) matrix.

The CC's PLL is non-linear as its angular alignment of the synchronous reference frame is achieved by feeding back the park transformed voltage components ΔU_d, which is itself defined using the output of the PLL. The action of the PLL can be linearised according to (115) [129].

$$\Delta\theta = \frac{K_{pPLL}s + K_{iPLL}}{s^2 + U_{q0}K_{pPLL}s + U_{q0}K_{iPLL}}\Delta U_d \tag{115}$$

Where U_{q0} is the initial value of the converter voltage q component (measured from the initialised equilibrium operating point of the TDM).

The SSM is implemented in the synchronous reference frame, however, the individual submodules of the model use independent synchronous reference frames that may not be angularly aligned with one another. To connect each submodule, the independent reference frames can be aligned with an arbitrary global reference frame by accounting for the angular displacement between them θ. However, as well as aligning the reference frames, the transform itself is a non-linear function that needs to be linearised. Therefore, the following linearised transform (116) can be used to change a variable from one reference frame to a global linearised frame (117), where the linearised variable is labelled using the l superscript.

$$[T_{qd}^{l}] = \begin{bmatrix} \cos(\theta_0) & -\sin(\theta_0) & -\sin(\theta_0)\,x_{q0} - \cos(\theta_0)\,x_{d0} \\ \sin(\theta_0) & \cos(\theta_0) & \cos(\theta_0)\,x_{q0} - \sin(\theta_0)\,x_{d0} \end{bmatrix} \tag{116}$$

$$x_{qd}^{l} = [T_{qd}^{l}][\Delta x_q\ \Delta x_d\ \Delta\theta]^T \tag{117}$$

θ_0 is the initial value of angle between the independent reference frame and the global reference frame and x_{qd0} is the initial value of the variable of interest that is being aligned with the global reference frame. Alternatively, the following linearised inverse transform (118) depicts the method used to change the global linearised variable back to the local reference frame (119).

$$[T_{qd}^{l}]^{-1} = \begin{bmatrix} \cos(\theta_0) & \sin(\theta_0) & -\sin(\theta_0)\,x_{q0} + \cos(\theta_0)\,x_{d0} \\ -\sin(\theta_0) & \cos(\theta_0) & -\cos(\theta_0)\,x_{q0} - \sin(\theta_0)\,x_{d0} \end{bmatrix} \tag{118}$$

$$x_{qd} = [T_{qd}^{l}]^{-1}[\Delta x_q^{l}\ \Delta x_d^{l}\ \Delta\theta]^T \tag{119}$$

The calculation of non-linear electrical system variables (voltage magnitude U, active power P, and reactive power Q) from the network current and voltage measurements at the PCC also needs to be linearised. The calculation can be linearised and expressed as (120).

$$\Delta y^l = D\Delta u \tag{120}$$

Where the input and output variables are (121) and (122).

$$\Delta u = \left[\Delta i_{cq}\ \Delta i_{cd}\ \Delta U_q\ \Delta U_d\right]^T \tag{121}$$

$$\Delta y^l = [\Delta U^l\ \Delta P^l\ \Delta Q^l]^T \tag{122}$$

The direct transition matrix is (123).

$$D = \begin{bmatrix} 0 & 0 & \frac{U_{q0}}{U_{m0}} & \frac{U_{d0}}{U_{m0}} \\ \frac{3U_{q0}}{2} & \frac{3U_{d0}}{2} & \frac{3I_{q0}}{2} & \frac{3I_{d0}}{2} \\ -\frac{3U_{d0}}{2} & \frac{3U_{q0}}{2} & \frac{3I_{d0}}{2} & -\frac{3I_{q0}}{2} \end{bmatrix} \tag{123}$$

The linearisation of the electrical system variables is carried out in different locations for the two SSM models (CC and PI VSM) depending on the requirement for the linearised variables at different stages within the control strategies. The VSM linearisation is carried out in an outer module, allowing the active power and voltage magnitude to be input to the inner controller module and the reactive power to be input to the reactive power droop module (after each of the variables has been filtered). In contrast, the CC carries out the linearisation in the inner control module, where the same input signals to the transform Δu are already being used, allowing the active power and voltage magnitude to be input to the outer controller module while the reactive power can be fed to the reactive power droop module again (also after being filtered). The simple relationship between the linearised variables' calculation inputs and outputs can be lumped onto existing state-space matrices or formed independently, and the interactions between sub-module inputs and outputs are detailed for the CC and VSM SSMs in and , respectively.

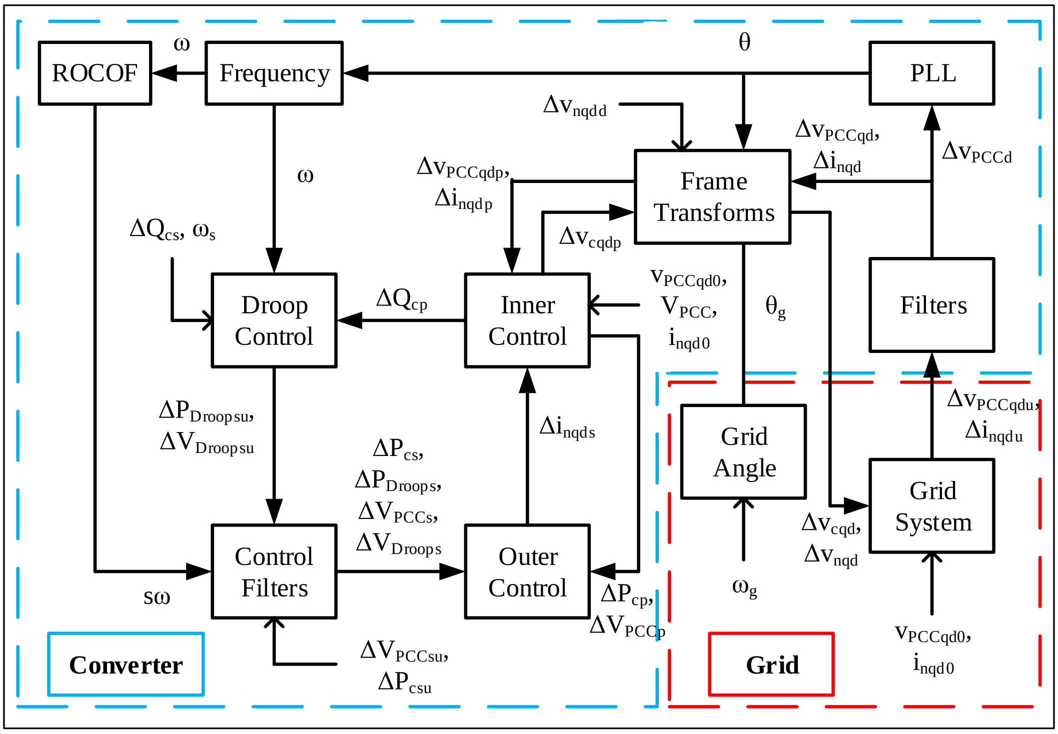

Figure 4-17 CC with frequency support capability small-signal model configuration.

The filtering of the network measurements is the final process that needs to be linearised for the SSM. The linearised expression of the filtering is carried out to account for the bandwidth of the filter and is depicted in (124) and (125) (identical for both CC & VSM).

$$\Delta\dot{x} = \begin{bmatrix} -\dfrac{1}{T_f} & -\omega_g \\ \omega_g & -\dfrac{1}{T_f} \end{bmatrix} \Delta x + \begin{bmatrix} \dfrac{1}{T_f} & 0 \\ 0 & \dfrac{1}{T_f} \end{bmatrix} \Delta u \qquad (124)$$

$$\Delta y = \begin{bmatrix} 1 & 0 \\ 0 & 1 \end{bmatrix} \Delta x \qquad (125)$$

The linearised filtering can be applied to both the network voltage and current measurements using different input and output/state variable vectors. The voltage filter uses unfiltered network voltage inputs (126)

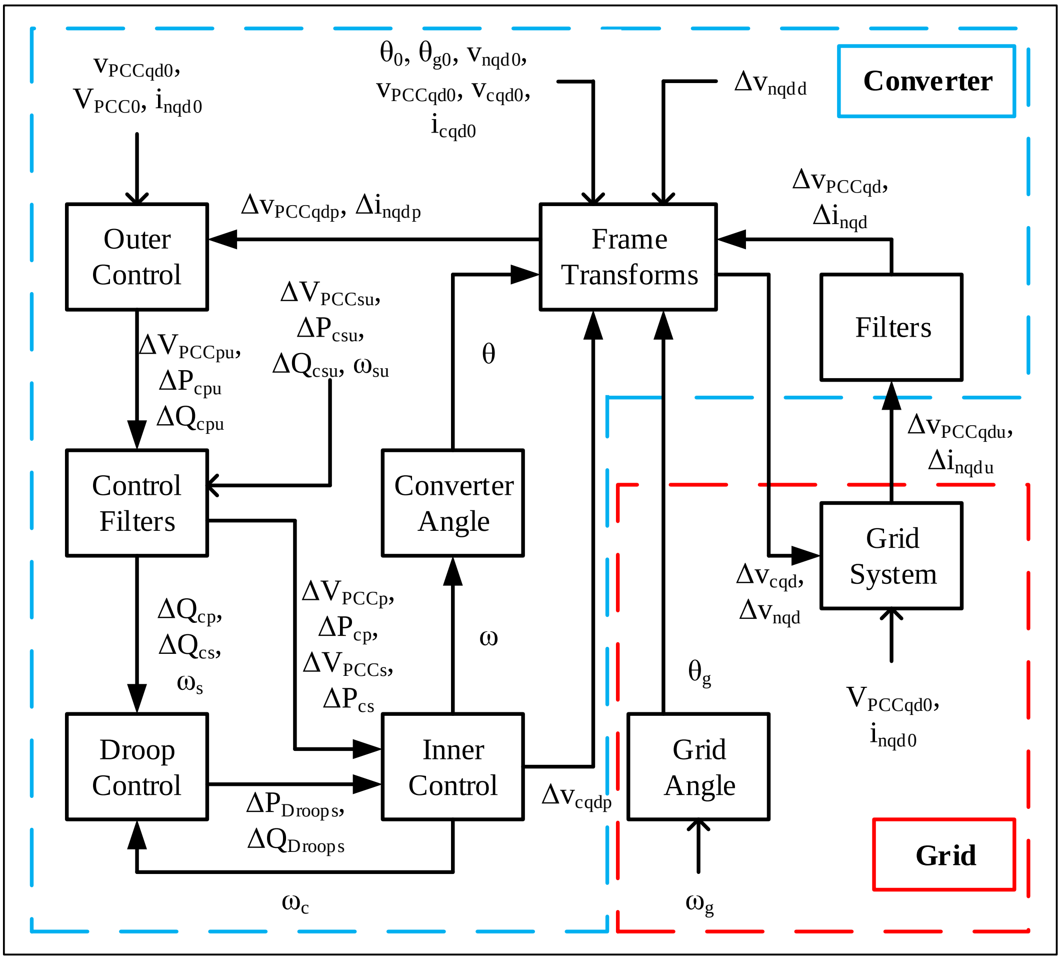

Figure 4-18 VSM small-signal model configuration.

$$\Delta u = \left[\Delta U_{qu}\ \Delta U_{du}\right]^T \tag{126}$$

and filtered network voltage outputs/states (127).

$$\Delta y = \Delta x = \left[\Delta U_q\ \Delta U_d\right]^T \tag{127}$$

The current filter uses unfiltered network current inputs (128)

$$\Delta u = \left[\Delta i_{cqu}\ \Delta i_{cdu}\right]^T \tag{128}$$

and filtered current outputs/states (129).

$$\Delta y = \Delta x = \left[\Delta i_{cq}\ \Delta i_{cd}\right]^T \tag{129}$$

The operating point of the system can be found by initialising the corresponding TDM for a given set of power inversion, network voltage magnitude and frequency, and SCR conditions. The equilibrium point can be recorded for these variables following sufficient time for any transient oscillations to be damped out of the system. The operating points can be loaded into the corresponding SSM to allow the assessment of the system using standard linear control methods around the given conditions.

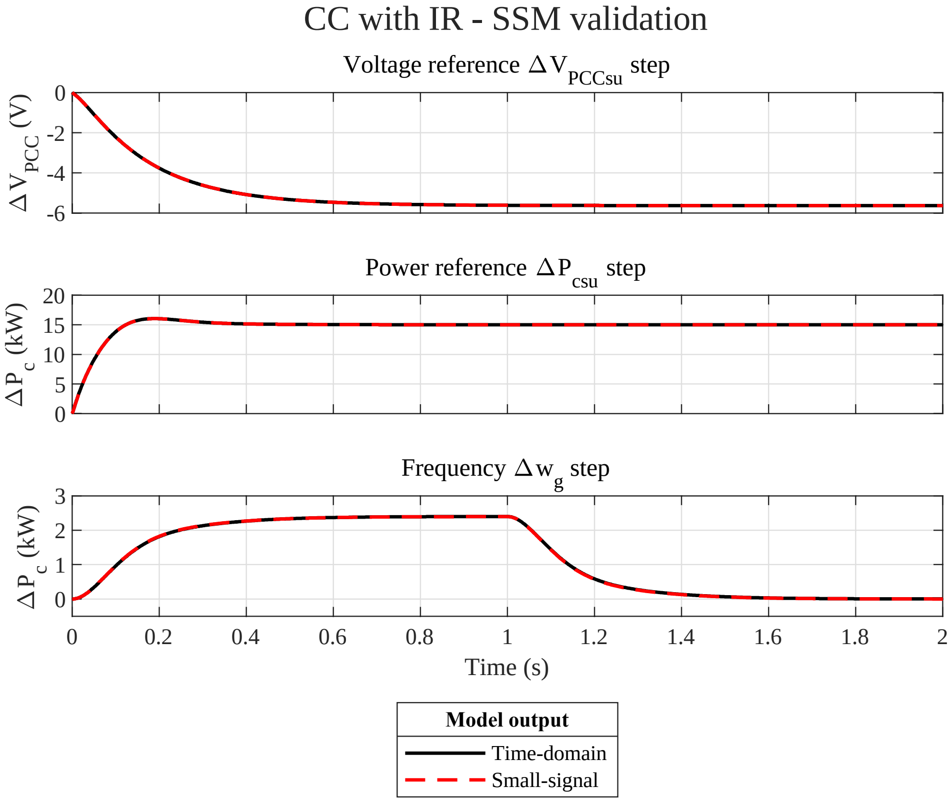

Figure 4-19 Validation of the CC with IR SSM with respect to its time-domain EMT model for three different input-output pairs. Each input takes the form of a 1 % step of its base value. The frequency step is limited to a $ROCOF = -0.5\ Hz/s$.

Both SSMs are subject to input steps to identify their validity with respect to their corresponding time-domain EMT models. The output to input pairs of: 1) PCC voltage to converter voltage reference, 2) converter power to converter power reference, and 3) converter power to grid frequency are validated for steps corresponding to 1 % of each input's base value ($\Delta V_{PCCsu} = 0.01 * V_n$, $\Delta P_{csu} = 0.01 * OP * S_n$, $\Delta\omega_g = 0.01 * \omega_0$). The validation of the CC with IR SSM is pictured in Figure 4-19 and the validation of the PI VSM SSM is pictured in Figure 4-20.

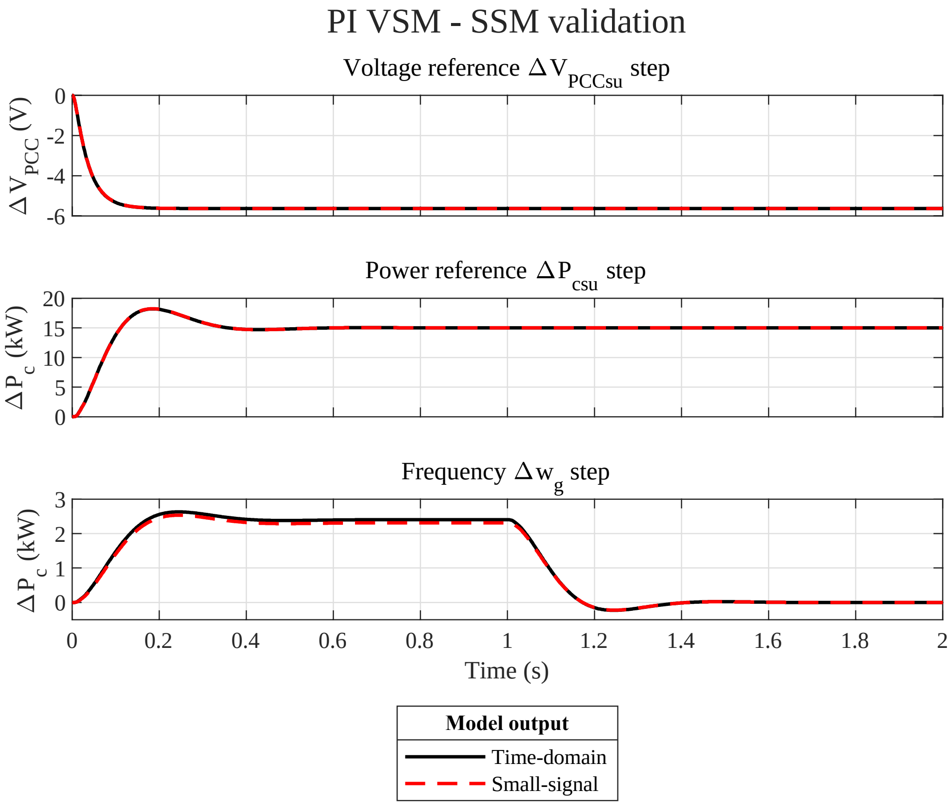

Figure 4-20 Validation of the PI VSM SSM with respect to its time-domain EMT model for three different input-output pairs. Each input takes the form of a 1 % step of its base value. The frequency step is limited to a $ROCOF = -0.5\ Hz/s$.

4.8. **Summary**

This chapter provides a detailed overview of the modelling techniques that will be used throughout the rest of the thesis. The frames of reference that the models will be assessed in are introduced. Then, the dynamic equations of each relevant component needed to analyse the issues introduced in Chapter 3 are provided. The wind turbine system, represented by an electromechanical model resolving the wind power input, wind turbine rotor, drivetrain, and back-to-back power converter, is detailed first. Then an ideal battery energy source system that includes an ideal current source feeding an inverter is described. Finally, two power system representations are introduced. Firstly, an infinite bus representation that allows the assessment of ideal disturbances is described, before a multi-bus power system that resolves generation, transmission, and load is described.

The strategies that control each system component are then detailed. Several network-side converter control strategies are introduced, whose stability and dynamics constitute a significant focus of the thesis. Finally, a brief theoretical overview of small-signal modelling is given and linked to the development of the small-signal models used in the thesis. Results validating the equivalence of the small-signal models to their corresponding electromagnetic transient time-domain models are also provided.

Using the models and techniques provided in this section, the characteristics of different combinations of energy source, power system, and control configuration can be assessed with the objective of improving the understanding of converter-interfaced frequency-stabilising solutions and easing their deployment on real power systems.

Chapter 5. Validation of tuning guides and assessment on the impact of the cascaded controllers

5.1. Introduction

Chapter 4 details the control strategies that can be used to enable any of the feasible technologies identified in Chapter 3 to provide frequency support. Chapter 4 also derived guides for these controllers that allows their tuning in terms of the standard inertial and droop response settings that System Operators (SOs) will specify. These guides differ from other approaches that suggest that one of the frequency support parameters (e.g. inertial constant H) should be specified and then the remaining parameter (e.g. P-f droop coefficient K_{pD}) should be adjusted to ensure the controller's stability [130]. The guides derived in Chapter 4 offer a more appropriate tuning approach to provide the SO with exact frequency support characteristics. One of this chapter's objectives is to validate the accuracy of the tuning guides to provide the stipulated frequency support.

Additionally, GFM Droop and Synchronverter controllers have been reported to be equivalent in different configurations [62], [63], [66]. However, an initial example of a single-loop Synchronverter's and a multi-loop GFM Droop's response to a frequency disturbance in Chapter 3 shows that the two converters possess different dynamic properties. [67] highlights that a GFM Droop experiences a smaller coupling impedance (and therefore different dynamics and stability) when implemented in the multi-loop configuration with cascaded controllers compared to the single-loop configuration. Additionally, [68] shows that the tuning of the cascaded controller impacts the dynamics and stability of a multi-loop Synchronverter. Despite these findings, and the suggestion that the tuning of the cascaded controllers will also impact the GFM Droop's operation [67], an explicit study has not been carried out to assess their impact.

This chapter aims to validate the tuning guides developed in Chapter 4 for the GFM Droop and Synchronverter controllers to improve the understanding of their reported equivalence [62], [63], [66]. The two controllers are implemented on a model of an ESS connected to the transmission network and their stability and dynamics are compared for a range of frequency support specifications and grid conditions. Comparisons are made to identify if any differences exist between the two controllers, either due to the different single- versus multi-loop configurations of the Synchronverter versus GFM Droop (as has been suggested between single- and multi-loop GFM Droop controllers [67]) or simply due to the different configuration of the power controllers. Parametric sweeps of the GFM Droop's current and voltage controllers are then carried out to assess their impact on the controller's stability and dynamics. The conclusions will be compared with those that have been made for the tuning of cascaded controllers present in multi-loop Synchronverters [68] to assess if the control tuning impacts are true for both GFMs.

The study provides an overview of the full capability of the two control approaches to provide inertial and droop responses that can be referred to by either SOs to specify feasible and useful frequency stabilising solutions or by device owners/ developers to properly match frequency support functionality with a device's technical capabilities (following on from the device specific analysis in Chapter 3).

5.2. System under study

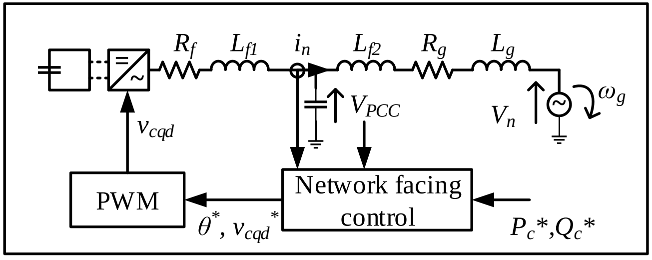

Figure 5-1 Electrical diagram of converter model with ideal DC energy source connected to infinite bus representation of grid via an LC filter.

An ideal-battery energy source connected to an infinite bus representation of the grid (pictured in Figure 5-1) is modelled as described in Chapter 4. The battery's network-side converter is controlled using either the single-loop Synchronverter or multi-loop

GFM Droop control strategy. The parameters used throughout this study are detailed in Table 5-1, whose tuning is described and justified in Chapter 4. The model specifically features a high ratio of grid reactive to resistive components to represent the highly inductive nature of the high voltage grid that frequency supporting device is likely to be connected to. This high reactance is driven by the increased presence of highly inductive components such as long AC lines and transformers and from the use of series compensation equipment to improve the transfer capability of the long lines [131], [132].

Table 5-1 Base network and converter control parameters.

Electrical		Control	
$V_n = V_0$	$1\ (kV)$	Q^*	$0\ (MVAr)$
Z_n	$0.1\ (\Omega)$	$K_{qD} = \frac{1}{D_q}$	$0.1\ (\%)$
R_f	$160\ (\mu\Omega)$	$\omega_q = \frac{1}{\tau_q K_{qD}}$	$1\ (Hz)$
L_f	$50.516\ (\mu H)$	ω_{CC}	$1000\ (Hz)$
S_n	$10\ (MW)$	$\omega_{VC} \approx K_{iVC}$	100
ω_0	$50\ (Hz)$	K_{pVC}	40
X/R	100		

The two control strategies can be tuned in terms of inertial constant H and P-f droop coefficient K_{pD} using the guides detailed in Sections 4.6.3.3 and 4.6.3.4, respectively.

5.2.1. Dynamic properties of the grid-forming controllers

The damping ratio of both controllers' transfer functions from grid frequency to active power is a by-product of the setting of the two frequency response parameters (as shown in Chapter 4). The damping ratio of the Grid-forming Droop converter's frequency response ζ_{GFMD} is expressed by (130), which can be transformed to (131) by representing the active power filter's cut-off frequency ω_p in terms of the inertial constant, droop coefficient, and synchronising torque coefficient K_s that it is tuned to provide (all detailed in Chapter 4).

$$\zeta_{GFMD} = \frac{1}{2}\sqrt{\frac{\omega_p}{K_s K_{pD}}} \tag{130}$$

$$\zeta_{GFMD} = \frac{1}{2}\sqrt{\frac{\omega_0}{2HS_n K_s K_{pD}^2}} \tag{131}$$

The damping ratio of the Synchronverter's frequency response ζ_{Syn} is expressed by (132). (132) can be updated to express ζ_{Syn} in terms of the inertial constant and droop coefficient by inserting the expressions for D_p and J that have been derived in Chapter 4 (133).

$$\zeta_{Syn} = \frac{D_p}{2\sqrt{\omega_0 J K_s}} \tag{132}$$

$$\zeta_{Syn} = \frac{1}{2K_{pD}}\sqrt{\frac{\omega_0}{2HS_n K_s}} = \zeta_{GFMD} \tag{133}$$

The updated damping coefficient expressions of the two controllers ((131) and (133)) are equivalent, both depending inversely on K_{pD} and inversely on the square root of H and K_s. The synchronising torque depends itself on the grid voltage V_n, converter voltage V_c, the angular difference δ and the coupling impedance X_L between the two voltages (134).

$$X_L = \left(X_f + X_g\right) = \omega(L_f + L_g) = \omega(L_f + \frac{Z_n}{\omega SCR}) \tag{134}$$

The coupling impedance can be expressed in terms of a filter and grid reactance (X_f and X_g) and the grid reactance can be defined as the grid inductance L_g that depends on the nominal impedance Z_n and the system SCR (134). Accordingly, we can consider that the damping coefficients of the two controllers (131) and (133) are inversely dependent on K_{pD} and the square root of H and SCR.

5.3. Method

The objectives and procedure of this chapter are pictured in Figure 5-2. Firstly, the tuning guides developed in Chapter 4 are validated, before the equivalence of the combined inertial and droop response by the GFM Droop and Synchronverter controllers is assessed. Then, the impact of the cascaded control parameters on the properties of the GFM Droop controller's response is analysed to allow a final recommendation for their appropriate tuning.

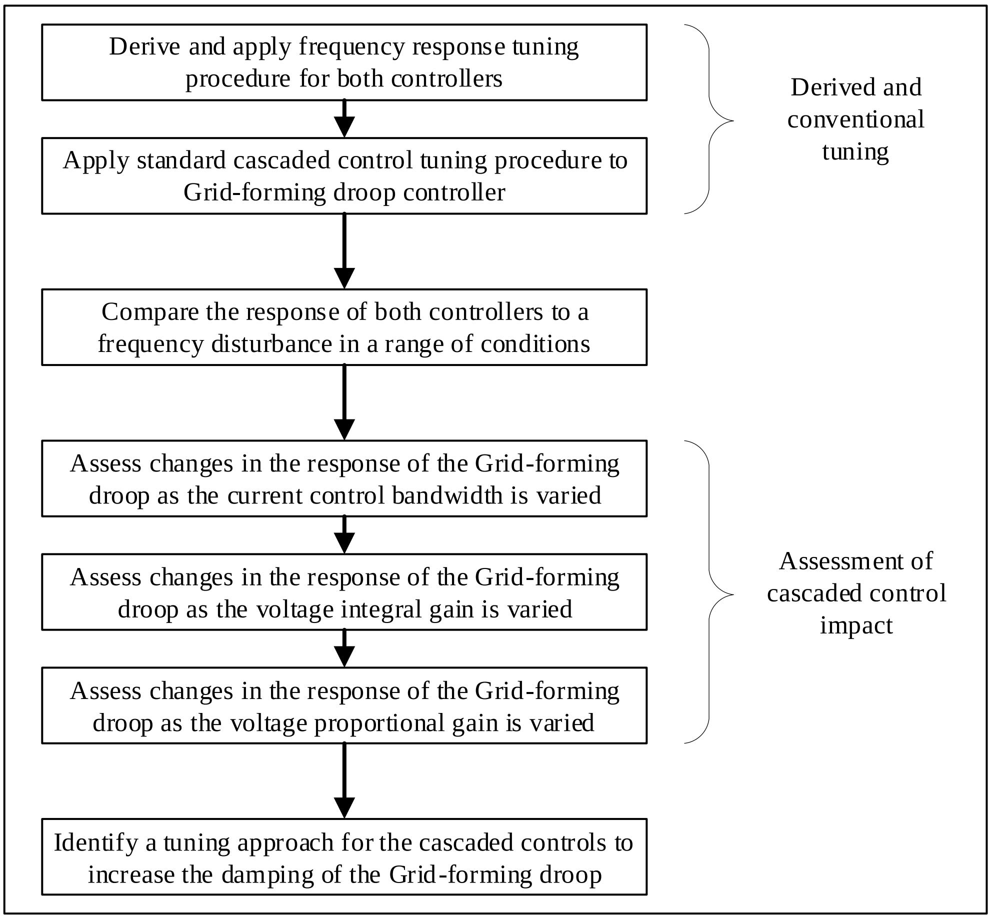

Figure 5-2 Methodology flowchart shoring the procedure to validate the GFM droop and Synchronverter controller's frequency response tuning guides detailed in Chapter 4, compare the responses equivalence, and assess the impact that the GFM Droop's cascaded control parameters.

The time-domain converter models are tuned to achieve a range of inertial constants $H = 0.5\ to\ 5\ s$ and P-f droop coefficients $K_{pD} = 0.01\ to\ 0.2\ PU$. The controllers' responses to a frequency disturbance with deviation $\Delta f = -1\ Hz$ and rate $ROCOF =$

$-0.5\ Hz/s$ will be compared to validate the tuning guides in Chapter 4, and to assess the equivalence of the two controllers in terms of stability, steady state, and dynamic features.

The inertial constants represent a range from small settings that could be supported by smaller power density devices to a standard value for a SM [39]. The droop settings represent a range from a low coefficient that would provide a full rated power response for a frequency deviation $\Delta f = 0.5\ Hz$ (the maximum frequency deviation that devices participating in GB's dynamic containment service must provide response to [76]) to a high coefficient that would provide a full rated power response for a frequency deviation of $\Delta f = 10\ Hz$. The low coefficient would be required if the system were inflexible to endure large frequency deviations while the higher coefficients might be implemented to enable lower energy density devices to contribute to frequency stability (but would not be utilised as the global allowable P-f relationship).

As well as assessing the controllers' responses to the frequency disturbance for a range of H and K_{pD} settings, the responses are simulated on a range of SCRs. SCR is varied due to the dependence of the frequency response dynamics on the grid properties depicted in (131) and (133), and the suggestion that the different voltage control location for single- and multi-loop GFM Droop controllers affects the effective coupling reactance [67]. The grid SCR is varied across very weak $SCR < 2$, weak $SCR = 2$, and strong $SCR = 5$ levels [133].

Due to observations that the equivalence between the GFM Droop and Synchronverter may not always be true [44], [62], [63], [66], and that the tuning of the cascaded controls may impact the short term response dynamics [67], [68], a parametric sweep is carried out to identify if differences in the control properties are introduced by the GFM Droop's cascaded control. Conventionally, the cascaded controls are tuned by setting the current control (CC) bandwidth $\omega_{CC} = 1000\ Hz$ and then setting the voltage control (VC) bandwidth ω_{VC} to be one order of magnitude slower [91]–[93]. Additional gains (e.g. the VC integral gain K_{pVC}) are conventionally tuned to achieve an acceptable overshoot and settling time in response to a power reference step. Instead, this study will assess the impact of the cascaded control tuning by varying the bandwidths of both the CC and the VC by a full logarithmic decade centred around a base setting. The base settings are identified using the conventional tuning approach described here. Of course, different results may be observed when a different baseline tuning approach is used compared to the assessment of changes from this specific baseline. However, the trends throughout the parametric sweeps will remain the same and the information found throughout the study can inform a range of tuning approaches.

The current control bandwidth is varied from $\omega_{CC} = 316\ to\ 3160\ Hz$ (around the base setting $\omega_{CC} = 1000\ Hz$) using (69). The integral gain of the voltage controller (K_{iVC}) can be used as a proxy for the VC bandwidth (ω_{VC}). The VC integral gain is varied from $K_{iVC} = 31.6\ to\ 316$, where the base setting is $K_{i,VC} = 100$, one decade slower than ω_{CC}. The VC proportional gain is varied around a base value that is identified using the conventional tuning to achieve acceptable $OS < 10\ \%$ in response to a $0.1\ PU$ voltage reference step. The base value is $K_{pVC} = 40$ and the logarithmic decade spans $K_{pVC} = 12.6\ to\ 126$.

5.4. **Results**

The GFM Droop and Synchronverter control strategies are tuned to provide the combined inertial and droop response magnitudes for the range of H and K_{pD} settings on the range of SCR grids. Each combination of the three settings is implemented on the infinite bus model and initialised to deliver a steady-state power $P_0 = 1\ MW$. The converters are then subject to the frequency disturbance. Section 5.4.1 provides an assessment of the two controllers to provide the desired inertial and droop magnitudes before analysing their equivalence/difference to one another. The GFM Droop model is then assessed in more detail by varying the tuning of the cascaded controls and assessing the changes in the response properties. The results of the current control and voltage control parametric sweeps are presented in Sections 5.4.2 and 5.4.3, respectively. Finally, Section 5.4.4 shows how the GFM droop can be tuned to increase its damping and hence maximise its stability.

5.4.1. Control comparison

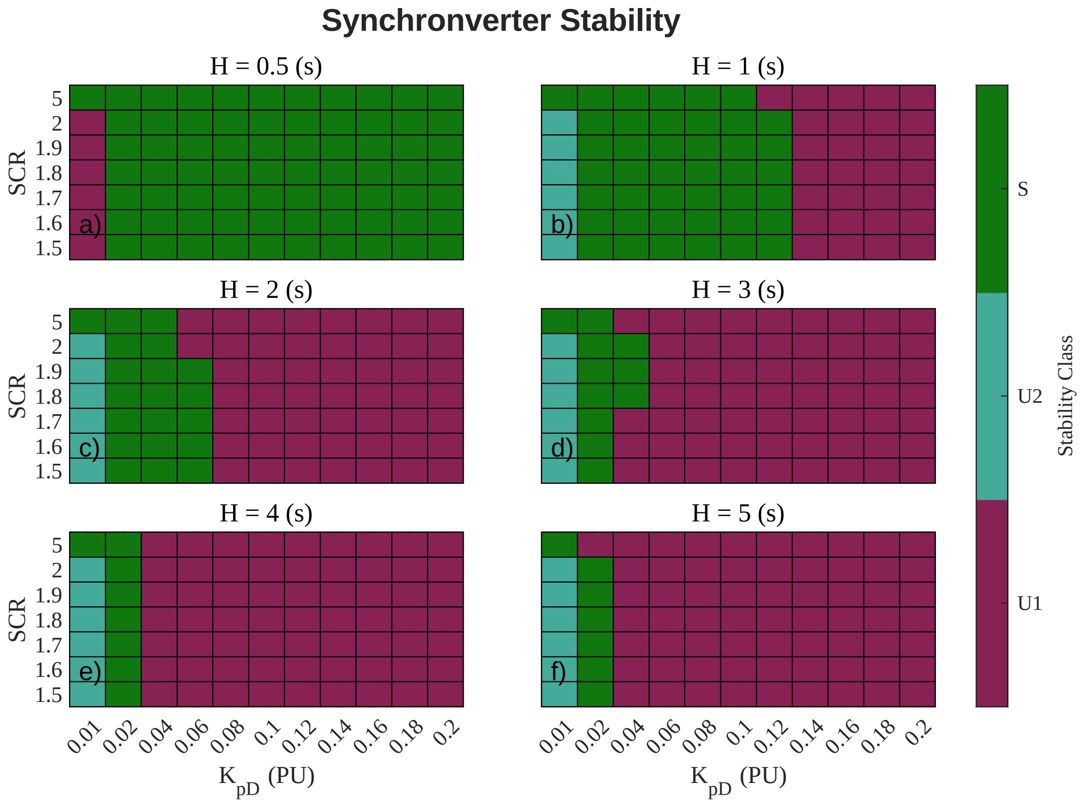

Figure 5-3 Synchronverter stability in different K_{pD}, SCR, and H conditions. The stability is described as either: Unstable 1 (U1) - unable to converge on an initial operating point, Unstable 2 (U2) - destabilised following the frequency disturbance, or Stable (S).

Figure 5-3 and Figure 5-4 show the stability of the Synchronverter and GFM Droop converter models throughout the simulated frequency disturbances across the range of tested K_{pD}, SCR, and H conditions. The figures are colour coded to highlight the stability class that each configuration of the converters possesses, either: Unstable 1 (U1) – unable to converge on the initial operating point (within a set time period of 2 seconds), Unstable 2 (U2) – destabilised following the frequency disturbance event, or Stable (S) throughout the entire simulation.

The stability of both controllers diminishes significantly as K_{pD} and H increase and to some degree as SCR increases. Both controllers are restricted to low droop coefficient settings around $K_{pD} = 0.02$ to maintain stability as H increases. In some cases, the controllers are able to support larger droop settings on lower SCR systems.

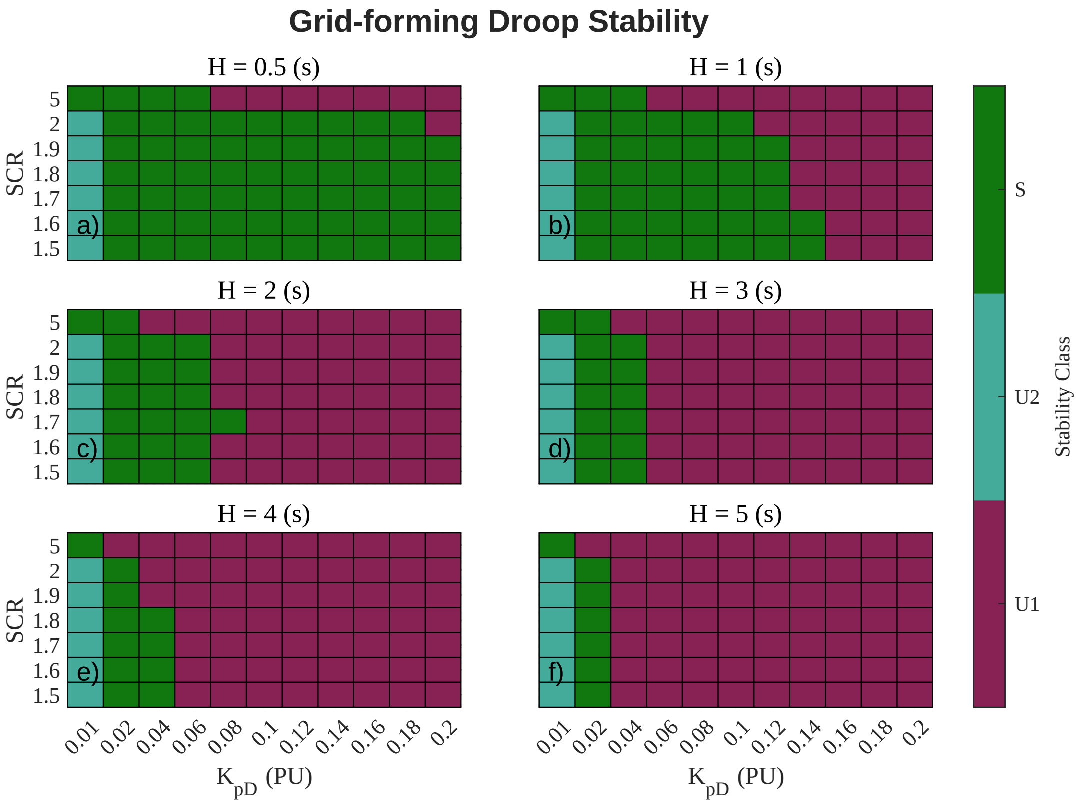

Figure 5-4 Grid-forming Droop stability in different KpD, SCR, and H conditions. The stability is described as either: Unstable 1 (U1) - unable to converge on an initial operating point, Unstable 2 (U2) - destabilised following the frequency disturbance, or Stable (S).

Neither controller is capable of supporting low droop coefficients below $K_{pD} = 0.02$ on grids with $SCR \leq 2$. Many of these configurations are destabilised following the disturbance, unlike the other (low damping) unstable conditions which do not converge on the initial operating point.

Although both controllers follow similar trends in stability, the exact stable operating ranges they each possess are different. For $H = 0.5\,s$ configurations, the Synchronverter is capable of supporting all of the droop coefficients on all of the SCR systems (excluding the extreme low K_{pD} on weak grids mentioned before). In contrast, the GFM Droop cannot support high K_{pD} settings on strong grids when $H = 0.5\,s$. However, as H increases the GFM Droop controller is capable of supporting a wider range of K_{pD} settings than the Synchronverter, particularly on low $SCRs$.

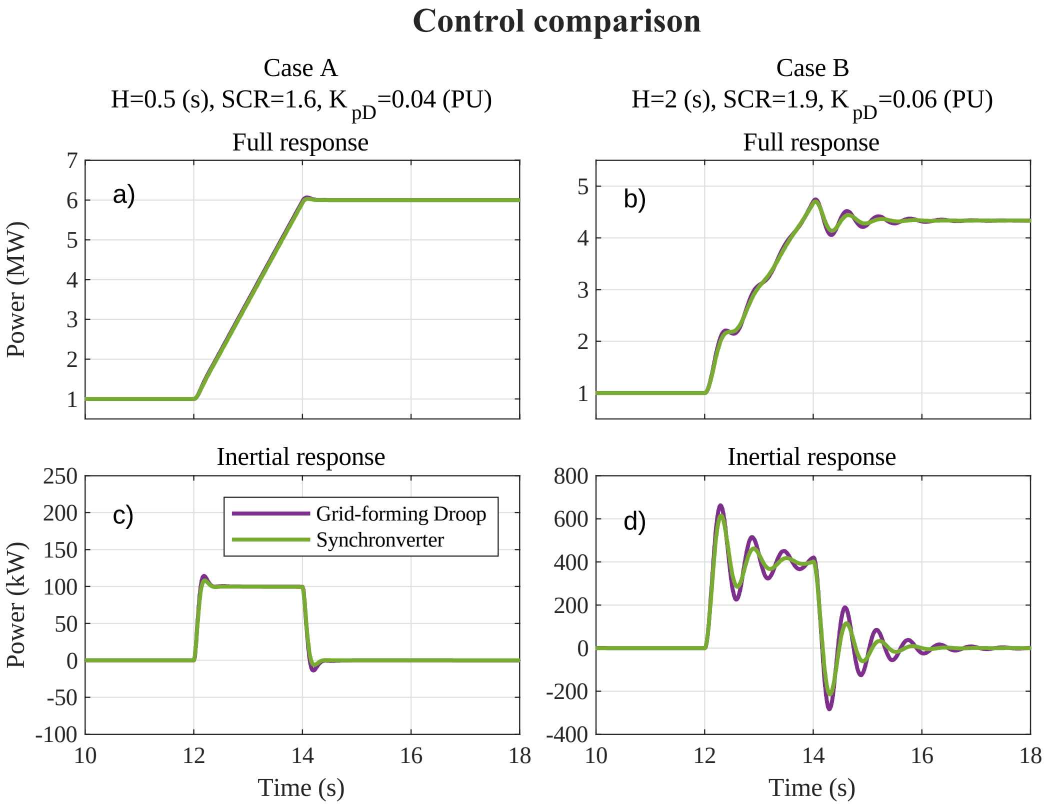

Figure 5-5 Time-domain comparison of the Synchronverter and Grid-forming Droop responses to the frequency disturbance for two example cases. The full active power response of the controllers is pictured in a) and b) while c) and d) show the isolated inertial response.

Figure 5-5 compares the time-domain active power outputs of the two controllers in response to the frequency disturbance for two examples cases. The example cases are stable configurations for both of the controllers (identified using Figure 5-3 and Figure 5-4). The full active power response for each case is pictured on the top tiles while the inertial response power has been isolated and compared on the bottom tiles.

In both cases, both controllers deliver the same steady-state droop and inertial active power injections. For each case, the expected droop injections are $\Delta P_{DR,A} = 5\ MW$ and $\Delta P_{DR,B} = 3.33\ MW$ (using (7)) and the expected inertial injections are $\Delta P_{IR,A} = 100\ kW$ and $\Delta P_{IR,B} = 400\ kW$ (using (78)). The time-domain signals in Figure 5-5 agree with these expected active power injections, proving the accuracy of the tuning guide to achieve given inertial and droop responses

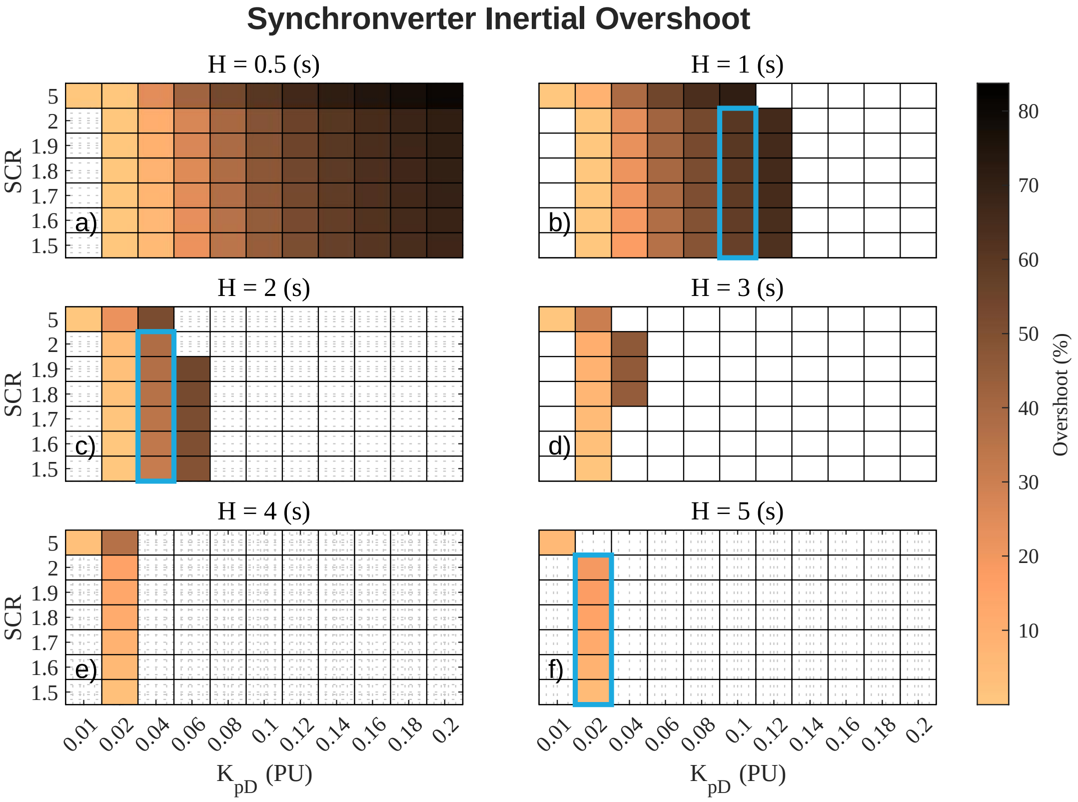

Figure 5-6 Overshoot of the Synchronverter inertial response beyond the expected magnitude following the frequency disturbance for a range of K_{pD}, SCR, and H configurations. Some example conditions that are stable for both the Synchronverter and GFM Droop are highlighted with blue outlines.

However, despite the equivalent frequency response magnitudes, the two controls exhibit different dynamics. In both cases the GFM Droop appears to be less damped than the corresponding Synchronverter, exhibiting larger overshoot (OS) and settling time (ST). The differences in the time-domain properties are especially visible in the isolated inertial response tiles (Figure 5-5 c) and d)), where the second order inertial dynamics are less masked by the large power change from the first order droop dynamic. The difference between the controllers also appears to be more significant in the higher H, SCR, and K_{pD} (and hence lower ζ) case (Figure 5-5 d)).

The damping coefficients of each case are calculated as $\zeta_A = 1.15$ and $\zeta_B = 0.36$ using (133). The OS expected from second order systems with these damping coefficients is $OS_A = 0\ \%$ and $OS_B = 29.97\ \%$. Although neither controller matches the expected OSs, the GFM Droop controller exhibits worse emulation of the expected behaviour in both cases.

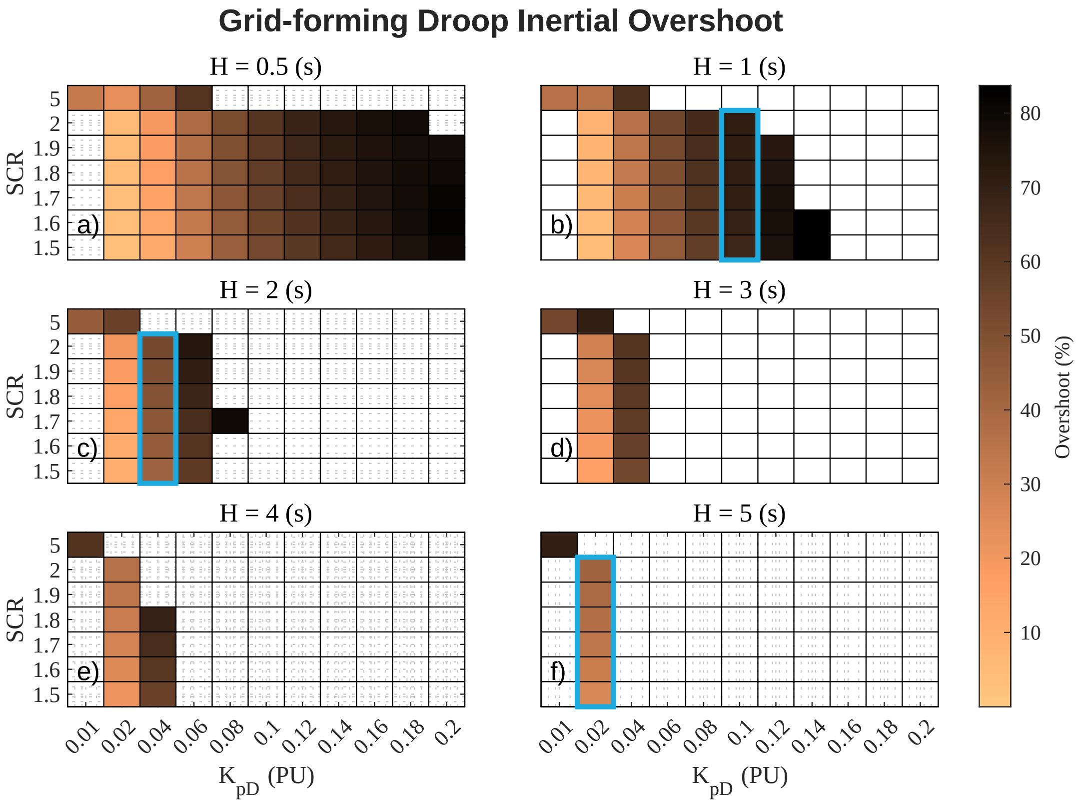

Figure 5-7 Overshoot of the GFM Droop inertial response beyond the expected magnitude following the frequency disturbance for a range of K_{pD}, SCR, and H configurations. Some example conditions that are stable for both the Synchronverter and GFM Droop are highlighted with blue outlines.

Figure 5-6 and Figure 5-7 show the Synchronverter and GFM Droop's inertial response OS for the full range of K_{pD}, SCR, and H conditions, respectively. Both controllers show an increase in OS as K_{pD}, SCR, and H increase, as expected. In agreeance with the damping expressions, the change in OS appears to depend most on the K_{pD} setting that is inversely proportional to ζ.

Despite showing similar trends in OS as K_{pD}, SCR, and H vary, a comparison of the example common stable conditions outlined in blue in Figure 5-6 and Figure 5-7 highlights that the GFM Droop always experiences worse OS than the Synchronverter for any given configuration.

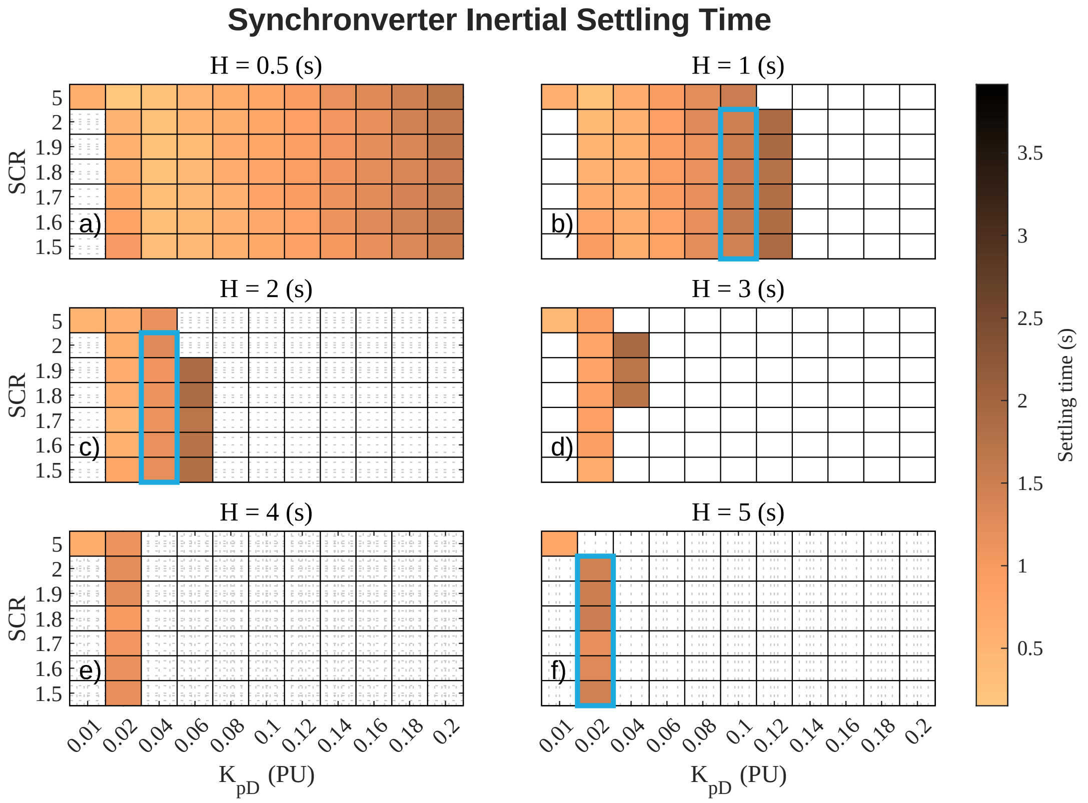

Figure 5-8 Settling time of the Synchronverter inertial response beyond the expected magnitude following the frequency disturbance for a range of K_{pD}, SCR, and H configurations. Some example conditions that are stable for both the Synchronverter and GFM Droop are highlighted with blue outlines.

Figure 5-8 and Figure 5-9 depict the ST of the two controllers' inertial responses across the range of K_{pD}, SCR, and H conditions. Similar to OS, both controllers exhibit the expected increase in ST as the analytical expression of damping decreases. The ST trend also appears to be dominated by K_{pD}, with smaller impacts from SCR and H. Finally, the example common stable conditions that are highlighted in blue in Figure 5-8 and Figure 5-9 also always depict a larger ST for the GFM Droop compared to the Synchronverter despite these conditions theoretically possessing equivalent damping.

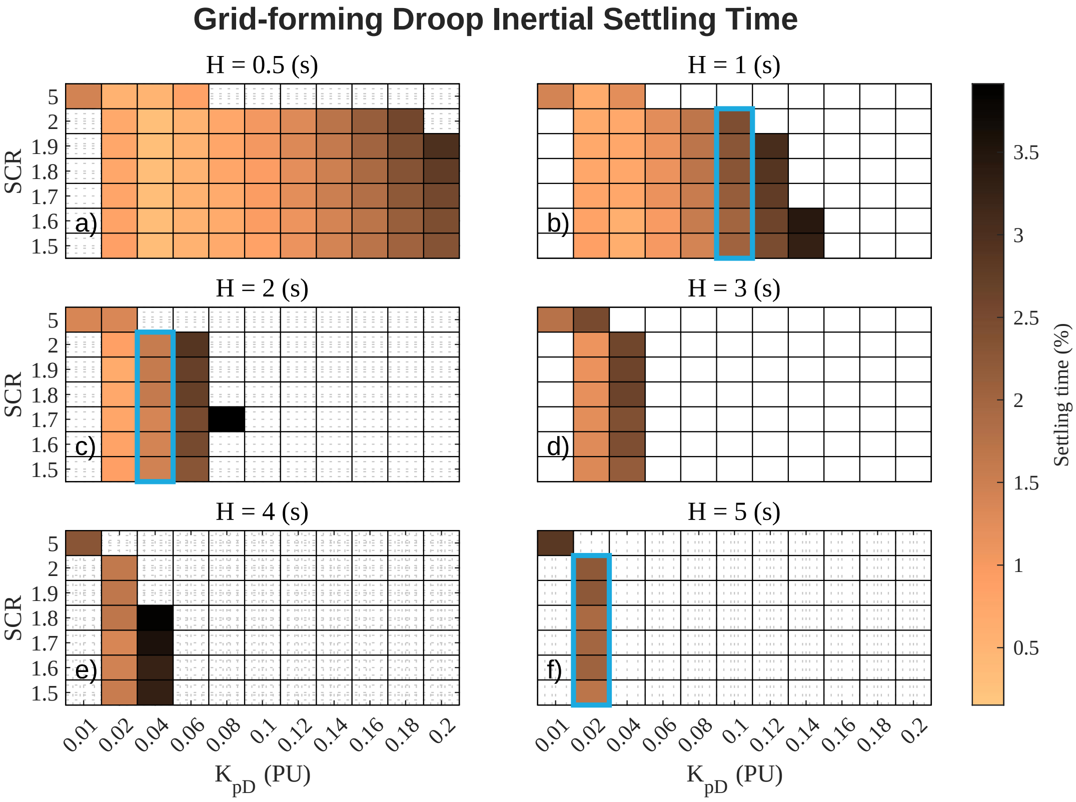

Figure 5-9 Settling time of the GFM Droop inertial response beyond the expected magnitude following the frequency disturbance for a range of K_{pD}, SCR, and H configurations. Some example conditions that are stable for both the Synchronverter and GFM Droop are highlighted with blue outlines.

5.4.2. Impact of current control

Figure 5-10 depicts the change in stability of the GFM Droop controller as its current control bandwidth is varied from $\omega_{CC} = 316$ to $3160\ Hz$ in each of the different K_{pD}, SCR, and H configurations. The stability is described as either: always, sometimes, or never stable throughout the ω_{CC} sweep. A coloured circle is included in the Figure for sometimes stable conditions to indicate the stability class of the corresponding base tuning configuration in Figure 5-4.

The stability of the GFM Droop is only found to be affected by ω_{CC} in three of the tested conditions. The affected cases are low damping conditions that exist on the boundary of the base tuning configuration's stable operating range. All of the sometimes-stable cases were stable in the base tuning configuration depicted in Figure 5-4.

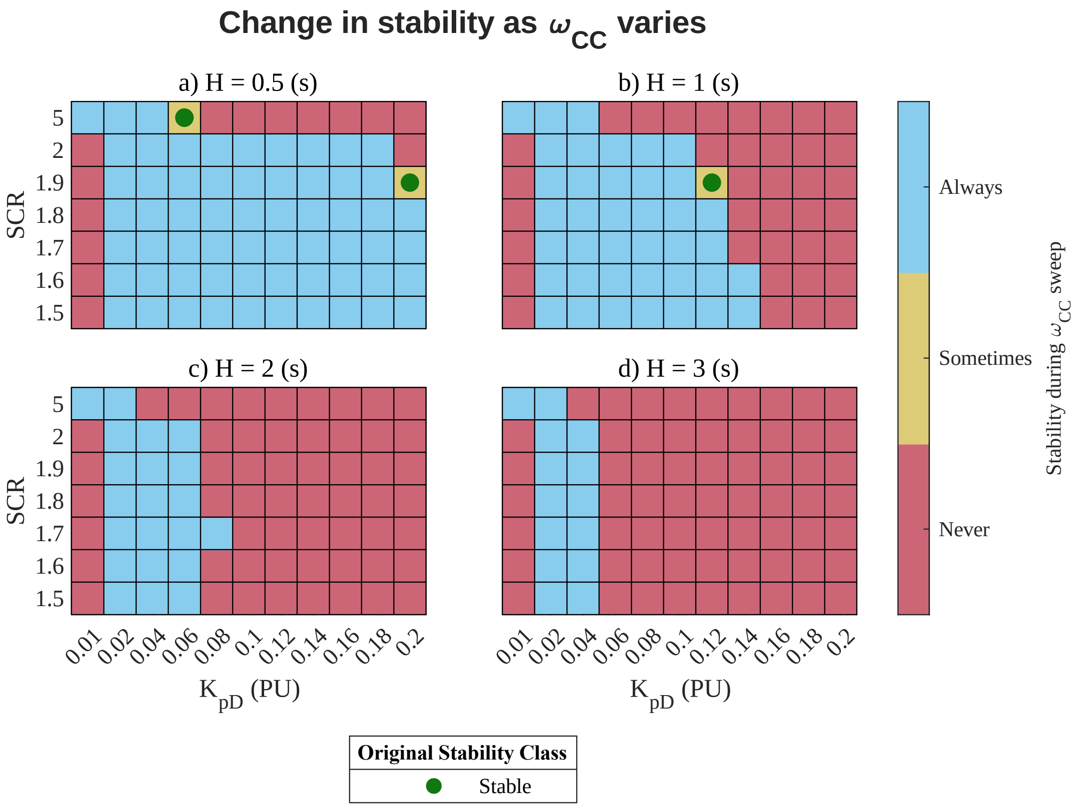

Figure 5-10 Change in GFM Droop stability as the current controller bandwidth ω_{CC} is varied for the tested range of K_{pD}, SCR, and H configurations. The stability is described as either: always, sometimes, or never stable for the range of ω_{CC} settings defined in Section 5.3. A coloured circle is overlain on sometimes stable conditions to indicate the stability class of the corresponding base tuning configuration that is shown in Figure 5-4.

Figure 5-11 depicts the time-domain disturbance responses of the GFM Droop for three different cases throughout the ω_{CC} sweep. The cases include one that is always stable (Case D), and two different inertial settings that are only sometimes-stable (Cases C and E).

The two sometimes-stable cases are destabilised for low ω_{CC} settings but remain stable up to the highest tested ω_{CC} settings. Alongside the minor variations in stability, the time-domain properties of the GFM Droop response do not exhibit any significant variations throughout any of the pictured ω_{CC} sweep cases.

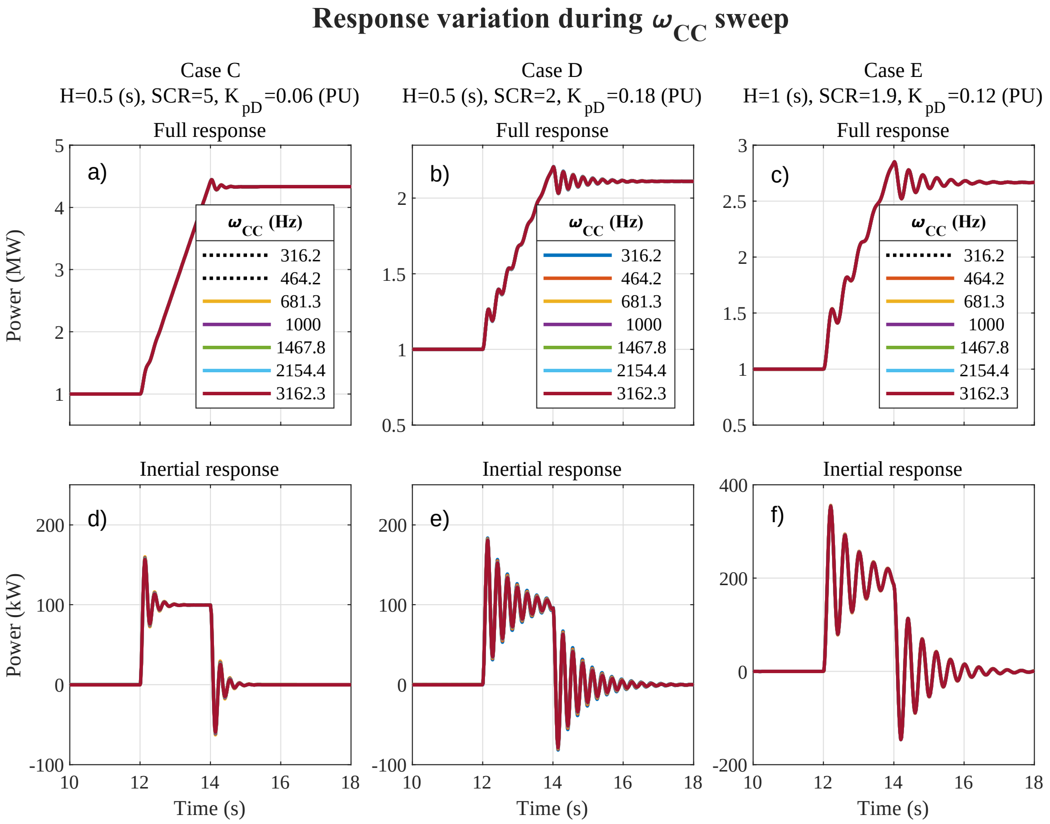

Figure 5-11 Variation in the GFM droop's time-domain response to the frequency disturbance for three different cases as the current control bandwidth ω_{CC} is varied. The dotted line represents unstable configurations.

and Figure 5-13 show the change in the GFM Droop's time domain properties (inertial rise time and settling time, respectively) during the ω_{CC} sweep across the full range of tested K_{pD}, SCR, and H conditions.

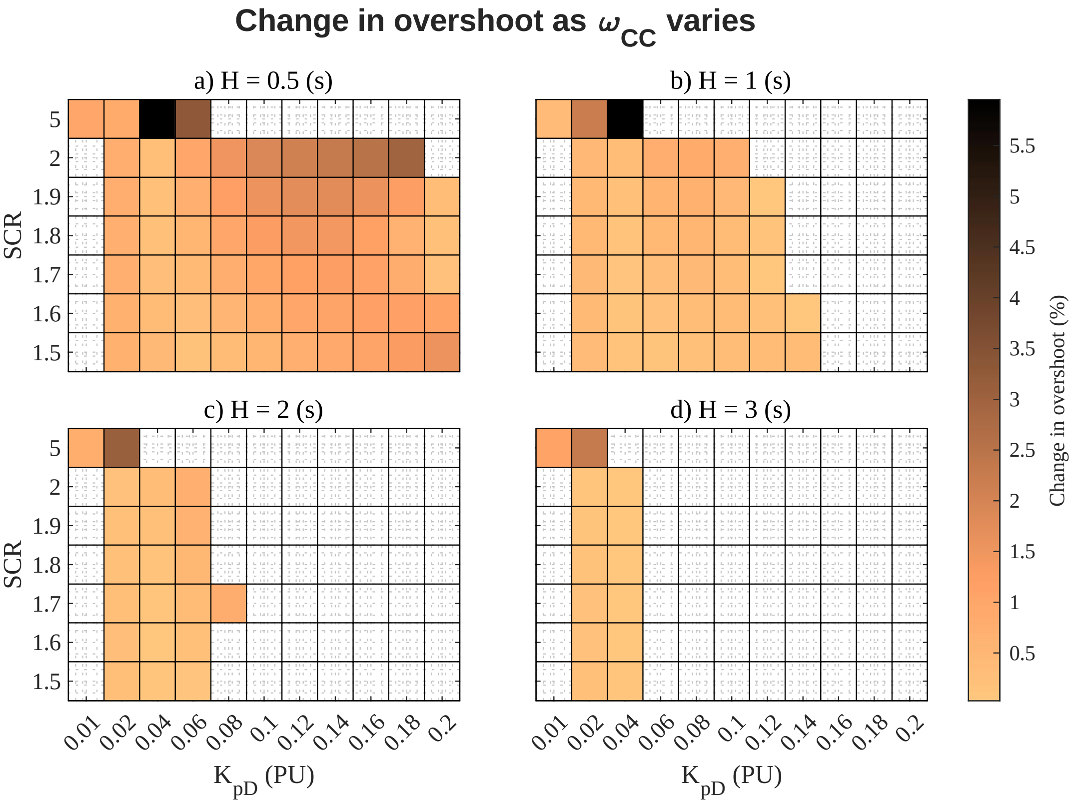

Figure 5-12 Change in GFM Droop inertial overshoot as the current controller bandwidth ω_{CC} is varied across the range of settings defined in Section 5.3.

The GFM Droop experiences a minor change in OS during the ω_{CC} sweep in some conditions, however, many of the configurations show very little change. The largest change in OS is generally experienced for high SCR configurations and to a lesser degree high K_{pD} configurations, both of which drive low damping. However, even in these most extreme cases the change in OS never exceeds 6 %, which is less than 10 % of the maximum inertial OS exhibited by any of the base tuning GFM Droop configurations (Figure 5-7).

Similarly, the GFM Droop doesn't experience any significant variations or trends in ST throughout the ω_{CC} sweep (Figure 5-13). The maximum change during the ω_{CC}

sweep never exceeds $0.27\ s$, which is also less than $10\ \%$ of the maximum ST experienced by the controller during all of the base tuning configurations in Figure 5-9.

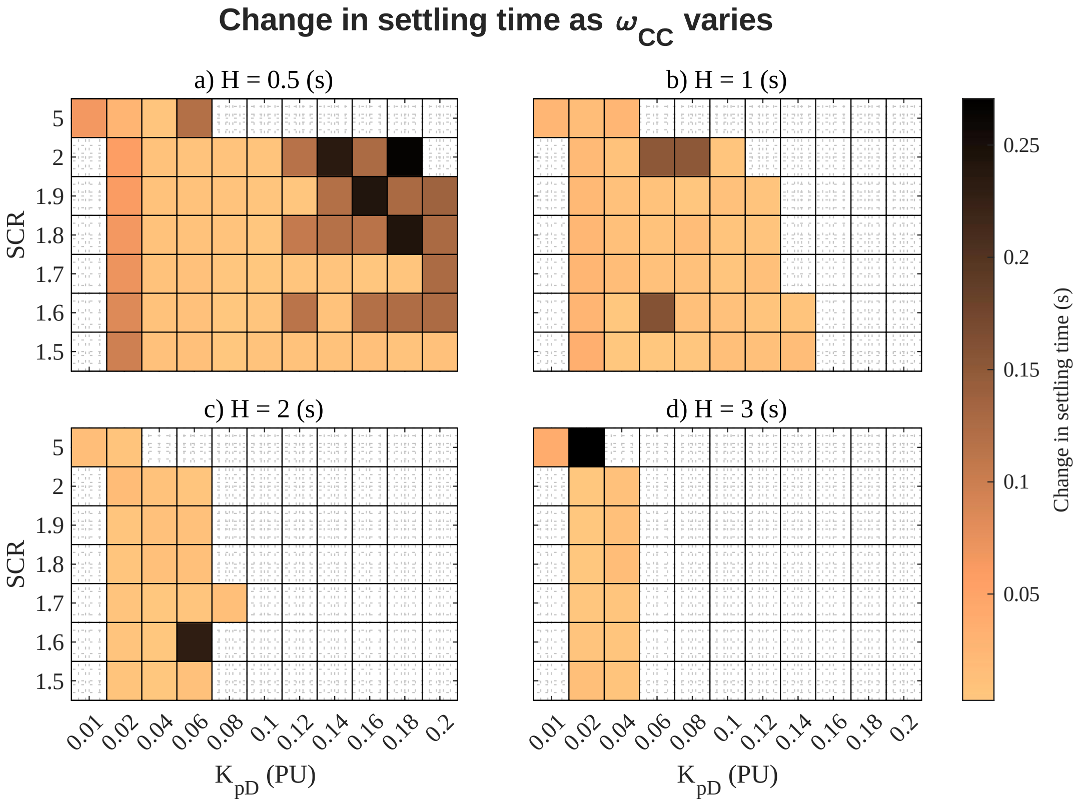

Figure 5-13 Change in GFM Droop inertial settling time as the current controller bandwidth ω_{CC} is varied across the range of settings define in Section 5.3.

5.4.3. Impact of voltage control

Figure 5-14 shows the change in the stability of the GFM Droop controller as its voltage control integral gain is varied. The tested range of K_{iVC} settings are shown to have a variable impact on the controller's stability. Highly damped configurations (low K_{pD}, SCR, and H) are shown to be relatively unaffected by the tuning of K_{iVC} and remain stable or unstable across the tested range of settings. In contrast, low damped configurations are shown to depend on K_{iVC}. In fact, some conditions that were unable to converge on the initial OP for the base tuning configuration are shown to be stabilised at some point during the K_{iVC} sweep (depicted in Figure 5-14 by yellow squares overlain by red circles). Particular improvement in the GFM Droop stability are achieved for conditions with $H \geq 1$ and on low $SCRs$.

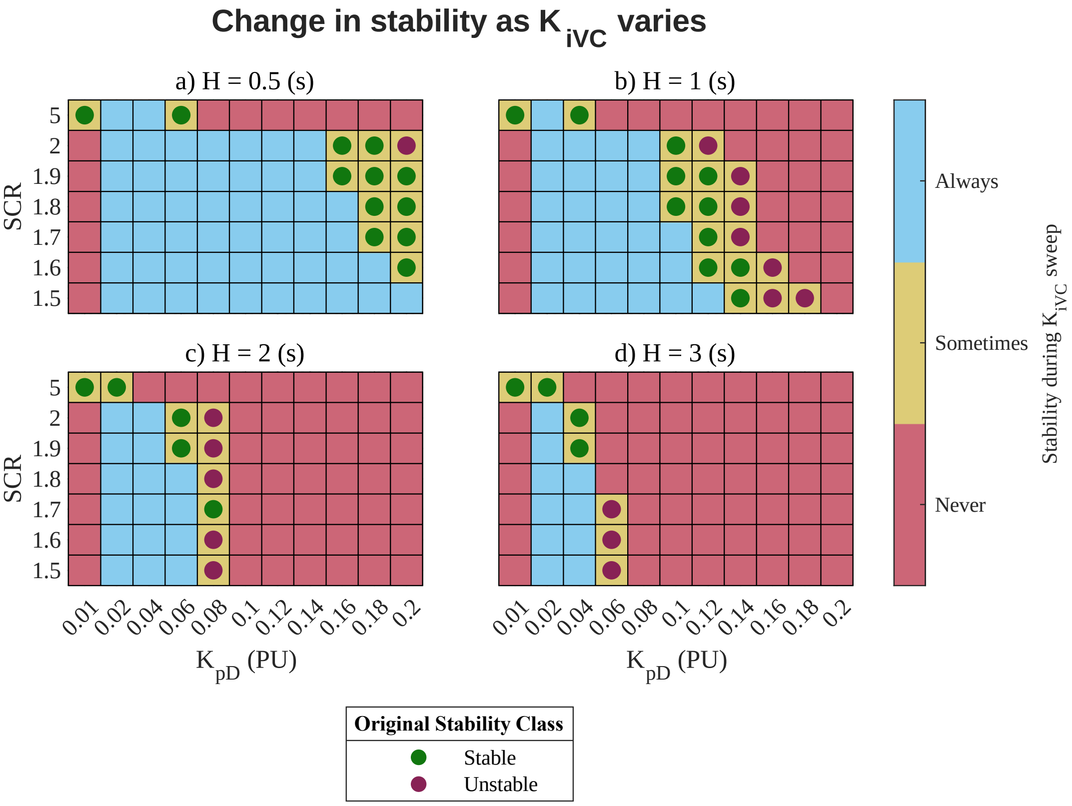

Figure 5-14 Change in GFM Droop stability as the voltage controller integral gain K_{iVC} is varied for the tested range of K_{pD}, SCR, and H configurations. The stability is described as either: always, sometimes, or never stable for the range of K_{iVC} settings defined in Section 5.3. A coloured circle is overlain on sometimes-stable conditions to indicate the stability class of the corresponding base tuning configuration that is shown in Figure 5-4.

Figure 5-15 shows the time-domain response of the GFM Droop controller in response to the frequency disturbance for different K_{iVC} settings and for three different cases. Two sometimes-stable configurations are assessed, where the base tuning configuration for Case F is unstable and for Case G is stable (Figure 5-4). Case H is assessed as it is shown to be stable for all of the K_{iVC} settings. Both of the sometimes-stable cases are stable for low K_{iVC} settings and unstable for high settings. The highest stable K_{iVC} setting increases from $K_{iVC} = 68.1$ to $K_{iVC} = 215.4$ as the damping derived for the given case from (133) increases from $\zeta_F = 0.25$ to $\zeta_G = 0.78$.

However, the analytical expression of damping for the always stable Case H is $\zeta_H = 0.37$. Despite the calculated damping being lower than Cases F and G, the low SCR Case H can support higher K_{iVC} settings.

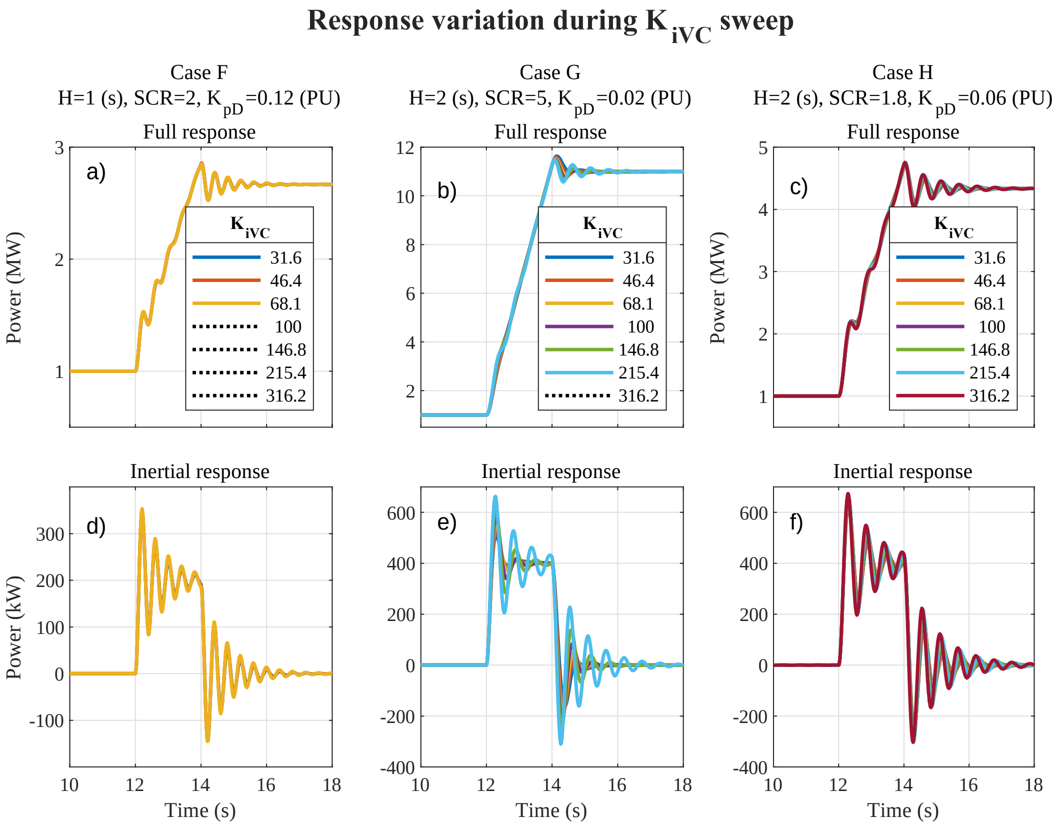

Figure 5-15 Variation in the GFM Droop's time-domain response to the frequency disturbance for three different cases as the voltage control integral gain K_{iVC} is varied.

The change in stability in the GFM Droop response during the K_{iVC} sweep agrees with the change in time-domain properties. The low K_{iVC} settings that stabilise the sometimes-stable cases also appear to drive a decrease in the OS and ST (and hence an increase in the damping). All of the cases experience some change in the time-domain properties, however, Case G appears to experience the largest change throughout the K_{iVC} sweep.

Figure 5-16 depicts the change in overshoot experienced by all of the tested K_{pD}, SCR, and H conditions throughout the K_{iVC} sweep. Many conditions experience significant variations in OS throughout the parametric sweep, however, the most extreme variations are always experienced on the $SCR = 5$ system. These large changes can correspond to a change in OS of over 35 %, which corresponds to almost 50 % of the most extreme OS experienced by the base tuning configuration of the GFM Droop (Figure 5-7). The change in OS doesn't appear to show as significant trends as any of K_{pD}, H, or ζ vary.

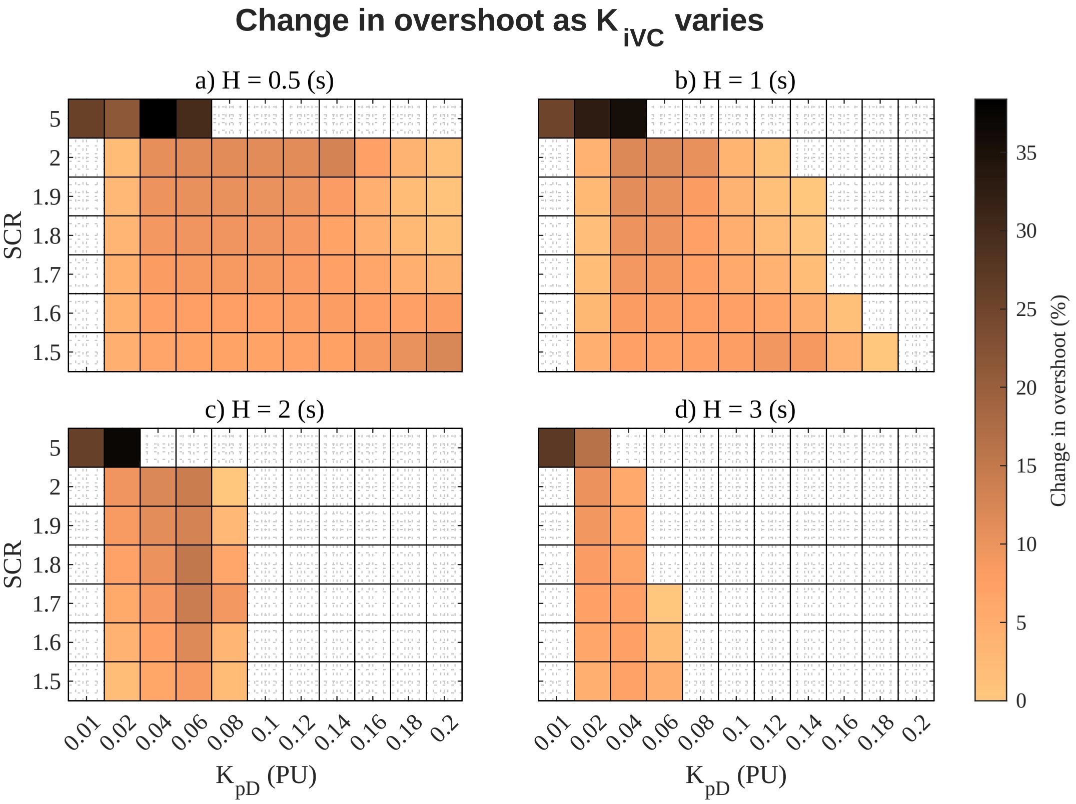

Figure 5-16 Change in GFM Droop inertial overshoot as the voltage controller integral gain K_{iVC} is varied across the range of settings define in Section 5.3.

Figure 5-17 shows the change in the GFM Droop's inertial settling time during the K_{iVC} sweep for all of the tested conditions. The settling time is also shown to be affected significantly by K_{iVC}, however, unlike the OS, the change in ST throughout the sweep appears to increase as the damping decreases (as K_{pD}, SCR, and H increase). The largest change in ST recorded throughout the sweep can be as large as 2 s for low damping conditions. The changes in ST pictured in Figure 5-17 are lower at the boundary of the stable conditions due to the reduced number of stable K_{iVC} settings that the change can be recorded across.

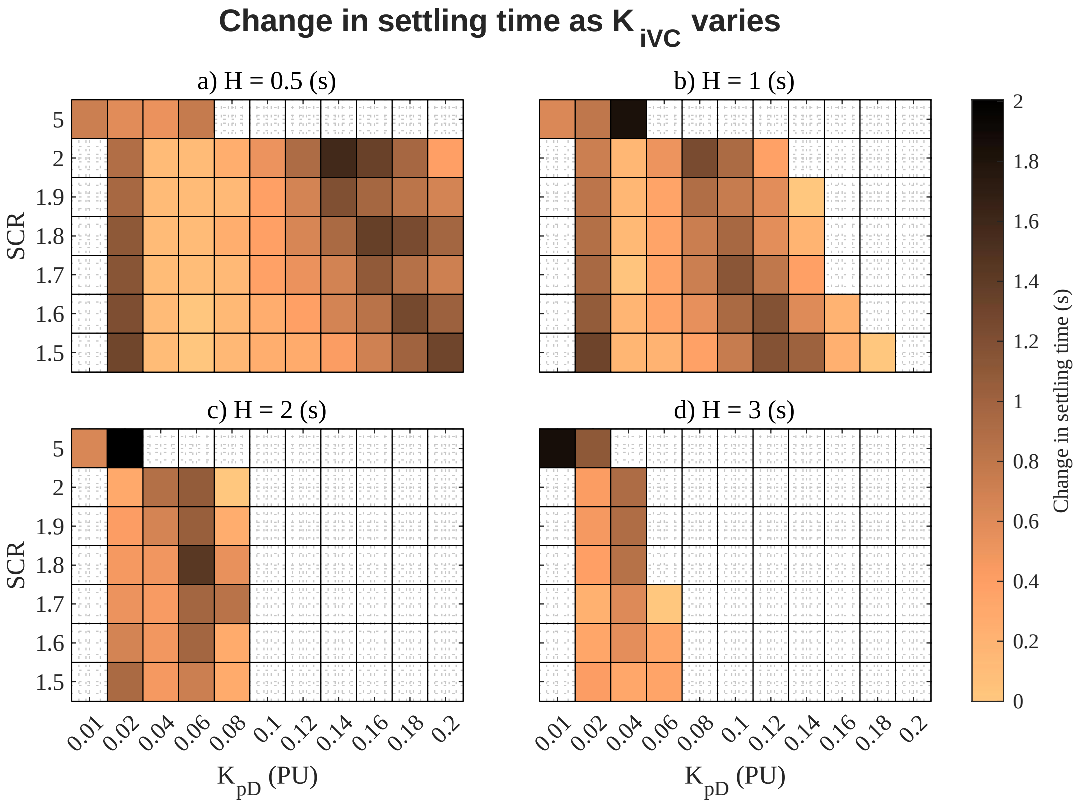

Figure 5-17 Change in GFM Droop inertial settling time as the voltage controller integral gain K_{iVC} is varied across the range of settings define in Section 5.3.

The GFM Droop response also experiences a large change in ST throughout the K_{iVC} sweep for high damping configurations (with $H \leq 1$ and $K_{pD} = 0.02$ settings) on all $SCRs$. Figure 5-18 exhibits the time-domain responses for an example of this highly damped case that experiences a large change in ST throughout the sweep. Although the OS remains relatively constant, the ST increases as K_{iVC} decreases. This change opposes the change experienced by lower damping cases, whose ST decreases as K_{iVC} decreases. The slow inertial ST manifests as a delayed peak in the total active power injection pictured in Figure 5-18 a).

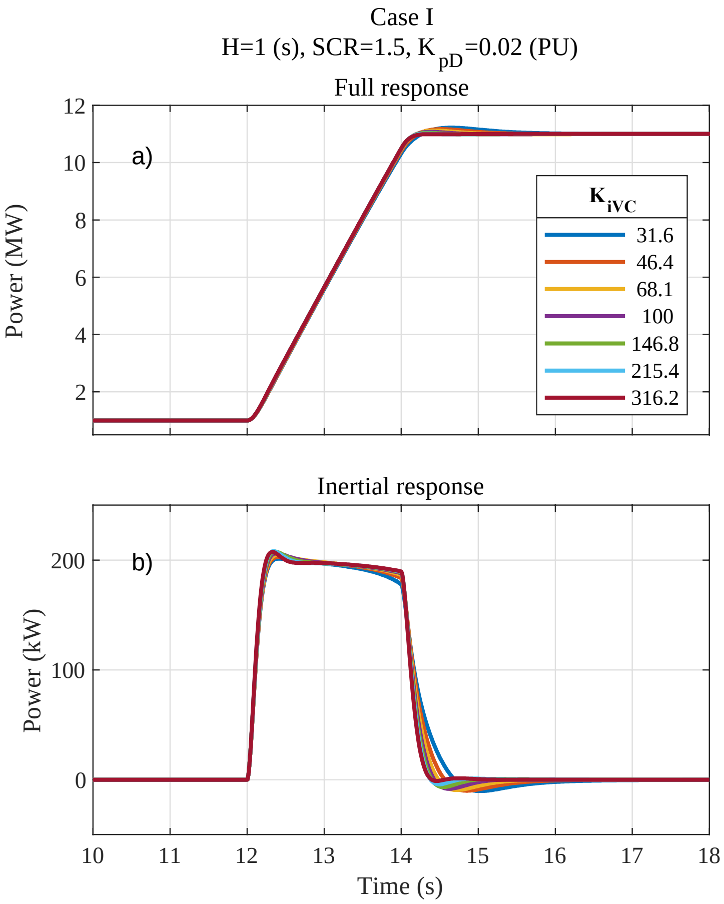

Figure 5-18 Example time-domain response of a high damping case that experiences a large change in ST throughout the K_{iVC} sweep, as identified in Figure 5-17.

Figure 5-19 shows the change in stability of the GFM Droop throughout the voltage control proportional gain K_{pVC} parametric sweep. The tested range of K_{pVC} settings is shown to have a large impact on the GFM Droop's stability in many of the K_{pD}, SCR, and H conditions. Tuning K_{pVC} enables the GFM Droop to be stabilised for low damping configurations with high $K_{pD}s$ and high $SCRs$. K_{pVC} is more capable of improving the stability of the GFM Droop in high SCR conditions than K_{iVC}. K_{pVC} is particularly effective at stabilising low H configurations ($H \leq 1$) but improvements in stability are also made for higher $H \geq 2$. Despite these impacts for low damping conditions, the updated tuning of K_{pVC} cannot stabilise the high damping low K_{pD} conditions on $SCR < 5$ that have remained unstable throughout all of the tests.

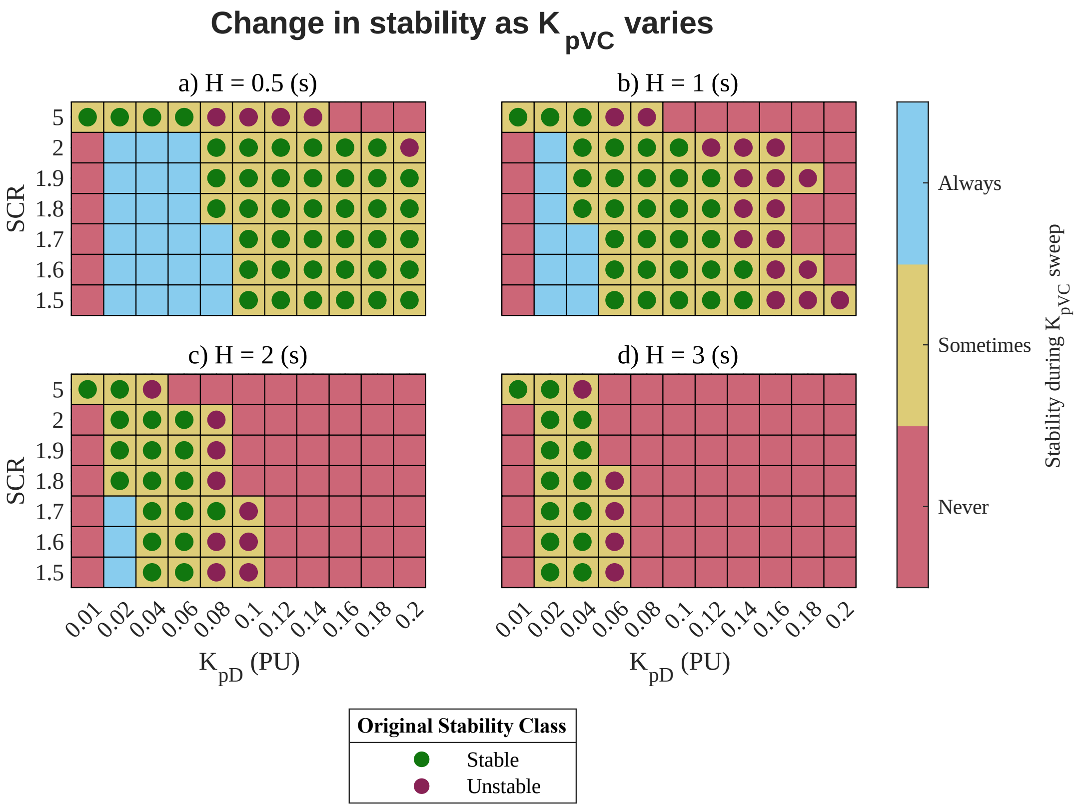

Figure 5-19 Change in GFM Droop stability as the voltage controller proportional gain K_{pVC} is varied for the tested range of K_{pD}, SCR, and H configurations. The stability is described as either: always, sometimes, or never stable for the range of K_{pVC} settings defined in Section 5.3. A coloured circle is overlain on sometimes-stable conditions to indicate the stability class of the corresponding base tuning configuration that is shown in Figure 5-4.

Figure 5-20 shows the time-domain response of the GFM Droop in three example cases as the voltage control proportional gain K_{pVC} is varied. The two low damping cases (Case J and K) are stabilised by increasing K_{pVC}. The boundary of the stable K_{pVC} setting doesn't appear to change as the analytical damping calculated using (133) varies from $\zeta_J = 0.39$ to $\zeta_K = 0.19$. The time-domain properties of Cases J and K do not vary significantly across the two exhibited stable K_{pVC} settings. In contrast, the highly damped Case L ($\zeta_L = 2.11$ according to (133)) is stable for the full range of K_{pVC} settings and experiences a large change in the OS and ST throughout the parametric sweep.

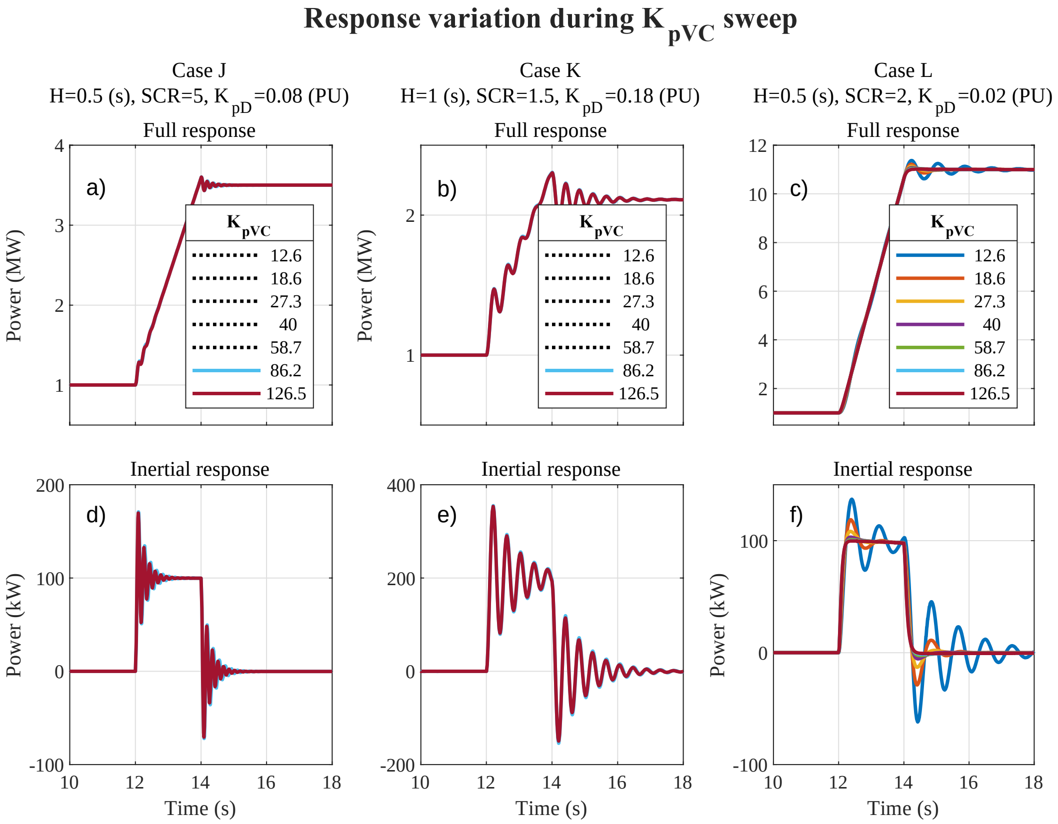

Figure 5-20 Variation in the GFM Droop's time-domain response to the frequency disturbance for three different cases as the voltage control proportional gain K_{pVC} is varied.

Figure 5-21 exhibits the recorded changes in OS for the GFM Droop throughout the K_{pVC} sweep in all of the tested conditions. The GFM Droop generally only experiences large changes in OS throughout the K_{pVC} sweep in low K_{pD} conditions, with the change becoming more extreme as SCR increases. The largest changes in OS approach 200 %, exceeding any change experienced by the GFM Droop throughout either of the other parametric sweeps. The change in OS throughout the K_{pVC} sweep doesn't appear to vary with H.

Figure 5-22 exhibits the changes in the GFM Droop's inertial response ST during the K_{pVC} sweep across all of the tested conditions. The GFM Droop experiences large changes in ST in low K_{pD} conditions and does not exhibit any significant dependence H, similar to the changes in OS. The largest changes in ST also exceed any recorded throughout either of the other parametric sweeps. However, unlike the changes in OS throughout the K_{pVC} sweep, the GFM Droop exhibits large changes in ST in a range of SCR conditions.

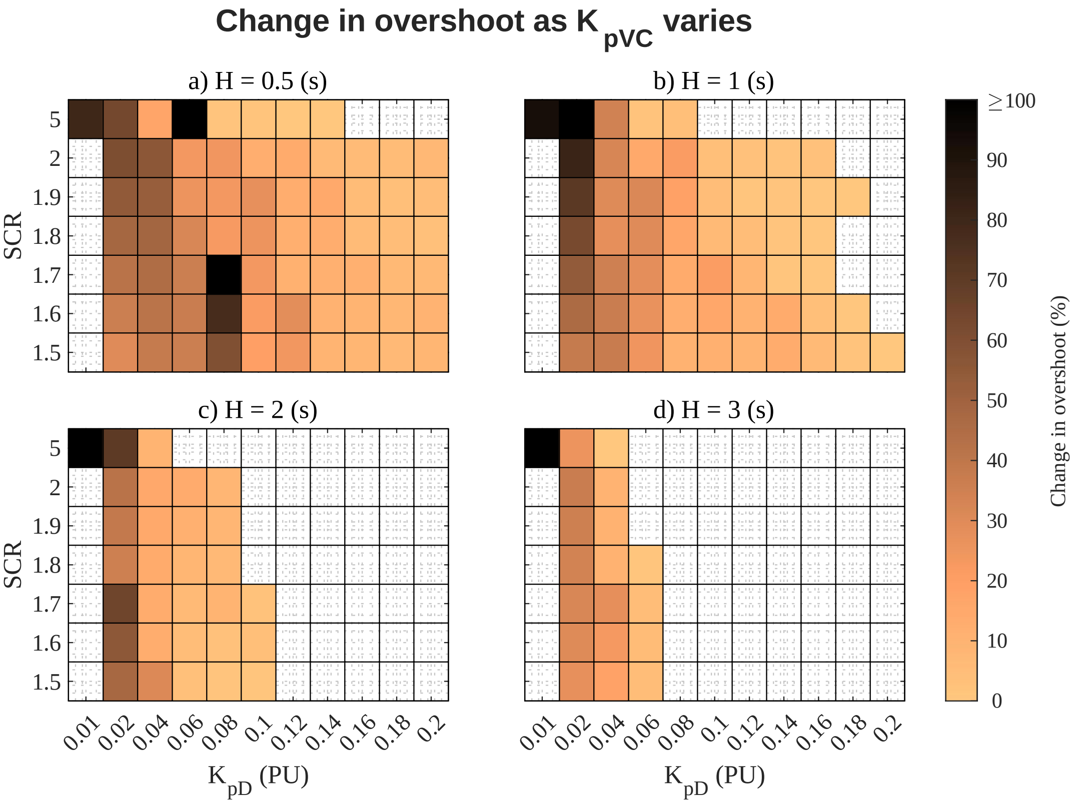

Figure 5-21 Change in GFM Droop inertial overshoot as the voltage controller proportional gain K_{pVC} is varied across the range of settings define in Section 5.3.

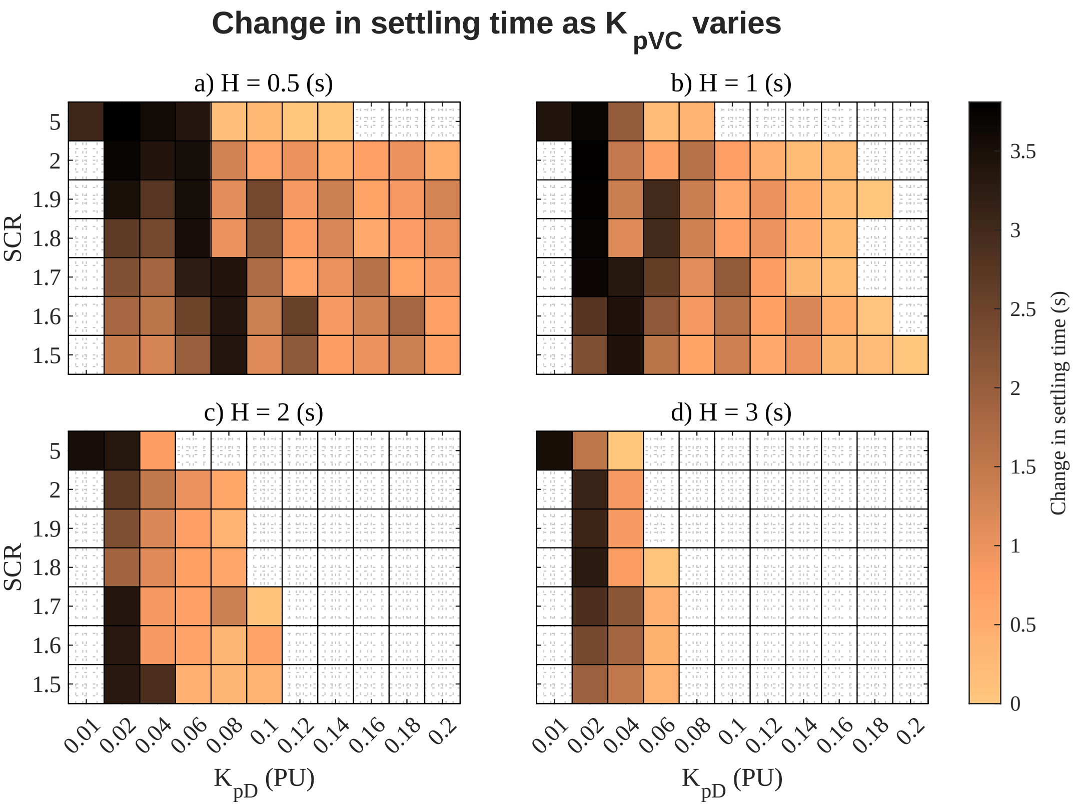

Figure 5-22 Change in GFM Droop inertial settling time as the voltage controller proportional gain K_{pVC} is varied across the range of settings define in Section 5.3.

5.4.4. Tuning for increased damping

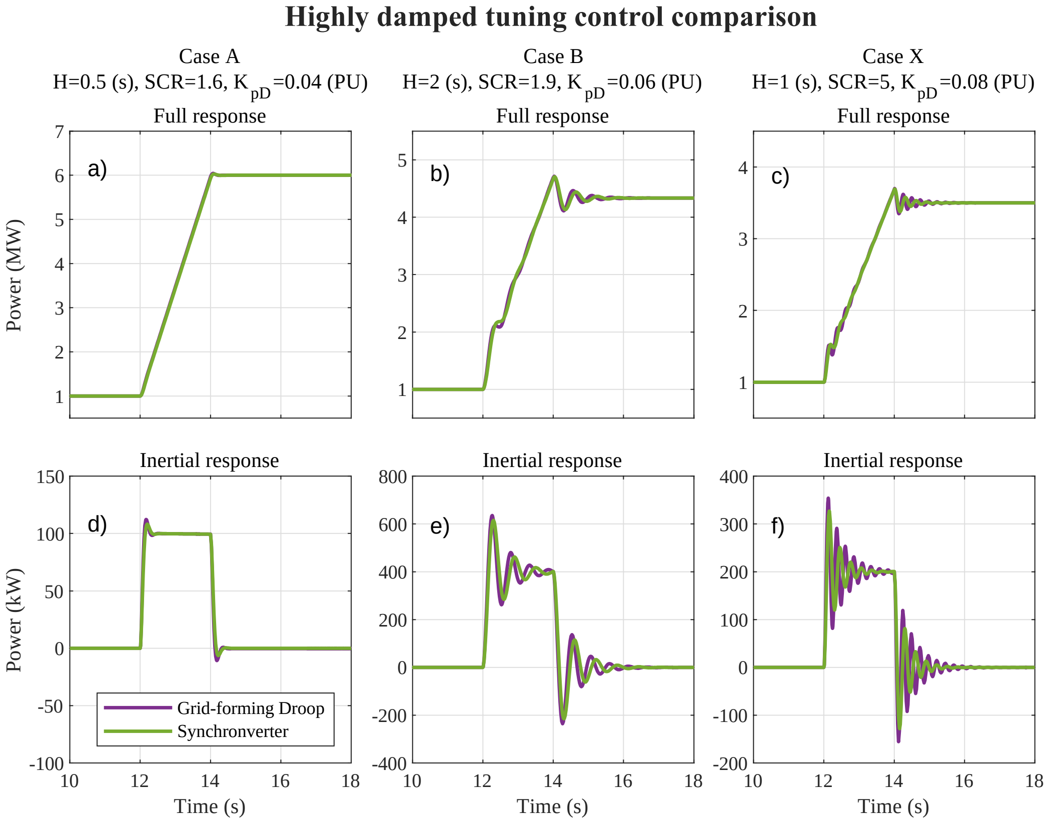

Figure 5-23 Time-domain comparison of the Synchronverter and Grid-forming Droop (with updated cascaded control tuning) responses to the frequency disturbance for three example cases. The full active power response of the controllers is pictured in a), b) and c) while d), e), and f) show the isolated inertial response.

Figure 5-23 compares the time-domain response of the GFM Droop with updated cascaded control tuning to achieve increased damping (using the results of Sections 5.4.2 and 5.4.3) to better match the Synchronverter for three different cases. The updated GFM Droop is tuned with the lowest tested voltage control integral gain $K_{iVC} = 31.6$ and highest tested voltage control proportional gain $K_{pVC} = 126.5$, both of which are shown to improve the stability and increase the damping of the controller. The current control bandwidth is not updated as it is shown to have a minimal impact on the controller's stability and dynamic properties. Case A and B are the two original cases that the controllers are compared for in Figure 5-5, while Case X is an additional case that the base tuning GFM Droop configuration was originally unstable for.

The updated cascaded control tuning increases the apparent damping of the GFM Droop, allowing it to better resemble the corresponding Synchronverter response in the original comparison cases. The GFM Droop exhibits a large increase in damping for the low damping Case B ($\zeta_B = 0.36$ according to (133)), which now closely resembles the Synchronverter response. The updated GFM droop controller has been stabilised for the other low damping conditions in Case X ($\zeta_X = 0.28$ according to (133)). Although the updated cascaded control configuration has improved the stability of the GFM Droop controller in the high SCR Case X, it continues to appear to be less damped than the Synchronverter response.

5.5. Discussion

This overview of the capability of the single-loop Synchronverter and the multi-loop GFM Droop controllers to provide P-f droop and inertial response offers an improved approach compared to [130], which suggests that the GFM droop should choose an inertial constant and then carefully tune the P-f droop or damping coefficients to achieve stable operation. Both controllers are shown to be capable of supporting small inertial constants in combination with a range of droop settings on many of the tested SCRs but that the optimal P-f droop coefficient to support large inertial provision is $K_{pD} = 0.02$ %.

The damping expressions derived from the tuning procedures in Section 5.2.1 describe the trends in both controllers' dynamics well. The controllers' OS and ST are both shown to decrease as the expression of damping increases. The inversely proportional dependence of ζ on K_{pD} appears to be significant; changes in K_{pD} are associated with more significant variations in the time-domain properties than changes in SCR or H, both of which are related to ζ by their square roots.

However, the observed damping (and stability) of the two controllers is shown to differ from one another for any given K_{pD}, SCR, and H case despite the analytical damping expressions suggesting that the two should be the same. These findings agree with [67]'s assessment of single versus multi-loop GFM Droop controllers, which suggests that: 1) the GFM Droop's stability can be described by the balance of gains between the P-f droop coefficient K_{pD} and the coupling reactance between the controlled voltage and the grid X_L, 2) single-loop configurations experience the full coupling reactance between the converter and grid, and 3) multi-loop configurations only experience the coupling reactance after the PCC (where the location of the voltage control has been moved to).

The first conclusion can be observed (and therefore extended to apply beyond just GFM Droop controllers) in the results in Section 5.4.1 where both controllers are better capable of supporting larger K_{pD} settings on weaker grids (where X_L is larger) and the overall system gain is not too large. Inversely, this can describe why both controllers are incapable of supporting very low $K_{pD} = 0.01$ % settings on very weak grids (high reactances that would drive a very low overall system gain) but become stable when $SCR = 5$.

The difference in the single- and multi-loop configurations' coupling reactance described by the second and third conclusions from [67] can be observed and therefore also extended to apply beyond just GFM Droop controllers by comparing the stability of the single-loop Synchronverter with the multi-loop GFM Droop; the GFM Droop is less capable than the Synchronverter at supporting high K_{pD} settings on high SCRs (low reactances) due to its inability to benefit from the impedance before the PCC and the resulting high overall system gain. Considering this conclusion, it is suggested that the tuning procedure of the GFM Droop with cascaded controls should be updated to reflect the altered voltage control location.

Hereon, the GFM Droop's coupling reactance should only include the reactance between the PCC and the receiving voltage source (and not any reactance between the converter and the PCC). For example, for the cases pictured in Figure 5-23, the damping of the GFM Droop becomes $\zeta_{A,GFMD} = 1.03$, $\zeta_{B,GFMD} = 0.31$, and $\zeta_{X,GFMD} = 0.21$. By considering only the reactance between the PCC, the effective damping of the GFM Droop is reduced compared to the (single-loop)

Synchronverter's damping in the same cases: $\zeta_{A,Syn} = 1.15$, $\zeta_{B,Syn} = 0.36$, and $\zeta_{X,Syn} = 0.28$, which agrees with the increased OS and ST observed in Figure 5-23. Moreover, the increased difference in the two controllers' dynamics for large SCRs can be linked to this characteristic, where the grid reactance is low and the presence or lack of reactance before the PCC is more significant.

The tuning of the current control bandwidth is shown to have a very minor impact on the GFM Droop's characteristics, which agrees with other studies that suggest that the large frequency separation of the fast current control can be assumed to equate to unity tracking with respect to the frequency disturbance response [130]. In contrast, the tuning of both of the voltage control parameters was shown to have a significant impact on the GFM Droop's stability and dynamics. These results agree with the assessment of the impact of cascaded controllers on a multi-loop Synchronverter in [68] that found the tuning of the voltage controller to have the largest impact on the GFM's stability and dynamics. The increase in damping with the voltage controller's proportional gain observed in Section 5.4.3 agrees with the automatic tuning procedure for the Synchronverter in [68].

The proposed high damping configurations enabled the multi-loop GFM Droop to better emulate the single-loop Synchronverter (and hence improve its damping) however, some minor differences remained between the two control approaches. The controllers' inherent differences were especially visible on high SCR (low reactance) grids where the different coupling reactances (due to the different voltage control locations) are especially significant. Also, the application of the tuning should avoid extreme low K_{iVC} settings that have been shown to drive a sluggish inertial response in already high damping configurations, in agreeance with the automatic tuning procedure in [68]. Therefore, the application of the results should consider the expected balance of the P-f droop coefficient and SCR before adjusting K_{iVC} too severely. These results suggest that the cascaded control tuning can be used to mitigate the differences between the two controllers but that they cannot be adapted to appear completely equivalent.

5.6. **Conclusions**

The procedures developed in Chapter 4 to tune the Synchronverter and GFM Droop controllers to provide inertial and P-f droop magnitudes have been proven to be accurate. The stability and dynamics are compared to provide a useful overview of each controller’s properties and capabilities with respect to the standard frequency response characteristics so that SOs can identify the feasible ranges of provision.

The single-loop Synchronverter and multi-loop GFM Droop controllers are shown to possess different stability and dynamic properties, which is suggested to related to the different location of the voltage control in each approach. Therefore, a proposal is made to update the tuning procedure to account for the reduced effective reactance of the multi-loop GFM Droop, which provides a better reflection of the observed damping.

The impact of the cascaded control tuning on the multi-loop GFM Droop is also observed. The current control tuning is shown to have a minimal impact, while both the proportional and integral gains of the voltage controllers are shown to impact the GFM Droop’s stability and dynamic properties. These findings agree with other studies that have assessed the impact of the cascaded control tuning on other GFM controllers.

Suggestions are made for the proportional and integral gains of the GFM Droop’s voltage controller to increase the damping and hence the stability and dynamic performance of the response to a frequency disturbance. Although the similarity between the single-loop Synchronverter and the multi-loop GFM Droop can be improved by tuning the GFM Droop’s cascaded controls, some inherent difference remains between the two controllers.

Chapter 6. Demystifying inertial specifications; supporting the inclusion of grid-followers.

6.1. Introduction

Some GFMs, although not all, provide inertial response inherently [28], [60], [134]. GFLs can be adapted to provide inertial response, however, it is formed using an additional power reference that is based on a filtered frequency measurement [25]. As described in Chapter 3, GFM IR is assumed to be “true” and useful, whereas, GFL IR is assumed to be slowed by its measurement and filtering procedure and is often described as “synthetic” and less useful at containing power system ROCOF. As a result, GFL IR is conventionally disqualified from the grid codes and specifications that SOs are developing to stimulate the provision of grid support from converters [18], [32], [33].

However, the examples of slow GFL IR are based either on a sluggish frequency measurement and filtering approach [54] or only consider a single tuning configuration [30], [96], [99]. Moreover, the industrial specifications appear to confuse inertial delivery timescales with those of voltage-source transient injections [18], [32], [33], [56]. In contrast, other studies have proven GFLs to be able to support a range of filter tunings [135] and for these tunings to have a significant impact on the GFL’s dynamics [101].

Following the explicit definition of the differences between inertial and transient response in Chapter 1, This chapter aims to provide:

- A conclusive assessment if useful IR can only be sourced from GFMs
- An assessment of the ability of industrial specifications to identify useful features of IR.

A standard GFM and GFL inertial controller are subject to parametric sweeps to assess the full range of their inertial capability with respect to existing industrial specifications (which are reviewed in Section 6.4). The results of the parametric sweeps are presented in Section 6.5.1 and 6.5.2, from which the optimal inertial configurations can be identified and assessed in Section 6.5.3. These configurations are validated and their impacts on frequency dynamics are assessed on a multi-bus power system model in Section 6.5.5. The results can inform the development of inertial specifications to either continue to focus on GFMs or expand and allow the consideration of GFLs. Including GFLs could take some of the strain off GFMs, who will be required to stabilise the future converter dominated power system in many other ways.

6.2. **System under study**

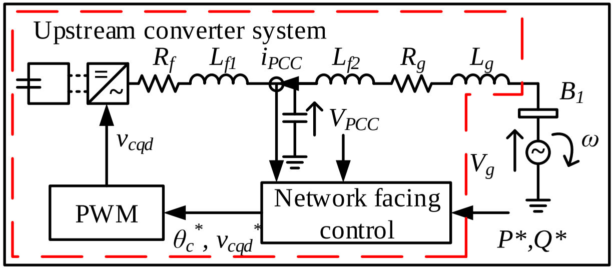

Figure 6-1 Electrical diagram of converter model with ideal DC energy source connected to infinite bus representation of grid, via LCL filter.

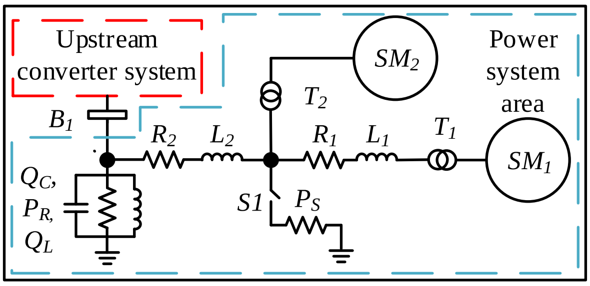

Figure 6-2 Electrical diagram of the power system model area that is connected via bus B1 to the upstream components of the converter system pictured in Figure 6-1.

The model of the ideal battery connected to an infinite bus representation of the power system described in Chapter 4 and pictured in Figure 6-1 is used to assess the ability of an example GFM (PI VSM) and GFL (CC with inertial capability) to provide inertial response. The same ideal batteries and controllers are then connected to the multi-bus power system model (also described in Chapter 4 and pictured in Figure 6-2) to validate the findings and assess their impact on the system frequency. The exact parameterisation for the studies is detailed in Table 6-1 and Table 6-2.

Table 6-1 Base control parameters.

		GFM			
H	Inertial constant	2 (s)	ζ_{VSM}	Damping coefficient	0.42
K_{pUVSM}	Voltage proportional gain	1 x 10^{-2}	K_{iUVSM}	Voltage integral gain	239
		GFL			
H	Inertial constant	2 (s)	D	Derivative gain	1
$\tau_{IR} = \frac{1}{\omega_{IR}}$	Inertial-filter time-constant	0.155 (s)	τ_{CC}	Current control time-constant	1 x 10^{-3} (s)
K_{pPLL}	PLL proportional gain	7.89 x 10^{-2}	K_{iPLL}	PLL integral gain	1.75
K_{pPC}	Power proportional gain	2.9 x 10^{-3}	K_{iPC}	Power integral gain	1
K_{pVC}	Voltage proportional gain	3	K_{iVC}	Voltage integral gain	200

An ideal energy source is utilised as the comparison is interested in the differences between the two controllers (both of which would be affected by specific energy source dynamics such as those exhibited for wind turbines in [136]). The control configurations assessed in this study are selected to resemble the GFM strategy detailed in the NG ESO industrial specification [32] and the standard industrial GFL inertial strategy. Moreover, they achieve similar fundamental inertial delivery properties as advanced strategies [100], [102]–[104] so provide an effective baseline to assess the ability of an example of a GFM and a GFL to meet the industrial criteria for useful IR, beyond which both approaches could be developed and improved upon in the future.

Table 6-2 Electrical model parameters.

Universal			
ω_0	$50\ (Hz)$	X/R	10
R_f	$0.0011\ (PU)$	C_f	$0.0675\ (PU)$
L_{f1}	$0.1\ (PU)$	L_{f2}	$0.01\ (PU)$
Infinite bus			
S_n	$3\ (MW)$	V_n	$690\ (V)$
Multi-bus			
$S_n = S_{SM}$	$200\ (MW)$	V_n	$230\ (kV)$
H_{SM}	$2\ (s)$	r	11.5
P_R	$100\ (MW)$	P_S	$10\ (MW)$
Q_C	$20\ (MVAr)$	Q_L	$50\ (MVAr)$
R_1	$5 * 10^{-3}\ (PU)$	R_2	$2 * 10^{-3}\ (PU)$
L_1	$4.17 * 10^{-2}\ (PU)$	L_2	$1.67 * 10^{-2}\ (PU)$

6.3. **Methodology**

GFM specifications from industry (particularly NG ESO’s [32]) and academia are reviewed in Section 6.4 to identify the criteria that are being used to qualify useful inertial response. Parametric sweeps of GFM and GFL controllers are then carried out at different operating points to assess how the converters’ inertial delivery varies. The ability of the GFM and GFL IRs to meet the criteria will be assessed. All of the sweeps are repeated for different voltage ($V_n = [0.9, 1, 1.1]\ PU$), power ($P = [0.1, 0.5, 0.9]\ PU$), and SCR ($SCR = [1.5, 3, 5]$) conditions. Finally, the optimal configurations of each controller are derived (according to the critical features of the industrial IR criteria) and are implemented on the adapted two area power system model in response to a load disturbance. The results are used to validate the stability of the controllers and to assess if either optimally tuned controller possess any inherently different properties that impact the power system's frequency.

6.3.1. Parallel control sweep

Sweeps of the parallel control parameters that do not explicitly impact the magnitude of the IR are carried out to assess their impact on the controllers' stability and dynamics. The GFM's parallel control parameters are: K_{pUVSM}, K_{iUVSM}, and ζ_{VSM} (which sets K_{pVSM}). The parallel control parameters assessed for the GFL are: τ_{IR} (which is represented by its inverse ω_{IR}), K_{pPLL}, K_{iPLL}, K_{pPC}, K_{iPC}, K_{pVC}, and K_{iVC}. The GFL's CC gains are not varied as they have previously been shown to have minimal impact on the IR (in [137] and in Chapter 5). Each parallel-control parameter (excluding ζ_{VSM}) is increased from two orders of magnitude below the base setting in Table 6-1 until the controller becomes unstable, while the remaining parameters are kept constant. ζ_{VSM} is varied between 0.155 and 1, spanning the range of acceptable settings described in [32]. Table 6-1 includes a list of the control parameters and the labels they are represented by.

6.3.2. Inertial constant sweep

The impact that the inertial constant setting has on the controllers' stability and dynamics is also assessed to highlight: 1) the ability of each controller to support different inertial constants and 2) the impact of the inertial constant on the IR dynamics and hence the weakness in the existing industrial approach to qualify IR by these variable features. Each controller's inertial constant is varied from $H = 0.5\ s$ to $6\ s$ while the remaining parameters are tuned with a low-burden but acceptable configuration (according to the industrial criteria identified in the review) using the results of the parallel-control sweep.

6.4. **Inertial response specification**

A review of the existing methods to qualify useful IR that have been proposed in the literature [30], [54], [56] and are used in industrial specifications [18], [32], [33] is carried out. The methods generally use time-domain properties of the active-power inertial response, which are detailed in Section 6.4.1. A frequency-domain tool is also utilised in some cases, which is discussed in Section 6.4.2. This paper aims to assess the ability of the two controllers to meet these criteria (using the parametric sweeps on the infinite bus) as well as the ability of the criteria to identify useful IR (using the results of the power system simulations).

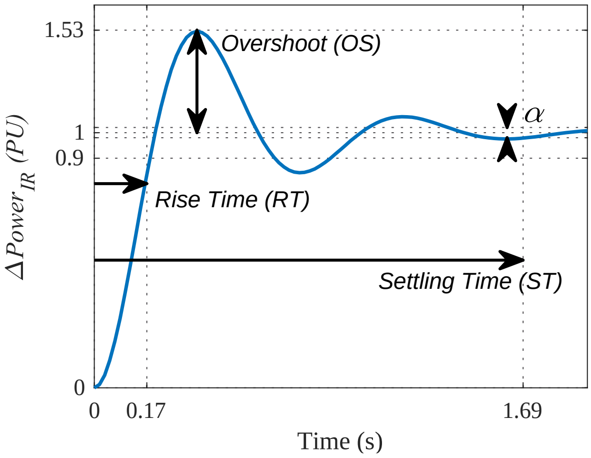

Figure 6-3 Critical time-domain properties and corresponding values to meet the acceptable inertial criteria for an inertial response power injection $\Delta Power_{IR}$ *during a frequency ramp. The power injection is normalised to the expected inertial response.*

6.4.1. Time-domain criteria for acceptable inertial response

Response speed is viewed as a key feature of IR in the industrial specifications [18], [32], [33]. GFMs delivering a large proportion of the IR before the nadir was linked to the better containment of a grid's ROCOF in [30]. To incorporate this finding, an acceptable IR speed criterion is determined by comparing the converter's RT to 90% of the inertial magnitude (pictured in Figure 6-3) to the average of three representative recent British nadir times. The representative nadir times include: two nadirs in 2017 both resulting from the tripping of the France-England Interconnector, $t_{Nad,31/05} =$

$0.12\ s$ and $t_{Nad,12/06} = 0.15\ s$ [70], and the nadir that led to significant electrical system disruption in Great Britain on the 9th of August, 2019, $t_{Nad,09/08} = 0.25\ s$ [138]. The resulting average nadir time that represents the critical speed that IR should be delivered before is: $t_{Nad,avg} = \mathrm{RT_{acc}} = 0.173\ s$. Due to the disagreement throughout industrial GFM specifications (and in academic studies) regarding "inherent and instantaneous" inertial provision, the power delivery will also be compared with the $t = 5\ ms$ timeframe that is often used as a threshold for instant behaviour and therefore useful inertial provision [18], [32], [33], [56], [57].

The NG ESO grid code update also included a minimum acceptable damping coefficient that GFMs could connect with: $\zeta = 0.2$ [32]. Presumably, this is defined to standardise the dynamic performance. Limiting the damping can mitigate undesired overshoot of converter components during the initiation of inertial delivery and the undershoot of nominal power during the cessation of inertial delivery – both quantified as the reduction of overshoot (OS). Furthermore, specifying the damping can limit the time that oscillations are present in the system – quantified as the reduction of settling time (ST).

Inertial devices can be considered as standard second order systems, which allows the definition of the acceptable limits of OS and ST from this minimum acceptable damping allowed by NG ESO. According to (135), the maximum OS accepted by NG ESO is $OS_{acc} = 52.7\%$.

$$OS = e^{-\frac{\zeta\pi}{\sqrt{1-\zeta^2}}} * 100 \tag{135}$$

Then, according to (136) and the range of grid voltage magnitudes V_g, coupling impedances X_L, and converter voltage angle differences δ tested throughout the study (that define the synchronising torque coefficient K_s (138) and hence the natural frequency of the Swing Equation transfer function ω_n (137)), the maximum ST accepted by NG ESO is $ST_{acc} = 1.69\ s$.

$$ST = -\frac{\ln\left(\alpha\sqrt{1-\zeta^2}\right)}{\zeta\omega_n} \tag{136}$$

$$\omega_n = \sqrt{\frac{K_s\omega_0}{2HS_n}} \tag{137}$$

$$K_s = \frac{V_cV_n}{X_L}\cos(\delta) \tag{138}$$

where $\alpha = 0.02$ is the ST tolerance and V_c is the PU converter voltage magnitude. The critical features identified in the inertial criteria and the corresponding thresholds for their acceptability in response to a frequency ramp are pictured in Figure 6-3.

6.4.2. Network Frequency Perturbation plot

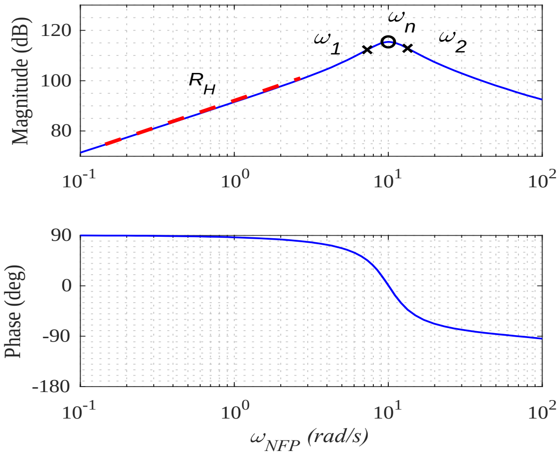

Figure 6-4 Example Network Frequency Perturbation (NFP) plot with inertial asymptote R_H, natural frequency ω_n, and frequency pair 3 dB below natural frequency $\omega_{1,2}$.

The Network Frequency Perturbation (NFP) plot (example in Figure 6-4), which was proposed for the assessment of frequency supporting devices in [47], was included in NG ESO's GFM grid-code document to aid the assessment of "true" IR [32]. The NFP plot is a bode plot of a device's active power response to grid frequency disturbances. If the device provides an IR its magnitude will track an inertial asymptote R_H (139)

and its phase will precede the steady state phase by 90^o, between the regions $\omega_{NFP} = 0.25$ to $13\ rad\ s^{-1}$, as defined by [47].

$$R_H(\omega_{NFP}) = -j2H\left(\frac{\omega_{NFP}}{\omega_0}\right) \tag{139}$$

where ω_{NFP} is the oscillation frequency of the input signal. The inertial resonant peak will occur at the natural frequency ω_n of the inertial transfer function [139], the same as that described in (137). The damping of the response can be found using classical control theory's Quality factor Q, by comparing this natural frequency with its two neighbouring frequencies ω_1, ω_2 that exist 3 db lower than the resonant peak (140).

$$Q = \frac{1}{2\zeta} = \frac{\omega_n}{\omega_2 - \omega_1} \tag{140}$$

Finally, the phase provides useful information about the delivery of the IR. The further (to higher ω_{NFP}) the device can sustain high phase (that precedes the steady-state phase by close to 90^o) the faster and more effective the IR will be.

Although there is no suggestion that any feature of the NFP plot will be used as a specific criterion to qualify provision, it has been suggested that it can be used to help identify useful responses. Therefore, the NFP plot will be included in the assessment of different tools to differentiate between GFM and GFL IR and hence the discussion of "true" inertial features.

6.5. **Results**

The ability of the GFM and GFL to provide acceptable IR with respect to the representative industrial criteria identified in Section 6.4.1. at different power, voltage, and SCR conditions are assessed in Sections 6.5.1 and 6.5.2, respectively. Comparisons of the optimal inertial configurations for the two controllers (defined in terms of the critical features identified from Sections 6.5.1 and 6.5.2) are made in Section 6.5.3 on different SCR infinite bus representations of a network. The ability of each control to sustain acceptable responses across a range of inertia constants is then assessed in Section 6.5.4. Finally, the findings from the infinite bus simulations are validated on the multi-bus power system model and the impact that the inertial properties have on the system's frequency stability are identified in Section 6.5.5.

6.5.1. Grid-forming control

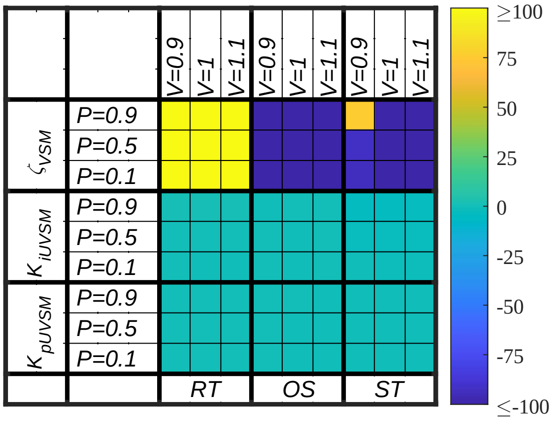

Figure 6-5 Maximum change of time-domain properties during GFM parallel-control parametric sweeps across different operating points on SCR=3 grid.

The maximum change ($\Delta diff$) in the inertial time-domain properties during different parallel-control parametric sweeps are shown for the GFM in Figure 6-5 $\Delta diff$ is expressed as a percentage of the mean of the property during its parametric sweep and the colour indicates the magnitude and direction (during the sweep) of the maximum change (while the controller remains stable). These property-parameter interactions are further broken down according to the power (on the y-axis) and the voltage conditions (on the x-axis), while the grid strength is constant at $SCR = 3$.

The maximum changes vary depending on the parameter and property. Neither K_{pUVSM} nor K_{iUVSM} have a significant impact on any of the transient properties of the inertial response. However, an increase of ζ_{VSM} increases the RT and decreases the OS and ST by more than 100 %. An outlier exists for $P = 0.9, V = 0.9$ due to the reduced stability range and apparent increase in ST.

Figure 6-6 exhibits the acceptability of the GFM inertial properties with respect to the criteria defined in Section 6.4.1. The acceptability is arranged in the same format as

Figure 6-5, with property-parameter interactions broken down according to power and voltage conditions on the $SCR = 3$ grid. The colour indicates the ability of the GFM to meet the relevant acceptable property criterion either always (green), sometimes (amber), or never (red) during the given parametric sweep.

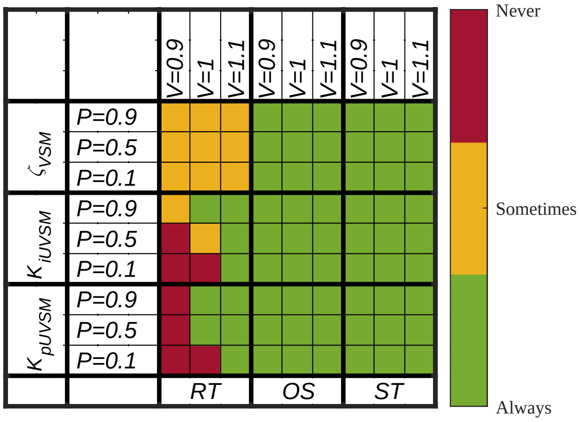

		V=0.9	V=1	V=1.1	V=0.9	V=1	V=1.1	V=0.9	V=1	V=1.1
ζ_{VSM}	P=0.9	🟧	🟧	🟧	🟩	🟩	🟩	🟩	🟩	🟩
	P=0.5	🟧	🟧	🟧	🟩	🟩	🟩	🟩	🟩	🟩
	P=0.1	🟧	🟧	🟧	🟩	🟩	🟩	🟩	🟩	🟩
K_{iUVSM}	P=0.9	🟧	🟩	🟩	🟩	🟩	🟩	🟩	🟩	🟩
	P=0.5	🟥	🟧	🟩	🟩	🟩	🟩	🟩	🟩	🟩
	P=0.1	🟥	🟥	🟩	🟩	🟩	🟩	🟩	🟩	🟩
K_{pUVSM}	P=0.9	🟥	🟩	🟩	🟩	🟩	🟩	🟩	🟩	🟩
	P=0.5	🟥	🟩	🟩	🟩	🟩	🟩	🟩	🟩	🟩
	P=0.1	🟥	🟥	🟩	🟩	🟩	🟩	🟩	🟩	🟩
		RT			OS			ST		

Figure 6-6 Acceptability of time-domain properties (with respect to the criteria defined in Section 5) during GFM parallel-control parametric sweeps across different operating points on SCR=3 grid.

The GFM is always capable of meeting the OS and ST limits (for the given $SCR = 3$ grid). However, the RT limits are not always met, meaning there are some configurations on the $SCR = 3$ grid when the GFM does not qualify according to the representative industrial inertial acceptability criteria. Both voltage-controller parametric sweeps achieve acceptable RT with the base ζ_{VSM} tuning in high voltage conditions but are slowed in low voltage conditions where the parameters' low impact is unable to affect the acceptability of the RT significantly. However, the high impact of ζ_{VSM} on the RT (as shown in Figure 6-5) means that the GFM can be tuned to be acceptable in all of the tested conditions. The GFM requires low ζ_{VSM} to provide an acceptably fast IR in the low voltage conditions on the $SCR = 3$ grid.

Figure 6-7 depicts the magnitude and direction of the mean change in inertial property ranges (across all of the parallel-control parametric sweeps) as the variable operating conditions increase. For example, no significant or consistent changes are observed in any of the property values as the power level increases. This finding is consistent with Figure 6-6 which did not show a consistent change in acceptability as power changes.

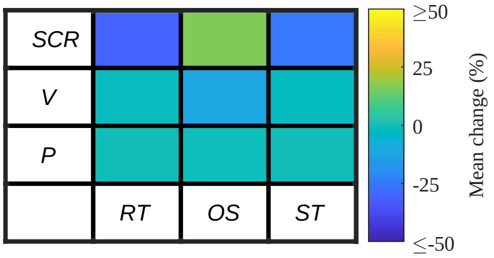

Figure 6-7 Mean change in GFM time-domain property ranges as Power (P), Voltage (V), and SCR vary.

RT experiences a small decrease as voltage increases. Despite the small magnitude of this average change (-1.1 %), the boundary acceptable GFM RT for $SCR = 3$ means that the minor decrease allows the property to become acceptable in high-voltage conditions during the voltage-control parametric sweeps, as shown in Figure 6-6. OS experiences a larger decrease as voltage increases.

The most significant relationship between the GFM's inertial properties and operating condition are observed for SCR. RT and ST decrease significantly (speed up) as SCR increases (grid strengthens), while OS increases. Neither OS nor ST break the relevant time-domain specifications in any grid-strength conditions, however, extreme low ζ_{VSM} settings combine with undesirable operating conditions to drive these inertial properties to approach the limits of the representative industrial inertial acceptability criteria. For low ζ_{VSM} settings, OS approaches 51 % on high SCRs and ST exceeds 1.1 s on low SCRs. On the very weak grid the GFM RT is slow, so requires a very low ζ_{VSM} to qualify as "useful" IR according to the industrial criteria, but is sped up and therefore meets the specifications across a wider range of ζ_{VSM} settings as the grid strengthens.

6.5.2. Grid-following control

The maximum change experienced by the GFL on a $SCR = 3$ grid during each parallel-control parametric sweep is pictured in Figure 6-8. The GFL's IR properties all exhibit a clear and strong dependence on the inertial-filter time-constant, where its inverse is labelled ω_{IR}. Each inertial property exhibits $|\Delta diff| \geq 100\ \%$ throughout the filter time-constant sweep for all power and voltage conditions. As the filter time-constant decreases (ω_{IR} increases) the RT decreases, the OS increases, and the ST decreases. The filter time-constant also has a significant impact on the stability of the GFL. The fastest filter time-constant that ensures a stable response across all of the simulation conditions is $\tau_{IR} = 0.155\ s$. Therefore, to achieve meaningful and comparable results in all conditions, this was chosen as the base setting for all of the other parallel-control parametric sweeps.

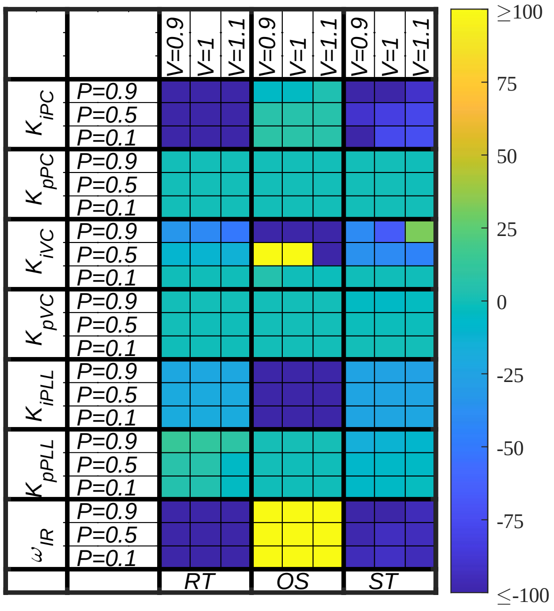

Figure 6-8 Maximum change of time-domain properties during GFL parallel-control parametric sweeps across different operating points on SCR=3 grid.

The GFL's inertial properties also show high dependence on some of the remaining parallel-control parameters. OS is shown to decrease with K_{iPLL} and K_{iVC} (although outliers skew colour coding for low voltage conditions). K_{iPC} is shown to have a large impact on RT and ST, both of which decrease significantly as K_{iPC} increases.

The acceptability of the GFL's inertial properties with respect to the representative industrial inertial criteria detailed in Section 6.4.1 are pictured in Figure 6-9 (for

$SCR = 3$). The GFL is always capable of meeting the OS and ST requirements throughout all of the parallel-control parametric sweeps on the $SCR = 3$ grid.

The GFL's RT can also be tuned to meet the acceptability criteria during the inertial-filter time-constant sweep due to its large impact on the time-domain properties. However, the remaining parallel-control sweeps are never able to meet the RT specifications due to the use of the slower base setting $\tau_{IR} = 0.155\ s$.

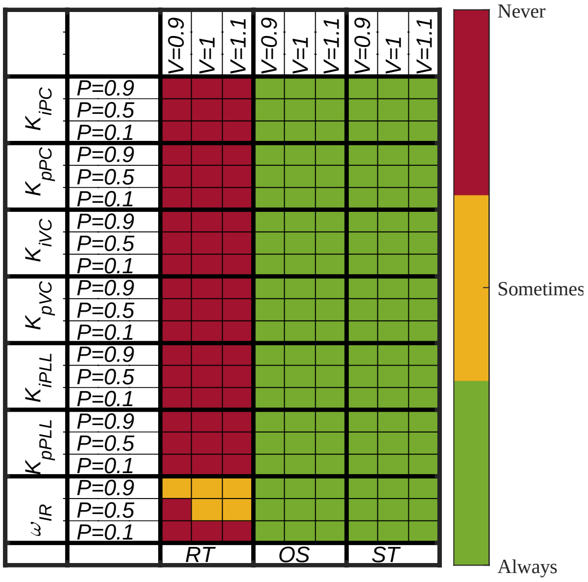

Figure 6-9 Acceptability of time-domain properties (with respect to the criteria defined in Section 5) during GFL parallel-control parametric sweeps across different operating points on SCR=3 grid.

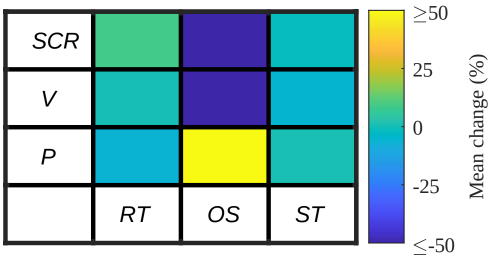

Figure 6-10 Mean change in GFL time-domain property ranges as Power (P), Voltage (V), and SCR vary.

The mean change in inertial property ranges as the operating conditions vary are pictured for the GFL in Figure 6-10. The average RT range increases by 9.2 % for each increase in SCR, inverse to the change experienced by the GFM. ST experiences minor increases with power and SCR. The GFL's inertial OS exhibits the largest dependence on all of the operating conditions, recording mean range changes an order of magnitude larger than any recorded for the GFM. The OS increases as power increases but decreases with voltage and SCR.

6.5.3. Optimal control settings

An optimal inertial tuning configuration for each controller is defined in Table 6-3 for each SCR using the findings of the sections above. An "optimal" configuration is one that minimises as many of the critical IR features detailed in the industrial specifications as possible. RT is prioritised as it is the feature that most commonly exceeds its acceptable threshold. The inertia constant is kept at $H = 2\ s$. Figure 6-11 compares the IRs of the optimally tuned controllers and Table 6-3 details the response's properties relating to the inertial criteria.

Table 6-3 Optimal parallel-control tuning on different grid strengths.

	$\boldsymbol{SCR}$	1.5	3	5
GFM	ζ_{VSM}	0.2	0.4	0.4
GFL	$\tau_{IR}\ (s)$	0.153	0.070	0.060
	K_{iPLL}	2.0	99.2	222.1
	K_{iPC}	1	1	1
	K_{iUC}	229.8	2316.8	1577.9

The inertial properties provided by the GFL are determined by its stability. On the very weak grid the controller is less capable of supporting aggressive tuning (particularly, small inertial-filter time-constants) so the RT is slowed. Therefore, the GFL is incapable of providing acceptable IR according to the industrial criteria when $SCR = 1.5$. However, as the grid strengthens the controller stabilises, can be tuned more aggressively, and achieves fast inertial RTs.

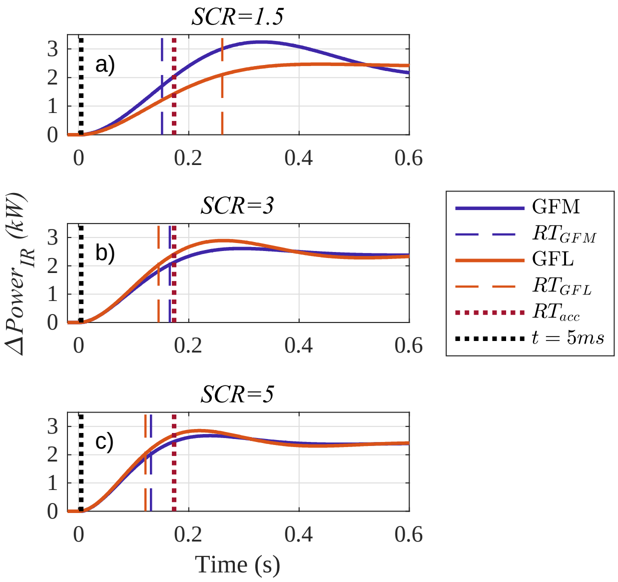

Figure 6-11 Comparison of optimally tuned GFM and GFL controllers' inertial responses during a frequency ramp on different SCR grids for P=0.5 and V=1.

Table 6-4 Optimally tuned GFM and GFL inertial time- and frequency-domain features on different grid SCRs.

$\boldsymbol{SCR}$	1.5		3		5	
Control	GFM	GFL	GFM	GFL	GFM	GFL
$\boldsymbol{RT}$ $(\boldsymbol{s})$	0.15	0.26	0.17	0.14	0.13	0.11
$\boldsymbol{OS}$ (%)	36.3	2.6	9.3	14.4	11.8	10.6
$\boldsymbol{ST}$ $(\boldsymbol{s})$	1.12	0.51	0.44	0.39	0.37	0.31
$\boldsymbol{\omega_n}$ $(\boldsymbol{rad/s})$	10.2	10.6	12.9	14.6	16.1	18.2
$\boldsymbol{\zeta_{app}}$	0.32	0.65	0.64	0.54	0.57	0.62

The GFM is stable across all of the SCRs. Therefore, the GFM can be tuned aggressively to continue to meet the inertial criteria on the very weak grid, where its RT is otherwise slowed. However, this tuning results in a decrease in the GFM's damping and costs a large degradation in OS and ST. To conserve the damping and associated OS and ST, the GFM is not tuned as aggressively on grids with $SCR > 1.5$. As a result, the corresponding optimally tuned GFLs provide faster IR. Neither controller shows the ability to ramp up to any significant power output within the 5 ms period following the frequency disturbance (shown as the black dotted line in Figure 6-11) in any of their configurations.

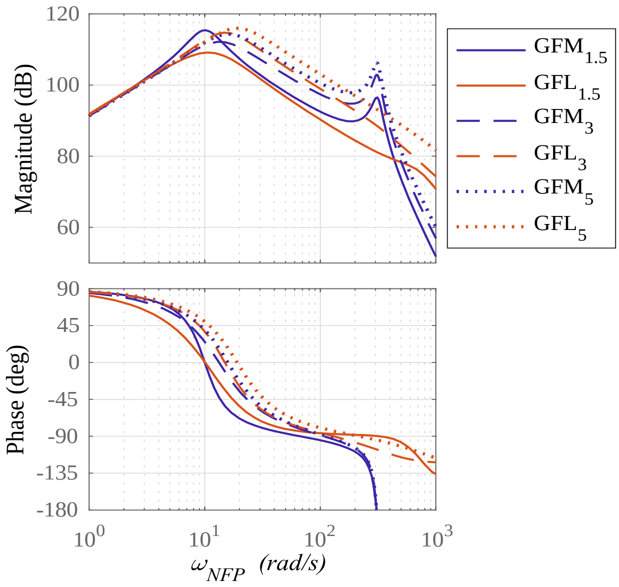

Figure 6-12 Comparison of NFP (bode plot from grid frequency to power output) of optimally tuned GFM and GFL controllers on different SCRs (indicated by subscript).

Figure 6-12 compares the NFP plots of the optimally tuned controllers on each SCR and Table 6-4 includes the additional frequency-domain metrics derived from the plots. The NFP plots do not depict any clear difference between GFM and GFL IR. However, the NFP plots do help to describe the driver of the change in inertial delivery speed as SCR varies. The NFP plots show the decrease of both converter's natural frequencies ω_n as SCR decreases, which can be described by (137) and (138), and the increase in the coupling impedance X_L. The decrease of ω_n means that on weak grids the phase is less sustained at high frequencies driving a slower response time.

6.5.4. Inertial constant sweep

Parametric sweeps are carried out for both controllers to assess how wide a range of inertia constants can be supported by the tuning configurations that are deemed to be acceptable by the industrial inertia criteria. The sweeps also highlight the change in time-domain properties as the inertia varies. The GFL is tuned with an inertial-filter time-constant $\tau_{IR} = 0.1\ s$, which is the lowest burden configuration that achieves an acceptable RT on the $SCR = 3$ grid. The GFM is tuned with a damping coefficient $\zeta_{VSM} = 0.4$, which is chosen as a comparable tuning as the GFL's configuration.

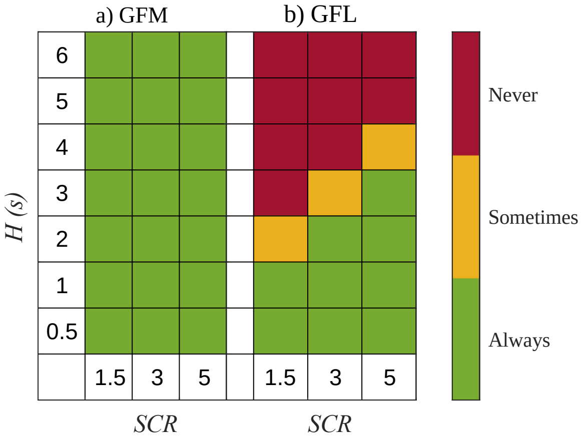

H (s)	a) GFM 1.5	a) GFM 3	a) GFM 5	b) GFL 1.5	b) GFL 3	b) GFL 5
6	🟩	🟩	🟩	🟥	🟥	🟥
5	🟩	🟩	🟩	🟥	🟥	🟥
4	🟩	🟩	🟩	🟥	🟥	🟧
3	🟩	🟩	🟩	🟥	🟧	🟩
2	🟩	🟩	🟩	🟧	🟩	🟩
1	🟩	🟩	🟩	🟩	🟩	🟩
0.5	🟩	🟩	🟩	🟩	🟩	🟩

Figure 6-13 Stability of an acceptably tuned a) GFM and b) GFL to support inertial constants, either always, sometimes, or never across the tested range of power and voltage grids on different SCRs.

Figure 6-13 exhibits the stability of the two controllers as the inertia constant is increased. The figure is coloured to show if the controller is either: always (green), sometimes (amber), or never (red) stable for the range of tested power and voltage conditions. The GFM is always stable across all of the power and voltage conditions for all of the inertia constants. The GFL is only stable for small inertia constants and this range is reduced as the grid weakens; the maximum stable setting reduces from $H = 4\ s$ to $H = 2\ s$ as the grid weakens from $SCR = 5$ to $SCR = 1.5$.

The controllers' (stable) time-domain properties during the inertia constant sweep are pictured in Figure 6-14. The GFM exhibits a roughly linear increase in RT and ST and an exponential decrease in OS as H increases. The GFL exhibits a largely constant RT, a similar linear change in ST as the GFM, and an increase in OS as H increases.

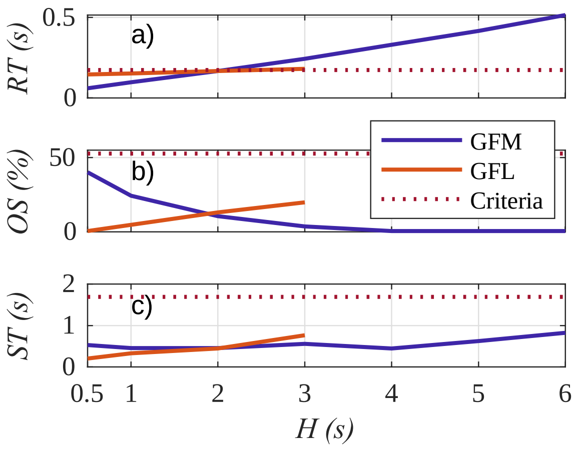

Figure 6-14 Comparison of inertial properties a) rise time (RT), b) overshoot (OS), and c) settling time (ST) during the inertial constant sweep for a GFM and GFL when P=0.5, V=1, and SCR=3.

6.5.5. Validation of inertial properties and impact on system frequency

The optimal tuning configurations are implemented for both aggregated converter stations on each SCR of the adapted multi-bus power system. The impact that each controllers' configuration has on the system's ability to contain a frequency excursion in response to a load power step is assessed and the system signals are pictured in Figure 6-15. The figure excludes the system initialisation period from t=0 to 40 s. On the weak $SCR = 1.5$ grid the less aggressively tuned GFL reaches its inertial peak ($RT = 0.15\ s$) slower than the GFM ($RT = 0.10\ s$) (Figure 6-15 c)). As a result, from $0.05\ s$ to $0.3\ s$ following the disturbance, the GFL system's ROCOF is more negative, frequency signal dips slightly lower, and SMs are required to deliver more power compared to the GFM system (Figure 6-15 a), b), and d) and Table 6-5).

On the $SCR \geq 3$ grids, both the GFM and GFL controllers achieve similar inertial deliveries, however, both controllers' peaks are masked by a growing transient injection (Figure 6-15 g) and k) and Table 6-5). The inertial peaks appear to be distinct from the faster transient injections that likely result from an angular jump, similar to the voltage-source phase response properties described in Section 2.2.1, and not from a ROCOF. Although hard to identify, the inertial peaks are measured $< 0.20\ s$, which agrees with the infinite bus simulations that showed inertial $RT \geq 0.14\ s$.

Table 6-5 Power system features on different grid SCRs when support is provided by either the optimally tuned GFM or the optimally tuned GFL (where times features are measured since the disturbance at t=21 s).

SCR	1.5		3		5	
Control	GFM	GFL	GFM	GFL	GFM	GFL
Transient injection $(\boldsymbol{PU})$	0.063	0.052	0.085	0.083	0.102	0.119
$\boldsymbol{RT}$ $(\boldsymbol{s})$	<0.10	0.15	<0.20	<0.20	<0.18	<0.15
Min $\boldsymbol{ROCOF}$	-	-	-	-	-	-
$(\boldsymbol{Hz/s})$	0.657	0.733	0.574	0.605	0.559	0.530
Min $\boldsymbol{ROCOF}$ **time** $(\boldsymbol{s})$	41.02	41.02	41.03	41.01	41.14	41.20

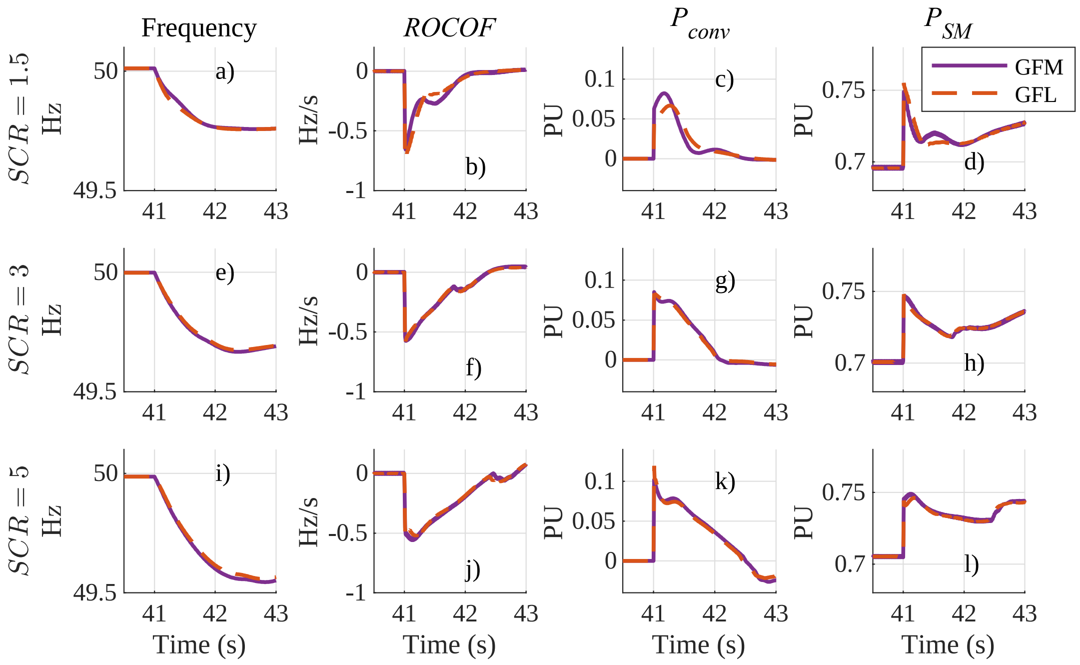

Figure 6-15 Power system signals following a load step equal to 5% of the system's generating power capacity on different SCRs when either the optimally tuned GFM or the optimally tuned GFL provide support to the grid. Subplots a), e), and i) show the frequency of a SM near the load disturbance, b), f), and j) show the corresponding ROCOF, c), g), and k) show the active power output by whichever converter is supporting the grid P_{conv}*, and d), h), and l) show the SM's power output* P_{SM}.

On the grids where $SCR \leq 3$, the minimum ROCOF is recorded for both GFM and GFL controller systems during the first $0.03\ s$ following the disturbance (Table 6-5). The minimum ROCOF occurs before either controller ramps up to any significant inertial output but is more aligned with the timescales that the transient injections occur on. This suggests that, on these grids, the IR is not the critical feature that constrains the worst ROCOF. Instead, the transient injections appear to determine the critical ROCOFs. This theory is supported by the observed improvement in the minimum ROCOF as the transient injection increases (Table 6-5). In fact, on the $SCR = 5$ grid, both controllers' transient injections are much larger and the minimum ROCOF occurs much later, indicating a shift to a dependence on the IR to limit the (already initially better contained) ROCOF.

Irrespective of the determining feature, the GFL is shown to: 1) provide sufficiently fast IR on $SCR \geq 3$ that contains the ROCOF as well as a GFM between $0.05\ s$ and $0.3\ s$ following the disturbance and 2) also provide an equivalent transient injection that is as effective as the GFM at containing the ROCOF within the first instances ($t < 0.05\ s$) following the disturbance.

6.6. Discussion

SOs use the swing equation (6) to describe inertial power responses to ROCOFs on the grid [9], [10], [11]. The converters' responses to pure ROCOF events on the infinite bus system clearly show that neither the GFM nor the GFL provide IR instantaneously. Specifications that expect GFMs to provide IR instantaneously (or within 5 ms) [18], [56] may have confused IR with the voltage-source transient phase response properties detailed in (3). This expectation of inertial delivery on short timescales could hinder the ability to develop and standardise system stabilising solutions.

GFL IR is conventionally disqualified from "true" status (and hence consideration for service procurement) due to the frequency measurement delay that is perceived to degrade its usefulness [32], [57]. However, the delay appears to have been observed when the GFL uses a slow averaging window-based ROCOF measurement [54]. The GFL in this paper, which uses a different Laplace-domain filtered-derivative, has been shown to be able to meet the critical delivery periods defined by the industrial criteria on grids with $SCR \geq 3$ (and even beat optimally tuned GFM alternatives). The stability, and not the delivery speed, is identified as the distinctive feature of the GFL IR, where the controller struggles to support fast inertial-filter time-constants on very weak grids. A similar range of stable GFL inertial tuning configurations was experimentally validated in [135], supporting the conclusion that fast IR can be provided from GFLs without sacrificing an acceptable level of oscillations from the frequency derivative mechanism. Advanced GFL control strategies can also be developed to mitigate their instability on weak grids [55].

The proof that these optimally tuned GFLs are equally capable at containing the grid frequency as some GFMs opposes the findings in [30], which failed to account for the full capability of the GFL, and supports the inclusion of GFLs in inertial services on stronger grids. This inclusion would increase the availability of frequency stabilising solutions and could enhance the uptake of converter-based solutions due to the increased confidence surrounding GFL's effective current limitation and the simple control adaptation. Of course, specific inertial dynamics may vary with different control (both GFM and GFL) configurations, but these results have highlighted that useful IR is not unique to GFMs.

The time-domain specifications being used by SOs to qualify IR could be used in their current state (so long as they properly reflect realistic IR timescales) as this paper has confirmed that the provision of faster IR can better contain ROCOF after the initial instances of the disturbance (and that both useful controllers can qualify according to this criterion). However, the industrial specifications may be flawed due to the intrinsic link between inertia constant, delivery speed, and nadir time. The RT criterion was integrated into this paper from the specifications to capture the critical nature of useful inertial provision before the frequency nadir [30]. It could be difficult for a SO to establish a meaningful critical delivery period to qualify new supporting devices if the critical period (nadir time) depends on the efficacy of the inertial provision from the new devices themselves.

A reliable approach needs to be developed to ensure that if the time domain criteria are used the corresponding tests and qualifying thresholds are sufficient to ensure acceptable inertial provision in all of the expected operating conditions. Equally, the time-domain property based specification encourages low damping responses to achieve the critical delivery speed criterion, which is a particular problem on weak grids where issues associated with current and voltage oscillations and interactions between devices are already a key issue [10].

The power system simulations also highlighted the importance of transient injections for the initial containment of the ROCOF, resembling the voltage-source transient phase response described by (3). The results agree with [140] that highlighted the importance of synchronising torque and voltage-source behaviour for frequency stability and [141] that conveys the distinction of these voltage-source features from IR. An additional interesting implication is that the transient phase response may be more critical on weaker grids where the synchronising torque is reduced by the larger impedance (138).

A final complication is the apparent provision of voltage-source properties by the GFL with inertial capability exhibited by the instantaneous power injections on the multi-bus power system model. Theoretically, GFL converters are operated as current sources so should not provide power instantly in response to grid disturbances, however, the added inertial capability introduces a coupling between the GFL’s power output and the grid angle that is thought to drive the transient phase response. This suggests that certain GFL configurations are capable of providing transient grid-stabilising injections that are also conventionally assumed to be a unique feature of GFMs.

Further work needs to be carried out to explore the ability of converters to provide voltage-source properties irrespective of their controls and to consider the impact that current limiters will have on the feasibility of their grid stabilisation, which will affect both converters (due to their equally strict thermal limits). System-wide considerations may need to be made to ensure sufficient synchronising forces related to the transient phase responses are present to stabilise the voltage angle on future converter-dominated grids. It will also be important to validate that the same transient phase phenomena are observed on experimental and real-world converter configurations, despite this exemplification of their fundamental features.

6.7. **Conclusions**

This study has been developed to improve the transparency of the provision of frequency stabilising solutions from converters. The blanket disqualification of grid-following (GFL) inertial response (IR) due to a perceived slow response in industrial specifications is found to have stemmed from a combination of limited tests of GFL control configurations and the confusion of qualifying IR features with the voltage-source transient phase response. A theoretical discussion highlights the distinction between the two response types and their properties.

Parametric sweeps on an infinite bus model are used to substantiate the features of the IR and assess the ability of an example grid-forming (GFM) and GFL controller to meet the criteria used in the industry. The claim that IR is instant in some industrial specifications is proven to be wrong. The GFL is less stable than the GFM on weak grids but its IR can be tuned to meet the industrial criteria on stronger grids, including the critical delivery speed requirement.

Multi-bus power system simulations test the optimal configurations of the controllers that best meet the criteria, validating the time-domain features of the example GFM and GFL IRs on a more realistic system, and confirming that there are no hidden features of the GFM IR that better stabilises the system frequency.

The existing industrial time-domain approach to qualify useful IR can continue to be used but needs to be updated to accurately represent inertial (and not voltage-source related transient) timescales and allow at least the consideration of GFL solutions. One flaw in the time-domain approach is the interdependence of the critical inertial delivery speed criterion and the nadir time, which needs to be considered when establishing the qualifying procedure.

The results also highlight the importance of the transient phase response to limit the initial frequency excursion. The voltage-source behaviour was particularly critical for frequency containment on weak grids. It is suggested that SOs should consider and specify the need for the transient phase response for the initial containment of the frequency more explicitly in future grid code requirements. However, more work needs to be carried out in this field to understand the critical characteristics of the phenomenon.

Inertial response may not be the optimal approach to stabilise a converter dominated system, however, it currently appears to be necessary to support the transition towards net-zero operation while SMs continue to operate on our networks. The assessed GFL IR is not suggested to be superior to any or all GFM IRs, however, recognising that useful inertial response is not unique to GFMs and allowing the consideration of all appropriate solutions could support a more effective transition, where GFMs will be needed to support the grid in many other ways.

Chapter 7. The measurement of inertial response from wind turbines

7.1. Introduction

Inertia measurement and monitoring are critical tools to support the increased penetration of converter interfaced devices. On a system-wide scale, accurate monitoring of online inertia can inform SOs of the security of the system to withstand a given probabilistic range of power disturbances and allow them to take preventative actions [105]. On a device-scale, inertial measurement (and general performance monitoring) is important to increase the transparency surrounding the implementation of new stability sources whose dynamic behaviour may not be consistent and/ or fully understood [32]. This device-scale application is the main objective of the following chapter. The methods may be suitable to extended for the system-scale application, however, this is outside the scope of this thesis.

Measurement and monitoring methods have been developed for inertial provision from WTs [27], [114]–[116] but several of the methods disagree on fundamental aspects of the provision and the most accurate approach has not yet been confirmed. Findings from the ScottishPower Renewables (SPR) GFM WF experiment in 2019 suggests that the variation of the wind has a significant impact on the inertial power injection [70]. Despite these findings, some approaches in the literature neglect the impact of the wind on the inertial power during the measurement [27], [114], [115]. The International Electrotechnical Commission (IEC) Standard for WT inertia measurement does account for the wind's impact, but is poorly described and may not account for the wind's impact effectively [116]. These inaccuracies are continued in online inertia monitoring tools that also struggle to accurately account for WT provisions [99], [106], [110].

This chapter aims to validate the findings of the SPR GFM WF experiment to find out if the wind impacts WT inertial power and to assess the accuracy of two approaches to measure their inertial response. Two proposals are made to improve the measurement accuracy and better enable the integration of inertial response from WTs.

7.1.1. WT inertial response measurement approaches

SM inertia measurement approaches can relate the power injected to the grid with the maximum rate of change of frequency (ROCOF) during a disturbance $\dot{\omega}_{max}$ to find the inertial contribution (inertial constant H) of a single or group of SMs using (141) [108], [142]. Generally, these approaches assume that the mechanical input of the SM does not vary during the short period of the frequency disturbance, due to the longer time-constant associated with ramping the machine up, so the inertial power injection ΔP_{IR} can be identified as any power change during the event.

$$H = \frac{\Delta P_{IR}\omega_0}{2S_n\dot{\omega}_{max}} \tag{141}$$

Where S_n is the rated power of the WT and ω_0 is the base grid frequency. Initial proposals of WT inertia measurement carried these assumptions forwards; the methods assume that the WT's electrical system responds significantly faster to the disturbance than the variation of the mechanical system so do not account for power variations on this short timescale due to the variation of the wind [27], [115]. Although some differences exist between the identification functions that each approach uses to pre-process the power and frequency signals, both effectively measure an electrical power change from the initial power at the onset of the frequency disturbance to the maximum during the disturbance at the terminals of the WT. This power change is the inertial power ΔP_{IR} that can be used with the maximum recorded ROCOF in (141) to find the equivalent inertial contribution of the WT in the same way as a SM. The accuracy of this method will be assessed throughout this chapter, and will be referred to as the Initial Power Method hereon. If the wind's variation does impact the inertial power injection of a WT, as suggested by the data from the SPR GFM WF experiment, the Initial Power Method may not be able to accurately measure a WT's inertia provision.

Recently, the IEC Standard 61400-21-1:2019 was developed, which describes the standard industrial approach to measure and qualify inertial capability of WTs connecting to the grid [116]. Again, the inertial response is measured using power and frequency measurements at the terminals of the WT, however, the Standard also proposes the use of a baseline to account for the wind's impact on the WT power output. This method will be referred to as the IEC Standard Method hereon.

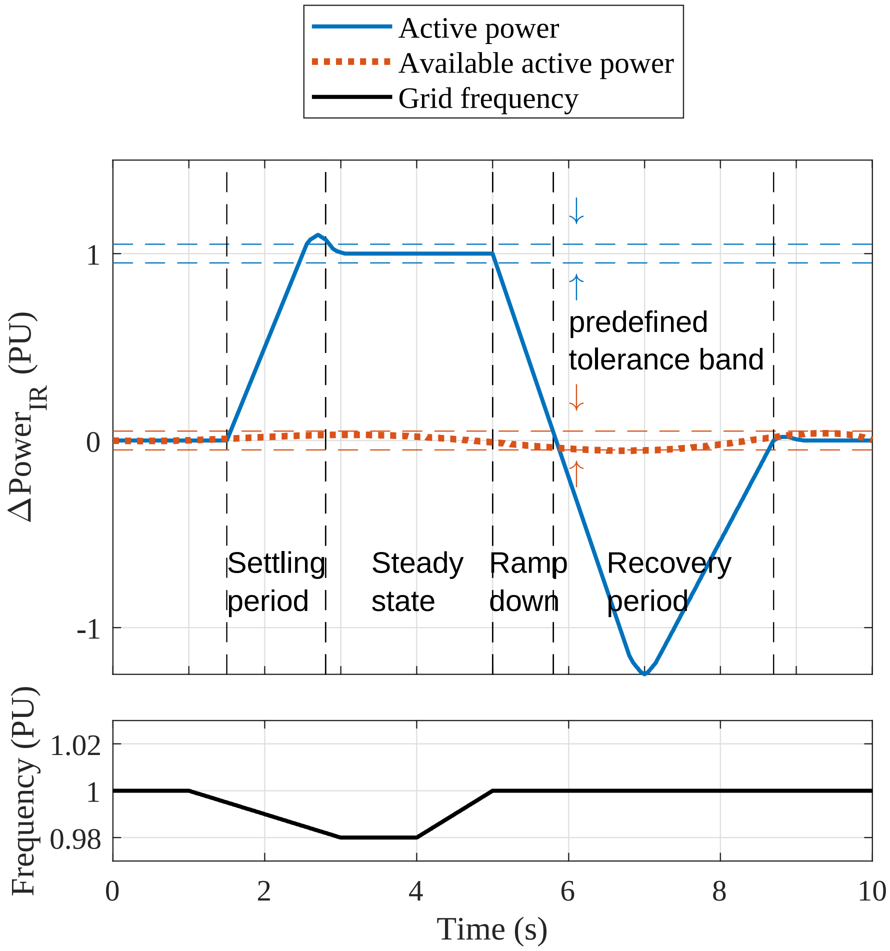

Figure 7-1 Standard IEC WT inertia test methodology, reconstructed from [116]. The power and frequency signals, inertial power bands, and operating time periods are included.

The Standard IEC Method requires the measurement of three signals from five seconds before to five seconds after a grid frequency disturbance: the power injected to the grid at the terminals of the WT, the WT's Available Active Power (using a wind speed measurement), and the grid frequency at the terminals of the WT [116]. The inertial power change $\Delta P_{IR,IEC}$ is described as the difference between the power injected to the grid and the Available Active Power, where the Available Active Power is thought to represent the power that would be output by the WT if the frequency disturbance hadn't occurred. The inertial constant can then be determined in the same way as the Initial Power Method using the rearranged Swing Equation (141), $\dot{\omega}_{max}$, and the new formulation of $\Delta P_{IR,IEC}$. Figure 7-1 depicts a recreation of the information in the Standard that describes the inertia measurement process.

Although the IEC Standard begins to account for the wind's impact on WT inertial response (as suggested to be necessary from the SPR GFM WF trial [70]) there are several issues with the approach. Firstly, there is no clear definition of the Available Active Power. The signal appears to be related to NG ESO's Power Available signal, which describes the maximum power that could be extracted from the rotor of a WT [143], and can also be derived from a wind speed measurement [144]:

$$P_{Avlb} = 0.5\rho\pi R^2 C_p(\lambda, \beta)\mathrm{u}^3 \tag{142}$$

Hereon, Power Available, as defined by (142), will be used in the place of the undefined Available Active Power.

The second issue associated with the Standard IEC Method is that the Power Available may not be an appropriate baseline to measure inertial response from. Power Available describes the power in the rotor of the WT. It is distinct from the power at the terminals of the WT due to the action of the mechanical and electrical systems between the two. Even if losses are accounted for, the timescales of the WT system (dominated by the physical inertia of the drivetrain) will slow the rate at which a change in Power Available can be translated to the power injected to the grid. Moreover, the power injected to the grid may vary according to higher level controls that can adjust WT output according to operating conditions. Therefore, although the Standard appears to account for the wind's impacts, the Power Available may not properly represent the baseline that the WT would output before the inertial response, so may not support accurate inertia measurement.

7.2. Findings from Dersalloch GFM WF experiment

Data from the ScottishPower Renewables (SPR) test of a grid-connected VSM at Dersalloch WF, using SiemensGamesa RE WTs, is shown in Figure 7-2 during two frequency disturbances. The experimental data is used here to highlight the impact of wind on inertial response by real WTs and how it impacts the accuracy of basic inertia measurement approaches. Full analysis of the experiment is detailed in [70]. The data includes the external signals that SPR use for a conventional inertial response measurement: the frequency and power at the PCC. The internal WF reference signal is also included.

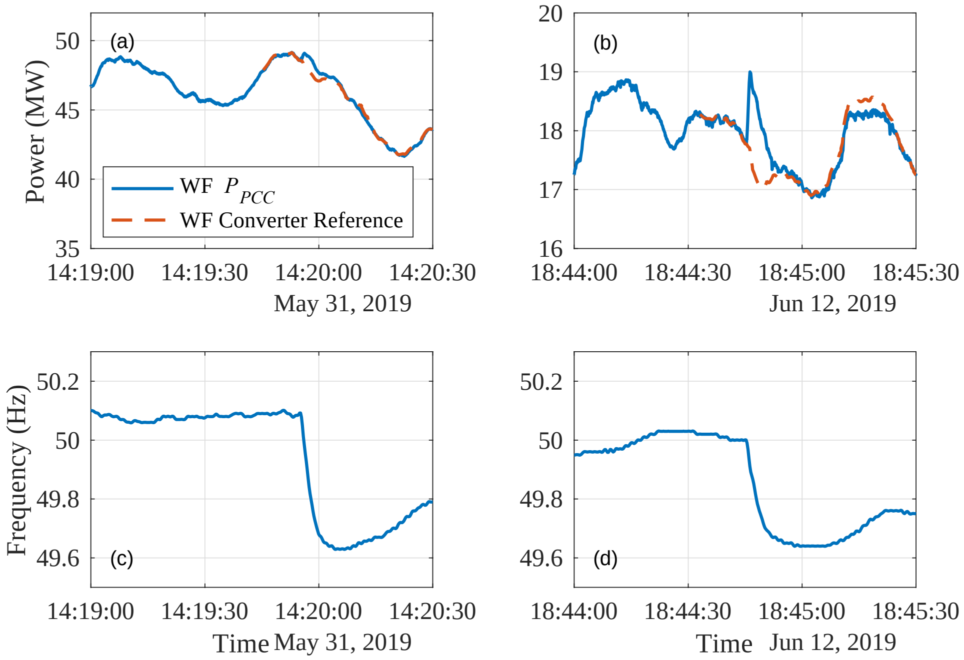

Figure 7-2 Dersalloch WF PCC power and reference power in response to two different frequency disturbances on a) the 31st of May and b) the 12th of June. The corresponding frequency excursions are shown in c) and d).

Both of the frequency disturbances pictured in Figure 7-2 are triggered by the tripping of the France-England Interconnector. On the 31st of May the WF is operating at a rated power of 69 MW with an equivalent inertial constant of $H = 4\,s$ when the interconnector trip drives a ROCOF of 0.11 Hz/s. On the 12th of June the WF is operating at a rated power of 60 MW with an equivalent inertial constant of $H = 7.5\ s$ and the interconnector trip drives a ROCOF of 0.08 Hz/s.

The WF power varies due to the wind's impact during both of the pictured operational periods. The changes occur on short timescales that coincide with the timescales of the inertial response.

The Initial Power Method, which is representative of the proposals in [27], [107], [108], [115], suggests that the inertial response could be measured as the difference between the initial and boosted PCC power. The SPR experimental data can be used to compare the power change observed on the grid with that expected from the WF. (78) calculates the expected inertial response ΔP_{exp} using the WF equivalent inertial constant H, rated power S_n, and synchronous speed ω_0, and the maximum ROCOF of the frequency event $\dot{\omega}_{max}$:

$$\Delta P_{exp} = \frac{2HS_n}{\omega_0}\dot{\omega}_{max} \tag{143}$$

The expected power changes calculated using (78) for each event are $\Delta P_{31/05,exp} = 1.21\ MW$ and $\Delta P_{12/06,exp} = 1.44\ MW$, respectively. The inertial power changes measured as the difference between the initial and boosted PCC power are $\Delta P_{31/05,PCC} = 0.54\ MW$ and $\Delta P_{12/06,PCC} = 1.21\ MW$. The measurement is incapable of resolving the inertial response, particularly for the event on the 31st of May that coincides with a severe wind decrease and hence total power decrease. The measurement inaccuracy on the 31st of May is also affected by the low inertial constant, which drives a response that is small compared to the wind driven changes.

Instead of using the initial PCC power, the converter reference could be used to represent the inertial baseline. Figure 7-2 shows the WF power reference for both events and highlights good tracking of the PCC power outside of the frequency disturbance, other than some discrepancies 15 to 30 seconds after each inertial response during the WT's speed recovery.

The inertial power changes measured as the average difference between the converter reference and the PCC power are $\Delta P_{31/05,ref} = 0.83\,MW$ and $\Delta P_{12/06,ref} = 1.34\,MW$. The measurement using the converter reference as the baseline gives power changes closer to the expected values but still contains considerable error for the event on the 31st of May. The discrepancy between the reference and the PCC power during the speed recovery after the frequency event suggests that the internal reference used here doesn't account for the impact of all of the (non-frequency dependent) operating conditions on the power output, which is insufficient to remove all of the error from the inertial response measurement.

7.3. Proposals to improve WT inertial response measurement

The following sections outline the proposed adaptations and novel measurement approaches to improve the measurement of inertial response by wind turbines by better accounting for the wind's impact. Section 7.3.1 proposes an adaptation to the Standard IEC method [116] that uses a different baseline to measure inertial power from. Section 7.3.2 proposes an alternate approach that utilises the same power and frequency signals as the method proposed in Section 7.3.1 but harnesses a system identification algorithm to increase the inertia measurement estimation accuracy.

7.3.1. Improvements to IEC industrial standard

To achieve accurate inertial response measurement the Standard IEC method that was introduced in Section 7.1.1 needs to use a baseline that is representative of the WT's steady state operation. Power Available is expected to be unable to resolve WT output on short timescales as it fails to account for the mechanical and electrical systems between the WT rotor and the PCC. The attempts to measure inertial response in Section 7.2 suggest that the initial PCC power is not an appropriate baseline either as it doesn't account for variations in the wind.

The Improved IEC Method is proposed, which uses the maximum power point tracking (MPPT) reference as the baseline for inertial response measurement. The MPPT reference is the power value that the WT attempts to track to achieve optimal operation [119]. The reference uses the rotor speed to determine the active power set-point so will account for any event that affects a turbine's steady-state operation. It should be noted that the MPPT reference is inspired by, but distinct from, the converter reference in Section 7.2, which didn't account for the adjusted power during the turbine speed recovery phase.

7.3.2. Equivalent Swing Method

The IEC methodology uses a simple difference of two averages to measure the inertial response. The Improved IEC Method may accurately measure inertial response using the MPPT baseline, however, if the reference is affected by improper tuning it could introduce error to the measurement. An alternative approach, the Equivalent Swing method, is proposed that derives the inertial constant from the dynamic properties of the inertial response and not just from the magnitude of the power change.

The Equivalent Swing method uses the same information as the Improved IEC Method: the frequency at the PCC and the inertial power change ΔP_{MPPT} (the difference between the PCC and MPPT powers). However, the measurements are input to a system identification algorithm to find the inertial constant.

A SG's PU inertial power output ΔP_{SG} in response to a grid frequency change input $\Delta \omega_g$ can be described by the transfer function $G_{SG}(s)$ (144), which is derived in full in Section 4.5.2.1.

$$G_{SG}(s) = \frac{\Delta P_{SG}(s)}{\Delta \omega_g(s)} = \frac{-K_s s - \frac{K_{\omega D}\omega_0 K_s}{2HS_n}}{s^2 + \frac{(K_{\omega D} + K_d)\omega_0}{2HS_n} s + \frac{K_s \omega_0}{2HS_n}} \tag{144}$$

K_d is the damping coefficient, K_s is the synchronising torque, ω_0 is the synchronous speed, and H is the inertial constant of the SG. The Equivalent Swing Method aims to identify the apparent synchronous inertial response that is provided to the grid by a WT by fitting the WT's response with the SG's dynamics in (144).

The measured grid frequency change $\Delta\omega_g$ and the WT's PU inertial power change ΔP_{MPPT} are fed as an input and output, respectively, to the MATLAB continuous-time transfer function estimation algorithm [145]. Both the power and frequency data streams are pre-processed to remove any offset before system identification. The system identification estimates a 2nd order transfer function $G_{est}(s)$ that describes this inertial response to a frequency disturbance:

$$G_{est}(s) = \frac{\Delta P_{MPPT}(s)}{\Delta\omega_g(s)} = \frac{As^2 + Bs + C}{Ds^2 + Es + F} \tag{145}$$

Coefficients A, B, C, D, E, and F are the estimated parameters that represent the measured WT system. The estimated parameters in $G_{est}(s)$ can be equated to the physical parameters they represent in $G_{SG}(s)$ e.g. $F = \frac{K_s\omega_0}{2HS_n}$.

Parameter B is an estimate of the negative synchronising torque that can be used with parameter F (and the known synchronous speed and rated power) to estimate the inertial constant H_{est}:

$$H_{est} = \frac{K_s\omega_0}{2S_nF} = -\frac{B\omega_0}{2S_nF} \tag{6}$$

7.4. Sensitivity analysis

A sensitivity analysis is carried out to find the accuracy of the reviewed and proposed inertial response measurement methods (from Sections 7.1.1 and 7.3, respectively) throughout wind variations. The methods are also assessed to ensure that they are robust for different frequency events and inertial constant settings. The inertial response is measured using the power and frequency signals that are output by a model of a type four WT with a GFM controller (detailed in Chapter 4 and pictured in Figure 7-3) that is subject to coincident wind and frequency disturbances. The model parameters are shown in Table 7-1. The accuracy of the methods throughout the sensitivity scenarios are defined relative to the inertial constant set in the model's control. The methods under assessment are detailed in Section 7.4.1 and the sensitivity scenarios are described in Section 7.4.2.

Table 7-1 Model wind turbine, electrical, and control parameters.

Wind Turbine		**Electrical**	
R	$43.5\ (m)$	SCR	10
ρ	$1.225\ (kg/m^3)$	$V_n = V_0$	$690\ (V)$
J_T	$1.3 * 10^7\ (kg\ m^2)$	Z_n	$0.1\ (\Omega)$
J_G	$1.4 * 10^6\ (kg\ m^2)$	S_n	$3\ (MW)$
p	$60\ (pairs)$	ω_0	$50\ (Hz)$
ψ	$22.3\ (Wb)$	X/R	10
$L_{sd} = L_{sq}$	$4\ (mH)$	C_f	$3\ (mF)$
R_s	$5.4\ (m\Omega)$	L_{f1}	$50.5\ (\mu H)$
c_1	1	R_f	$1.6\ (m\Omega)$
c_2	39.52	V_{DC}	$800\ (V)$
c_3	0	C_{DC}	$0.5\ (F)$
c_4	0	**Control**	
c_5	0	ζ	0.31
c_6	2.04		
c_7	14.47		
c_8	0		
c_9	0		

7.4.1. Measurement methods

Four measurement methods are subject to the sensitivity analysis. The first method is the Initial Power Method. This method is representative of the existing external information available for inertial response measurement and of the approximation made for the wind in some of the inertia estimators in the literature [27], [107], [108], [115]. The second measurement method is the Standard IEC Method, which measures the inertial response as the mean power change from the onset of the frequency disturbance to the nadir between the PCC power and the Power Available baseline.

Power Available is calculated using (142). The third method is the Improved IEC Method, which uses the mean MPPT reference during the frequency event as the baseline, as proposed in Section 7.3.1. Finally, the Equivalent Swing Method, proposed in Section 7.3.2, is subject to the sensitivity analysis.

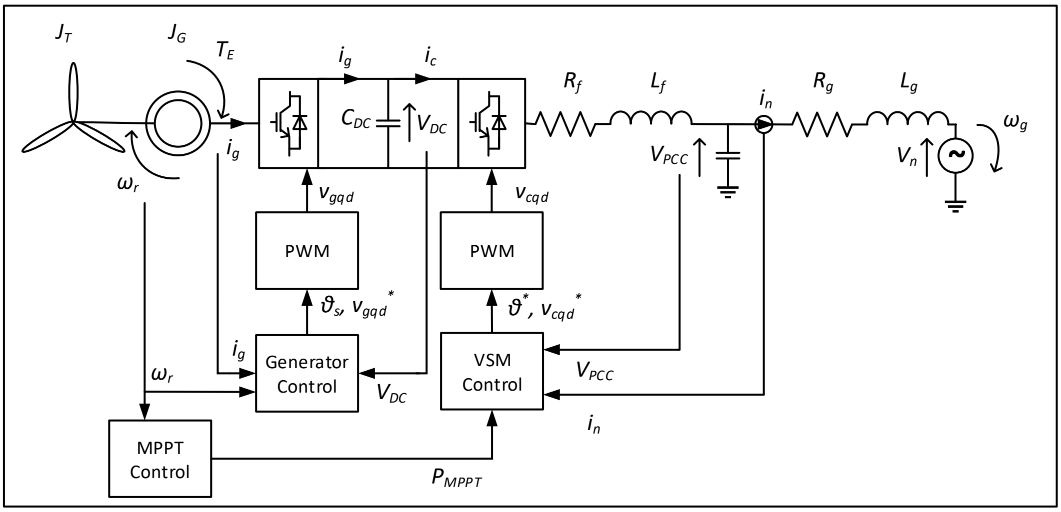

Figure 7-3 Electromechanical model of PMSG WT connected to the Thevenin Equivalent representation of the grid. The converter control blocks are also included. The constant parameter values are detailed in Table 7-1.

7.4.2. Sensitivity scenarios

The sensitivity scenarios are grouped according to frequency, wind, and inertial constant settings. Frequency and wind scenario labels (FX and UX, respectively) refer to a specific magnitude and rate of change of disturbance while inertial constant scenario labels (HX) simply refer to the equivalent inertial constant.

Table 7-2 Frequency disturbance sensitivity scenarios.

Event	**Deviation (Hz)**	**ROCOF (Hz/s)**
F1	0.1	0.1
F2	1	0.5
F3	5	0.5
F4	1	2.5
F5	5	2.5

Table 7-3 Wind disturbance sensitivity scenarios. Multiple wind scenarios are grouped according to the rate of change of wind speed.

Event	**Deviation (m/s)**	**Rate (m/s^2)**
U1	0	0
U2 to U5	[1 2.2 2.6 3]	0.5
U6 to U9	[1 2.2 2.6 3]	1
U10 to U13	[1 2.2 2.6 3]	1.5
U14 to U17	$[-1\ -2.2\ -2.6\ -3]$	-0.5
U18 to U21	$[-1\ -2.2\ -2.6\ -3]$	-1
U22 to U25	$[-1\ -2.2\ -2.6\ -3]$	-1.5

All of the frequency disturbances, which initiate at t=4 s, are shown in Table 7-2. The magnitude of the frequency change scenarios are: 0.1 Hz (representing a small deviation), 1 Hz (representing the maximum permissible steady state frequency deviation for European Grid operators [146]), and 5 Hz (representing a large deviation considered in the ENTSO-E document describing future grid needs [147]). The ROCOF of the frequency disturbance scenarios are: 0.1 Hz/s (representing a low ROCOF), 0.5 Hz/s (representing a threshold that activates Loss-of-Mains protection relays [148]), and 2.5 Hz/s (also derived from the ENTSO-E document describing future grid needs [147]).

Table 7-4 Equivalent inertia constant sensitivity scenarios.

Configuration	**Inertial constant (s)**
H1	1
H2	2
H3	3

Wind speed is constant at $u = 8.5\ m/s$ until a disturbance is forced at $t = 2\ s$. The wind speed is kept below rated speed as the study is interested in the variation of power with wind. A wind step-up or step-down Δu is applied, equivalent to the maximum 20 second gust speed for each of the IEC's turbulent wind classes [149], as defined by (146) from [144]).

$$\Delta u = u_{mean}\left(1 + \left[1 + I0.42\ln\left(\frac{3600}{T_G}\right)\right]\right) \tag{146}$$

u_{mean} is the average wind speed, I is the turbulence intensity, and T_G is the gust period. Constant and smaller wind steps are also applied to see the effects of less severe wind environments. All of the wind disturbances are detailed in Table 7-3.

Finally, the control parameters of the network side converter are varied. The VSM inertial constant is varied between three settings, all of which maintain stable converter operation but result in increasingly large inertial responses. The range of inertial constants are detailed in Table 7-4.

7.5. Results and analysis

The following section details the results of the sensitivity study described above. Section 7.5.1 analyses the impact that wind disturbances have on the inertial response of a wind turbine. Sections 7.5.2 and 7.5.3 assess the accuracy of the Standard IEC and Initial Power Methods to measure inertial response throughout the sensitivity study. Following this, the accuracy of the proposed measurement methods are detailed in Sections 7.5.4 (Improved IEC Method) and 7.5.5 (Equivalent Swing Method respectively). Section 7.5.6 overviews the sensitivity of all of the measurement methods to the properties of the frequency disturbance.

7.5.1. Impact of wind on inertial response

Figure 7-4 shows the Power Available for the WT (red line) and the corresponding PCC Power output (blue line) during three example scenarios. Each scenario is subject to frequency disturbance F2 and inertial constant H1 but different wind conditions: a) step-down (U25), b) constant (U1), and c) step-up (U13).

The PCC power differs during the varying wind conditions despite the constant frequency disturbance and inertial constant. This confirms the findings of the Dersalloch tests that inertial response is affected by the wind [70] and that it needs to be properly accounted for in the measurement methods.

The impact of the wind will affect the net inertial response on the grid. Consider an under-frequency event: the total power level will be reduced as the wind decreases (below rated speed) and the magnitude of the inertial response is diminished. Above rated, constant, or rising wind speeds will not reduce the net inertial power injected to the grid during under-frequency events, however, any upwards power variations will reduce the transparency of the inertial response if inaccurate measurement methods are used.

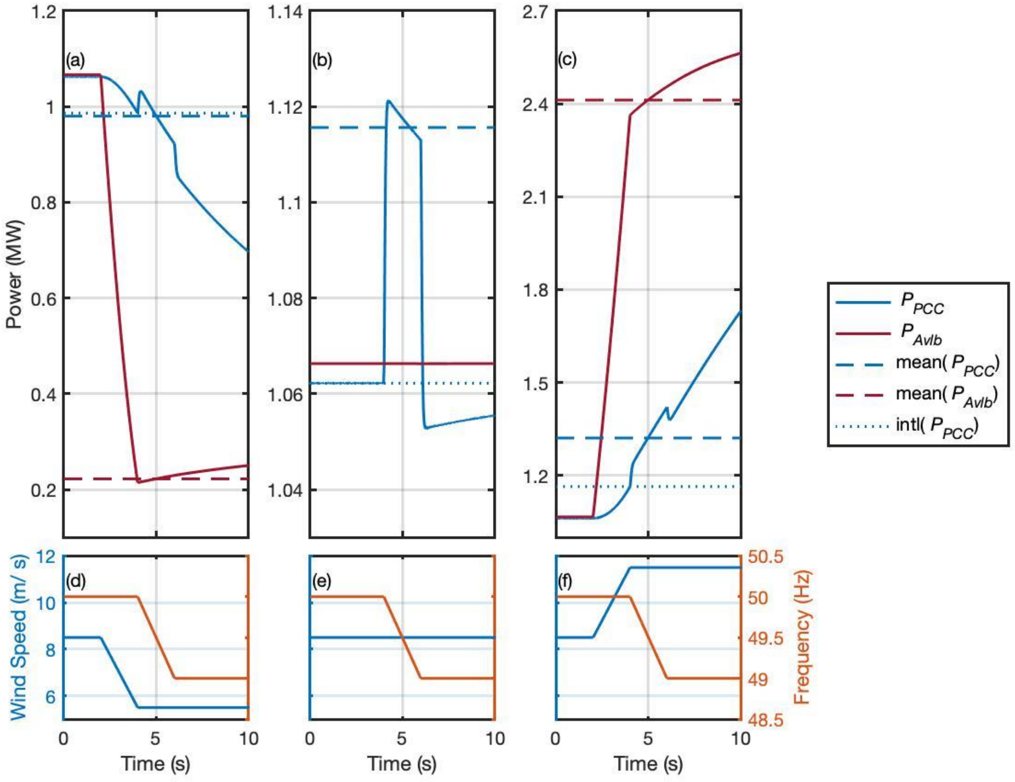

Figure 7-4 Power signals and their representative values used to carry out the Standard and Initial Power IEC Methods for a) step-down (U25), b) constant (U1), and c) step-up (U13) wind conditions. The inertial constant configuration is H1 and the frequency scenario is F2 for all of the pictured responses. The corresponding wind and frequency conditions are shown in subplots d), e), and f).

7.5.2. Standard IEC Method accuracy

The mean of the Power Available (red dash) and the PCC power (blue dash) during the frequency events (between t=4 to 6 s for the pictured frequency scenario F2) are also included in Figure 7-4. The two mean values represent the baseline and boosted inertial power values used in the Standard IEC Method.

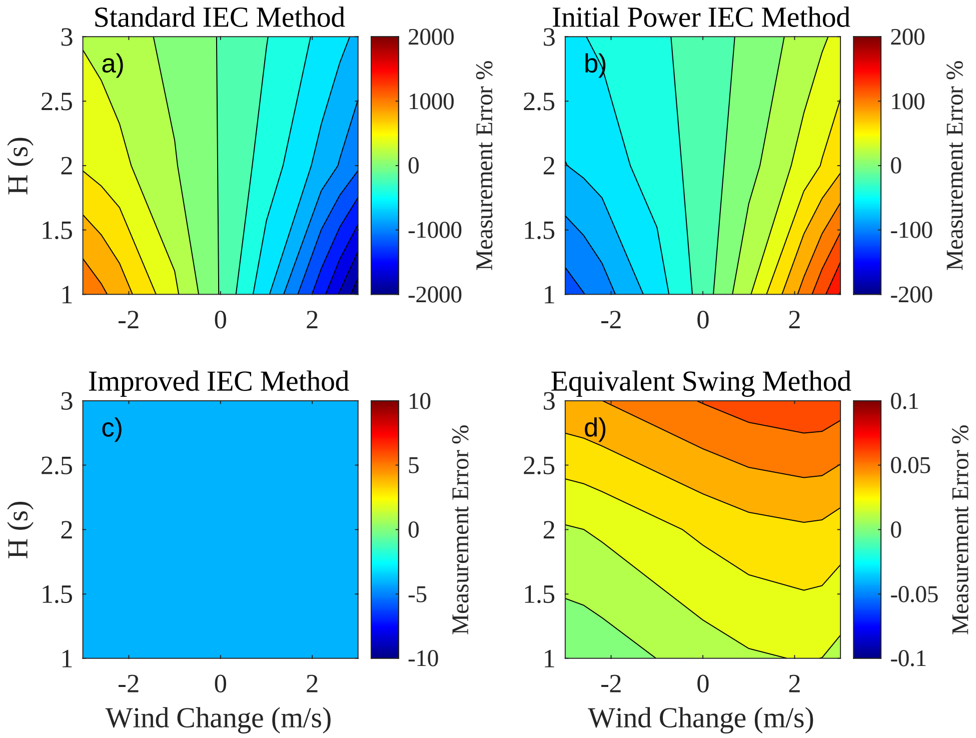

Figure 7-5 Inertia measurement error for frequency scenario F2 as the wind condition and inertia constant changes. Subplots exhibit the error for different methods: a) Standard IEC, b) Initial Power IEC, c) Improved IEC, and d) Equivalent Swing Methods.

Power Available is shown to overestimate the wind's impact on the WT baseline (Figure 7-4). The baseline changes instantaneously with the wind and at a greater rate than the PCC power. During the wind step-down this results in a low baseline and overestimation of the inertial response (Figure 7-4 a)). During the wind step-up this results in a high baseline and underestimation of the inertial response so that it appears to be negative (Figure 7-4 c)).

The Standard IEC Method remains unable to capture the WT dynamics fully even during constant wind speeds; the base power is overestimated by around 10 kWs (Figure 7-4 b)). The overestimation results from the inability of the Power Available to account for the transformation of the power in the wind to the electrical power injected to the PCC.

A particularly important feature of this process is the transformation of the WT's rotational kinetic energy (KE) into electrical energy during the inertial response. By removing KE the WT rotor is decelerated. As discussed in Sections 7.1 to 7.3 the WT operating point is determined by the rotor speed. The rotor deceleration will reduce the power baseline and, therefore, the total power injected to the PCC during the frequency event, irrespective of the constant wind. Power Available does not account for this baseline variation so the Standard IEC Method measures a reduced inertial response.

Table 7-5 Range of inertia measurement errors (%) for tested methods across the sensitivity scenarios.

Method	**Inertial constant measurement error (%)**		
	Minimum	**Average (absolute)**	**Maximum**
Standard IEC	-9800	830	6100
Initial Power	-420	87	740
Improved IEC	-17	6.2	-0.6
Equivalent Swing	-0.43	0.05	0.2

Table 7-5 shows the range of the inertial constant measurement errors (with respect to the inertial constant control setting) recorded throughout the sensitivity study using the Standard IEC Method. The inappropriate Power Available baseline results in inaccuracies approaching 10000 %. Figure 7-5 a) shows the Standard IEC Method error for frequency disturbance F2 as the wind and inertial constant scenarios vary. The measurement is most inaccurate when the inertial response coincides with extreme wind step-ups or step-downs. The inaccuracy translates to a larger percentage error for small power changes resulting from low inertial constants.

7.5.3. Initial Power Method accuracy

The Initial Power Method achieves better inertial response measurement for constant wind conditions using the initial PCC power as the baseline (blue dot in Figure 7-4 b)) compared to the Standard IEC Method. However, the method also fails to account for the impact of the wind in other scenarios. For example, as the wind speed decreases in Figure 7-4 a), the mean PCC power decreases and the apparent inertial power is reduced (to appear negative) relative to the constant initial PCC power baseline. The underestimation of the inertial response for wind step-downs and overestimation for wind step-ups is visible in Figure 7-4 b).

The Initial Power Method achieves an absolute error of 11 % during the constant wind case pictured in Figure 7-4 b). This is similar to the errors reported by the other individual device estimators in the literature that use an initial PCC power baseline during constant wind conditions: 8 % [27] and 4 % [115]. Inertial response measurement methods that approximate the impact of the wind in this manner should also expect similar inaccuracies to those recorded for the Initial Power Method when subject to variable wind conditions (between -420 % and 740 %).

7.5.4. Improved IEC Method Accuracy

Figure 7-6 shows the MPPT reference (green line) and the PCC power output (blue line) during a coinciding frequency disturbance (F2) and wind step-up (U13). The MPPT reference tracks the steady state PCC power accurately. The inertial power change identified using the MPPT baseline is similar, but not identical, to the Regulating Power signal [113] that is used in the FDF based inertia estimator in [111]. The inertial power is the WT power that responds to changes in frequency above the MPPT reference, however, variations in the remaining portion of the WT output set by the MPPT reference will also affect the network frequency.

The Improved IEC Method achieves good measurement accuracy; the maximum absolute error for the entire range of sensitivity scenarios is 17 % (Table 7-5). The accuracy of the Improved IEC Method is independent of wind disturbance and inertial constant, depicted by the constant error contour in Figure 7-5 c).

Although the FDF based inertia estimator considers the variation of the wind, it is not applied to a WT with an inertial controller [111]. The FDF based estimator is tested on an ESS with a massive inertial constant $H = 40\ s$, whose inertial response is large and does not experience the complex WT dynamics such as the transformation of KE to electrical power. In contrast, the Improved IEC Method has been proven to measure WT inertial response accurately across a range of inertial constants and can improve the existing industrial standard.

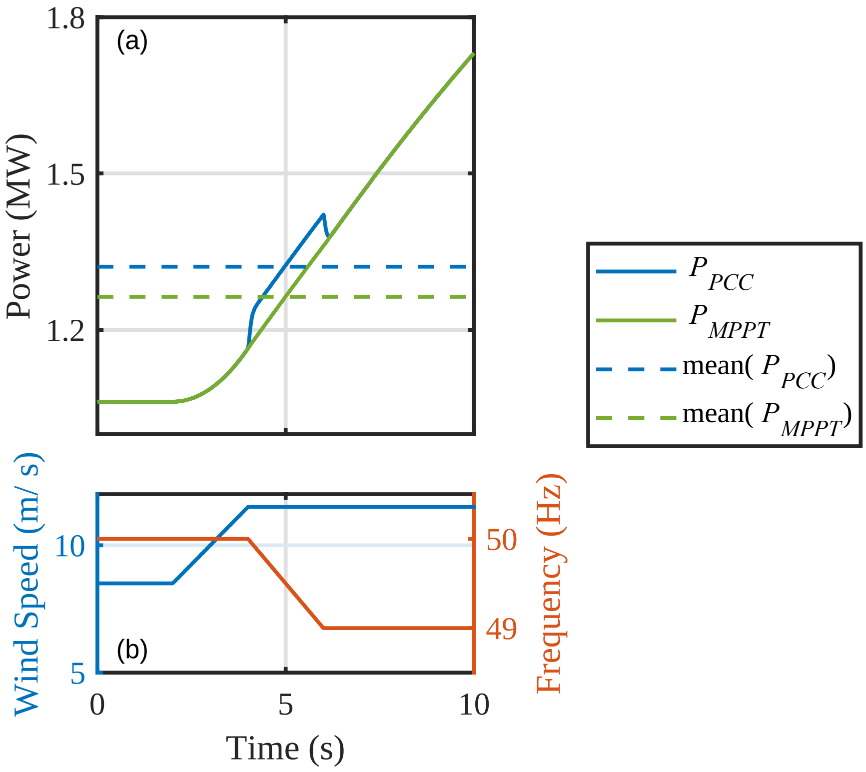

Figure 7-6 a) Power signals used for the Improved IEC Method and b) the corresponding wind and frequency conditions.

7.5.5. Equivalent Swing Method accuracy

Figure 7-7 shows the estimated output of a WT inertial response using the system identification stage of the Equivalent Swing Method. The estimated output depicts the accuracy of the estimation by passing the measured frequency (the input to the WT system $\Delta\omega_g$) through the identified transfer function (the representation of the WT system $G_{est}(s)$). This accuracy represents a training error, as the model is both trained and applied to the single set of input and output data whose inertial constant the Equivalent Swing method aims to measure.

The identification is independent of the wind conditions due to the use of the MPPT baseline. The system identification process achieves a fit of at least 97 % between the measured power output and the estimated output for all of the sensitivity scenarios, proving the accuracy of the approximation of the WT inertial response to a 2nd order system.

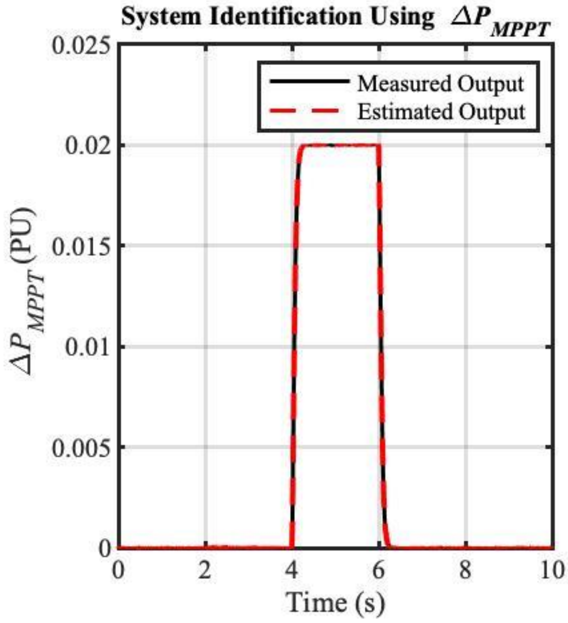

Figure 7-7 System identification estimated output compared to measured PU MPPT inertial power change output for wind step down (U25). The inertial constant setting is H1 and the frequency scenario is F2.

Using these well-fitted models, the Equivalent Swing Method is the most accurate of the tested inertial response measurement methods. The maximum absolute error is constrained below 0.50 % (Table 7-5). Figure 7-5 d) shows higher relative error for wind step-ups and for higher inertial constants but the consistently small error means the trends are not significant.

The accurate inertial response measurement proves the applicability of the Equivalent Swing methodology to VSM WTs. However, the accurate relation of the SG swing equation to the inertial response of a Current Control based strategy in [115] and to GFM Droop controllers in [62], [130] suggests that the SG equivalence may be appropriate beyond VSMs. The findings of Chapter 6, which highlight the similarities between GFM & GFL inertial response also support this theory. The results of Chapter 5, which showed that different GFM controllers possessed different dynamic properties that depend on the exact configuration and tuning of cascaded controllers, may manifest in inertial measurement as different SG damping characteristics that can either be recognised or ignored by a SO, depending on the requirements that they define for WTs.

7.5.6. Sensitivity to frequency disturbance

The measurement methods are subject to frequency disturbances with varying frequency change magnitudes and ROCOFs to ensure they remain robust throughout a range of events. Figure 7-8 shows the sensitivity of the inertial response measurement methods to the frequency disturbance properties for a wind step-down (U25) and inertia constant H1. Frequency disturbance F1 (with frequency deviation 0.1 Hz and ROCOF 0.1 Hz/s) is plotted independently from the contour as it doesn't share its low frequency change or ROCOF with other scenarios. The Standard IEC and Initial Power Methods show some sensitivity to the ROCOF. The inaccuracy introduced to both methods by the baselines drive a larger error when the ROCOF and inertial power change are smaller. The direction of the error is dependent on the given wind step-up and the respective overestimation (Standard IEC Method) and underestimation (Initial Power Method) of the wind's impact by each method. For example, during the pictured frequency event F1, wind step-down U25, and inertial constant H1, the Standard IEC Method overestimates the inertia measurement by 6100 %, whereas, the Initial Power Method underestimates the same scenario by 270 %.

The methods that incorporate the MPPT have reduced dependency on the frequency disturbance properties compared to the Standard IEC and Initial Power Methods. However, the Improved IEC Method regularly overestimates frequency event F4, which has a deviation of 1 Hz and a ROCOF of 2.5 Hz/s, by around 10 % more than other events. The Equivalent Swing Method is generally least accurate for either frequency event F4 or F1, but again, the low error magnitude means this is not a weakness in the measurement approach.

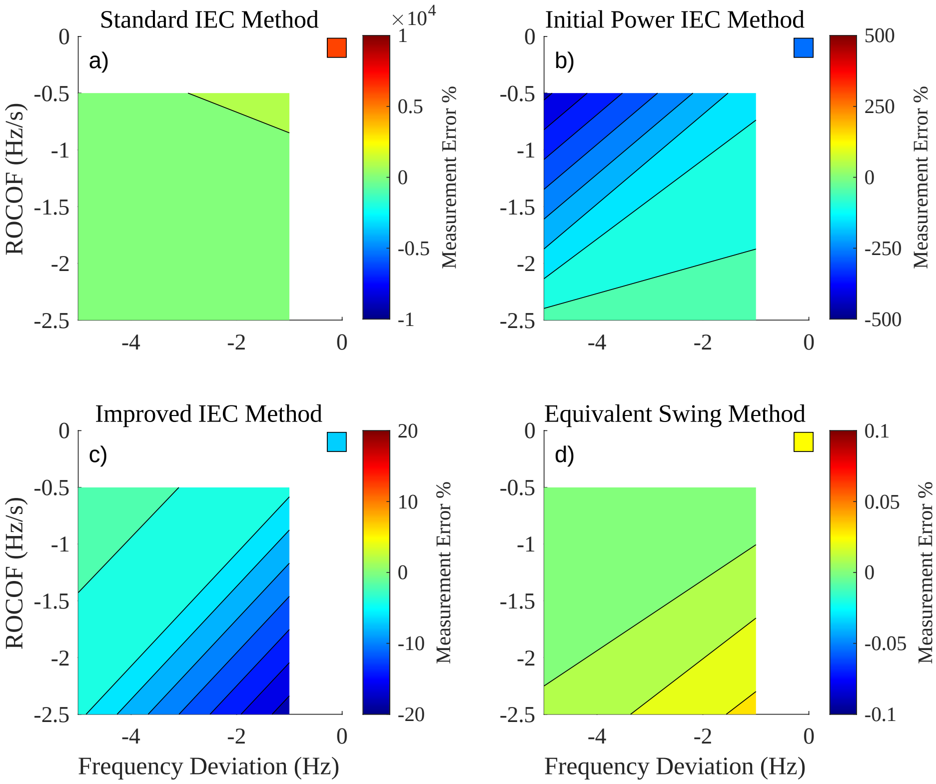

Figure 7-8 Inertia measurement error for a wind step-down (U25) and inertia constant H1 as the frequency change magnitude and ROCOF vary. Subplots exhibit the error for different methods: a) Standard IEC, b) Initial Power IEC, c) Improved IEC, and d) Equivalent Swing Methods. Frequency disturbance F1 is plotted as an independent point from the contour.

7.6. Application of improved methods to Dersalloch data

The inertial response measurement methods that are assessed throughout the sensitivity study are applied to the data from the SPR Dersalloch inertial provision test. The objective is to validate the accuracy of each method when applied to real WT systems.

The measurement methodologies used in this Section are the same as those described in Section 7.4.1 other than a few key approximations that have to be made due to the availability of the experimental data. The Standard IEC Method uses an approximated Power Available for the entire wind farm. The MPPT reference is replaced with the wind farm converter reference for both the Improved IEC and Equivalent Swing Methods. The inertial constant measured by each method is recorded as a percentage error of the inertial constant of the wind farm during the given disturbance. Although the exact structure of the WT control is unknown, the wind farm is known to operate with an inertial constant of $H_{31/05} = 4\ s$ on the 31st of May and of $H_{12/05} = 7.5\ s$ on the 12th of June.

Table 7-6 Range of inertial response measurement errors (%) for tested methods when applied to the Dersalloch experimental data.

Method	**Inertial constant measurement error (%)**	
	31/05	**21/06**
Standard IEC	340	-150
Initial Power	-160	-100
Improved IEC	-33	-25
Equivalent Swing	-12	13

Table 7-6 shows the inertial constant measurement errors using each method for both disturbances. In general, the Dersalloch data confirms the findings of the sensitivity study. The Standard IEC Method is the least accurate approach. The Power Available baseline overestimates the impact of the wind, which is exhibited by the large overestimation of the inertial response (340 %) on the 31st of May that coincides with a severe drop in wind. The underestimation of the inertial constant by 160 % during the same disturbance by the Initial Power Method confirms its underestimation of the wind's impacts. The less severe wind conditions on the 12th of June do not provide as conclusive results for the Standard and Initial Power Methods.

The Improved IEC Method that was proposed in Section 7.3.1 achieves better inertial response measurement accuracy than the existing measurement methods. However, the use of the alternate reference as the baseline introduces more error (between 25 % and 33 %) than is observed when using the MPPT reference throughout the sensitivity study (constrained below 17 %). The sub-optimal baseline signal also reduces the accuracy of the Equivalent Swing method for the Dersalloch data. However, the system identification approach is able to capture the dynamic response of the wind farm and constrains the error to be less than 13 % during both events. By extending the inertial response measurement to consider properties of the dynamic response the Equivalent Swing Method is able to remove some of the error introduced to the Improved IEC Method by the alternate converter reference baseline. The Equivalent Swing Method is confirmed to be the most accurate approach to measure WT inertial response.

7.7. Conclusions

This study assesses the impact of wind variations on inertial responses from wind turbines. The previously available methods for the measurement of WT inertial response disagree how to approximate the wind's effects on the rapid power injections. Particular focus is paid to the IEC industrial standard, which is thought to use an inappropriate Power Available baseline to measure inertial response from. The need for internal information to accurately measure inertial response, such as the Power Available, is also assessed.

The analysis of data from a test at a grid connected ScottishPower Renewables wind farm confirms that inertial provision is affected by wind variability and that it should not be neglected from inertial measurement. The simple approach using the difference between the initial and boosted external PCC measurements was incapable of accurately measuring the inertia, particularly during large wind variations.

A type 4 wind turbine model is subject to a sensitivity study. Four measurement methods are applied to the simulated data to assess their accuracy throughout varying wind, frequency, and inertial constant conditions. The methods that are assessed are: the Standard IEC Method and the Initial Power Method, from the literature, and the Improved IEC Method and the Equivalent Swing Method, the two methods proposed in this paper.

When the Standard IEC method uses the Power Available as the baseline it is found to be very inaccurate (errors as large as -9800 %). The Power Available overestimates the impact of the wind on the short timescales and may not be appropriate for inertial analysis, despite being proposed to increase transparency of wind turbines on longer timescales. The sensitivity study finds the Initial Power Method to underestimate the wind’s impact during the inertial response. The error in both methods is worse when the ROCOF is low and the wind's impact masks the small inertial response more. The results of the sensitivity study confirm the findings of the grid connected wind farm that external data is insufficient to measure WT inertial response, however, the internal Power Available is not the appropriate solution.

The IEC Method is proposed to be improved by incorporating the maximum power point tracking reference as the baseline. The reference is an alternative internal signal that provides an accurate representation of the WT steady state conditions and enables accurate inertia measurement (maximum error of -17 %). An alternative approach to the IEC method is proposed that accounts for the full inertial response dynamics. This alternative, the Equivalent Swing Method, achieves the most accurate inertial measurement across all of the sensitivity scenarios (error less than 0.50 %). The tested measurement methods are then applied to the Dersalloch Wind Farm experimental data to confirm their accuracy for real-world wind turbines. The Equivalent Swing Method is also found to be the most accurate inertial measurement method for the experimental data but as the MPPT reference is not available the maximum error extends to 12 %.

Chapter 8. Conclusions

This thesis has aimed to identify and solve some of the main hurdles that are restricting the provision of frequency support from power converter interfaced devices. Initially, technologies and control strategies were identified that are capable of providing this support. The remaining hurdles relate to the understanding of the new solutions and the means that System Operators (SOs) can use to implement them on power systems.

Three specific hurdles were addressed in this thesis:

- The ability and equivalence of different grid-forming (GFM) control configurations to provide droop and inertial responses, particularly considering the presence of cascaded controllers.
- The ability to quantify the effective containment of the initial frequency excursion following a disturbance and the potential unnecessary exclusion of suitable grid-following (GFL) inertial solutions.
- The ability to effectively account for the impact of wind turbine (WT) dynamics on inertial response and the resulting ability to understand and properly test/monitor these solutions.

The study in Chapter 5 was carried out to assess the equivalence between different GFM controllers and to improve the understanding of the impact of different low-level control configurations and tunings on frequency support functions. The tuning guides were used to set the inertial and droop responses of the single-loop Synchronverter and multi-loop GFM Droop controllers; a comparison showed that the two controllers possessed different steady-state and dynamic features. This opposes some studies that suggest the two are equivalent. The difference is suggested to stem from the different voltage control location of the two strategies, which is driven by the cascaded controller in the GFM Droop. A proposal is made to update the damping expression of the GFM Droop to account for the different voltage control location.

The impact of the cascaded controller’s parametric tuning was also assessed. Unlike the current controller, the voltage control gains were shown to impact both the stability and dynamics of the frequency support. Tuning suggestions were made to increase the damping of the GFM Droop, however, some inherent differences remained between the two controllers. These suggestions can be incorporated into controllers that use conventional simple tuning approaches, but while still informative, are not as explicitly relevant to advanced controllers, which might use adaptive or machine learning algorithms to achieve similar performance.

The study in Chapter 6 was carried out to improve the transparency of features that stabilise the initial frequency excursion following a disturbance. Inertial response is shown to occur slower than instantaneously and to be distinct from the voltage-source transient injections that it appears to be confused with in some industrial specifications. A GFL is shown to be able to provide sufficiently fast (and effective) inertial response on medium to high strength grids. Therefore, it is suggested that GFL inertial solutions should also be considered to support grid frequency as their additional provision could reduce some of the energy strain that will be placed on GFMs. The reviewed time-domain criteria appear to be able to describe effective inertial response but need to be properly specified to reflect appropriate inertial timescales. The importance of voltage-source transients for the initial containment of the frequency excursion was also observed.

The final study in Chapter 7 was carried out to explore the disagreement on how to account for the wind’s impact in inertial response measurement methods. The analysis subjected existing methods to a sensitivity analysis to assess their ability to measure inertial response for a range of frequency and wind disturbances and inertial settings. The previously available methods were shown to either under- or overestimate the wind’s impacts on the inertial response, which drove inaccurate measurement. Two methods were proposed to improve the wind turbine inertial response measurement, both of which used a converter reference as the baseline of the inertial response. The Improved IEC Method offers a simple adaptation to improve the accuracy of wind turbine inertial measurement throughout wind disturbances. The Equivalent Swing

Method offers a more advanced approach that achieves the most accurate measurement. All of the study’s findings were validated using experimental data from a grid-connected GFM wind farm. The results provided insight to the inherent features of inertial provision from wind turbines and offered solutions that SOs can use to accurately measure/monitor devices and improve the transparency of the state of the power system.

8.1. **Future works**

The impact of the controller configuration and tuning on frequency support functions can be further explored using small-signal models. The small-signal models can be incorporated to describe the explicit impact that the different configurations or tunings have on the converter’s stability margins and dynamic features. A wider range of control strategies and configurations could also be considered. By comparing different control strategies with varying configurations (e.g. with/without cascaded controllers, virtual impedances, and current limiters) a comprehensive understanding of the impact of each outer and inner control structure on the frequency support can be developed. If this study is implemented using small-signal models, linear control analysis can be carried out rapidly for each of the different structural iterations.

One flaw in the existing time-domain approach to quantify useful inertial response is the interdependence of the inertial delivery speed criterion and the nadir time. The consequences of this qualifying procedure should be studied in more detail for a range of grid configurations.

Further studies should be carried out to clearly quantify the dependence of different periods of a disturbance on the different frequency stability phenomena, including the transient phase response. The ability of GFLs to provide the transient injections should also be explored in more detail. Then, a separate specification for transient phase responses should be established independently from inertial response. These studies can help to inform SOs to develop a robust specification for solutions that effectively contain the grid frequency.

The proposed wind turbine inertial measurement methods both required internal data that is not currently available to the SO. The means for this information to be communicated needs to be assessed. Limited data availability may limit the methods to only be used as inertial response measurement tools for the qualification of useful support before grid-connection. Alternatively, if the power reference could be measured or provided to the SO, the Equivalent Swing Method could be implemented for inertia monitoring to track system operation. Further studies should also consider the impact of different converter control implementations on the proposed measurement methods, although the results in Chapters Chapter 5 and Chapter 6 suggest that the specific features of the inertial response are not necessarily unique to any given control strategy or family.

8.2. Final conclusions

Each chapter has taken actions to improve the understanding of available frequency stabilising solutions. The increased transparency provided by the proposals and results can enhance SOs’ understanding of the new devices that are being used to stabilise the transforming power systems. This information should enable the choice of the most effective solutions from the full range of technologies and the accurate dispatch and monitoring of the system to have the highest chance of remaining secure throughout the transition to net zero carbon operation.

Chapter 9. References

[1] U. N. Environment, “Emissions Gap Report 2022,” *UNEP - UN Environment Programme*, Oct. 21, 2022. http://www.unep.org/resources/emissions-gap-report-2022 (accessed Mar. 30, 2023).

[2] “National Grid’s net zero commitment | National Grid Group.” https://www.nationalgrid.com/stories/journey-to-net-zero/national-grids-net-zero-commitment (accessed Mar. 30, 2023).

[3] “End to coal power brought forward to October 2024,” *GOV.UK*. https://www.gov.uk/government/news/end-to-coal-power-brought-forward-to-october-2024 (accessed Mar. 30, 2023).

[4] “Levelized Cost Of Energy, Levelized Cost Of Storage, and Levelized Cost Of Hydrogen 2021,” *https://www.lazard.com*. https://www.lazard.com/research-insights/levelized-cost-of-energy-levelized-cost-of-storage-and-levelized-cost-of-hydrogen-2021/ (accessed Mar. 30, 2023).

[5] “Wind energy in Europe: 2021 Statistics and the outlook for 2022-2026,” *WindEurope*. https://windeurope.org/data-and-analysis/product/wind-energy-in-europe-2021-statistics-and-the-outlook-for-2022-2026 (accessed Mar. 30, 2023).

[6] “Global Market Outlook For Solar Power 2021 - SolarPower Europe.” https://www.solarpowereurope.org/insights/market-outlooks/global-market-outlook-for-solar-power-2021 (accessed Mar. 30, 2023).

[7] “New plans to make UK world leader in green energy,” *GOV.UK*. https://www.gov.uk/government/news/new-plans-to-make-uk-world-leader-in-green-energy (accessed Mar. 30, 2023).

[8] Ofgem, “Electricity interconnectors,” 2021. https://www.ofgem.gov.uk/electricity/transmission-networks/electricity-interconnectors (accessed Feb. 17, 2021).

[9] J. Van Putten, J. Antolin Morales, V. Sewdien, and N. Kirby, “Capabilities and requirements definition for power electronics based technology for secure and efficient system operation and control,” CIGRE, Paris, France, C2/B4, Nov. 2020.

[10] J. Matevosyan *et al.*, “Grid-Forming Inverters: Are They the Key for High Renewable Penetration?,” *IEEE Power Energy Mag.*, vol. 17, no. 6, pp. 89–98, Nov. 2019, doi: 10.1109/MPE.2019.2933072.

[11] H. Iswadi, R. J. Best, and D. J. Morrow, “Irish power system primary frequency response metrics during different system non synchronous penetration,” in *2015 IEEE Eindhoven PowerTech*, Eindhoven, Netherlands: IEEE, Jun. 2015, pp. 1–6. doi: 10.1109/PTC.2015.7232425.

[12] A. Adrees and J. V. Milanovic, “Study of frequency response in power system with renewable generation and energy storage,” in *2016 Power Systems Computation Conference (PSCC)*, Genoa, Italy: IEEE, Jun. 2016, pp. 1–7. doi: 10.1109/PSCC.2016.7540912.

[13] J. O’Sullivan, A. Rogers, D. Flynn, P. Smith, A. Mullane, and M. O’Malley, “Studying the Maximum Instantaneous Non-Synchronous Generation in an Island System—Frequency Stability Challenges in Ireland,” *IEEE Trans. Power Syst.*, vol. 29, no. 6, pp. 2943–2951, Nov. 2014, doi: 10.1109/TPWRS.2014.2316974.

[14] R. Ierna *et al.*, “Effects of VSM Convertor Control on Penetration Limits of Non-Synchronous Generation in the GB Power System,” in *15th Wind Integration Workshop*, Nov. 2016, p. 8.

[15] C. Edmunds, S. Martín-Martínez, J. Browell, E. Gómez-Lázaro, and S. Galloway, “On the participation of wind energy in response and reserve markets in Great Britain and Spain,” *Renew. Sustain. Energy Rev.*, vol. 115, p. 109360, Nov. 2019, doi: 10.1016/j.rser.2019.109360.

[16] R. Pearce, “In-depth: The whole system costs of renewables,” *Carbon Brief*, Feb. 22, 2017. https://www.carbonbrief.org/in-depth-whole-system-costs-renewables/ (accessed Mar. 30, 2023).

[17] “Markets Roadmap March 2022.” National Grid ESO, Mar. 2022.

[18] “Application of Advanced Grid-scale inverters in the NEM,” AEMO, Apr. 2021.

[19] “National Grid ESO Stability Pathfinder RFI V1.pdf,” 2019.

[20] H. Gu, R. Yan, and T. Saha, “Review of system strength and inertia requirements for the national electricity market of Australia,” *CSEE J. Power Energy Syst.*, Aug. 2019, doi: 10.17775/CSEEJPES.2019.00230.

[21] “Putting some momentum in inertia,” *Australian Energy Council*. https://www.energycouncil.com.au/analysis/putting-some-momentum-in-inertia/ (accessed Mar. 30, 2023).

[22] "Accelerated Loss of Mains Change Programme WindCare case study | ESO." https://www.nationalgrideso.com/news/accelerated-loss-mains-change-programme-windcare-case-study (accessed Mar. 30, 2023).

[23] Q. Hong, M. A. U. Khan, C. Henderson, A. Egea-Àlvarez, D. Tzelepis, and C. Booth, "Addressing Frequency Control Challenges in Future Low-Inertia Power Systems: A Great Britain Perspective," *Engineering*, vol. 7, no. 8, pp. 1057–1063, Aug. 2021, doi: 10.1016/j.eng.2021.06.005.

[24] L. Meng *et al.*, "Fast Frequency Response From Energy Storage Systems—A Review of Grid Standards, Projects and Technical Issues," *IEEE Trans. Smart Grid*, vol. 11, no. 2, pp. 1566–1581, Mar. 2020, doi: 10.1109/TSG.2019.2940173.

[25] J. Morren, S. W. H. de Haan, W. L. Kling, and J. A. Ferreira, "Wind Turbines Emulating Inertia and Supporting Primary Frequency Control," *IEEE Trans. Power Syst.*, vol. 21, no. 1, pp. 433–434, Feb. 2006, doi: 10.1109/TPWRS.2005.861956.

[26] N. Pogaku, M. Prodanovic, and T. C. Green, "Modeling, Analysis and Testing of Autonomous Operation of an Inverter-Based Microgrid," *IEEE Trans. Power Electron.*, vol. 22, no. 2, pp. 613–625, Mar. 2007, doi: 10.1109/TPEL.2006.890003.

[27] Y. Zhang, J. Bank, Y.-H. Wan, E. Muljadi, and D. Corbus, "Synchrophasor Measurement-Based Wind Plant Inertia Estimation," in *2013 IEEE Green Technologies Conference (GreenTech)*, Denver, CO: IEEE, Apr. 2013, pp. 494–499. doi: 10.1109/GreenTech.2013.85.

[28] H.-P. Beck and R. Hesse, "Virtual synchronous machine," in *2007 9th International Conference on Electrical Power Quality and Utilisation*, Barcelona, Spain: IEEE, Oct. 2007, pp. 1–6. doi: 10.1109/EPQU.2007.4424220.

[29] P. Winter and H. Wrede, "Impact of Power Converter Control on Transient Stability of Power Systems," in *NEIS 2018; Conference on Sustainable Energy Supply and Energy Storage Systems*, Sep. 2018, pp. 1–6.

[30] J. Marchgraber *et al.*, "Comparison of Control Strategies to Realize Synthetic Inertia in Converters," *Energies*, vol. 13, no. 13, p. 3491, Jul. 2020, doi: 10.3390/en13133491.

[31] H. Beltran, S. Harrison, A. Egea-Àlvarez, and L. Xu, "Techno-Economic Assessment of Energy Storage Technologies for Inertia Response and

Frequency Support from Wind Farms,” *Energies*, vol. 13, no. 13, p. 3421, Jul. 2020, doi: 10.3390/en13133421.

[32] “GC0137: Minimum Specification Required for Provision of GB Grid Forming (GBGF) Capability (formerly Virtual Synchronous Machine/ VSM Capability),” National Grid ESO, Workgroup Consultation, Mar. 2021.

[33] “FNN-Guideline Grid forming behaviour of HVDC systems and DC-connected PPMs,” VDE FNN, Berlin, Germany, Jan. 2020.

[34] P. Kundur *et al.*, “Definition and Classification of Power System Stability IEEE/CIGRE Joint Task Force on Stability Terms and Definitions,” *IEEE Trans. Power Syst.*, vol. 19, no. 3, pp. 1387–1401, Aug. 2004, doi: 10.1109/TPWRS.2004.825981.

[35] J. H. Eto, J. Undrill, C. Roberts, P. Mackin, and J. Ellis, “Frequency Control Requirements for Reliable Interconnection Frequency Response,” Feb. 2018, Accessed: Mar. 30, 2023. [Online]. Available: https://escholarship.org/uc/item/0z77p518

[36] N. Hatziargyriou *et al.*, “Stability definitions and characterization of dynamic behavior in systems with high penetration of power electronic interfaced technologies,” IEEE Power & Energy Society, PES-TR77, Apr. 2020.

[37] E. Ebrahimzadeh, F. Blaabjerg, X. Wang, and C. L. Bak, “Harmonic Stability and Resonance Analysis in Large PMSG-Based Wind Power Plants,” *IEEE Trans. Sustain. Energy*, vol. 9, no. 1, pp. 12–23, Jan. 2018, doi: 10.1109/TSTE.2017.2712098.

[38] L. Fan and Z. Miao, “Wind in Weak Grids: 4 Hz or 30 Hz Oscillations?,” *IEEE Trans. Power Syst.*, vol. 33, no. 5, pp. 5803–5804, Sep. 2018, doi: 10.1109/TPWRS.2018.2852947.

[39] P. Kundur, *Power System Stability and Control*. New York, USA: McGraw-Hill Education, 1995.

[40] A. Egea-Alvarez, A. Junyent-Ferre, and O. Gomis-Bellmunt, “Active and Reactive Power Control of Grid Connected Distributed Generation Systems,” in *Modeling and control of sustainable power systems: towards smarter and greener electric grids*, L. Wang, Ed., in Green energy and technology. Berlin ; Heidelberg: Springer, 2012.

[41] T. Ackermann, T. Prevost, V. Vittal, A. J. Roscoe, J. Matevosyan, and N. Miller, “Paving the Way: A Future Without Inertia Is Closer Than You Think,”

IEEE Power Energy Mag., vol. 15, no. 6, pp. 61–69, Nov. 2017, doi: 10.1109/MPE.2017.2729138.

[42] Y. Lin *et al.*, “Research Roadmap on Grid-Forming Inverters,” National Renewable Energy Laboratory, Golden, CO, 2020.

[43] T. Breithaupt *et al.*, “MIGRATE D1.1 Report on systemic issues.” Dec. 15, 2016.

[44] A. Tayyebi, D. Gross, A. Anta, F. Kupzog, and F. Dorfler, “Frequency Stability of Synchronous Machines and Grid-Forming Power Converters,” *IEEE J. Emerg. Sel. Top. Power Electron.*, vol. 8, no. 2, pp. 1004–1018, Jun. 2020, doi: 10.1109/JESTPE.2020.2966524.

[45] M. Paolone *et al.*, “Fundamentals of power systems modelling in the presence of converter-interfaced generation,” *Electr. Power Syst. Res.*, vol. 189, p. 106811, Dec. 2020, doi: 10.1016/j.epsr.2020.106811.

[46] M. P. Kazmierkowski and L. Malesani, “Current control techniques for three-phase voltage-source PWM converters: a survey,” *IEEE Trans. Ind. Electron.*, vol. 45, no. 5, pp. 691–703, Oct. 1998, doi: 10.1109/41.720325.

[47] M. Yu *et al.*, “Instantaneous penetration level limits of non-synchronous devices in the British power system,” *IET Renew. Power Gener.*, vol. 11, no. 8, pp. 1211–1217, Jun. 2017, doi: 10.1049/iet-rpg.2016.0352.

[48] “Performance of Phase-Locked Loop Based Converters,” National Grid ESO, 2017.

[49] K. Givaki, D. Chen, and L. Xu, “Current Error Based Compensations for VSC Current Control in Weak Grids for Wind Farm Applications,” *IEEE Trans. Sustain. Energy*, vol. 10, no. 1, pp. 26–35, Jan. 2019, doi: 10.1109/TSTE.2018.2820386.

[50] J. Z. Zhou, H. Ding, S. Fan, Y. Zhang, and A. M. Gole, “Impact of Short-Circuit Ratio and Phase-Locked-Loop Parameters on the Small-Signal Behavior of a VSC-HVDC Converter,” *IEEE Trans. Power Deliv.*, vol. 29, no. 5, pp. 2287–2296, Oct. 2014, doi: 10.1109/TPWRD.2014.2330518.

[51] M. F. M. Arani and Y. A.-R. I. Mohamed, “Analysis and Performance Enhancement of Vector-Controlled VSC in HVDC Links Connected to Very Weak Grids,” *IEEE Trans. Power Syst.*, vol. 32, no. 1, pp. 684–693, Jan. 2017, doi: 10.1109/TPWRS.2016.2540959.

[52] J. F. Morris, K. H. Ahmed, and A. Egea-Àlvarez, “Analysis of Controller Bandwidth Interactions for Vector-Controlled VSC Connected to Very Weak AC Grids,” *IEEE J. Emerg. Sel. Top. Power Electron.*, vol. 9, no. 6, pp. 7343–7354, Dec. 2021, doi: 10.1109/JESTPE.2020.3031203.

[53] D. Duckwitz and B. Fischer, “Modeling and Design of df/dt -Based Inertia Control for Power Converters,” *IEEE J. Emerg. Sel. Top. Power Electron.*, vol. 5, no. 4, pp. 1553–1564, Dec. 2017, doi: 10.1109/JESTPE.2017.2703814.

[54] M. Yu *et al.*, “Use of an inertia-less Virtual Synchronous Machine within future power networks with high penetrations of converters,” in *2016 Power Systems Computation Conference (PSCC),* Genoa, Italy: IEEE, Jun. 2016, pp. 1–7. doi: 10.1109/PSCC.2016.7540926.

[55] G. Wu *et al.*, “Analysis and design of vector control for VSC-HVDC connected to weak grids,” *CSEE J. Power Energy Syst.*, vol. 3, no. 2, pp. 115–124, Jun. 2017, doi: 10.17775/CSEEJPES.2017.0015.

[56] M. Kersic *et al.*, “Testing Characteristics of Grid Forming Converters Part I: Specification and Definition of Behaviour,” p. 9, Nov. 2020.

[57] P. Christensen *et al.*, “High Penetration of Power Electronic Interfaced Power Sources and the Potential Contribution of Grid Forming Converters,” ENTSO-E Technical Group on High Penetration of Power Electronic Interfaced Power Sources, 2020.

[58] R. W. Kenyon, A. Sajadi, M. Bossart, A. Hoke, and B.-M. Hodge, “Interactive Power to Frequency Dynamics Between Grid-Forming Inverters and Synchronous Generators in Power Electronics-Dominated Power Systems.” arXiv, Oct. 08, 2022. Accessed: Mar. 30, 2023. [Online]. Available: http://arxiv.org/abs/2102.12332

[59] Y. Chen, R. Hesse, D. Turschner, and H.-P. Beck, “Comparison of methods for implementing virtual synchronous machine on inverters,” *Renew. Energy Power Qual. J.*, pp. 734–739, Apr. 2012, doi: 10.24084/repqj10.453.

[60] Q.-C. Zhong and G. Weiss, “Synchronverters: Inverters That Mimic Synchronous Generators,” *IEEE Trans. Ind. Electron.*, vol. 58, no. 4, pp. 1259–1267, Apr. 2011, doi: 10.1109/TIE.2010.2048839.

[61] A. Abdelrahim, P. McKeever, M. Smailes, A. Egea-Àlvarez, and K. Ahmed, “Modified grid forming converter controller with fault ride through capability without PLL or current loop,” presented at the 18th International Wind Integration Workshop, Dublin, Ireland, Oct. 2019, p. 8.

[62] S. D’Arco and J. A. Suul, “Virtual synchronous machines — Classification of implementations and analysis of equivalence to droop controllers for microgrids,” in *2013 IEEE Grenoble Conference*, Grenoble, France: IEEE, Jun. 2013, pp. 1–7. doi: 10.1109/PTC.2013.6652456.

[63] J. Liu, Y. Miura, and T. Ise, “Comparison of Dynamic Characteristics Between Virtual Synchronous Generator and Droop Control in Inverter-Based Distributed Generators,” *IEEE Trans. Power Electron.*, vol. 31, no. 5, pp. 3600–3611, May 2016, doi: 10.1109/TPEL.2015.2465852.

[64] W. Zhang, D. Remon, and P. Rodriguez, “Frequency support characteristics of grid-interactive power converters based on the synchronous power controller,” *IET Renew. Power Gener.*, vol. 11, no. 4, pp. 470–479, Mar. 2017, doi: 10.1049/iet-rpg.2016.0557.

[65] M. A. Torres L., L. A. C. Lopes, L. A. Moran T., and J. R. Espinoza C., “Self-Tuning Virtual Synchronous Machine: A Control Strategy for Energy Storage Systems to Support Dynamic Frequency Control,” *IEEE Trans. Energy Convers.*, vol. 29, no. 4, pp. 833–840, Dec. 2014, doi: 10.1109/TEC.2014.2362577.

[66] R. Ofir, U. Markovic, P. Aristidou, and G. Hug, “Droop vs. virtual inertia: Comparison from the perspective of converter operation mode,” in *2018 IEEE International Energy Conference (ENERGYCON)*, Limassol: IEEE, Jun. 2018, pp. 1–6. doi: 10.1109/ENERGYCON.2018.8398752.

[67] W. Du *et al.*, “A Comparative Study of Two Widely Used Grid-Forming Droop Controls on Microgrid Small-Signal Stability,” *IEEE J. Emerg. Sel. Top. Power Electron.*, vol. 8, no. 2, pp. 963–975, Jun. 2020, doi: 10.1109/JESTPE.2019.2942491.

[68] S. D’Arco, J. A. Suul, and O. B. Fosso, “Automatic Tuning of Cascaded Controllers for Power Converters Using Eigenvalue Parametric Sensitivities,” *IEEE Trans. Ind. Appl.*, vol. 51, no. 2, pp. 1743–1753, Mar. 2015, doi: 10.1109/TIA.2014.2354732.

[69] J. Are Suul and S. D’Arco, “Comparative Analysis of Small-Signal Dynamics in Virtual Synchronous Machines and Frequency-Derivative-Based Inertia Emulation,” in *2018 IEEE 18th International Power Electronics and Motion Control Conference (PEMC)*, Aug. 2018, pp. 344–351. doi: 10.1109/EPEPEMC.2018.8522010.

[70] A. Roscoe *et al.*, “Practical Experience of Operating a Grid Forming Wind Park and its Response to System Events,” in *18th Int’l Wind Integration Workshop*, Dublin, Ireland, Oct. 2019, p. 7.

[71] M. Ashabani, F. D. Freijedo, S. Golestan, and J. M. Guerrero, “Inducverters: PLL-Less Converters With Auto-Synchronization and Emulated Inertia Capability,” *IEEE Trans. Smart Grid*, vol. 7, no. 3, pp. 1660–1674, May 2016, doi: 10.1109/TSG.2015.2468600.

[72] F. Milano, F. Dorfler, G. Hug, D. J. Hill, and G. Verbic, “Foundations and Challenges of Low-Inertia Systems (Invited Paper),” in *2018 Power Systems Computation Conference (PSCC)*, Dublin: IEEE, Jun. 2018, pp. 1–25. doi: 10.23919/PSCC.2018.8450880.

[73] A. Stock, “Augmented control for flexible operation of wind turbines,” 2015.

[74] A. Ingalalli *et al.*, “Energy Storage Systems in Emerging Electricity Markets: Frequency Regulation and Resiliency,” in *2019 IEEE Power & Energy Society General Meeting (PESGM)*, Atlanta, GA, USA: IEEE, Aug. 2019, pp. 1–5. doi: 10.1109/PESGM40551.2019.8973490.

[75] D. Feldmann and R. V. de Oliveira, “Operational and control approach for PV power plants to provide inertial response and primary frequency control support to power system black-start,” *Int. J. Electr. Power Energy Syst.*, vol. 127, p. 106645, May 2021, doi: 10.1016/j.ijepes.2020.106645.

[76] National Grid ESO, “Dynamic Containment.” https://www.nationalgrideso.com/industry-information/balancing-services/Frequency-Response-Services/dynamic-containment?technical-requirements= (accessed Nov. 09, 2022).

[77] National Grid ESO, “Grid Code (GC),” *nationalgrideso*, 2021. https://www.nationalgrideso.com/industry-information/codes/grid-code (accessed Jan. 11, 2020).

[78] X. Luo, J. Wang, M. Dooner, and J. Clarke, “Overview of current development in electrical energy storage technologies and the application potential in power system operation,” *Appl. Energy*, vol. 137, pp. 511–536, Jan. 2015, doi: 10.1016/j.apenergy.2014.09.081.

[79] O. Schmidt, A. Hawkes, A. Gambhir, and I. Staffell, “The future cost of electrical energy storage based on experience rates,” *Nat. Energy*, vol. 2, no. 8, p. 17110, Aug. 2017, doi: 10.1038/nenergy.2017.110.

[80] P. D’Aprile, J. Newman, and D. Pinner, *The New Economics of Energy Storage*. New York, USA: McKinsey & Co., 2016.

[81] "Electricity Storage and Renewables: Costs and Markets to 2030," Internation Renewable Energy Agency (IRENA), Abu Dhabi, UAE, 2017.

[82] O. Schmidt, S. Melchior, A. Hawkes, and I. Staffell, "Projecting the Future Levelized Cost of Electricity Storage Technologies," *Joule*, vol. 3, no. 1, pp. 81–100, Jan. 2019, doi: 10.1016/j.joule.2018.12.008.

[83] A. Schneuwly, "Maxwell Technologies White Paper-High Reliability Power Backup with Advanced Energy Storage," Maxwell Technologies, Inc., San Diego, California, USA, 2009.

[84] FREQCON, "Ultracapacitor Grid Stabilizer," 2018. https://www.freqcon.com/wp-content/uploads/FREQCON-datasheet-grid-storage-ultracapacitor-grid-stabilizer.pdf (accessed Jul. 09, 2019).

[85] E.-H. El Brouji, O. Briat, J.-M. Vinassa, N. Bertrand, and E. Woirgard, "Impact of Calendar Life and Cycling Ageing on Supercapacitor Performance," *IEEE Trans. Veh. Technol.*, vol. 58, no. 8, pp. 3917–3929, Oct. 2009, doi: 10.1109/TVT.2009.2028431.

[86] K. Pullen, "Low cost flywheel energy storage: supporting the transformation to renewables," Energy Institue - London and Home Counties Branch, London, UK, 2017.

[87] "Chem L.G. Global Catalog," 2018. http://m.lgchem.com/upload/file/product/LGChem_Catalog_Global_2018.pdf (accessed Jul. 09, 2019).

[88] C. Henderson, D. Vozikis, D. Holliday, X. Bian, and A. Egea-Àlvarez, "Assessment of Grid-Connected Wind Turbines with an Inertia Response by Considering Internal Dynamics," *Energies*, vol. 13, no. 5, p. 1038, Feb. 2020, doi: 10.3390/en13051038.

[89] "NCESS service specification: fast frequency response service Version 2.0," AEMO, 08/22. Accessed: Nov. 09, 2022. [Online]. Available: https://aemo.com.au/-/media/files/stakeholder_consultation/tenders/ncess-service-specification-ffr.pdf?la=en

[90] K. Das, M. Altin, A. D. Hansen, and P. E. Sørensen, "Inertia Dependent Droop Based Frequency Containment Process," *Energies*, vol. 12, no. 9, p. 1648, Apr. 2019, doi: 10.3390/en12091648.

[91] W. Leonhard, *Control of Electrical Drives*. Springer Science & Business Media, 2001.

[92] C. Bajracharya, M. Molinas, J. A. Suul, and T. M. Undeland, *Understanding of tuning techniques of converter controllers for VSC-HVDC*. Helsinki University of Technology, 2008. Accessed: Mar. 08, 2023. [Online]. Available: https://aaltodoc.aalto.fi:443/handle/123456789/814

[93] J. A. Suul, M. Molinas, L. Norum, and T. Undeland, "Tuning of control loops for grid connected voltage source converters," in *2008 IEEE 2nd International Power and Energy Conference*, Dec. 2008, pp. 797–802. doi: 10.1109/PECON.2008.4762584.

[94] D. Pattabiraman, R. H. Lasseter., and T. M. Jahns, "Comparison of Grid Following and Grid Forming Control for a High Inverter Penetration Power System," in *2018 IEEE Power & Energy Society General Meeting (PESGM)*, Portland, OR: IEEE, Aug. 2018, pp. 1–5. doi: 10.1109/PESGM.2018.8586162.

[95] M. Sinha, F. Dörfler, B. B. Johnson, and S. V. Dhople, "Uncovering Droop Control Laws Embedded Within the Nonlinear Dynamics of Van der Pol Oscillators," *IEEE Trans. Control Netw. Syst.*, vol. 4, no. 2, pp. 347–358, Jun. 2017, doi: 10.1109/TCNS.2015.2503558.

[96] A. Peña Asensio, F. Gonzalez-Longatt, S. Arnaltes, and J. L. Rodríguez-Amenedo, "Analysis of the Converter Synchronizing Method for the Contribution of Battery Energy Storage Systems to Inertia Emulation," *Energies*, vol. 13, no. 6, p. 1478, Mar. 2020, doi: 10.3390/en13061478.

[97] C. Phurailatpam, Z. H. Rather, B. Bahrani, and S. Doolla, "Measurement-Based Estimation of Inertia in AC Microgrids," *IEEE Trans. Sustain. Energy*, vol. 11, no. 3, pp. 1975–1984, Jul. 2020, doi: 10.1109/TSTE.2019.2948224.

[98] R. Eriksson, N. Modig, and K. Elkington, "Synthetic inertia versus fast frequency response: a definition," *IET Renew. Power Gener.*, vol. 12, no. 5, pp. 507–514, 2018, doi: 10.1049/iet-rpg.2017.0370.

[99] C. Phurailatpam, Z. H. Rather, B. Bahrani, and S. Doolla, "Estimation of Non-Synchronous Inertia in AC Microgrids," *IEEE Trans. Sustain. Energy*, pp. 1–1, Feb. 2021, doi: 10.1109/TSTE.2021.3070678.

[100] S. Chen, X. Zhang, Y. Wu, Q. Zhu, C. Bao, and X. Zhan, "Segmented Adaptive Control of Virtual Inertia for Virtual Synchronous Machines," in *2022 7th International Conference on Power and Renewable Energy (ICPRE)*, Sep. 2022, pp. 176–181. doi: 10.1109/ICPRE55555.2022.9960672.

[101] S. Coffey, J. F. Morris, and A. Egea-Alvarez, "Stability limits and tuning recommendation of the classical current control providing inertia support," in

2021 IEEE Madrid PowerTech, Madrid, Spain: IEEE, Jun. 2021, pp. 1–6. doi: 10.1109/PowerTech46648.2021.9495074.

[102] G. C. Kryonidis, K.-N. D. Malamaki, J. M. Mauricio, and C. S. Demoulias, "A new perspective on the synchronverter model," *Int. J. Electr. Power Energy Syst.*, vol. 140, p. 108072, Sep. 2022, doi: 10.1016/j.ijepes.2022.108072.

[103] A. Shekhar *et al.*, "Report on laboratory tests," Horizon 2020, D6.2, Jan. 2021.

[104] A. Suvorov, A. Askarov, Y. Bay, B. Maliuta, A. Achitaev, and K. Suslov, "Comparative small-signal stability analysis of voltage-controlled and enhanced current-controlled virtual synchronous generators under weak and stiff grid conditions," *Int. J. Electr. Power Energy Syst.*, vol. 147, p. 108891, May 2023, doi: 10.1016/j.ijepes.2022.108891.

[105] E. Heylen, G. Strbac, and F. Teng, "Challenges and opportunities of inertia estimation and forecasting in low-inertia power systems," *ArXiv200812692 Cs Eess*, Aug. 2020, Accessed: Jan. 26, 2021. [Online]. Available: http://arxiv.org/abs/2008.12692

[106] B. Tan, J. Zhao, M. Netto, V. Krishnan, V. Terzija, and Y. Zhang, "Power system inertia estimation: Review of methods and the impacts of converter-interfaced generations," *Int. J. Electr. Power Energy Syst.*, vol. 134, p. 107362, Jan. 2022, doi: 10.1016/j.ijepes.2021.107362.

[107] K. Tuttelberg, J. Kilter, D. Wilson, and K. Uhlen, "Estimation of Power System Inertia From Ambient Wide Area Measurements," *IEEE Trans. Power Syst.*, vol. 33, no. 6, pp. 7249–7257, Nov. 2018, doi: 10.1109/TPWRS.2018.2843381.

[108] V. Sagar and S. Kumar Jain, "Estimation of Power System Inertia Using System Identification," in *2019 IEEE Innovative Smart Grid Technologies - Asia (ISGT Asia)*, Chengdu, China: IEEE, May 2019, pp. 285–290. doi: 10.1109/ISGT-Asia.2019.8881308.

[109] F. Allella, E. Chiodo, G. M. Giannuzzi, D. Lauria, and F. Mottola, "On-Line Estimation Assessment of Power Systems Inertia With High Penetration of Renewable Generation," *IEEE Access*, vol. 8, pp. 62689–62697, 2020, doi: 10.1109/ACCESS.2020.2983877.

[110] A. Fernández-Guillamón, A. Vigueras-Rodríguez, and A. Molina-García, "Analysis of power system inertia estimation in high wind power plant integration scenarios," *IET Renew. Power Gener.*, vol. 13, no. 15, pp. 2807–2816, Nov. 2019, doi: 10.1049/iet-rpg.2019.0220.

[111] M. Liu, J. Chen, and F. Milano, “On-line Inertia Estimation for Synchronous and Non-Synchronous Devices,” *IEEE Trans. Power Syst.*, pp. 1–1, 2020, doi: 10.1109/TPWRS.2020.3037265.

[112] F. Milano and A. Ortega, “Frequency Divider,” *IEEE Trans. Power Syst.*, pp. 1–1, 2016, doi: 10.1109/TPWRS.2016.2569563.

[113] F. Milano and A. Ortega, “A Method for Evaluating Frequency Regulation in an Electrical Grid Part I: Theory,” *IEEE Trans. Power Syst.*, pp. 1–1, 2020, doi: 10.1109/TPWRS.2020.3007847.

[114] T. Littler, B. Fox, and D. Flynn, “Measurement-based Estimation of Wind Farm Inertia,” in *2005 IEEE Russia Power Tech*, Jun. 2005, pp. 1–5. doi: 10.1109/PTC.2005.4524432.

[115] O. Beltran, R. Peña, J. Segundo, A. Esparza, E. Muljadi, and D. Wenzhong, “Inertia Estimation of Wind Power Plants Based on the Swing Equation and Phasor Measurement Units,” *Appl. Sci.*, vol. 8, no. 12, p. 2413, Nov. 2018, doi: 10.3390/app8122413.

[116] “Wind energy generation systems. Part 21-1: Measurement and assessment of electrical characteristics - Wind turbines (IEC 61400-21-1:2019),” BSI Standards Limited 2019, Brussels, Belgium, 07 2019.

[117] R. H. Park, “Two-reaction theory of synchronous machines generalized method of analysis-part I,” *Trans. Am. Inst. Electr. Eng.*, vol. 48, no. 3, pp. 716–727, Jul. 1929, doi: 10.1109/T-AIEE.1929.5055275.

[118] E. Clarke, “Circuit Analysis of A-C Power Systems,” *Symmetrical Relat. Compon.*, vol. 1, 1943, Accessed: Mar. 31, 2023. [Online]. Available: https://cir.nii.ac.jp/crid/1573950401099563392

[119] A. Junyent-Ferre and O. Gomis-Bellmunt, “Control of power electronic converters for the operation of wind generation systems under grid disturbances,” Universitat Politecnica de Catalunya, Barcelona, Spain, 2011.

[120] A. Rolan, A. Luna, G. Vazquez, D. Aguilar, and G. Azevedo, “Modeling of a variable speed wind turbine with a Permanent Magnet Synchronous Generator,” in *2009 IEEE International Symposium on Industrial Electronics*, Seoul, South Korea: IEEE, Jul. 2009, pp. 734–739. doi: 10.1109/ISIE.2009.5218120.

[121] H. Geng, D. Xu, B. Wu, and G. Yang, “Active Damping for PMSG-Based WECS With DC-Link Current Estimation,” *IEEE Trans. Ind. Electron.*, vol. 58, no. 4, pp. 1110–1119, Apr. 2011, doi: 10.1109/TIE.2010.2040568.

[122] R. Peña-Alzola, M. Liserre, F. Blaabjerg, M. Ordonez, and Y. Yang, “LCL-Filter Design for Robust Active Damping in Grid-Connected Converters,” *IEEE Trans. Ind. Inform.*, vol. 10, no. 4, pp. 2192–2203, Nov. 2014, doi: 10.1109/TII.2014.2361604.

[123] P. Krause, O. Wasynczuk, S. D. Sudhoff, and S. Pekarek, “Theory of Electromechanical Energy Conversion,” in *Analysis of Electric Machinery and Drive Systems*, IEEE, 2013, pp. 1–52. doi: 10.1002/9781118524336.ch1.

[124] M. Klein, G. J. Rogers, and P. Kundur, “Analytical investigation of factors influencing power system stabilizer.,” *IEEE Power Eng. Soc. Iner-Area Oscil. Power Syst.*, pp. 144–15, 1994.

[125] “Performance of Three PSS for Interarea Oscillations - MATLAB & Simulink - MathWorks United Kingdom.” https://uk.mathworks.com/help/sps/ug/performance-of-three-pss-for-interarea-oscillations.html (accessed Mar. 31, 2023).

[126] D. Goodfellow and G. Smith, “Control strategy for variable speed of a fixed-pitch wind turbine operating in a wide speed range,” in *Proceedings of 8th BWEA Conference*, 1986, pp. 219–228.

[127] A. Egea-Alvarez, S. Fekriasl, F. Hassan, and O. Gomis-Bellmunt, “Advanced Vector Control for Voltage Source Converters Connected to Weak Grids,” *IEEE Trans. Power Syst.*, vol. 30, no. 6, pp. 3072–3081, Nov. 2015, doi: 10.1109/TPWRS.2014.2384596.

[128] M. Cheah-Mane, A. Egea-Alvarez, E. Prieto-Araujo, H. Mehrjerdi, O. Gomis-Bellmunt, and L. Xu, “Modeling and analysis approaches for small-signal stability assessment of power-electronic-dominated systems,” *WIREs Energy Environ.*, vol. 12, no. 1, p. e453, 2023, doi: 10.1002/wene.453.

[129] L. Zhang, L. Harnefors, and H.-P. Nee, “Modeling and Control of VSC-HVDC Links Connected to Island Systems,” *IEEE Trans. Power Syst.*, vol. 26, no. 2, pp. 783–793, May 2011, doi: 10.1109/TPWRS.2010.2070085.

[130] D. Pan, X. Wang, F. Liu, and R. Shi, “Transient Stability of Voltage-Source Converters With Grid-Forming Control: A Design-Oriented Study,” *IEEE J. Emerg. Sel. Top. Power Electron.*, vol. 8, no. 2, pp. 1019–1033, Jun. 2020, doi: 10.1109/JESTPE.2019.2946310.

[131] X. Xie, W. Liu, H. Liu, Y. Du, and Y. Li, “A System-Wide Protection Against Unstable SSCI in Series-Compensated Wind Power Systems,” *IEEE Trans.*

Power Deliv., vol. 33, no. 6, pp. 3095–3104, Dec. 2018, doi: 10.1109/TPWRD.2018.2829846.

[132] C. Karunanayake, J. Ravishankar, and Z. Y. Dong, “Nonlinear SSR Damping Controller for DFIG Based Wind Generators Interfaced to Series Compensated Transmission Systems,” *IEEE Trans. Power Syst.*, vol. 35, no. 2, pp. 1156–1165, Mar. 2020, doi: 10.1109/TPWRS.2019.2938230.

[133] *IEEE Guide for Planning DC Links Terminating at AC Locations Having Low Short-Circuit Capacities*. 1997.

[134] I. Cvetkovic, D. Boroyevich, R. Burgos, C. Li, and P. Mattavelli, “Modeling and control of grid-connected voltage-source converters emulating isotropic and anisotropic synchronous machines,” in *2015 IEEE 16th Workshop on Control and Modeling for Power Electronics (COMPEL)*, Vancouver, BC, Canada: IEEE, Jul. 2015, pp. 1–5. doi: 10.1109/COMPEL.2015.7236454.

[135] Y. Qi, H. Deng, X. Liu, and Y. Tang, “Synthetic Inertia Control of Grid-Connected Inverter Considering the Synchronization Dynamics,” *IEEE Trans. Power Electron.*, vol. 37, no. 2, pp. 1411–1421, Feb. 2022, doi: 10.1109/TPEL.2021.3106948.

[136] S. Harrison, P. N. Papadopoulos, R. D. Silva, A. Kinsella, I. Gutierrez, and A. Egea-Alvarez, “Impact of Wind Variation on the Measurement of Wind Turbine Inertia Provision,” *IEEE Access*, vol. 9, pp. 122166–122179, 2021, doi: 10.1109/ACCESS.2021.3109504.

[137] S. Harrison, C. Henderson, P. N. Papadopoulos, and A. Egea-Alvarez, “Assessment of droop and VSM equivalence considering the cascaded control dynamics,” presented at the ACDC 2021, Submitted, p. 6.

[138] “Technical Report on the events of 9 August 2019,” ofgem, Jun. 2019. Accessed: Jan. 02, 2022. [Online]. Available: https://www.ofgem.gov.uk/sites/default/files/docs/2019/09/eso_technical_report_-_final.pdf

[139] A. Dyśko *et al.*, “Testing Characteristics of Grid Forming Converters Part III: Inertial Behaviour,” p. 8, Nov. 2020.

[140] D. Orihara *et al.*, “Contribution of Voltage Support Function to Virtual Inertia Control Performance of Inverter-Based Resource in Frequency Stability,” *Energies*, vol. 14, no. 14, p. 4220, Jul. 2021, doi: 10.3390/en14144220.

[141] M. Bakhtvar, E. Vittal, K. Zheng, and A. Keane, "Synchronizing Torque Impacts on Rotor Speed in Power Systems," *IEEE Trans. Power Syst.*, vol. 32, no. 3, pp. 1927–1935, May 2017, doi: 10.1109/TPWRS.2016.2600478.

[142] K. Tuttelberg, J. Kilter, and K. Uhlen, "Comparison of system identification methods applied to analysis of inter-area modes," presented at the e International Conference on Power Systems Transients (IPST2017), Seoul, South Korea, Jun. 2017, p. 6.

[143] National Grid ESO, "Power Available: Unlocking Renewables' Potential to Help Balance the Electricity System," May 19, 2020. https://www.nationalgrideso.com/news/power-available-unlocking-renewables-potential-help-balance-electricity-system (accessed Sep. 03, 2021).

[144] T. Burton, D. Sharpe, N. Jenkins, and E. Bossanyi, "The Wind Resource," in *Wind Energy Handbook*, John Wiley & Sons Ltd, 2003, pp. 11–39.

[145] MathWorks, "System Identification Toolbox," 2020. https://uk.mathworks.com/products/sysid.html (accessed Jan. 08, 2020).

[146] "Load-Frequency Control Annual Report 2018," ENTSO-E, Brussels, Belgium, Sep. 2019.

[147] C. Broderick, "Rate of Change of Frequency (RoCoF) withstand capability," ENTSO-E, Brussels, Belgium, Jan. 2018.

[148] "Changes to the Distribution Code and Engineering Recommendation G59: Frequency Changes during Large Disturbances and their Impact on the Total System." ofgem, Jul. 23, 2014.

[149] "IEC 61400-1 INTERNATIONAL STANDARD Wind turbines - Part 1: Design requirements," International Electrotechnical Commission, Geneva, Switzerland, 2005.